Universidad de Alcalá

Escuela Politécnica Superior

Máster Universitario en Ingeniería Industrial

Trabajo Fin de Máster

Control Analysis and Design of Medium Voltage Converter with Multirate Techniques

Autor: Javier Serrano Delgado

Tutor/es: Emilio José Bueno Peña

Mario Rizo Morente

2018

UNIVERSIDAD DE ALCALÁ
Escuela Politécnica Superior

Máster Universitario en Ingeniería Industrial

Trabajo Fin de Máster

Control Analysis and Design of Medium Voltage Converter with Multirate Techniques

Autor: Javier Serrano Delgado
Tutor/es: Emilio José Bueno Peña
Mario Rizo Morente

TRIBUNAL:

Presidente: Santiago Cóbreces Álvarez

Vocal 1º: Manuel Roza Zurera

Vocal 2º: Emilio José Bueno Peña

FECHA: 11/09/2018

Acknowledgements

Las casualidades no existen, solo creo en las probabilidades y, por eso, la consecución de este objetivo ha sido gracias al apoyo de mi familia, pareja y amigos. Así que, por un lado, no quiero dejar de agradecer a mis padres, Fernando y Victoria, todo lo que nos han aportado a mis hermanos y a mí, destacando dos cosas fundamentales: cariño y valores. También a Jésica, por ser mi mejor amiga y compañera de vida, con la que puedo compartir mis penas y glorias porque siempre está ahí. Y a mis amigos, Álvaro, Sergio, Ricardo y Jairo, por darme buenos momentos desde que tengo uso de razón, los cuales han permitido a mi cabeza abandonar los compromisos durante un par de horas.

Por otro lado, me gustaría agradecer a Emilio y Mario su tutela, porque, aunque el tema que hemos propuesto sea complicado, me han apoyado y he alcanzado los objetivos. Espero que este sea el comienzo de nuevos e interesantes proyectos.

También agradecer a los compañeros de despacho, Javier y Marco, sus consejos y conversación durante este tiempo. A los que además deseo lo mejor en su futuro profesional.

Gracias a todos ellos tengo un equilibrio vital que me permite vivir sin miedo a las aspiraciones futuras.

"*Vivir es enfrentar un problema tras otro. La forma en que lo encaras hace la diferencia*"

Benjamin Franklin

Contents

List of figures

List of tables

List of acronyms

AC	Alternating Current
ADC	Analog-to-Digital Converter
ANPC	Active Neutral Point Clamped
APF	Active Power Filter
APOD	Alternate Phase Opposite Disposition
BJT	Bipolar Junction Transistor
BMIO	Block Multirate Input Output
CSC	Current-Source Converter
DBS	Distributed Bus Signaling
DC	Direct Current
DG	Distributed Generator
DNPC	Diode Neutral Point Clamped
DSP	Digital Signal Processor
DSPWM	Digital Sinusoidal Pulse Width Modulation
EES	Energy Storage System
EMF	Electromotive Force
EMS	Energy Management System
ER	External Representation
EU	European Union
FACTS	Flexible AC Transmission Systems
FPGA	Field-Programmable Gate Array
GCD	Greatest Common Divisor
GTO	Gate Turn-Off Thyristors
IGCT	Integrated Gate-Commutated Thyristors
IGBT	Insulated Gate Bipolar Transistor
IPD	In-Phase Disposition
IR	Internal Representation
LC	Local Controller
LQR	Linear Quadratic Regulator
LTI	Linear Time-Invariant
LV	Low Voltage
MAS	Multi-Agent System
MIMO	Multiple-Input Multiple-Output
MG	MicroGrid
MGCC	MicroGrid Central Controller
MOSFET	Metal-Oxide-Semiconductor Field-Effect Transistor
MRFORC	Multi-Rate Fractional-Order Repetitive Control
MRIC	Multi-Rate Input Controller
MROC	Multi-Rate Output Controller

MV	Medium Voltage
NCO	Numerically Controller Oscillator
NLM	Nearest Level Modulation
NPC	Neutral Point Clamped
PI	Proportional Integral
PLC	Power Line Communication
PLL	Phase-Locked Loop
POD	Phase Opposite Disposition
PVT	Periodically Variable in Time
PWM	Pulse Width Modulation
RC	Repetitive Control
ROGI	Reduced Order Generalized Integrator
SCR	Silicon Controlled Rectifier
SISO	Single-Input Single-Output
SHE	Selective-Harmonic Elimination
SPWM	Sinusoidal Pulse Width Modulation
SRF-PLL	Synchronous Reference Frame Phase-Locked Loop
STATCOM	Static synchronous Compensator
SVM	Space Vector Modulation
THD	Total Harmonic Distortion
THSPWM	Third Harmonic Sinusoidal Pulse Width Modulation
TRIAC	Triode for Alternating Current)
VSC	Voltage-Source Converter
VSD	Vectorial Switch Decomposition
WBG	Wide-Bandgap
ZOH	Zero-Order Hold

Resumen

Este trabajo pretende unir el conocimiento actual sobre controladores multitasa o multifrecuencia (*multirate*) con técnicas de diseño para convertidores conectados a la red, en este caso concreto, a la red alterna (AC) de Media Tensión. Por tanto, se estudian las contribuciones multirate realizadas hasta la fecha, así como todo lo relacionado con la modulación de la señal de control para los convertidores. Las implicaciones temporales del actuador DSPWM se relacionarán con el análisis multitasa, así como se explicarán posibles alternativas para aplicaciones con una frecuencia de muestreo menor que la de modulación. Finalizando con la explicación y presentación de resultados de controladores trabajando entre dos frecuencias o tasas, mediante simulaciones del convertidor disponible en laboratorio.

Palabras clave: Tiempo discreto, Modelado, Media tensión, Convertidores de potencia, Multitasa.

Abstract

This work aims to unify the current knowledge about multirate controllers with design techniques for grid-tied converters, in this occasion, connected to Medium Voltage AC grid. Therefore, the multirate contributions, that have been given so far, are studied, as well as everything related to modulation techniques for power converters. The temporal implications of the DSPWM actuator will be correlated to multirate analysis, in addition to possible alternatives for applications with a lower sampling frequency than modulation one. Finalizing with explanations and result demonstrations of controllers working between two frequencies or rates, by means of the available power converter in laboratory.

Keywords: Discrete-time, Modelling, Medium Voltage, Power converters, Multirate.

Extended abstract

Multirate control is an unusual technique in power electronics, so this works aims to give an alternative for controller designers in power electronics when hardware or software constraints can be found. These limitations could be related to sampling and actuation rates, when hardware ADC or switching frequency, respectively, cannot be correctly synchronized. Even, computational burden can lead to this situation, if the designer wants to maximize the performance of the converter.

These reasons lead to a detailed analysis of modulation techniques, directly related with control actuation, and current proposals in power electronics. The DSPWM is an interesting modulation technique, that is profoundly analyzed in this document to keep clear what are the consequences of applying multirate methods to it. Besides, its temporal characteristics are related with the modified Z-transform, which is also linked with multirate analysis. In addition, two multirate studies in power electronics are presented, each of them with a different point of view. One takes internal representation to get a single-rate equivalent that is analyzed with usual techniques of stability and robustness. Hence, the internal representation using Kranc methodology with three different situations is introduced. The other example uses the external representation to also get a single-rate equivalent to analyze its stability and robustness.

The complex-coefficient systems are usual in power electronics due to phasor nature of controlled variables. For that reason, this document works with complex-valued models of the L-filter for each reference frame to be studied. Besides, its discretization is detailed, because computational delay interferes in rotating reference frame transformation.

Then, some multirate applications must be presented to give context to the possibilities of multirate control in power electronics. Firstly, a relationship is inferred between DSPWM and SHE modulation techniques with a sinusoidal extrapolation technique. For DSPWM, the crossing between modulating and carrier signals could compromise the switching device, so proper gate drive signals must be generated. For SHE modulation, this document presents a possible alternative using polynomial extrapolation, but the correct extrapolation is the same taken for DSPWM. These situations are related to multirate current control, but there are possibilities for hierarchical control in power converters too. Frequently, every control level has its own rate, so maybe multirate techniques could be used for enhancing the overall system performance. To associate this later concept with an actual application, few explanations are given about Microgrids.

The main goal of this document is to introduce multirate analysis in the current control loop. The multirate approach needs single-rate control structures on which to be based, so two complex-valued controllers in stationary and rotating reference frame

are introduced. Then, a possible example using internal representation (space-state) is shown to obtain single-rate equivalents that allow the designer to use habitual stability and robustness analysis tools. Detailed simulation will endorse the single-rate equivalents.

Nevertheless, a more sophisticated multirate technique must be used to properly control the system. Consequently, a model-based dual-rate controller is presented. In these proposals, the sampling frequency is lower than the modulation one, so the goal is to maximize the performance of the control system and to obtain the same response that could be obtained by using a fast single-rate controller. The controller gets extraordinary results that are endorsed by detailed simulation of the grid-tied power converter.

The grid-tied power converter parameters are those from the 3L-DNPC-VSC in research laboratory, which works in Low Voltage. In this way, the simulation results that will be shown here can be compared with future experimental test. The issue is in MV, but tests are adapted to available resources.

Furthermore, appendix given in this document will help to the reader to consider the bases that supports some concepts. Firstly, modified Z-transform is explained and related with multirate systems. Then, vector representation of three-phase systems is briefly introduced, because it is needed for controller design and plant modelling. Finally, two basic control structures in VSC are presented.

Chapter 1. Introduction

1.1. Motivation

Nowadays, the electric energy powers the world and its demand is growing every year, what is a challenge because the electric power system complexity rises with it. The complexity increases with the renewable energy resources added by the increasing demand of CO_2-free energy, which is enforced by the laws. The European Union target is a 20% final energy consumption from renewable sources by 2020. Each EU country is committed to reach its own national renewable energy action plan, which includes sectorial targets for electricity, heating and cooling, and transport. Figure 1.1 shows the trend in the recent years. Besides, the Europe 2020 target is a 20% increase in energy efficiency. In absolute terms this means that by 2020 EU energy consumption should not exceed 1483 Mtoe (million tonne of oil equivalent) of primary energy or 1086 Mtoe of final energy.

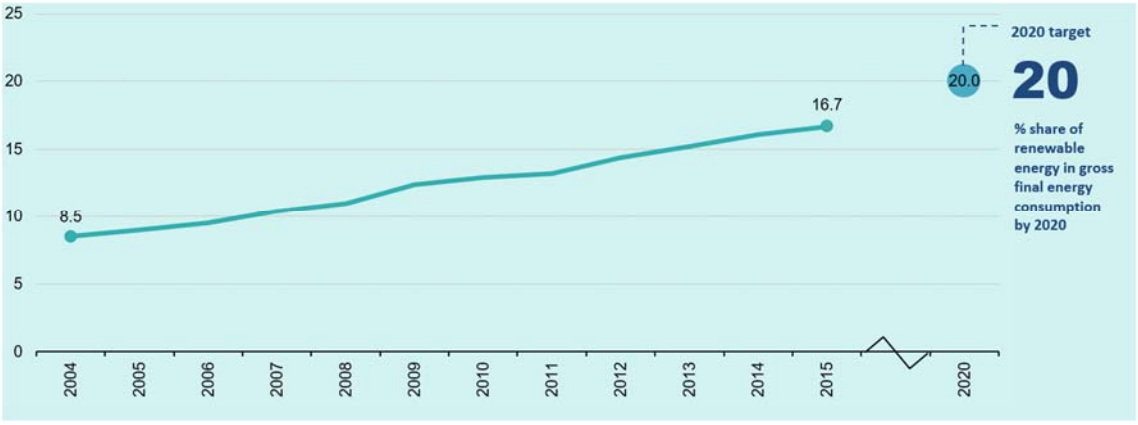

Figure 1.1. Share of renewable energy in gross final energy consumption. Source: Eurostat

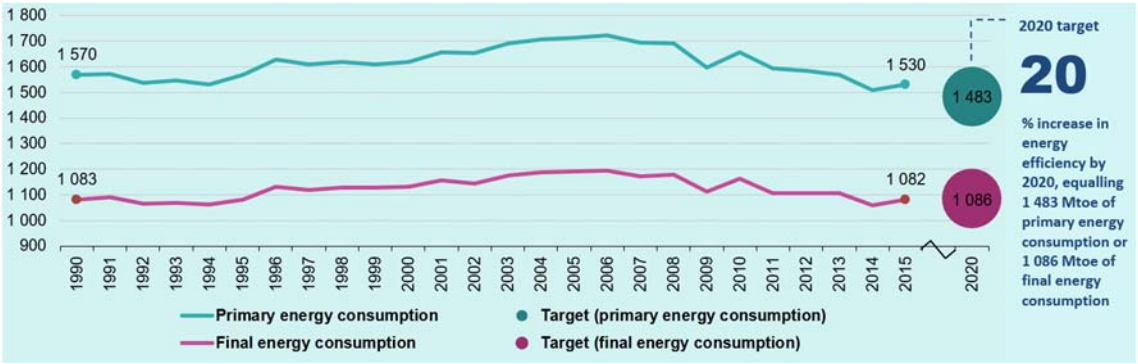

Figure 1.2. Primary energy consumption and final energy consumption. Source: Eurostat

The energy losses occurring during energy transformation (particularly electricity generation), transmission and distribution determine the difference between primary and final energy consumption. In Figure 1.2 is shown the path over the past years.

A new target of at least 27% of final energy consumption is set for 2030 for helping the EU meet its energy needs beyond 2020. The European Commission wants to make the EU a global leader in renewable energy. These reasons lead to an active research of renewable energy sources and efficiency in each energy conversion.

The distribution approach is changing in the recent years, since the spreading of distributed generators. The management of small distributed producers, essentially renewable sources, have become an important issue to get a reliable and stable network. There is where the power electronic systems have an important role as they could manage the energy exchange between grid and producers, as well as grid quality. Hence, the new distribution approach is a smart high-power medium-voltage (MV) system, where power converters are used in applications such as motor drives, flexible AC transmission systems (FACTS), renewable energy resources integration, or efficient conversion. Note that IEC 60038 defines each voltage level as it is shown in Table 1.1.

Table 1.1. Voltage ranges. Source: IEC 60038

IEC voltage range	AC three-phase RMS voltage [V]
Extra-low Voltage	< 50
Low Voltage	100 to 1000
Medium Voltage	1000 to 35000
High Voltage	35000 to 230000
Extra-high Voltage	> 245000

On one hand, Flexible AC Transmission Systems (FACTS) technology enhances the controllability and increase power transfer capability of the power system. FACTS technology lead to new opportunities for controlling the power and improving the usable capability of lines. The used technology is power electronic-based and other static controllers, where the words “other static controllers” is referred to those which are not based on power electronics. The power electronic-based static controllers provide control of one or more AC transmission system parameters as line impedance, angle, or voltage.

On the other hand, power electronic converters provide an efficient and stable power flow between the utility grid and renewable sources, and even among forms of transport. Electric vehicles need converters to charge their batteries and most trains are electric-based. Also, metropolitan trains need an efficiency energy consumption, so the regenerative brake provides an energy recovery to the own railway electric grid through power electronic converters.

The power electronic converters are essential to enhance grid flexibility and to achieve the new efficiency requirements. Therefore, the power converter operation must be reliable, flexible, efficient, and economic, so must the controllers.

The power switching device is the essential component of each converter. The semiconductor switching device evolution has been always aimed to achieve an ideal switch. And evaluated switching device characteristics are the operating frequency, the blocking voltage, and the device current. Therefore, an ideal switch would have infinite operation frequency, infinite blocking voltage, null drop voltage when on, and null drive current when off and infinite when on. That is no conduction or switching losses.

The commercial devices are not ideal, and they never will, so each kind of semiconductor switching device is appropriated to each application according to the system requirements. Besides, the switching frequency determines the control rate for MV converters as it is intrinsically related by the actuator. Although multilevel converters could improve the management of more voltage, current or higher equivalent switching frequency, some MV converters use more economic topologies where the device switching frequency still constrains the control rate.

1.1.1. Flexible AC Transmission System (FACTS) controllers

FACTS controllers improve the power transfer capability of existing transmission and distribution lines. The delivery period of FACTS technology is lower than the installation of new lines, which makes this technology more attractive.

FACTS controllers could be classified into four categories[1]:

a) **Series controllers**: Could be a variable impedance, or a power electronic based variable source of main frequency, subsynchronous and harmonic frequencies (or a combination) to serve the desired need. Essentially, it injects voltage in series with the line.
b) **Shunt controllers**: May be variable impedance, variable source, or a combination of these. Essentially, it injects current into the system at the point of connection. If the injected current is in phase quadrature with the line voltage, this controller only supplies or consumes variable reactive power. Otherwise, a phase relationship involves a real power consumption.
c) **Combined series-series controllers**: Could be a combination of coordinated series controller in a multiline transmission, or a unified controller which provides independent series reactive compensation and transfers real power.
d) **Combined series-shunt controllers**: Could be a combination of coordinated series and shunt controller, or a unified controller which provides independent series reactive compensation and transfer real power. They inject current into the system with the shunt part and voltage in series in the line with the series part.

The different types of FACTS Controllers are summarized in Figure 1.3. The application defines the type of controller, e.g. if the purpose is to control the current/power flow and damp oscillations, the series Controller for a given rated power is more powerful than the shunt Controller. The shunt Controller is more willing to control voltage at and around the point of connection through the injection of reactive current, alone or a combination of active and reactive current for a more effective

voltage control and damping of voltage oscillations. The combination of the series and shunt Controllers can provide the best of both, that is an effective power flow and line voltage control. Also, a Controller with storage (large DC capacitors, storage batteries, or superconducting magnets) is much more effective for controlling the system dynamics, i.e. the dynamic pumping of active power. In addition, a converter can be designed to generate the compensate waveform to act as an active filter. Each one has its benefits and attributes, and a preliminary evaluation is needed.

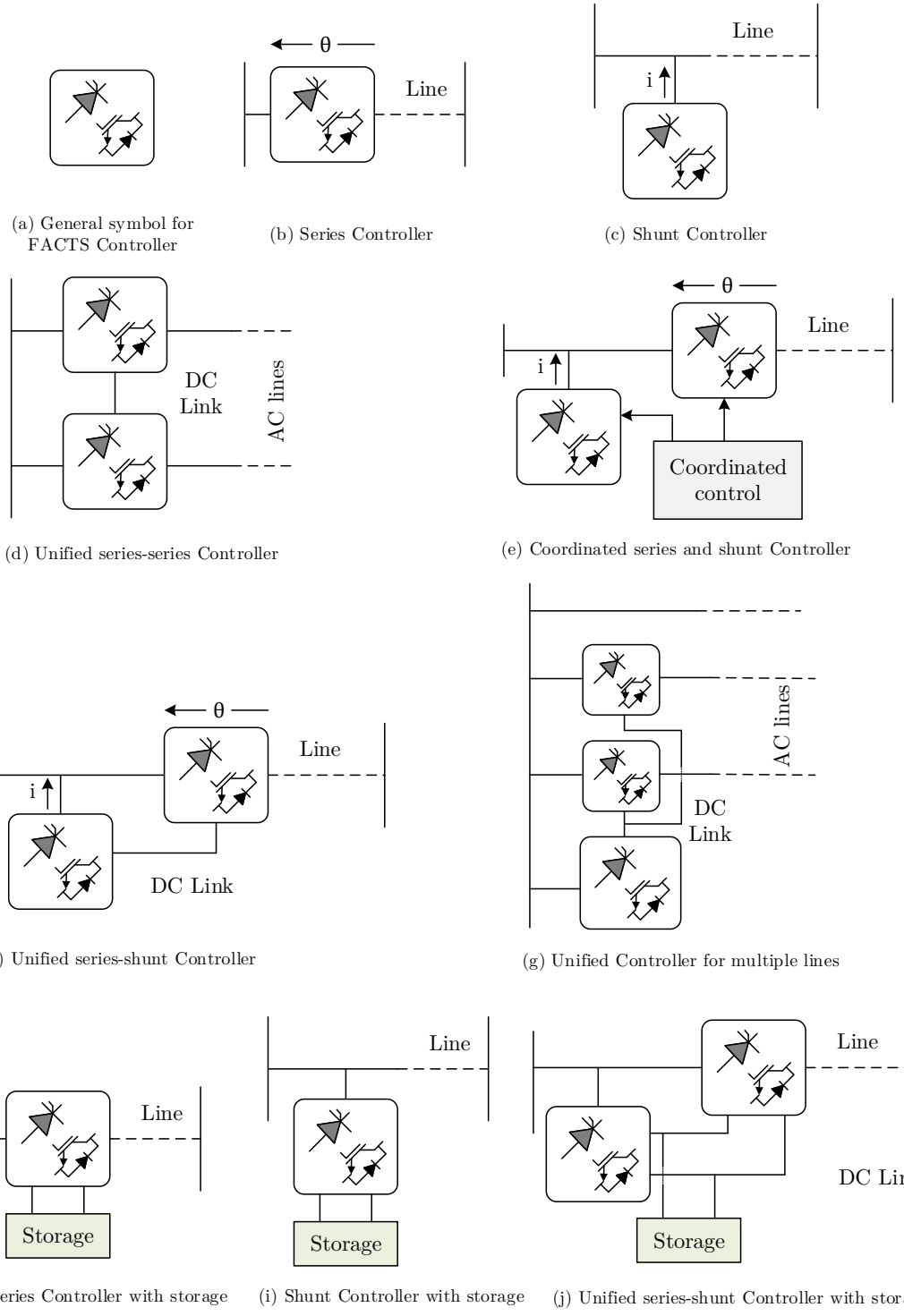

(a) General symbol for FACTS Controller

(b) Series Controller

(c) Shunt Controller

(d) Unified series-series Controller

(e) Coordinated series and shunt Controller

(f) Unified series-shunt Controller

(g) Unified Controller for multiple lines

(h) Series Controller with storage

(i) Shunt Controller with storage

(j) Unified series-shunt Controller with storage

Figure 1.3. Basic types of FACTS Controllers

To sum up, every FACTS is a variable impedance that is focused on the needed application.

Besides, for the converter-based controllers there are two types: voltage-sourced converters (VSC) and the current-sourced converters (CSC). CSC topology is used in high-power drivers, where GTO and IGCTs are the switching devices. The CSC operates at fixed current while the voltage is modulated. The most common topology is the VSC due to its controllability.

In summary, FACTS controllers will ensure the power system stability, and they will be enhanced by wider area control information systems.

1.1.2. Industrial applications

New highly efficient power electronic technologies and suitable control strategies are needed to reduce energy waste and to improve power quality [2]. Energy efficiency is a potential field in electric motor driven systems. Therefore, the aim is to introduce efficient MV adjustable speed drives in industrial applications.

In MV drives is fundamental a high-quality voltage and current at both terminals, input, and output. The waveforms are related to: topology used, the application, the control algorithm, the size of the filter, and chosen switching frequency. There are different approaches for the optimal solution, and each factor has a different weight in it. The hardware characteristics are not in the scope of this document, but some relation between factors must be considering. An elevated switching frequency increases the switching losses, what reduces the maximum output power, but a switching frequency reduction increases the harmonic distortion in the line and motor side current waveforms and it lead to solution with expensive LC filters. The goal is a converter that reduces harmonic distortion with low switching frequency, and this is accomplished with multilevel converters.

Multilevel converters improve the voltage waveforms compared to the basic two-level voltage source converter (2L-VSC), as they enhance power quality, reduce switching losses, and obtain a high voltage capability. The 2L-VSC cannot be used in applications where is required high converter efficiency and low harmonic distortion, because the LC filter constrains the low carrier frequencies.

The 3L neutral-point-clamped voltage source converter (3L-NPC VSC) is the most efficient among available solutions, and it is the preferred choice in several industrial MV applications [3]. For example, Table 1.2 gives some voltage and power rating of usual industrial MV drives. It requires high switch power, but the expense in the LC filter is moderate. Also, the high switching losses share causes a reduction in installed switch power at low switching frequency. The additional attractive features are: simple grid transformer, a small DC link capacitor, and modular realization of common DC-bus configurations. This multilevel topology is usually compared to flying capacitor voltage source converter (3L / 4L-FLC VSC), and series-connected H-bridge voltage source converters (5L-SCHB VSC). The FLC VSC rises the expense in capacitors, and the SCHB requires a complicated grid transformer, and high DC-link capacitance.

Table 1.2. Market overview of industrial 3L-NPC-VSC MV Drives. Source: [2]

Manufacturer	Type	Power (MVA)	Voltage (kV)	Semiconductor
ABB	ACS 1000	$0.3 - 5$	$2.3; 3.3; 4.0; 4.16$	IGCT
	ACS 6000	$3 - 27$	$2.3; 3; 3.3$	IGCT
Siemens	Sinamics SM120 CM	$6 - 13.7$	$3.3 - 7.2$	MV IGBT
	Sinamics SM150	$5 - 28$	3.3	IGCT
	Sinamics GM150	$0.6 - 10.1$	$2.3; 3.3; 4.16; 6; 6.6$	MV IGBT
Alstom	VDM7000	$0.3 - 8$	3.3	PP-MV-GTO
TMEIC GE	Dura-Bilt5i MV	7.5	$4 - 4.2$	IGBT

Therefore, the 3L NPC VSC is characterized by a relatively small DC-link capacitor, a simple power circuit topology, low number of components, and straightforward protection and modulation schemes. These features make it a competitive solution for a large variety of low and medium switching frequency applications.

The 3L-NPC VSC has positioned as an essential in more conventional high-power AC motor drive applications like conveyors, pumps, fans, and mills. Also, a back-to-back configuration is possible with this topology, which is attractive for regenerative applications, as in regenerative conveyors for the mining industry or grid interfacing of renewable energy sources. The regenerative applications are also present in transports, as electric trains, or vehicle applications.

As it is mentioned before, the control algorithm is one of the factors related to the waveform quality and converter response, and it is the taken power converter approach in this document.

Figure 1.4. SINAMICS SM120 CM Medium Voltage drive. Source: Siemens web

1.1.3. Power semiconductor devices

Every power converter is composed of semiconductor devices and the characteristics of each one determines its applications. The desirable characteristics on any of them are:

1. **On-state characteristics**: High-current rating, and low forward voltage drop.
2. **Off-state characteristics**: High forward and reverse voltage blocking capability, and low leakage current.
3. **Switching characteristics**: Low power and controllable turn-on and turn-off, high dv/dt and di/dt transitions ratings, and low switching power losses.
4. **Gate characteristics**: Low gate-drive voltage and low gate-drive current, and low gate drive power.
5. **Fault withstanding capability**: Withstand fault current for a long time.
6. **Thermal stability**: Low thermal impedance coefficient from the internal junction to ambient.

Hence, among other characteristics, the ideal device features high handling current, high blocking voltage and high switching frequency. However, there is no ideal device, and an equilibrium between these characteristics is obtained in each power semiconductor device.

Before start with an overview in the technologies and trends in power semiconductor devices, a first classification might be shown to differentiate them as a function of its controllability [4]:

a) **Uncontrolled turn-on and turn-off**: Commonly known diodes.
b) **Controlled turn-on and uncontrolled turn off**: A category that includes SCR (Silicon Controlled Rectifier), and TRIAC (Triode for alternating current).
c) **Controlled turn-on and controlled turn-off**: This category can be divided into two distinct groups:
    1. **Current-controlled devices**: A positive or negative current pulse is needed to open or block them, respectively. In this category can be found: BJT (Bipolar Junction Transistors), GTO (Gate Turn-Off Thyristors) and IGCT (Integrated Gate-Conmutated Thyristor).
    2. **Voltage-controlled devices**: Also known as MOS (Metal-Oxide-Semiconductor) gate or isolated gate. Since their low control power or high switching frequency, the power semiconductor research and the technological efforts involved in manufacturing have been focused on evolving these devices.
        i. **MOSFET power transistors (MOS Field Effect Transistors)**: They have high switching frequencies (tens or hundreds of kHz) with low power losses. Their limitation is an increase in the on-state resistance along with the rise of the maximum blocking voltage rating, which lead to important power losses during conduction. Therefore, they are not used in high power applications.

ii. **Insulated Gate Bipolar Transistor (IGBT)**: It is a mixture with the low on-state power losses of BJT, and the high switching frequency (low power losses) of MOSFET. It is a transistor that can be used with high-medium switching frequencies (units or tens of kHz) and megawatts power. It is the most widely used in power electronics.

As it was mentioned before, the characteristics of each semiconductor device determine what is the suitable application, as is shown in Figure 1.5.

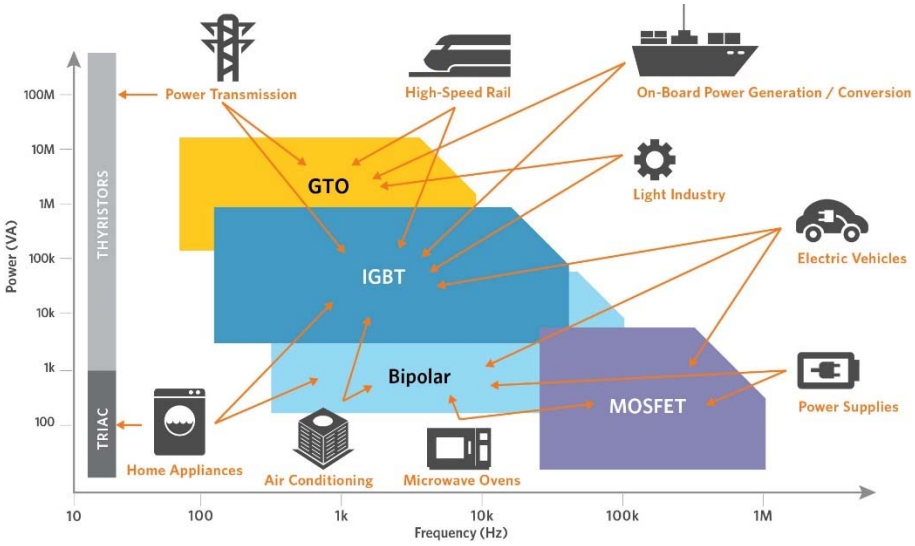

Figure 1.5. Classification of power devices according to their rated power and switching frequency, and their applications. Source: Yole Développement web

Silicon technology is the preferred choice in semiconductors, but in recent years there is an increasing penetration of wide-bandgap (WBG) semiconductors technology [5]. Silicon carbide (SiC) and gallium nitrite (GaN) devices are reaching different levels of maturity, with several manufacturers offering packaging solutions. In Figure 1.6 is shown the perspective on WBG technologies.

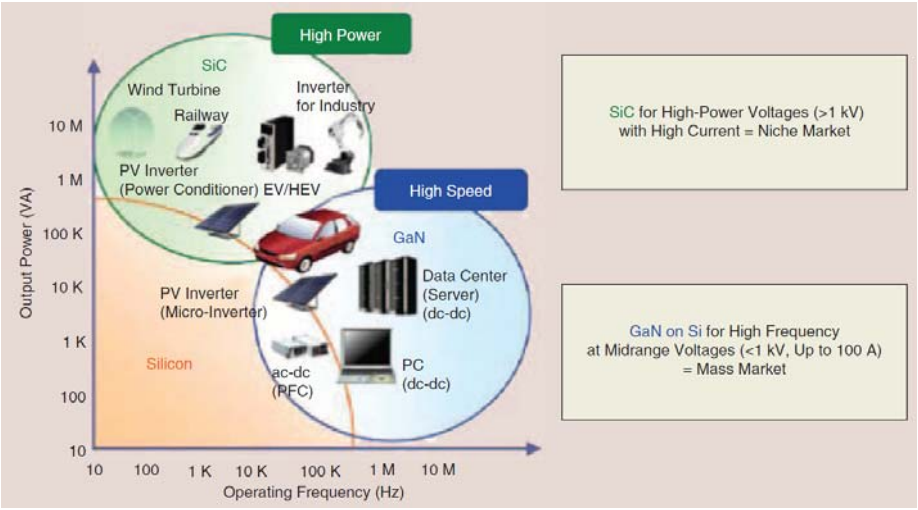

Figure 1.6. Perspective on WBG technologies in terms of frequency and power. Source: [6]

Silicon IGBT is used in high power applications, but the switching frequency is constrained to 2-5kHz due to high switching losses, so the Total Harmonic Distortion (THD) increases. The SiC based MOSFETs and IGBTs for high voltage devices are developed to mitigate these issues. The reduction in the specific on-state resistance in SiC-based devices compared to Si devices results in lower conduction loss.

The SiC MOSFETs feature very low on-state resistance and excellent switching performance, translating into more efficient and compact systems. These devices combine the excellent switching performance of Si MOSFETs and low on-state resistance of Si IGBT.

Hence, the rising in the switching frequency capabilities in high voltage applications around a boundary of 10kHz can change control concepts. Many applications have high computational burden, what constrains the switching frequency if a digital control is designe following conventional structures of modulation. New perspective frame is obtained with different sampling/control rate and modulation/switching rate.

1.1.4. Multirate approach

The multirate system is a structure where two or more variables are updated with different rates or frequencies. Usually, the sampling is considered synchronous and periodic, which is known as conventional sampling, but the samplers might be not synchronized, or they can be variable in time.

Some practical applications have economic and technological constraints that implies the use of control schemes where sensor sampling and control calculation of the actuation is updated with different rates or frequencies. One possible situation could be found when a MV power converter has a low frequency switching device, but the sampling and control frequency could be faster to get a better response. It is known as down-sampling (decimation), and its detailed modelling could improve the system performance, and get the better resources exploitation of the system. However, the inverse situation can be found when the actuation is faster than sampling and control. It is known as up-sampling. The later concept will be explained in this work with few examples as a different digital implementation of SPWM or SHE modulation techniques, or applications where the computational burden of additional control algorithms (e.g. impedance calculation) requires a stability analysis of the control loop. In addition, all hierarchical control with different rates (higher control level, lower bandwidth) can maximize its response with a correct multirate analysis of the system.

Besides, in multivariable systems might be advantageous to get different sampling frequencies for each different loop, so the system performance is improved, and the computational burden is reduced. This is related to what was previously mentioned as additional control algorithms.

In power electronics field, the multirate analysis has a wide niche, because there are few applications in literature correctly modelling or using the multirate approach. Most power electronics applications have their scope in grid synchronization part, but each one of them search for a signal processing to improve the signal acquisition with a

digital antialiasing filter, consequently a fast synchronization is obtained [7][8]. Also, a harmonic estimation can be reached with a multirate digital signal processing [9]. On the other hand, there are some multirate applications in DC/DC that are not in the scope of this work, but they are willing to use some techniques shown here. Thus, this document will only analyze a DC/AC converter in the following chapters.

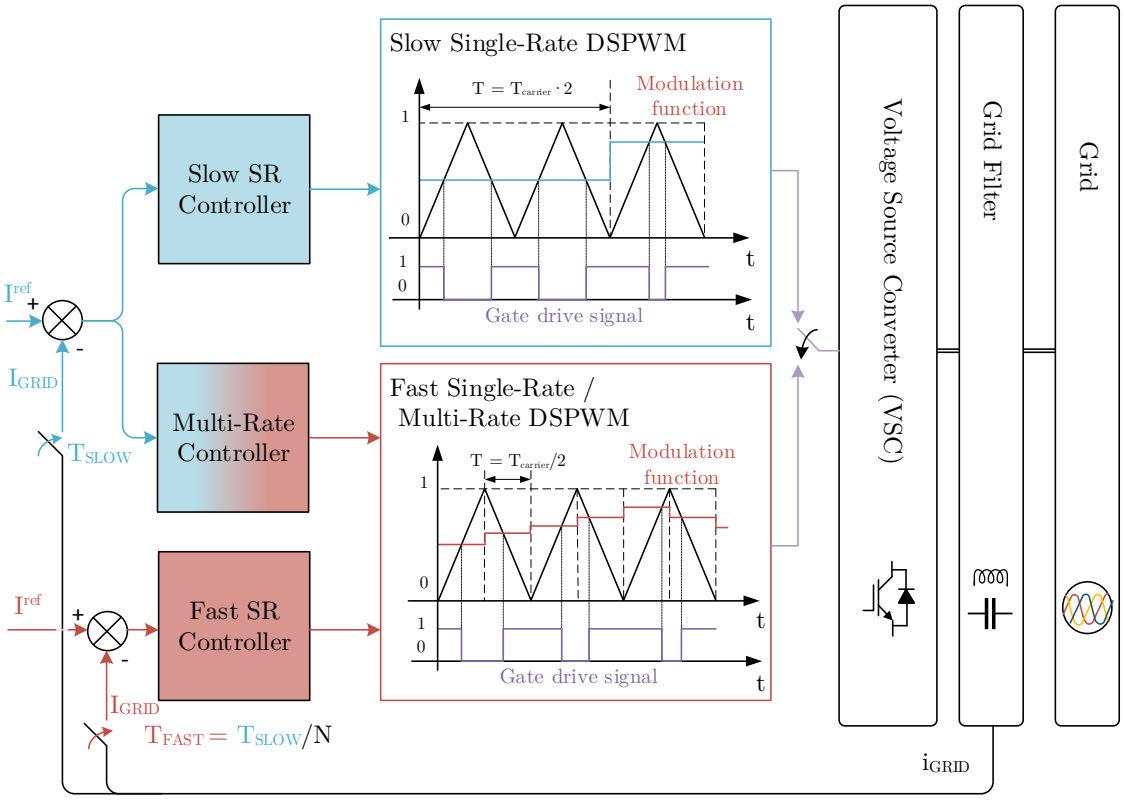

Figure 1.7. Simplified block diagram of single-rate and multirate example of current-controlled systems

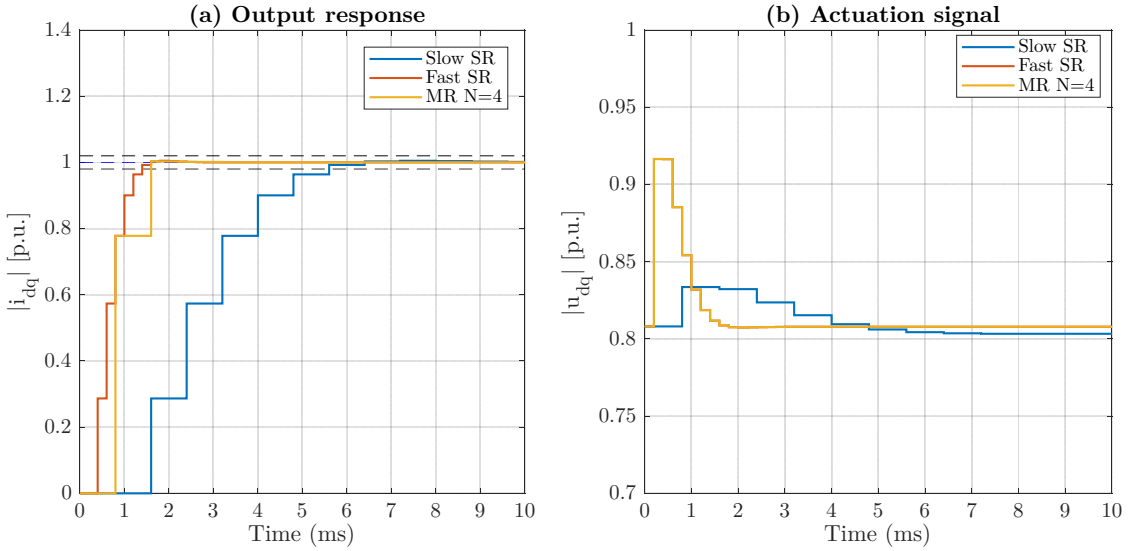

Figure 1.8. Comparison of slow and fast single-rate responses with the multirate approach of a current-controlled system.

For example, Figure 1.7 depicts a possible application where the power converter switching frequency is faster than sampling one. How can the designer obtain an optimum response from the current controller? If the controller works at the slowest rate, that is the sampling rate, the switching frequency will not be optimally used. Hence, the answer is a multirate controller with an input at slow rate and an output at fast rate.

Figure 1.8 shows the response of VSC to step change for a current control loop with a slow single-rate controller (constrained by sampling) and its multi-rate equivalent. The multi-rate controller is based on the possible fast single-rate equivalent, which is designed to reach the steady state in the same discrete steps, so this fast single-rate controller will be faster. Note that N is the multiplier that relates sampling and actuation rates. Detailed information will be given in this work.

1.2. Power converter topology

1.2.1. Classification

This document is based on the controlling of AC/DC topologies, where a few different types can be found, so the topology used in this document should be located into the MV power converter topologies. In MV, the topologies can be split in two categories depending on the imposed variable (source) regardless to the other one:

- **Current-Source Converter (CSC)**: They operate at fixed current (inductor at DC side) while the voltage is modulated. They are suitable to high-power drives, and the dynamic response is relatively slow [10]. This group can be divided into Pulse Width Modulation (PWM) CSC and Load-Commutated Converters (LCC). The difference resides on the switching device, the former uses GTO or IGCT, whereas the latter uses SCR. These topologies are not in the scope of this document.
- **Voltage-Source Converter (VSC)**: These converters operate at fixed voltage (capacitor at DC side). They are the typical topology due to its controllability. The voltage levels obtained at the AC side define the type of VSC, and all are known as multilevel converters. This term includes all the topologies that can supply an output voltage signal with more than two voltage levels, so a classification is shown based on the type of DC supply [11].

The scope of this document is in the 3-Level Neutral Point Clamped (NPC) VSC. It has the highest converter efficiency among the available solutions and is widely used in many industrial MV applications [3]. The most common 3L NPC VSC use a diode to connect each phase to the neutral point and is known as Diode NPC (DNPC). However, the Active Neutral Point Clamped (ANPC) solution is taking interest in MV applications due to the additional controllability of losses, because the diodes are substituted by voltage-controlled switching devices (e.g. IGBT).

1.2.2. Diode Neutral Point Clamped VSC

The 3L-DNPC-VSC was firstly described in [12] and published in [13], and Figure 1.9 shows electronic configuration of this converter with IGBTs and their corresponding free-wheeling diodes. The DC voltage is split into two capacitors, and a neutral point between them is formed. Therefore, each phase generates three voltage levels: $+V_{DC}/2$, 0, $-V_{DC}/2$. Usually an unbalance is generated on the voltage at this point, but the control and analysis are not on the scope of this document, so equal capacitor voltage is considered.

Table 1.3. Switching states on the 3L DNPC VSC

Switching state	**Switch**				**Phase voltage**
	S_1	S_2	S_3	S_4	
P	1	1	0	0	$+V_{DC}/2$
0	0	1	1	0	0
N	0	0	1	1	$-V_{DC}/2$

The clamping diodes are conducting when the switching devices S_2 or S_3 are activated, so the phase line is connected to the neutral point. The DNPC operating point is represented by the switching states on Table 1.3.

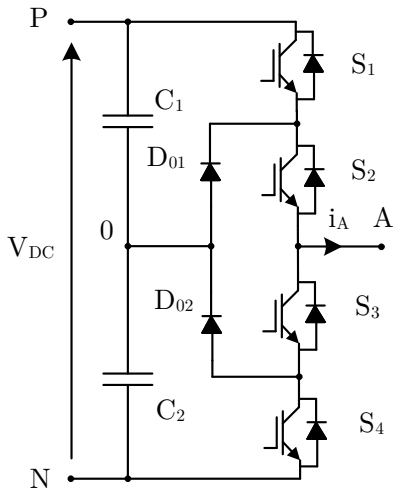

Figure 1.9. Phase structure of a 3L DNPC VSC

The phase current direction determines what device (diode) conducts in the zero (0) switching state. Two equivalent zero states are possible, at the positive or negative half cycle of the phase voltage signal. The devices D_{02} and S_3 conduct with incoming current, whereas D_{01} and S_2 conduct with outgoing current. This is depicted in Figure 1.10.

During the voltage positive half cycle, S_2 is always active and output voltage is controlled with the half-bridge formed by S_1 and S_3, which are complementarily activated. On the other hand, during the voltage negative half cycle, S_3 is always active and output voltage is controlled with the half-bridge formed by S_1 and S_3, which are complementarily activated.

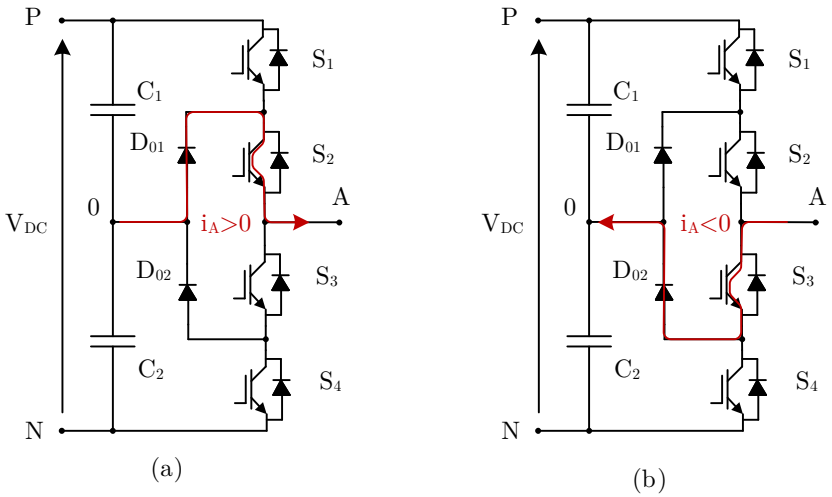

Figure 1.10. Phase current path in 3L-DNP-VSC: (a)Positive (outgoing); (b)Negative (incoming)

A modulation strategy must be followed to convert the reference signal to activation signals. The following chapter will analyze this issue in detail. The main disadvantage of this three-level topology are the non-homogeneous losses in each branch. This is one of the reasons why the maximum switching frequency is limited to the device with more losses, whereas the others are underutilized.

The number of devices could be variable depending on their characteristics. With MV or HV applications, the switching devices must be connected in series to secure the voltage blocking capability of each device.

1.3. Practical objectives

The scope of this work is to obtain the state of the art of the multirate analysis and implement some of its conclusion to the power electronics field, specifically in MV power converters. It is a hard issue due to the lack of literature in this specific branch of power electronics control applications. To achieve the general aim, the following objectives will be met:

1. Researching of current knowledge about multirate control. Multirate bases will be defined.
2. Review of power converter modulation strategies. Special emphasis will be shown in the sinusoidal pulse-width modulation (SPWM) and selective-harmonic elimination (SHE).
3. Temporal analysis of SPWM digital application, that is, delay and amplitude error. Besides, modelling techniques will be introduced, as modified Z-transform, which is related to multirate analysis.
4. Correct modelling of multirate systems, particularly the power converter applications with up-sampling processes.

5. Control possibilities considering the multirate design techniques found in the literature.
6. Validate the multirate modelling and control design with simulations.

1.4. Structure of this work

The organization of this document has been done as follows:

- **Chapter 2** presents a knowledge review of multirate situations in power electronics. First, the multirate basis are shown to get the correct approach of these techniques inside control theory, being Kranc's methodology one of the most useful. The studied three-phase power converter leads to a profound analysis of the actuator, and its correct modelling. Two modulation techniques are studied, SPWM and SHE, but the first one is profoundly detailed for its use in this document. Hence, the modified Z-transform is presented and linked with multirate approaches Later, two multirate applications examples are briefly introduced to enforce the possibilities of this approach in power electronics. Finally, two multirate modelling techniques are presented for its future use in the controller design and analysis. These techniques are also related to each multirate example presented in this chapter.
- **Chapter 3** introduces the plant modelling as a function of connected filter. The usual alternatives (L, LC, LCL, and LLCL-filter) are presented, and its corresponding discretization, which can lead to different situation depending on the utilized reference frame (stationary or rotating). Then few possible multirate applications are presented to obtain a framework for the following chapter and future multirate setups.
- **Chapter 4** contains the main goal of this work, which is the study and design of multirate controllers for the current control loop. First the proposed single-rate controllers for each reference frame are presented. Then the situation where the control and actuation rate are fastest than the current sampling rate without changing the controller structure is studied, that is, the controller makes the extrapolation operation through its integral part. Finally, the model-based multirate controller is presented (MRIC) with great results. All conclusions are based on simulation results for either mathematical model and detailed model of the grid-tied power converter.
- **Chapter 5** finalizes with some conclusions about the present work and its future possibilities inside power electronics.
- **Appendix A, B and C** give the background for several terms presented along the document. Must stand out the modified *Z*-transform in Appendix A.

Chapter 2. Theoretical study

2.1. Introduction

This chapter summarizes the current knowledge of multirate design of discrete/digital control systems in power electronics field. First, an overview of multirate analysis evolution through the last decades is displayed. The multirate approach is needed on several fields of control engineering, mainly in robotics and computer engineering branch. In power electronics a few applications have been found, but some concepts related to the actuation block have been studied that are directly related to the multirate design and modelling. The actuation block induces a certain delay that has been modeled and compensated in several ways in the literature, and mostly all of them are studied in this chapter. A critic point of view is taken in this chapter with every approach, and some conclusions will be obtained about the correct treatment of this delay. Related to this delay, there is a new concept in literature known as multisampling, that has some characteristics that must be evaluated to determine the accuracy of this approach. Also, a detailed overview of other multirate approaches in power electronics literature is shown. The most usual multirate research in power electronics is related to the digital signal processing, that is studied in this chapter, but other control strategies have also been proposed in the literature that must be considered. Two examples are presented, and each one is related to one way of obtaining a single-rate equivalent to be analyzed.

Later in the chapter, two multirate techniques are presented and they will be used in the following as a basis for this control approach. The technique has evolved over the last decades, but some initial concepts are useful to get the correct tactic in this issue. The multirate modelling is a key matter to get the best performance of multirate controllers. Besides, the up-sampling and down-sampling operations need a correct digital signal processing to avoid aliasing or imaging, but they will not be essential in this work because the controller will only work with one frequency, the grid frequency.

Finally, some conclusions are found around the introduced terms and thoughts in this chapter that will be useful for the following ones and further research in this knowledge field of control engineering. It is a specific field that will be defined by the practical limits, because it is an unusual processing of control signals. The mentioned literature in this chapter allows a further and interesting research in multirate approach inside power electronics.

2.2. State of the art

2.2.1. Multirate bases

2.2.1.1. Definitions

Before the multirate overview, some terms should be defined to get a better understanding of following explanations [14]. The sampling options for discrete-data (digital) systems are the following:

- **Conventional sampling**: Systems with different variables (inputs, outputs, and states) that are sampled each periodic T time units. It is shown in Figure 2.1(a). The conventional sampling is synchronous when all the samplers are synchronized, and nonsynchronous when a delay Δ is at the beginning of one variable sampling. The last definition is shown in Figure 2.1 (b).
- **Non-conventional sampling**: Systems that does not match the previous definition. This term comprises three different definitions of sampling:

  Multirate sampled systems: Sampled systems with two or more variables updated in two different rates. Usually, a synchronous and periodic sampling is considered. If the samplers are not synchronized, the system is known as asynchronous multirate system. The multirate control systems arises from this definition. Schematic is shown in Figure 2.1 (c).

  Cyclic-Rate sampled systems: It is also known as periodically variable in time (PVT) or multiple order. It is a sampling type where the samplers operate with a periodically variable rate, or cyclic rate, with the presence of a global period T, occasionally known as metaperiod. It is shown in Figure 2.1(d).

  Random sampled systems: Those where the sampling is applied in a certain variable amount of time, without the restriction of a repeated sampling pattern each global period T. It is depicted in Figure 2.1 (e).

The non-conventional sampling can be proposed in the known basic schemes: SISO (Single Input Single Output) and MIMO (Multiple Input Multiple Output).

The SISO structure is composed of two independent samplers, one at the controller output and other at the plant output. Figure 2.2 depicts this situation, where the controller output is sampled with a T/m period, and a T/n period the plant output. The regular multirate approach is the one that will be taken in this document, but, as it was said before, other sampling schemes might be chosen. Two regular multirate sampling strategies can be selected from the SISO structure:

- **MRIC (Multi-Rate Input Controller)**: The control signal is updated every T time units, whereas the plant output signal is sampled every NT time units. Therefore, following the previous definition, the resulting $m = 1$ and $n = 1/N$ are obtained. This structure is highly recommended when there is no access to

the controlled variable at high rates, and a conventional control rate might degrade the system performance.

- **MROC (Multi-Rate Output Controller)**: The control signal is updated every NT time units, whereas the plant output signal is sampled every T time units. This structure is highly recommended when the environment is disturbed, and the controlled variable must count with high number of samples to reject those degraded due to disturbance.

In this document, the MRIC scheme will be considered with different approaches, and the signal processing in each one might include up-sampling (expand) or down-sampling (skip) operations. However, the overall MRIC works as extrapolator, whereas MROC works as decimator.

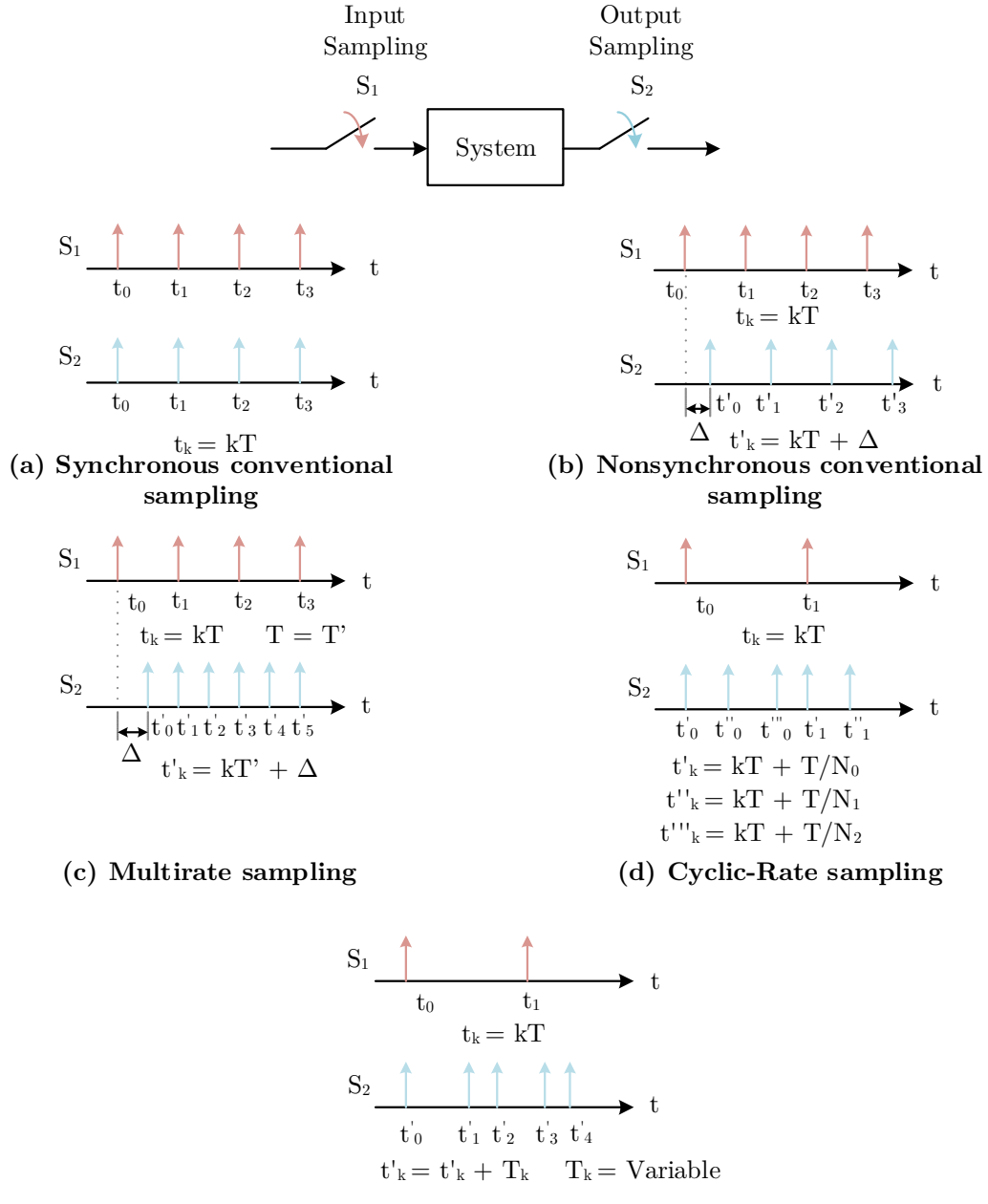

(a) Synchronous conventional sampling

(b) Nonsynchronous conventional sampling

(c) Multirate sampling

(d) Cyclic-Rate sampling

(e) Random sampling

Figure 2.1. Schematics of sampling processes

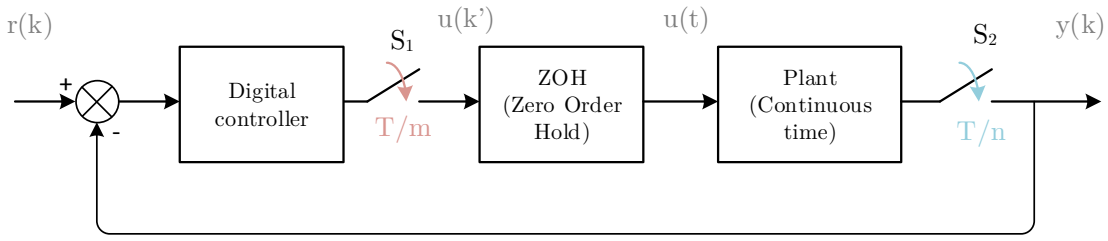

Figure 2.2. SISO structure with non-conventional sampling

MIMO structure is composed of two or more samplers at plant input and the corresponding ones at its output for controlling two or more variables. Figure 2.3 depicts the structure with N samplers at the input and output. It is interesting to remark this kind of analysis, because it is useful, if the different variables come from the time decomposing of a signal to finally obtain a close SISO expression from the analyzed multirate system.

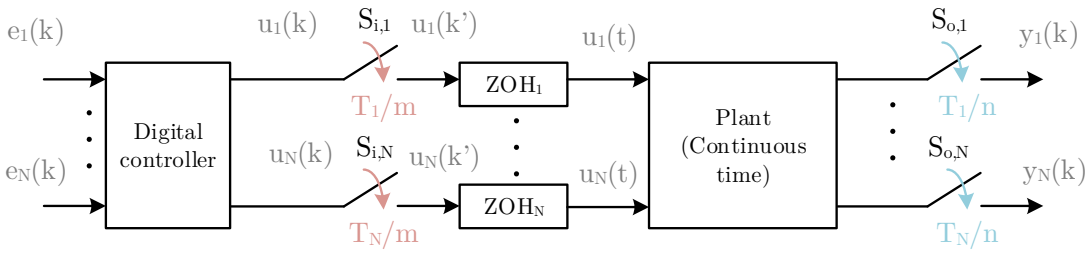

Figure 2.3. MIMO structure with non-conventional sampling

2.2.1.2. Background

The digital multirate control has been a research matter for more than 63 years, and there are a lot of contributions in modelling, design, analysis, and applications. The contributions could be distributed in two domains: frequency and time. To follow the evolution of multirate contributions, Figure 2.6 rebuild the one in [14].

1) Frequency domain

This domain is composed of two research branches: Frequency Decomposition; Vectorial Switch Decomposition.

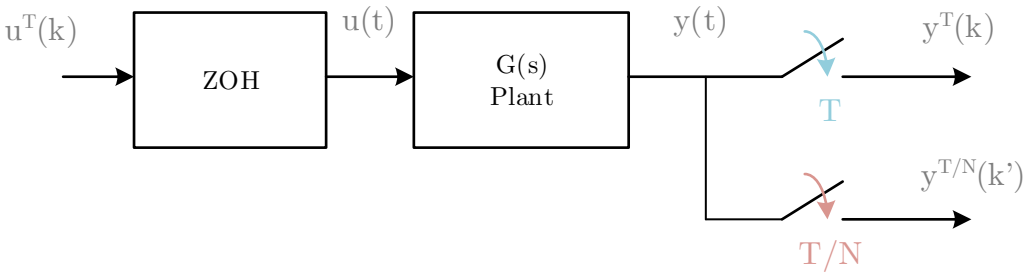

Figure 2.4. Frequency Decomposition scheme

The Frequency Decomposition research began in 1955 with Sklansky and Ragazzini [15], they proposed this approach with the location of fictitious samplers that,

operating in multiple frequencies of the original sampling frequency, allow the study of intersampling behavior. Figure 2.4 depicts the proposed analysis basis, where N samples could be placed in a T period. Later, Friedland (1961) applied this technique to the study of control structures in systems with periodically varying members, followed by Coffey and Williams (1966) and Boykin and Frazier (1975) [16] with the analysis of multivariable and multirate control systems. These approaches followed an external representation, i.e. discrete-time transfer function expression. Aracil and Feliu (1984) [17], and later Salt and Albertos (2000) [18], modeled the intersampling behavior to apply it to the dual-rate controllers design that reject the undesirable oscillations.

The Vectorial Switch Decomposition (VSD) is related to the beginnings of the frequency decomposition, and it was introduced by Kranc in 1957 [19]. This method represents the multirate sampler as a superposition of several conventional samplers working with the highest sampling rate considered in the system, along with the corresponding advance and delay for each branch. The method allows to analyze the multirate system using the usual single-rate discrete techniques, always keeping sampling rates related by an integer. Figure 2.5 represents this explanation, and it is remembered that the asterisk (*) represents the pulse expression of the signal.

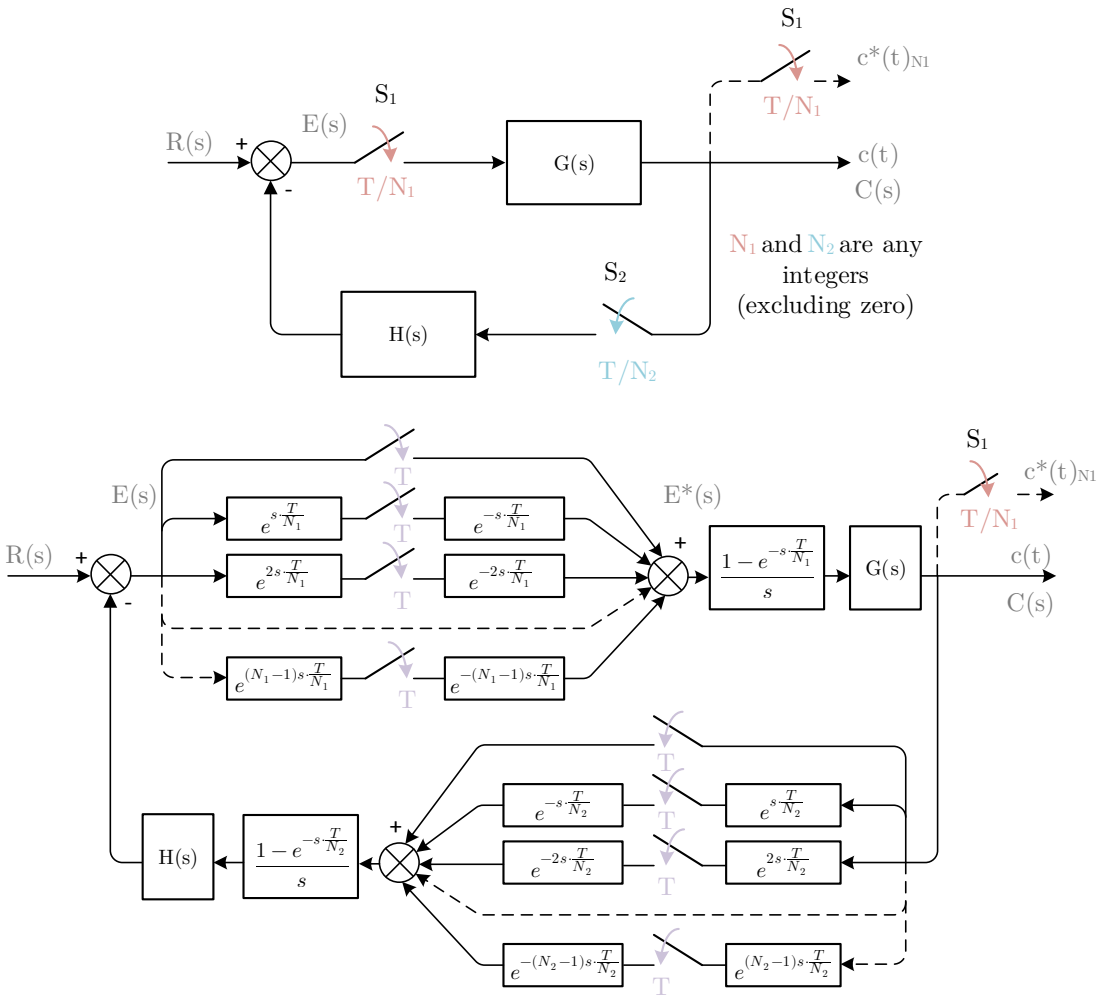

Figure 2.5. Vectorial Switch Decomposition of a control system with multirate sampling

The VSD allowed to put the basis in multirate analysis, as it will be shown later in this chapter, because it is very useful tool for internal representation (space-state modelling) and external representation (transfer function modelling).

The relation between both techniques is analyzed and argued by Ragazzini and Franklin (1958)[20] and Jury (1958)[21]. Before that, Jury presented the modified *Z*-transform as study tool for the proposed multirate modelling problem. The modified *Z*-transform is a powerful tool to model no unitary delays in a discrete-time system with period T, and a multirate system is composed of several of them as it is shown in Figure 2.5. This tool will be presented in Appendix A. Later, Whitbeck and Didaleusky (1980)[22] developed a program that use this tool to simulate discrete-time flight control systems.

The relationship between the frequency domain and the state-space had not been stablished until the contributions of Araki and Yamamoto (1986)[23]. They analyzed a multirate control structure where the different sampling rates related with an integral ratio N are associated with an input-output pair that divides the major period T in N different signals. Also, they developed the Multirate Impulse Modulation (MIM) from the pulse-transfer matrix of the discrete-time realization by multiplying shift operators. And they derived a Nyquist-type stability condition for closed-loop systems, that obtained a relation of the Kalman-Bertram[24] realization with the frequency response. The contribution approach is clearly based on the Kranc's Vector Switch Decomposition. As a logic consequence, a contribution series on controllers is developed, the authors named them MRIC (Multi-Rate Input Controller)[25] and MROC (Multi-Rate Output Controller)[26], as function of the input and output sampling of the plant, like it was presented before.

Few years later, Godbout, Jordan and Apostolakis (1990)[27] developed a model for a closed-loop digital control system that incorporated multirate sampling with dynamic compensation. The model represented the system behavior at the base sampling rate, that is an integer multiple of those presented in the system. The dimension of the proposed model was high, so they removed the unobservable states and outputs leading to minimum dimension matrices (1992)[28].

Thompson (1986)[29], independently to Araki and Yamamoto, introduced the Kranc's Operators that automated the VSD and allowed to apply model tools similar to the classic control approaches.

From other point of view, Albertos (1990)[30] proposed the modelling with BMIO (Block Multirate Input Output), which linked the external and internal representations and set an analogy design to state-feedback.

Contributions from Salt (2005)[31] might be considering in the MRIC field, where the controller was split into two parts acting at different sampling rates and its control target was to reach similar performance to the faster single-rate controller would have achieved. The latest contributions are focused in the application of multirate design approaches into networked control systems[32].

2) Time domain

The first relevant contribution came from Kalman and Bertram [24], where was shown the space-state flexibility to describe the evolution of non-conventional sampling systems and mainly in multirate systems. This first contribution was unnoticed. Years later, Barry (1975)[33] designed a state-space based multirate controller and showed that its performance was comparable to the one obtained with a single-rate controller with the base rate. Later, Amit and Powell (1981) [34] and Glasson and Dowd [35] developed a multirate control design technique based on the optimal control formulation.

Parallelly to the Araki, Goodbout and Thompson modelling in the frequency domain as space-state realization, some internal representation model from mathematical equivalent transformations were developed. Meyer and Burrus (1975) [36] presented a model with the splitting of the transition state matrix, that allowed the conversion of a linear periodic system to the LTI (Linear Time-Invariant) equivalent one.

Other relevant technique is the discrete lifting presented by Khargonekar (1985) [37], which showed the isometric isomorphism (both algebraic and analytic properties of systems are preserved) between the linear periodic system and the LTI equivalent one (lifted system). An illustrative comparison among discrete lifting options are presented in [38].

Tornero (1986)[39] took a different approach, the model supposed a multirate model generator and built a powerful simulation tool. To reach the solution the multirate system was characterized by a set of physical elements and events (sampling and holdings), so the event sequence caused a transformation sequence upon the state vector described by a single transition matrix.

In the 90's the discrete lifting was generalized to the continuous case [40]. The continuous lifting technique is a discretization that considers the continuous system as a periodic one and transform it to the equivalent LTI with finite dimension.

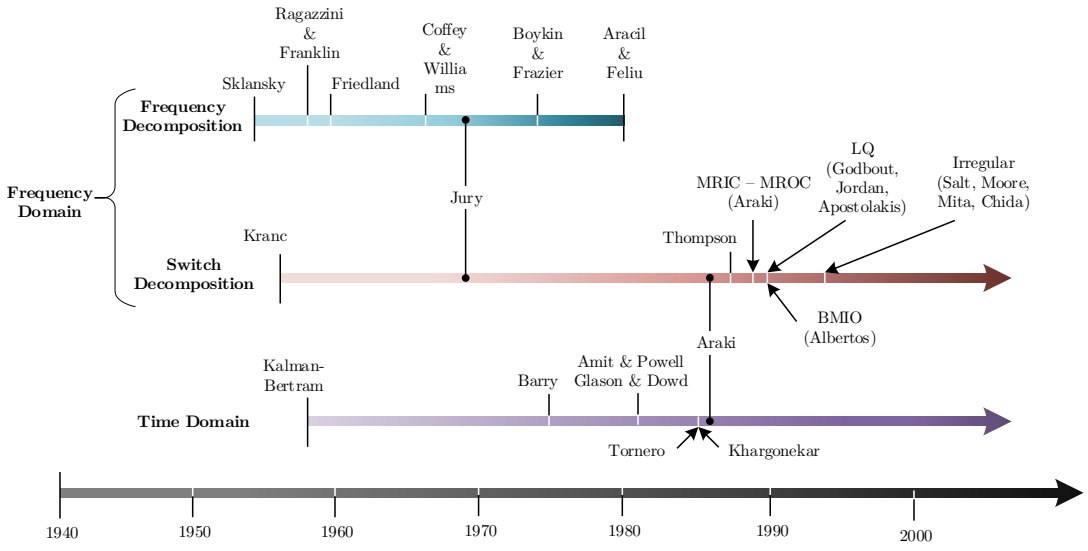

Figure 2.6. Historical background

2.2.2. Modulation techniques

2.2.2.1. Background

The controller actuation is modulated in the power converter through the corresponding system, and this might define the different provided control techniques by the multirate approach because it influences the actuation signal characteristics. There are several modulation techniques, so the application and converter topology must be considered.

The modulation techniques are divided between those based in carrier signal and those that do not. The most popular techniques in 3L-NPC-VSC topology are carrier-based. Figure 2.7 depicts a classification of the most used techniques.

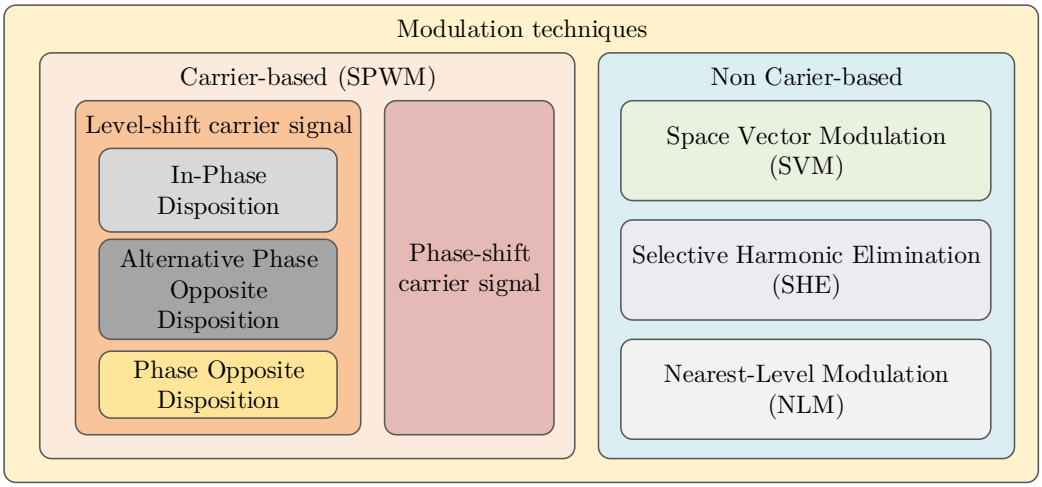

Figure 2.7. Main modulation techniques in power converters

The carrier-based are known as Sinusoidal Pulse-Width Modulation (SPWM), and they are based on the comparison of a modulating reference signal with a set of carrier signals that usually have triangular shape [41]. The differences between the techniques in this group come from the disposition of the carrier signals. The level-shift carrier signals are the preferred to NPC topologies [42], whereas the phase-shift signals are the best option for modular topologies [43]. In addition, the level-shift carrier signals are classified in three options depending on how the phases are interleaved: in-phase disposition (IPD), alternate phase opposite disposition (APOD), or phase opposite disposition (POD).

The Space Vector Modulation (SVM) is the modulation technique that uses the voltage reference as a rotary vector in a hexagonal space composed by all the possible switching states of the converter [44]. The modulation method become more complex as the number of voltage levels of the converter increases.

Other popular modulation technique is the Selective Harmonic Elimination (SHE) which is based on the offline calculation of the optimal switching angles to eliminate certain output voltage harmonics. It was originally implemented on a two level topology [45] but it is easily interpolated to higher level converters as 3L-NPC-VSC [46].

Finally, the Nearest Level Modulation (NLM) applies voltage level that is closest to the reference voltage in each period of time [47]. It is very useful for modular multilevel converters with a high number of modules, because with other techniques the complexity increases with the number of modules.

This document is focused on the SPWM and SHE modulation techniques because some interests can be found on them at multirate applications as it will be shown later. In the following, a detailed explanation of each modulation technique is given for a better understanding of the multirate application. A detailed analysis is shown in the digital implementation of the SPWM, as well as a correct modelling of this system.

2.2.2.2. Sinusoidal Pulse-Width Modulation

This modulation technique is one of the most used due to its simplicity and easy implementation. In three-phase power converters, this modulation scheme is based on the comparison between three sinusoidal signals (required phase voltage) known as modulating signals, with triangular signals with higher frequency called carriers signals. Detailed information can be found in [41], where the evaluation of PWM schemes has been examined through analytical solutions to compare the magnitude of the harmonic components. The SPWM depends on the studied converter, in this document the explanation will be based on the 3L-DNPC-VSC introduced before. Therefore, there are three modulating signals (one per phase) shifted 120 degrees one from each other, and they are compared with two level-shifted and in phase carrier signals. The activation PWM signals follow the switching rule from Table 2.1, being x the phase A, B and C. The modulating signals per x phase are called v_{mx}, and v_{cr1} and v_{cr2} are the carrier signals for all phases.

Table 2.1. Switching rule on a 3L-DNPC-VSC

Signal	**Switch device**			
Comparison	S_{x1}	S_{x2}	S_{x3}	S_{x4}
$\boldsymbol{v_{mx} > v_{cr1}}$	1	-	0	-
$\boldsymbol{v_{mx} > v_{cr2}}$	-	1	-	0

The modulation process defined in Table 2.1 is shown in Figure 2.8 for phase A. The signals are depicted in per unit ($p.u.$) to get a better comparison and understanding of the operating zone. The maximum amplitude is defined by the DC-bus voltage and it is $V_{DC}/2$.

The modulating signal and the carrier signals amplitude and frequency are related through two well-known indexes: amplitude modulation index (m_a) and frequency modulation index (m_f). The indexes are the defined as:

$$m_a = \frac{\hat{V}_m}{\hat{V}_{cr}} \quad m_f = \frac{f_{cr}}{f_m} \tag{2.1}$$

These are the general terms, but some differences might be found depending on the converter topology. For a 3L-DNPC-VSC, the carrier signals amplitude (peak-to-peak) is the half, but the relation is with the peak amplitude of one carrier signal.

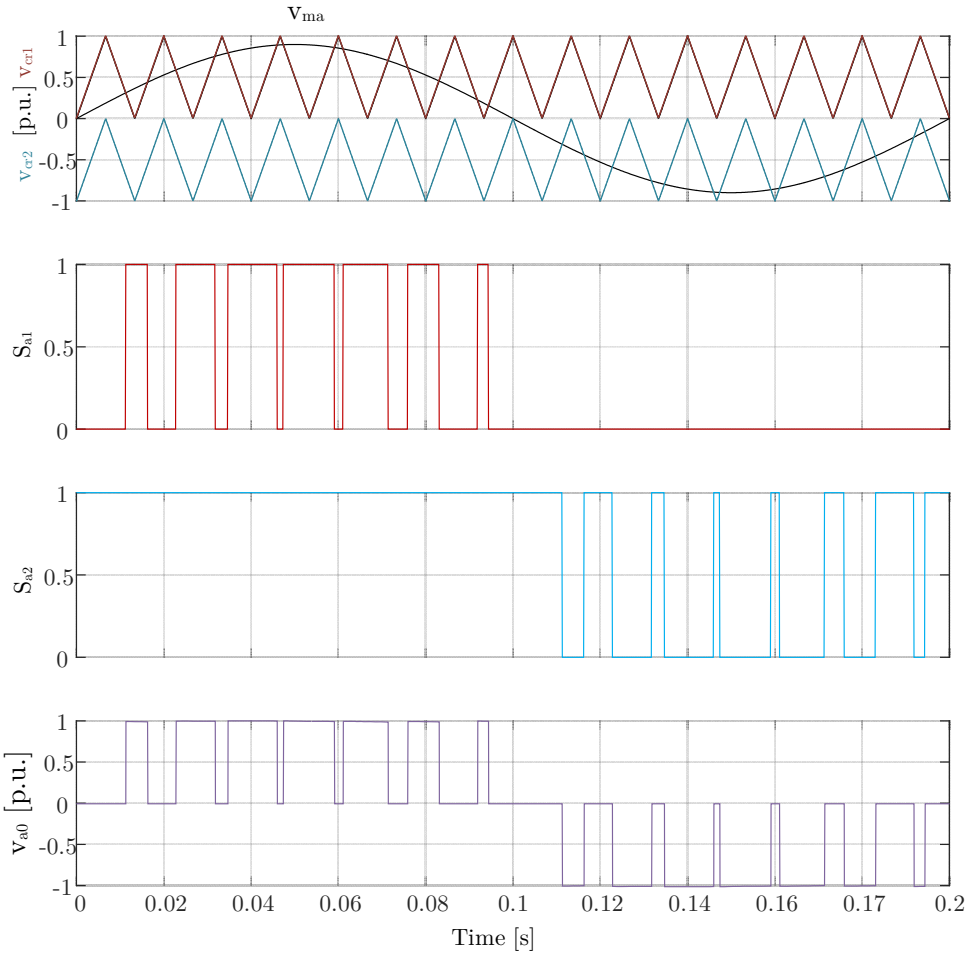

Figure 2.8. SPWM example with $m_a = 0.85$ and $m_f = 15$

There are three different operating zones depending on the value of the modulation index m_a: lineal, overmodulation and square wave. The lineal zone is the desirable in every application and it is got with $m_a < 1$. The overmodulation region is obtained with greater m_a, which produces higher line voltages, but they are not proportional to the modulation index. The square wave operation is obtained with very high modulation index.

Figure 2.8 depicts an example where the carriers are phase-shifted equally regarding modulating signal, what is known as In-Phase Disposition (IPD). If one carrier is opposite to the other one, the situation is known as Phase Opposite Disposition (POD). Both dispositions can be used for 3L-DNPC-VSC with similar results. The main harmonic band appears around the multiple integers of m_f, but in IPD case the first band is composed by odd harmonics and in POD case by even harmonics. The second band is composed by odd harmonics in both cases. Figure 2.9 and Figure 2.10 depict the harmonic content in each case.

The different carrier phase disposition determines the resultant voltage wave v_{a0}. Figure 2.8 depicts a half-wave symmetry because the carrier signals are not shifted regarding the modulating signal. If the carrier signals are phase-shifted $\pi/2$ radians, the resultant

voltage wave will have a quarter-wave symmetry. The differences are in the second band, with no phase shift it is only composed by even harmonics, and with phase shift it is composed by odd harmonics.

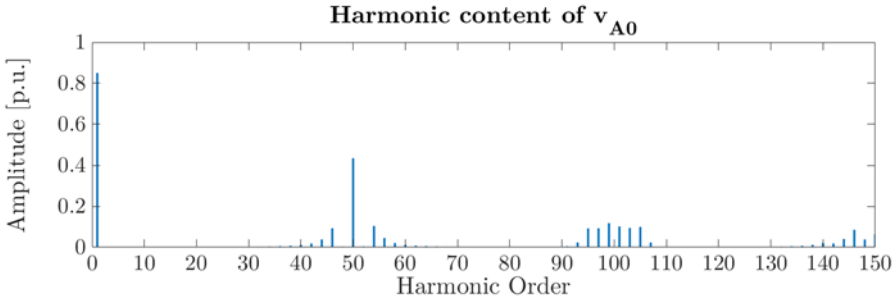

Figure 2.9. Harmonic content of phase-to-neutral voltage for $m_a = 0.85$ and $m_f = 50$ with IPD carrier signals.

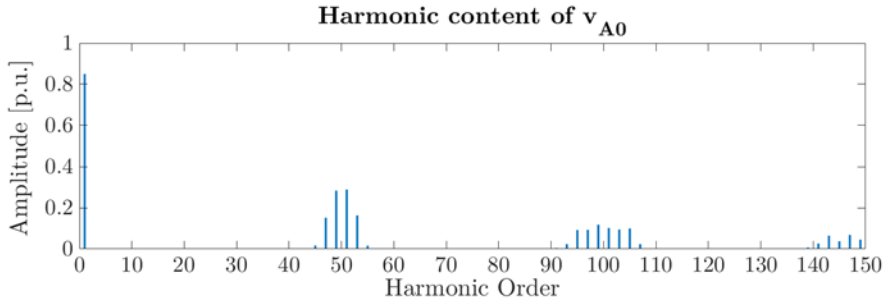

Figure 2.10. Harmonic content of phase-to-neutral voltage for $m_a = 0.85$ and $m_f = 50$ with POD carrier signals.

In three-phase systems, as those studied in this document, the Third Harmonic SPWM (THSPWM) technique is used for maximizing the lineal zone until $m_a = 1.15$ $(2/\sqrt{3})$. The maximum value for the phase-to-phase signal is equal to the one with SVM technique. The third harmonic injection is obtained through the expression (2.2) that is summed at each phase modulating signal.

$$v_{0s} = -\frac{1}{2} \cdot [\max\{v_{ma}, v_{mb}, v_{mc}\} + \min\{v_{ma}, v_{mb}, v_{mc}\}] \tag{2.2}$$

2.2.2.3. Digital SPWM

The previous modulation technique is usually implemented in digital platforms, so the comparison changes. The modulating signal is updated in a discrete period, because the sampled signals are digitally processed to obtain the actuation signal, i.e. the modulating signal. In [41] two terms are defined to differentiate the SPWM modulation, based on the modulating signal:

- **Naturally sampled PWM**: The modulating signal is continuous, and it is compared with carriers to obtain the respective switching patterns. It is commonly found on analog electronic PWM generation circuits. It is the case depicted in Figure 2.8.
- **Regular sampled PWM**: The modulating signal is discrete, and each sample is compared with the carriers to obtain the respective switching patterns. It is

the usual practice in software PWM generation, and it is the used one in this document.

Besides, the regular sampled PWM strategies are classified depending on the switching signals symmetry [48]:

- **Symmetrical regular sampled PWM (s-PWM)**: The generated switching patterns are symmetrical regarding carrier signal.
- **Asymmetrical regular sampled PWM (a-PWM)**: The generated switching patterns are asymmetrical regarding carrier signal.

The main regular sampled PWM strategies depend on the modulation update and current sampling instants regarding the carrier. Figure 2.11 summarizes these strategies, where each time instant corresponds to $t = k \cdot T$.

- **S-PWM-start**: Symmetrical PWM with regular sampling in the start of each carrier period. The modulation function update instant is also synchronized with the beginning of each carrier period. It is shown in Figure 2.11(a). There is a dead-time T_d between the phase current sampling instant and the modulation function update instant. In this case, the carrier period $T_{carrier}$ is equal to the sampling period T. Therefore, the overall dead-time introduced by the sampling, calculation and PWM update routine is:

$$T_{d|s-PWM-start} = T_{carrier} = T \tag{2.3}$$

- **S-PWM-middle**: Symmetrical PWM with regular sampling in the middle of each carrier period. The modulation function update instant is synchronized with the beginning of each carrier period. It is shown in Figure 2.11(b). The carrier period $T_{carrier}$ is equal to the sampling period T. For this occasion, the overall dead-time introduced by the sampling, calculation and PWM update routine is:

$$T_{d|s-PWM-middle} = \frac{1}{2} \cdot T_{carrier} = \frac{1}{2} \cdot T \tag{2.4}$$

- **A-PWM-double**: Asymmetrical PWM with regular sampling in the start and middle of each carrier period. The modulation function update instants are synchronized in the same sampling instants. It is shown in Figure 2.11(c). Here, the sampling period time T is half carrier period time. The overall dead-time introduced by sampling, calculation and PWM update routine is:

$$T_{d|a-PWM-double} = \frac{1}{2} \cdot T_{carrier} = T \tag{2.5}$$

In all these strategies the zero-state switching vectors are placed symmetrically around the carrier signals minima and maxima, so the AC current signals are sampled in their mean value, avoiding anti-aliasing filters. In other words, the measured current is sampled exactly at the transition of each half-carrier interval to avoid sampling the switching ripple current as well as the underlying fundamental current. As it is correctly indicated on [49], if the current is not synchronously sampled in this way, in most cases the measurement errors introduced will usually compromise the performance of the system. Hence, the samplings are constrained to both points each carrier period.

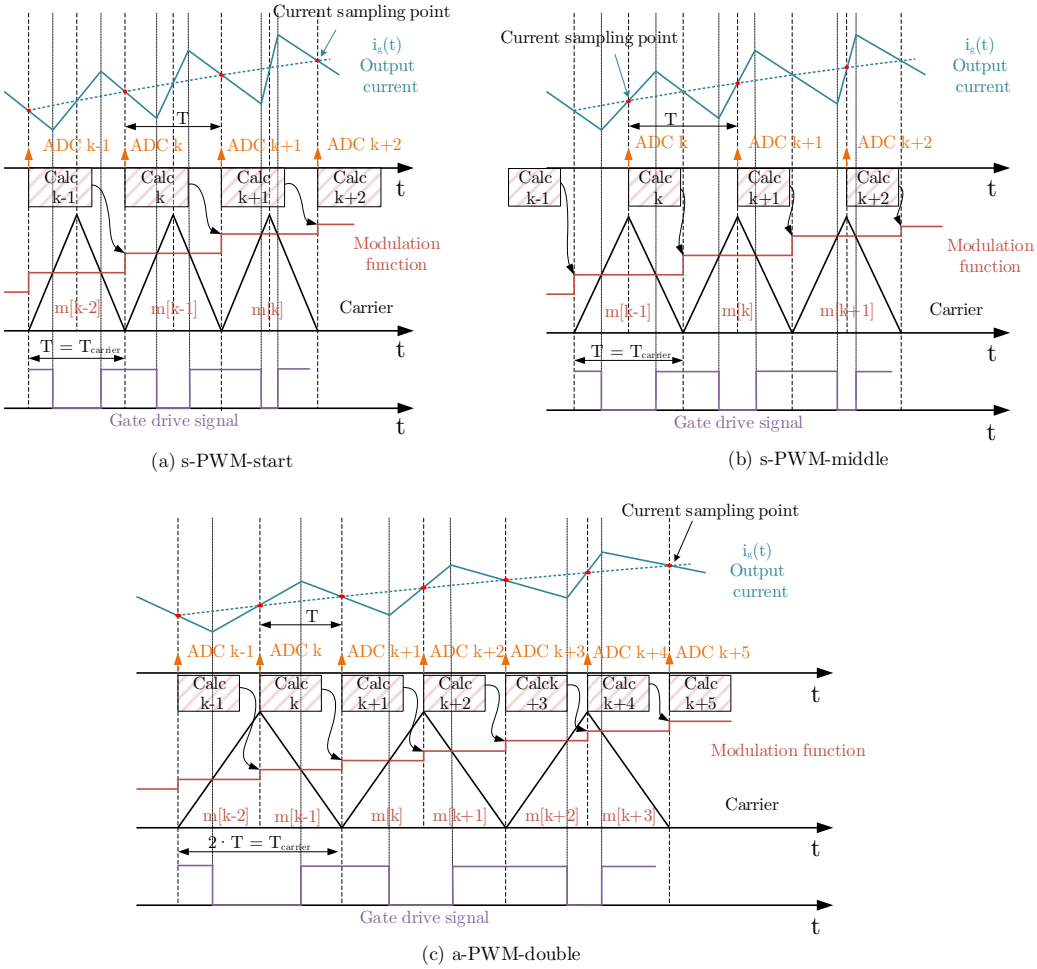

Figure 2.11. Schematic of regular sampled PWM strategies with equivalent carrier signal: (a) Symmetrical PWM with sampling at start; (b) Symmetrical PWM with regular sampling at middle; (c) Asymmetrical PWM with sampling at start and middle.

It must be said that the carrier signals depicted at Figure 2.11 are not continuous "ramps". The modulating signal references are compared against a triangular carrier "ramp" using a digital counter/comparator circuit that toggles the switch as the ramp crosses the sampled command voltage reference. Figure 2.12 depicts the strategy.

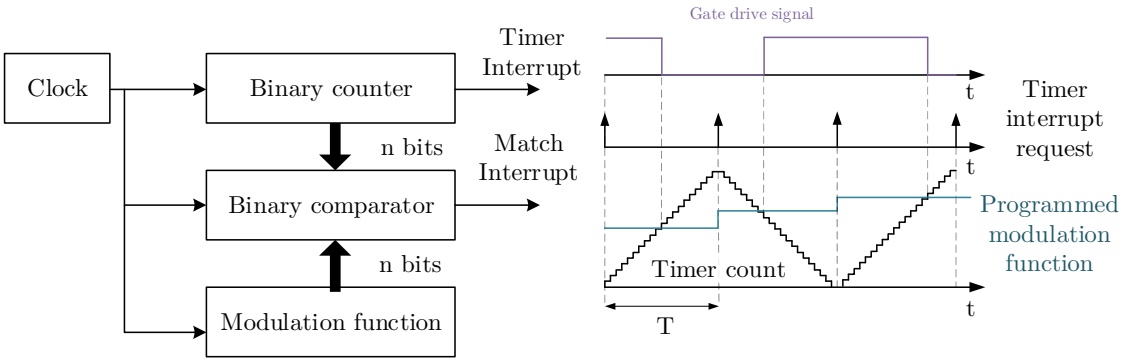

Figure 2.12. Simplified structure of a digital SPWM

The counter is incremented at every clock pulse, and, when the binary counter value is equal to the modulation function value (also known as programmed duty-cycle value),

that is match condition, the binary comparator triggers an interrupt to the microprocessor and, at the same time, sets the gate signal low. For double-update-mode, at each modulation period, the match condition is given two times, at the beginning with the run up and run-down phase. The counter and comparator have a given number of bits, n, and depending on the ratio between the durations of the modulation period and the counter block period, a lower number of bits, N_e, could be available to represent the duty-cycle. The parameter N_e is necessary to determine the quantization step. Detailed information about digital implementation of PWM can be found in [50].

In the previous analysis is not mentioned the one-half T phase delay introduced by the Zero-Order Hold (ZOH) operation at the modulating signal update, which is inherent to the regular sampled PWM comparison processes. Therefore, the overall dead-time or delay introduced into the control loop depends on the PWM strategy and the inherent one-half T phase delay from the ZOH process. For example, at a-PWM-double the overall delay is $1.5 \cdot T$. In [41], the one-half delay is compensated by phase advancing the modulating waveform using the reference frame transformation. However, the delays can be incorporated into the system model either using a modified Z-transform approach, or by simply including an e^{-sT_d} time delay operation in series with forward path controller. The temporal issues will be detailed in the following sections, because the scope of this section is to show the most usual ways of SPWM digital implementation.

2.2.2.4. Selective Harmonic Elimination

The Selective Harmonic Elimination (SHE) is a modulation technique originally proposed in [51] for two and three levels inverters. The technique is based on the off-line calculation of the angles in which the switching events occur to eliminate a chosen number of harmonics close to the fundamental one.

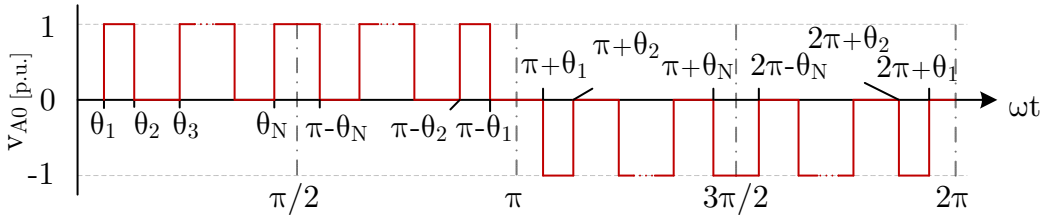

Figure 2.13. Generic three-level waveform with quarter-wave symmetry

The angles are placed in a lookup table and depending on the modulation index a switching angle is obtained every period T. The following description is based on the one presented in [11].

The generic waveform of a three-level signal with quarter-wave symmetry is shown in Figure 2.13, where $\theta_1, \theta_2, \ldots, \theta_N$ represent the switching event angles during a quarter period. Therefore, there are a total of 4N commutations each signal period.

The calculation of each commutation angle is done with the Fourier series transform to decompose the three-level signal:

$$v_{out}(\omega t) = \sum_{n=1}^{\infty} \left[a_n \cdot \sin(n \cdot \omega t) + b_n \cdot \cos(n \cdot \omega t)\right] \tag{2.6}$$

Where the coefficients are:

$$\begin{aligned} a_n &= \frac{1}{\pi} \int_0^{2\pi} v_{out}(\omega t) \cdot \sin(n \cdot \omega t) \quad d(\omega t) \\ b_n &= \frac{1}{\pi} \int_0^{2\pi} v_{out}(\omega t) \cdot \cos(n \cdot \omega t) \quad d(\omega t) \end{aligned} \tag{2.7}$$

Supposed the quarter-wave symmetry, it is deduced:

- For even harmonics (even n): $a_n = 0$
- For all harmonics (odd and even n): $b_n = 0$

The symmetry (half-wave and quarter-wave) produces the even harmonics cancellation, so these harmonics are not considered in the following process.

If the expression of a_n (2.6) is developed in the intervals between the switching events in the first quarter of the output signal, the following is obtained for an odd number of events (odd N):

$$\begin{aligned} a_n &= \frac{4V_{dc}}{\pi} \left[\int_{\theta_1}^{\theta_2} \sin(n \cdot \omega t) \quad d(\omega t) + \cdots + \int_{\theta_{N-1}}^{\pi/2} \sin(n \cdot \omega t) \quad d(\omega t) \right] \\ &= \frac{4}{n\pi} \cdot \sum_{k=1}^{N} (-1)^{k+1} \cdot \cos(n\theta_k) \end{aligned} \tag{2.8}$$

And for an even number of switching events (even N) at first quarter, it is obtained:

$$\begin{aligned} a_n &= \frac{4V_{dc}}{\pi} \left[\int_{\theta_1}^{\theta_2} \sin(n \cdot \omega t) \quad d(\omega t) + \cdots + \int_{\theta_{N-1}}^{\theta_N} \sin(n \cdot \omega t) \quad d(\omega t) \right] \\ &= \frac{4}{n\pi} \cdot \sum_{k=1}^{N} (-1)^{k+1} \cdot \cos(n\theta_k) \end{aligned} \tag{2.9}$$

From (2.8) and (2.9), it can be deduced that for any N:

$$a_n = \frac{4}{n\pi} \cdot \sum_{k=1}^{N} (-1)^{k+1} \cdot \cos(n\theta_k) \tag{2.10}$$

Hence, the harmonic amplitude, h_n, of the output signal can be expressed as a function of the N switching angles:

$$h_n = \frac{4}{n\pi} \cdot \left[\cos(n\theta_1) - \cos(n\theta_2) + \cdots + (-1)^{N+1} \cdot \cos(n\theta_N)\right] \tag{2.11}$$

The first N harmonics equations are:

$$\begin{aligned} f_1(\theta) &= \cos(\theta_1) - \cos(\theta_2) + \cdots + (-1)^{N+1} \cdot \cos(\theta_N) = \frac{\pi h_1}{4V_{dc}} = \frac{\pi}{4} \cdot m_a \\ f_2(\theta) &= \cos(3\theta_1) - \cos(3\theta_2) + \cdots + (-1)^{N+1} \cdot \cos(3\theta_N) = \frac{3\pi}{4V_{dc}} \cdot h_3 \\ &\vdots \\ f_N(\theta) &= \cos((2N-1)\theta_1) - \cdots + (-1)^{N+1} \cdot \cos((2N-1)\theta_N) = \frac{(2N-1)\pi}{4V_{dc}} \cdot h_{2N-1} \end{aligned} \tag{2.12}$$

Using the set of equations (2.12), it is possible to eliminate the N-1 harmonics following the fundamental one, and to control the first harmonic amplitude. The goal is achieved by setting 0 the N-1 last equations and giving to the modulation index, m_a, a desired value. If the SHE is applied to three-phase system, the triple harmonics are cancelled, so there is no need to calculate these harmonics. In such case the set of equations does not contain equations of any triple harmonic, and the last harmonic eliminated is

- Even N: $X = 3N - 1$
- Odd N: $X = 3N - 2$

$$\begin{aligned} f_1(\theta) &= \cos(\theta_1) - \cos(\theta_2) + \cdots + (-1)^{N+1} \cdot \cos(\theta_N) = \frac{\pi}{4} \cdot m_a \\ f_2(\theta) &= \cos(5\theta_1) - \cos(5\theta_2) + \cdots + (-1)^{N+1} \cdot \cos(5\theta_N) = 0 \\ f_3(\theta) &= \cos(7\theta_1) - \cos(7\theta_2) + \cdots + (-1)^{N+1} \cdot \cos(7\theta_N) = 0 \\ &\vdots \\ f_N(\theta) &= \cos(X\theta_1) - \cos(X\theta_2) \cdots + (-1)^{N+1} \cdot \cos(X\theta_N) = 0 \end{aligned} \tag{2.13}$$

Solving these equations with the desired value for m_a the first harmonic is eliminated, and the following N-1 odd, non-triple harmonics are eliminated. The problem is that equations are non-linear and transcendental, what means that they cannot be solved through conventional methods. Usually, approximation methods are used, like Newton-Raphson [51] or genetic algorithms.

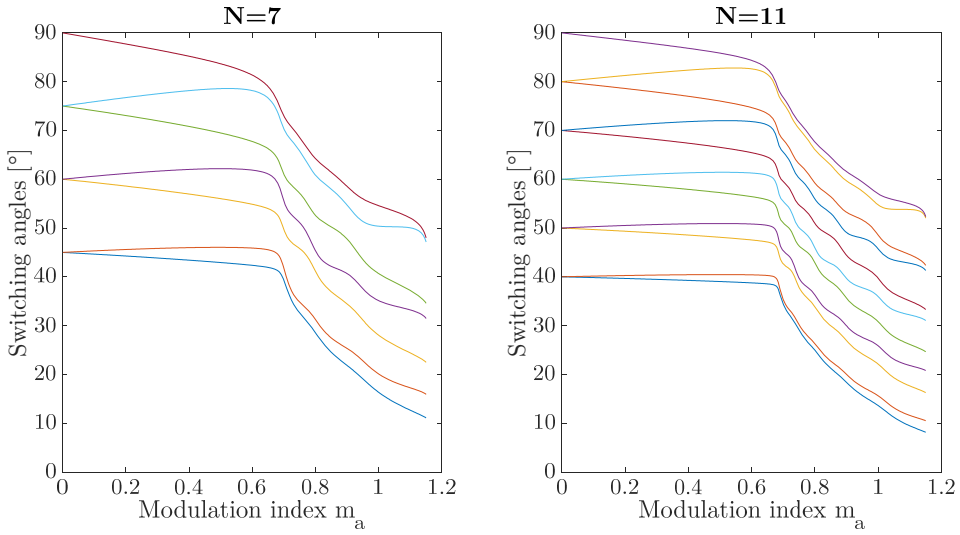

Figure 2.14. Switching angles versus amplitude modulation index for a three-phase three-level converter when N is 7 and 11

Figure 2.14 shows the angles sets obtained with Newton-Raphson method for a three-phase three level converter, with different number of events in a switching period.

These switching angles are calculated for all passible modulation indexes for each N commutation event. The N commutations value is related to the equivalent switching frequency of the devices through the fundamental harmonic:

$$f_{SW} = N \cdot 2 \cdot f_{h1} \tag{2.14}$$

The implementation of the SHE is interesting for its application in MV converters with differences between sampling and switching period. Also, this technique might be

combined with high order grid filters that include a notch-type branch as LLCL and it gives the optimal solution to optimize the harmonic content of the currents that are supplied to the grid in this kind of applications.

2.2.3. Modelling of the digital SPWM

There are some issues related to the digital implementation of SPWM (DSPWM) that has been studied in the literature. The correct modelling of this system is discussed in the following with an optimal comparison of modelling and control design strategies, as well as new approaches found in the literature.

2.2.3.1. Small signal modelling of regular sampled PWM

In [52], the non-linear modulation effects of the regular sampled PWM were studied. The dynamic behavior of digital PWM in the feedback chain is inherently different from those with analog PWM, as it was previously said and specified in [41].

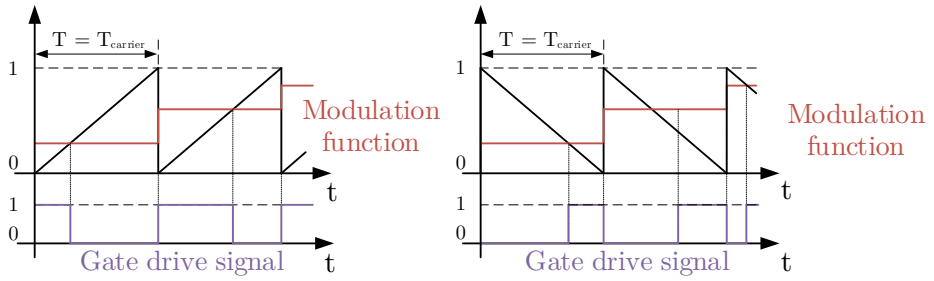

(a) End-of-on-time (b) Begin-of-on-time

Figure 2.15. Sawtooth carrier modulators

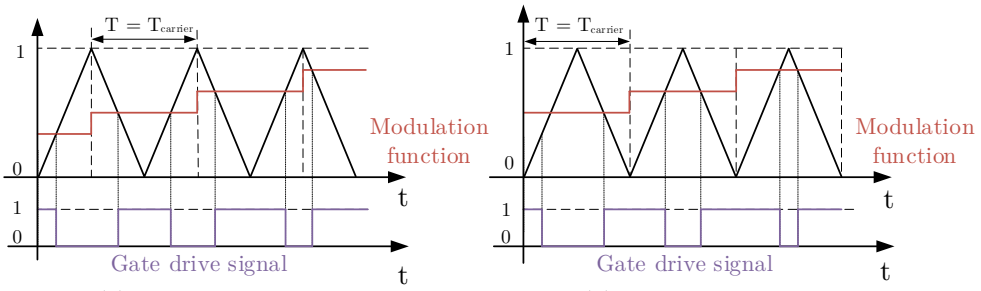

(a) Single-update-mode: symmetric-on-time

(b) Single-update-mode: symmetric-off-time

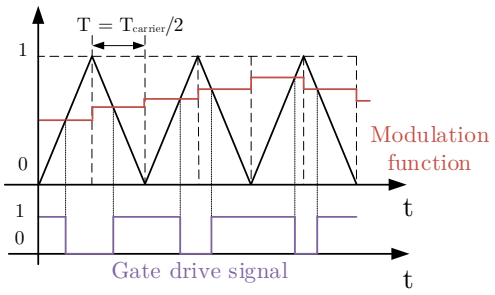

(c) Double-update-mode

Figure 2.16. Triangular carrier modulators

The author in [52] provides a small-signal Laplace-domain analysis to obtain a model that confirms the earlier statements about the delay. The models are obtained with a sawtooth carrier modulator and with triangular carrier modulators. They are summarized in Table 2.2 and based on the update instant of the modulating signal regarding the carrier, without the consideration of the sampling instant as it was presented in 2.2.2.3. The symmetric-off-time is the followed update strategy on s-PWM-start and s-PWM-middle, this means an update at the carrier minimum, whereas the double-update-mode is the one taken on a-PWM-double. The symmetric-off-time modulator updates the modulating signal at the triangular carrier peaks. They are depicted in Figure 2.15 and Figure 2.16. The sampling rate is T, that means a ZOH of period T to the modulating signal.

Table 2.2. The frequency and Laplace domain models for regular sampled PWM. Source:[52]

Carrier	**Regular sampled**	$\mathbf{G_{PWM}(s)}$	$\mathbf{G_{PWM}(j\omega)}$
Sawtooth	End-of-on-time	e^{-sDT}	$1\angle(-j\omega DT)$
	Begin-of-on-time	$e^{-s(1-D)T}$	$1\angle(-j\omega(1-D)T)$
Triangular	Symmetric-on-time	$\frac{1}{2}\left(e^{-s\frac{(1-D)T}{2}}+e^{-s\frac{(1+D)T}{2}}\right)$	$\cos\left(\frac{\omega DT}{2}\right)\angle\left(-\frac{\omega T}{2}\right)$
	Symmetric-off-time	$\frac{1}{2}\left(e^{-s\frac{DT}{2}}+e^{-s\frac{(2-D)T}{2}}\right)$	$\cos\left(\frac{\omega(1-D)T}{2}\right)\angle\left(-\frac{\omega T}{2}\right)$
	Double-update-mode	$\frac{1}{2}\left(e^{-s(1-D)T}+e^{-sDT}\right)$	$\cos\left(\omega\left(D-\frac{1}{2}\right)T\right)\angle\left(-\frac{\omega T}{2}\right)$

The frequency-domain models for sawtooth-carrier modulators show that these modulators behave as a pure delay that is depending on the average duty-cycle D. The delay is caused by the time instant between the sample is taken and the response of the modulator to this sample.

On one hand, the single-update-mode triangular carrier modulators (symmetric-on-time, symmetric-off-time) have a gain that is depending on frequency ω and average duty-cycle D, while the phase-shift represents a delay of one-half sampling period T. The $T/2$ delay can be understood as the response to a sample occurs, on average, at half of the switching period. On the other hand, the frequency domain model for the double-update-mode shows a dependency of the gain with average duty-cycle D and frequency of the input signal ω. The delay is fixed at one-half sampling period, *T/2*.

The previous analysis is focused on DC/DC converters, but they are useful for PWM on DC/AC converters. For sinusoidal modulating signals the duty-cycle varies along each semicycle, but it might be related to modulation index m_a. The duty-cycle varies in time, and its relationship with the modulation index, for a half-wave of a 3L DNPC VSC where two carrier signals are used and arranged as IPD, (there is a half-wave symmetry) is (2.15), where k is the time instant and $T \cdot k < 1/(2 \cdot f_0)$.

$$d(k \cdot T) = m_a \cdot |\sin(\omega_0 \cdot T \cdot k)| \tag{2.15}$$

Therefore, for a given frequency ω_0, the duty-cycle varies in time, so the small signal models presented before are not Linear Time-Invariant (LTI) and only an approximation around a given working point D is possible. That is an inherent assumption for proposed analysis in [52] to obtain the small signal modelling. For didactic proposes, the average duty-cycle is obtained as the root-mean-square (RMS) value for a given m_a and ω_0, that is $m_a/\sqrt{2}$.

In Figure 2.17 and Figure 2.18 is shown the gain dependence regarding m_a and frequency, f_0, of the modulating signal with single-update and double-update modes, respectively. From the figures, it is deduced that for higher modulating signal frequencies, the output signal of the PWM block has an amplitude error due to the falling gain.

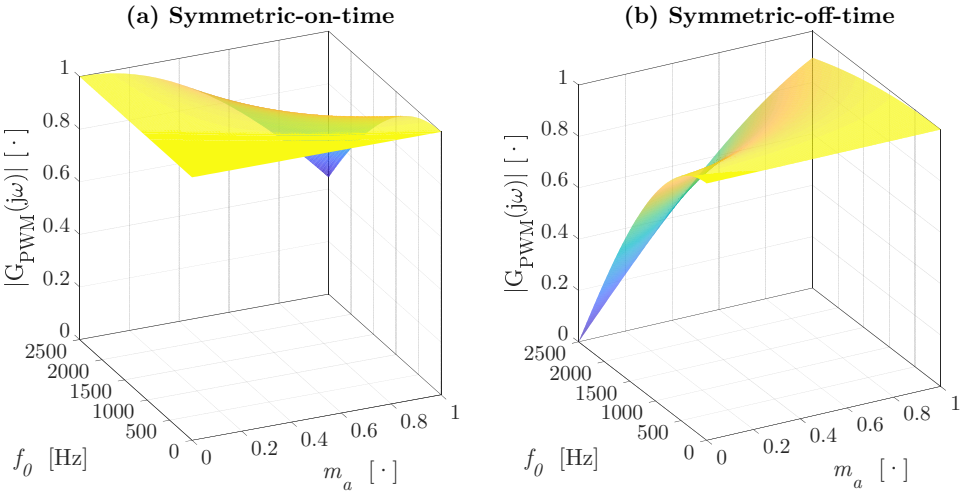

Figure 2.17. Dependence of the single-update-mode gain regarding modulating frequency f_0 and amplitude modulation index m_a, being $T = 200\ \mu s$ and $T_{carrier} = 200\ \mu s$

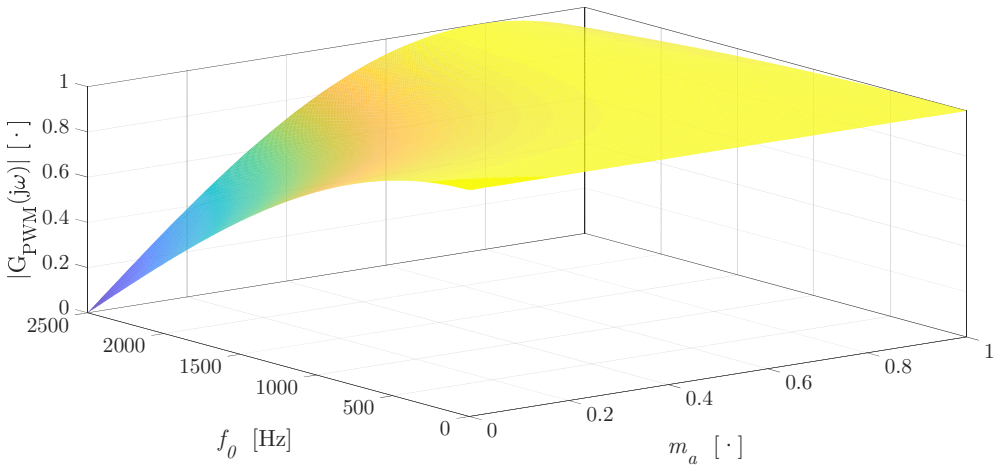

Figure 2.18. Dependence of the double-update-mode gain regarding modulating frequency f_0 and amplitude modulation index m_a, being $T = 200\ \mu s$ and $T_{carrier} = 400\ \mu s$

Note that the Nyquist frequency for both singe-update-mode and double-update-mode modulators is equal to half the sampling frequency, i.e., *T/2* (for double-update-mode

modulators $T = T_{SW}/2 = T_{carrier}/2$). Therefore, if these models are used to predict the closed-loop stability of a digitally controlled converter, their validity is limited to frequencies below half the sampling frequency.

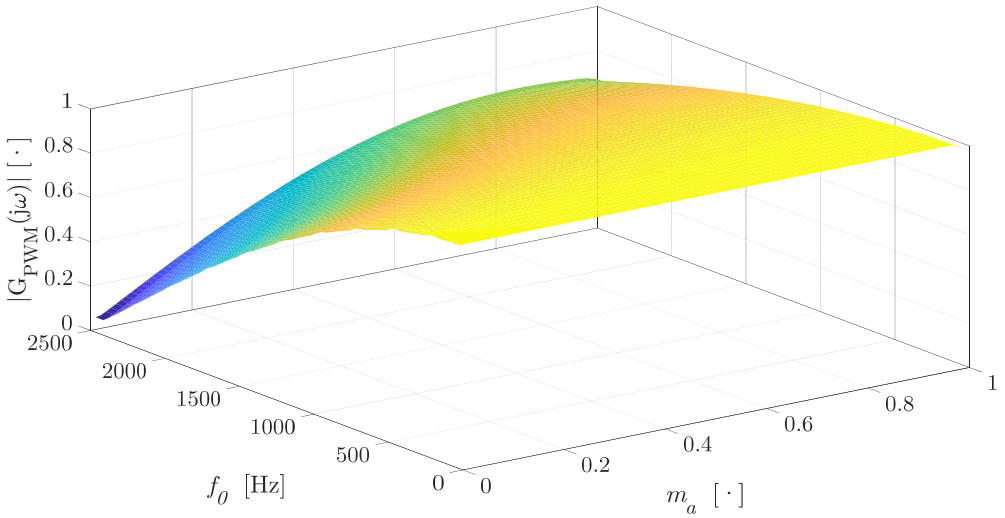

Figure 2.19. Parametric DSPWM simulation of double-update-mode gain regarding modulating frequency f_0 and amplitude modulation index m_a, being $T = 200\ \mu s$ and $T_{carrier} = 400\ \mu s$

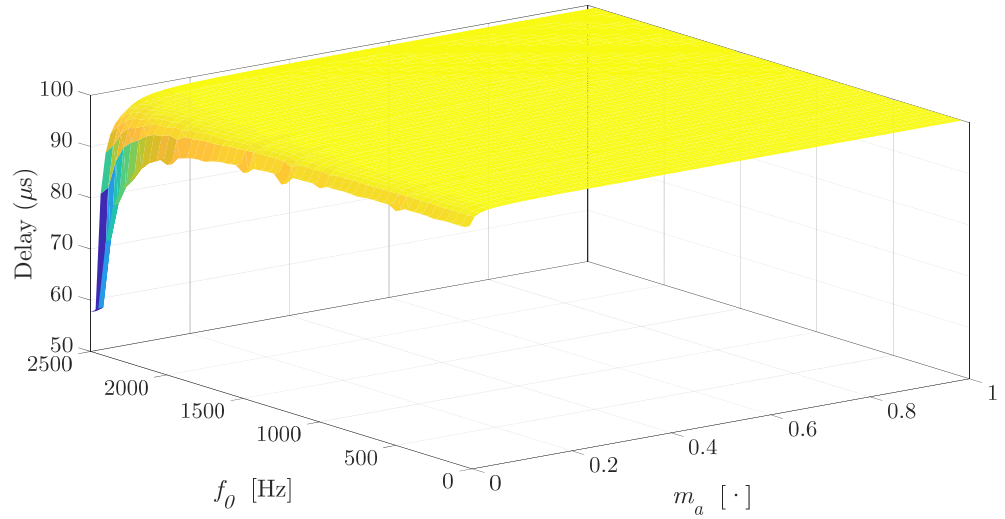

Figure 2.20. Parametric DSPWM simulation of double-update mode delay regarding modulating frequency f_0 and amplitude modulation index m_a, being $T = 200\ \mu s$ and $T_{carrier} = 400\ \mu s$

From Figure 2.17 and Figure 2.18, it is deduced that, for modulating frequencies among the hundreds of Hz, the gain is the unity, whatever is the amplitude modulation index. In Figure 2.19 a parametric DSPWM simulation is carried out, where the previous conclusion is validated for the double-update-mode case. The gain falls with higher frequencies and this falling is greater at low amplitude modulation index m_a. However, a difference is found at high frequencies, where there is not m_a to get a unitary gain.

Besides, Figure 2.20 confirms the constant delay *T/2* independently from m_a and modulating frequency f_0.

Hence, for $f_0 \ll f_{SW}$, the digital PWM block can be considered as a transfer function with unitary gain and constant delay of *T/2*. This shows that the introduced delay only depends on the sampling rate T of the application. This model is required to design the controller, and both continuous *s*-domain and discrete *z*-domain have been studied in the literature.

2.2.3.2. Multisampling

The modulator system delay plays a key role in limiting the achievable control bandwidth. The contributions at [50] and [53] suggested a different approach, which exploits the possibility of sampling control variables several times within the modulation period $T_{carrier}$ (T_{SW}). Hence, the PWM response delay is reduced and it increases the system phase margin, which is demonstrated in the previous analysis with the differences between the single-update and double-update modes where the delay only depends on the sampling rate T.

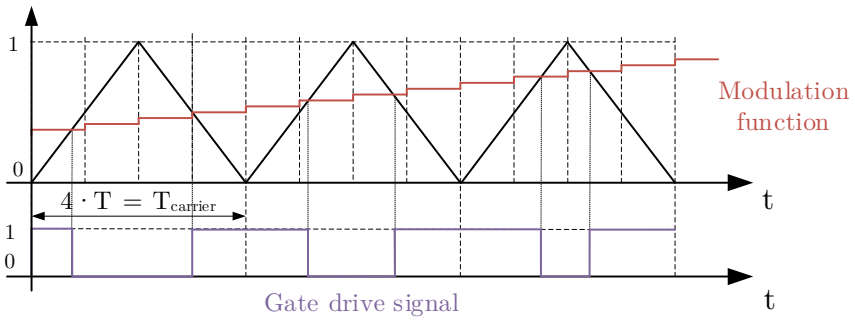

Figure 2.21. Multi-sampled PWM

Figure 2.21 shows the multisampling approach, where modulating signal is sampled 4 times during a switching period. Therefore, the control algorithm updates control signal or modulating signal at each sampling event. If the signal is sampled N times during the switching period, the hold time of the ZOH is now $T = T_{carrier}/N$. Following the statements from the later subsection, the digital PWM behavior is again that of a pure delay, and its equivalent delay time is a decreasing function of the multisampling factor N. The corresponding small-signal model for a multi-sampled digital PWM in the frequency domain is presented in (2.16) as deduced in [53], where D is the average duty-cycle.

$$\begin{aligned} G_{PWM}(j\omega) &= \cos\left(\omega\left(ND - 2\cdot floor\left(\frac{ND}{2}\right) - 1\right)\cdot\frac{T_{carrier}}{2N}\right)\cdot e^{-j\omega\cdot\frac{T_{carrier}}{2N}} \\ &= \cos\left(\omega\left(ND - 2\cdot floor\left(\frac{ND}{2}\right) - 1\right)\cdot\frac{T}{2}\right)\cdot e^{-j\omega\cdot\frac{T}{2}} \end{aligned} \tag{2.16}$$

Where $floor(ND)$ denotes the greatest integer that does not exceed $N \cdot D$. The unitary gain is maintained for higher frequencies as is shown in Figure 2.22, where $T_{carrier}$ is 400 µs and N is 4, so T is 100 µs. In any case, the PWM block is always considered as a unitary gain transfer function. Again, a validation is done through a parametric

simulation of digital SPWM. Figure 2.23 depicts how the gain is maintained for higher frequencies, contrary to Figure 2.19, and Figure 2.24 shows the constant *T/2* delay for the multi-sampled PWM. It is not appreciated in Figure 2.23, but the surface shape is almost like the one obtained in Figure 2.22, because there are two drops at high modulating frequencies when m_a is around 0 and 0.7. The second drop is smaller, but from the later parametric simulation is deduced that, for higher f_0 and m_a, the gain drops more than it is theoretically expected on the model. This is one consequence of linearization around a determined average duty-cycle and ZOH operation.

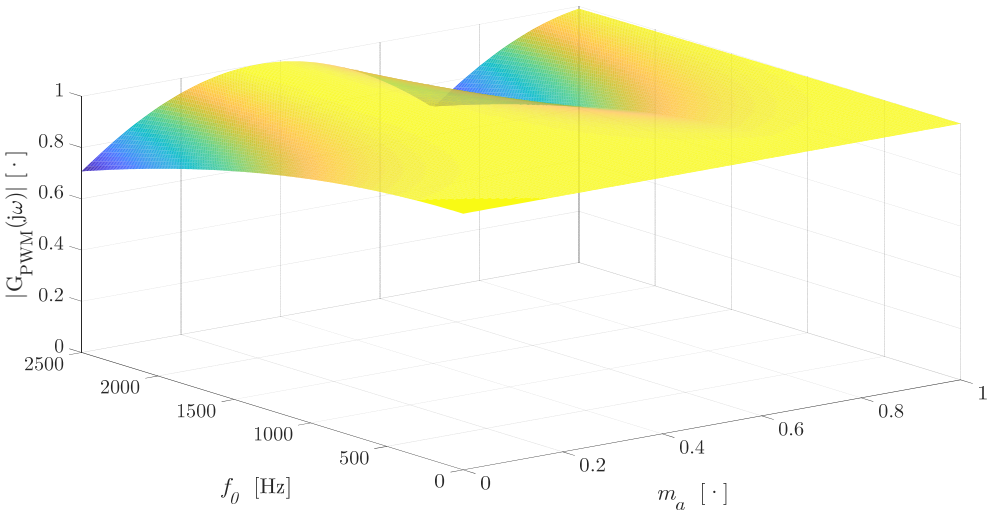

Figure 2.22. Multi-sampled (N = 4) mode gain regarding modulating frequency f_0 and amplitude modulation index m_a, being $T = 100\ \mu s$ and $T_{carrier} = 400\ \mu s$

From the previous, it can be inferred that, as N tends to infinity, the equivalent delay time tends to zero. The deduction is obvious because the multi-sampled PWM approaches the naturally sampled modulator, where the phase lag is known to be zero. Also, the half sampling period delay is an inherent result from the ZOH operation, which is always in digital control systems.

This approach requires a different hardware organization in comparison to the single-update and double-update modes. The main technologies required are:

- Large bandwidth AD converters, capable of operating at several mega sample per second (*MSample/s*) speeds.
- Programmable digital hardware, i.e., FPGA chips, that allows to minimize the computation time of the control algorithm, thus keeping pace with the ADC.

The multisampling approach is focused in the current control loop, and its performance maximizing might positively impact on other external control loops, increasing their stability margins and robustness [50]. The outer control loops are closed around the current control loop and their design is directly and heavily affected by the phase lag introduced by the current controller. It determines the phase margin of the outer loop at its desired cross-over frequency and, consequently, its achievable bandwidth and overall stability margin. The design goal is to minimize the phase lag introduced by the

current controller, and it is highly achieved with the multisampling approach presented here.

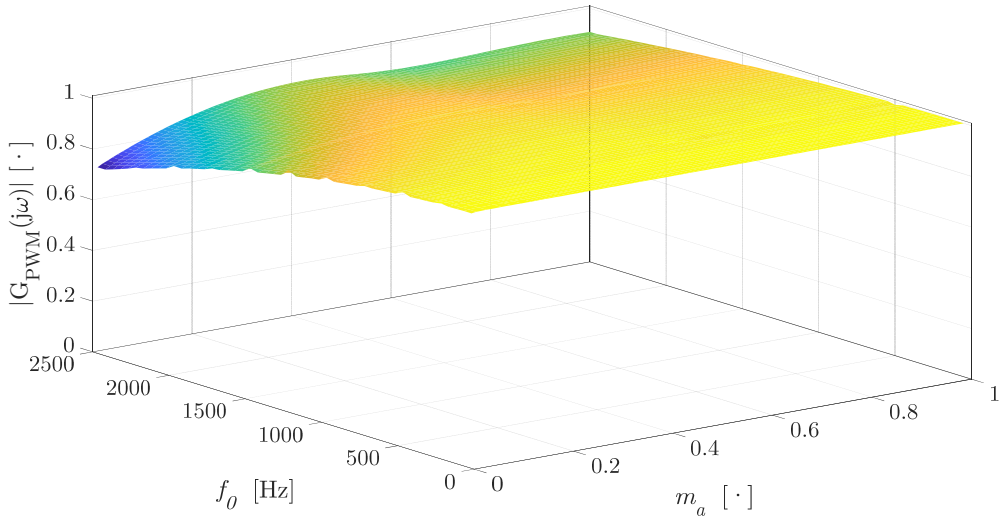

Figure 2.23. Parametric DSPWM simulation of Multi-sampled ($N = 4$) mode gain regarding modulating frequency f_0 and amplitude modulation index m_a, being $T = 100\ \mu s$ and $T_{carrier} = 400\ \mu s$

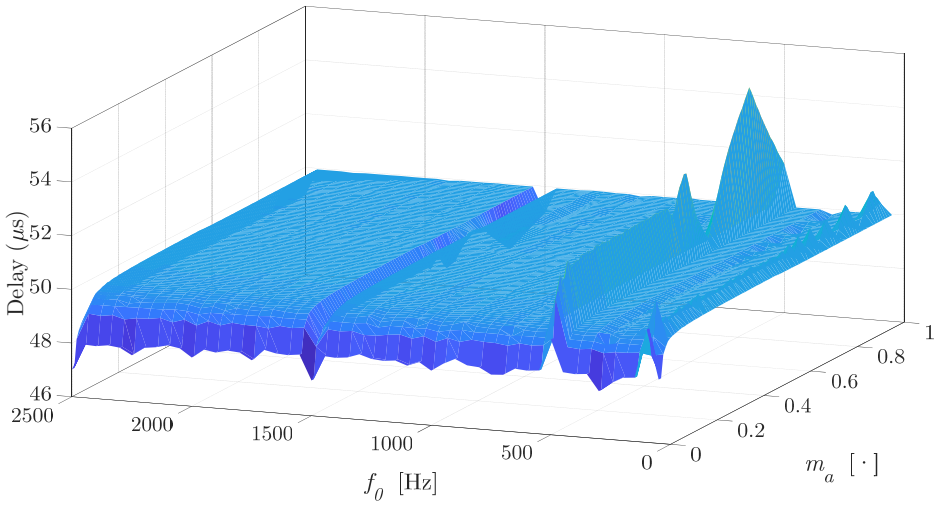

Figure 2.24. Parametric DSPWM simulation of Multi-sampled ($N = 4$) mode delay time regarding modulating frequency f_0 and amplitude modulation index m_a, being $T = 100\ \mu s$ and $T_{carrier} = 400\ \mu s$

The main drawback of this approach comes from the need of a proper filtering of the switching noise from controlled signals. In the single or double-update modes the current signal is sampled at the carrier signal minima and maxima to avoid the switching noise, but the multisampling approach samples the current in different instants, which include the noise. This is clearly shown in Figure 2.25. The system phase margin might be reduced due to filtering the control signals, reducing the advantage of the multi-sampled strategy.

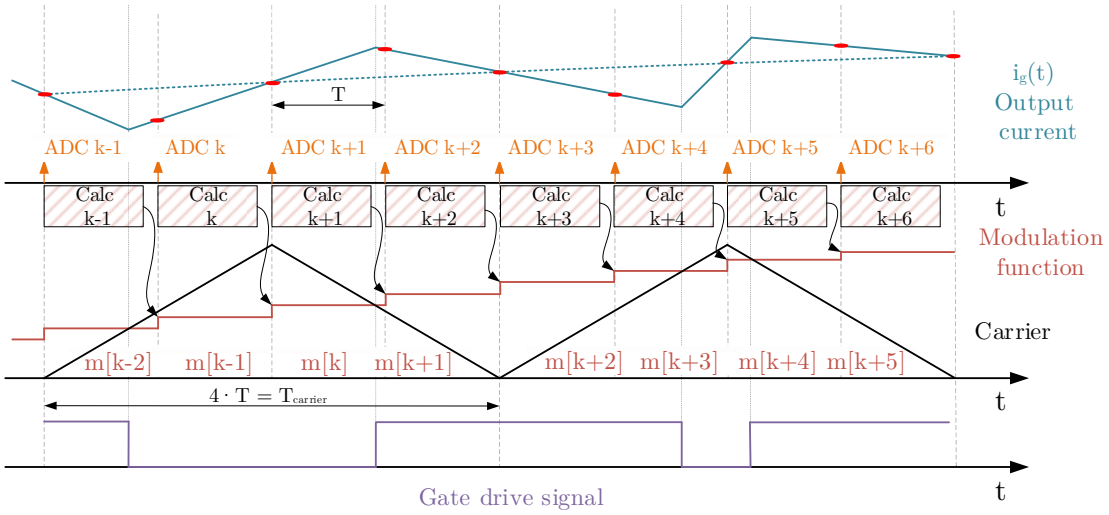

Figure 2.25. Multi-sampled PWM strategy with sampling of current noise

Switching-frequency ripple removal is recommended for practical multisampling implementation. The author in [53] showed some possible approaches. The first comes from a low-pass filter or moving average filters, but they significantly deteriorate the phase margin, consequently losing the advantages of the multisampling solution. The final solution is a low phase lag selective filter defined in [54] and shown in (2.17).

$$F(z) = \frac{(1+K)\cdot\left(1-\left(z^{-N}-\frac{1}{N}\cdot\sum_{n=1}^{N}z^{-N}\right)\right)}{1-\left(z^{-N}-\frac{1}{N}\cdot\sum_{n=1}^{N}z^{-n}\right)+K} \tag{2.17}$$

The filter $F(z)$ is defined by the constant K and relation N between the carrier period $T_{carrier}$ and modulating signal sampling period T. The higher is K, the faster is the filter dynamics. Figure 2.26 depicts the Bode diagram, where the integer multiples of the switching frequency are removed without significant phase lag at low frequencies.

However, this filter is excessively selective, and the generated switching noise is not at determined frequency $f_{carrier}$ (f_{SW}). The switching harmonics are sideband harmonics group around the switching frequency multiples (carrier harmonic) that are not removed with this filter due to its selectivity. In Figure 2.9 and Figure 2.10, it is shown how the sideband harmonics are distributed around the switching frequency multiples in the phase leg voltage for different carrier disposition in a 3L-DNPC-VSC. The sampled current takes the harmonics from the resulting phase-to-phase voltage that changes its harmonic content from the phase leg voltage one. The phase leg harmonic components that will not appear in the phase-to-phase output voltage are:

- Carrier harmonics. They are the same for all phase legs.
- Sideband harmonics with even combinations of $m_f \pm n$, being n the harmonic order.
- Triplen sideband harmonics, where n is a multiple of 3. The phase angles of these harmonics rotate by multiples of 2π for all phase legs and hence they are the same for all phase legs.

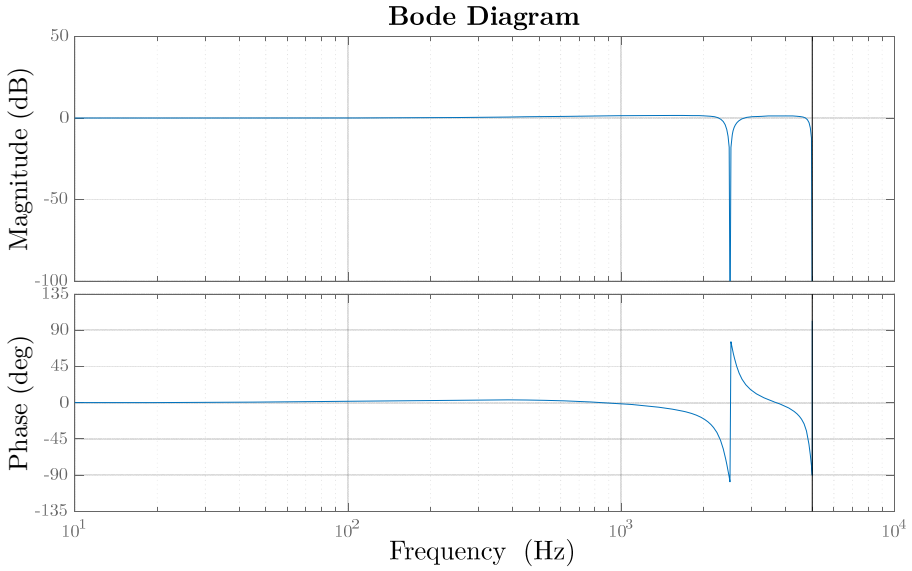

Figure 2.26. Bode diagram of $F(z)$ with $T_{carrier} = 400\ \mu s$ and $N = 4$

Usually, a sampling process have an antialiasing filter (cutoff frequency of $(1/T)/2$ established by Nyquist criterion) to avoid the alias in the sampling signal, but in this case is not enough because the first sideband harmonics group is always in the remained signal. In this document an alternative is shown in Chapter 3 to accomplish the delay reduction without changing the sampling frequency, so the current is sampled at its mean value by sampling at carrier maxima and minima.

Besides, there is an important issue to analyze the digital comparison between modulating signal and carrier signal. The modulating signal changes N/2 times each half carrier period $T_{SW}/2$, and the discrete values of modulating signal can lead to more carrier intersections than the allowed ones. Figure 2.27 depicts the situation where the discrete signal intersects the carrier signal more than one time per half carrier period.

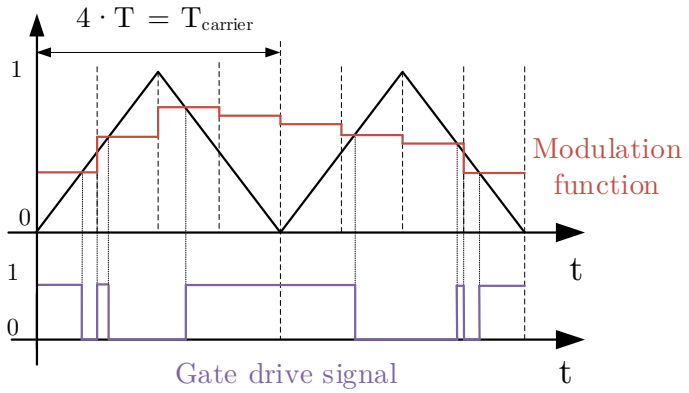

Figure 2.27. Multi-sampled PWM with multiple crossing per half carrier period

It might be solved with an algorithm that ensures one gate drive signal change per half carrier period, what drastically changes PWM signal of the corresponding modulating signal. On previous multi-sampled parametric DSPWM simulations, this algorithm is not applied and the PWM response is like the one obtained through the theoretical

model for some f_0 and m_a. However, if the algorithm is applied, the parametric simulations changes as it will be shown in Chapter 3.

2.2.3.3. ZOH model for DSPWM

From Figure 2.19 is deduced that the gain falls more than is expected for high modulating frequencies when the amplitude modulation index is high. The ZOH describes more accurately this behavior with high m_a but fails with the low ones. It is necessary to indicate that the ZOH is on the DSPWM process by the discretization of modulating signal. However, it is interesting to analyze the small-signal response due to the special treatment of the signal by this actuation system.

The transfer function of the Zero Order Hold is (2.18) and its frequency response is (2.19), obtained by the substitution of s by $j\omega$.

$$G_{h0}(s) = \frac{1 - e^{-sT}}{s} \tag{2.18}$$

$$G_{h0} = T \cdot \frac{\sin(\omega T/2)}{\omega T/2} \cdot e^{-j\omega \cdot \frac{T}{2}} \tag{2.19}$$

The magnitude is zero at multiplies of the sampling frequency, $1/T$. Also, whatever is the frequency, the delay time is maintained in $T/2$. Figure 2.28 shows the frequency response of the ZOH module normalized to T and frequencies below the corresponding Nyquist frequency. This curve represents what the small signal models do not characterize at high frequencies, as it is shown in parametric DSPWM simulation in Figure 2.19 and Figure 2.23. However, the ZOH does not characterize the gain falling at low m_a due to its independence from the duty-cycle D. Therefore, for high frequencies the two gain characteristics must be considered.

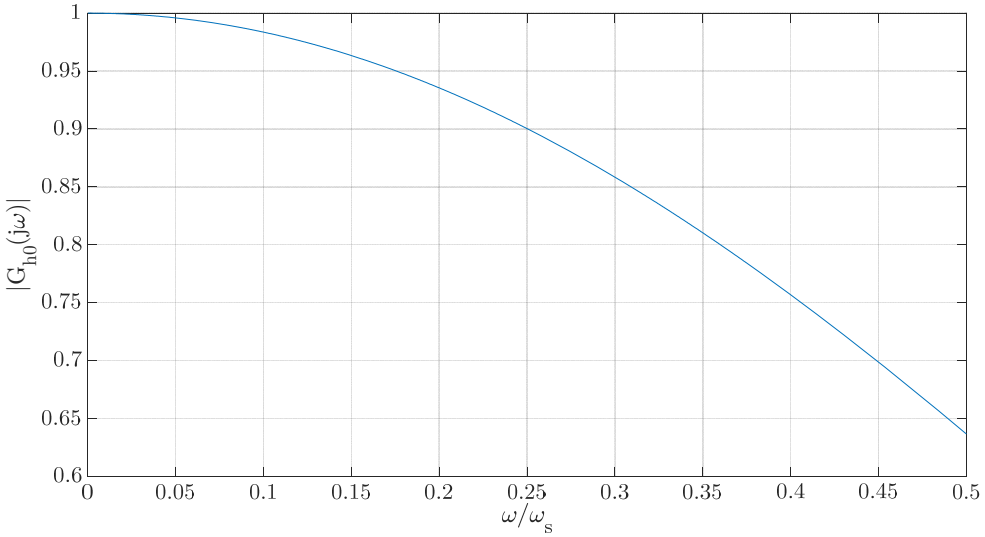

Figure 2.28. Frequency response of the ZOH operation

2.2.3.4. Continuous-time modelling of DSPWM

The previous analysis gives a Laplace-domain expression to the DSPWM operation, but the delay has some modelling problems in this domain because the exponential function that represents this delay is non-linear. Besides, the application of discretization techniques involves the obtaining of equivalent continuous-time model of the sampled data system. To use that in the design of a continuous-time controller stabilizing the feedback loop, and to turn the continuous-time controller into an equivalent discrete time one. It must be emphasized that the interpolation operation is inherent to the DSPWM, because it is the system where conversion from the digital to analog domain takes place. This is what equals the DSPWM to typical ZOH operation in discrete-time control systems. Once the hold effect is modeled in the DSPWM, the conversion of the sampled data system into an equivalent continuous time one will be completed. Two approximations have been found modeling the PWM block delay effect to design the controller at this domain.

1) Padé approximation

The first approach is detailed on [50], and a brief explanation is given here. From what was presented before, the model for the DSPWM is considered as one-half modulation period delay, $T/2$, cascaded to a frequency-dependent gain. The typical current controller bandwidth is limited well below the modulating frequency, $1/T$, so the gain term is approximated by unity. The simplified model is shown in (2.20). Again, it must be noted that this exactly coincides with the continuous-time model of the ZOH.

$$DSPWM(s) \cong e^{-s \cdot \frac{T}{2}} \tag{2.20}$$

The continuous rational transfer function of the DSPWM can be obtained considering a Padé approximation of (2.20), obtaining the first-order expression as (2.21) or the second-order expression as (2.22), where T is the sampling period. The first-order approximation is enough to model the delay.

$$e^{-s \cdot \frac{T}{2}} \cong \frac{1 - s \cdot \frac{T}{4}}{1 + s \cdot \frac{T}{4}} \tag{2.21}$$

$$e^{-s \cdot \frac{T}{2}} \cong \frac{1 - s \cdot \frac{T}{4} + s^2 \cdot \frac{T^2}{24}}{1 + s \cdot \frac{T}{4} + s^2 \cdot \frac{T^2}{24}} \tag{2.22}$$

The differences on the approximation are obtained at the beginning, corresponding to the first period delay, later the solution is equivalent.

The discrete-time controllers have a second, independent source of delay: the control algorithm computation delay. As it was previously indicated, this is the time required by the processor to compute a new m_a value, given the input variable sample. The input cannot be computed to the modulator during the same modulation period when it is applied as was depicted in Figure 2.11. This means that the control algorithm implies an additional modulation period delay that must be modeled. It can be done increasing the delay effect represented by the Padé approximation with T, i.e., a total

delay of $3T/2$. Therefore, the continuous-time controller design must consider the calculation and PWM delay effects to get a satisfactory performance from the equivalent digital controller. The block diagram of the continuous-time equivalent of the digital current PI control loop is depicted in Figure 2.29, as an example. The discretization methods of the designed continuous-time controller could be: Backward Euler; Forward Euler or Trapezoidal (Tustin).

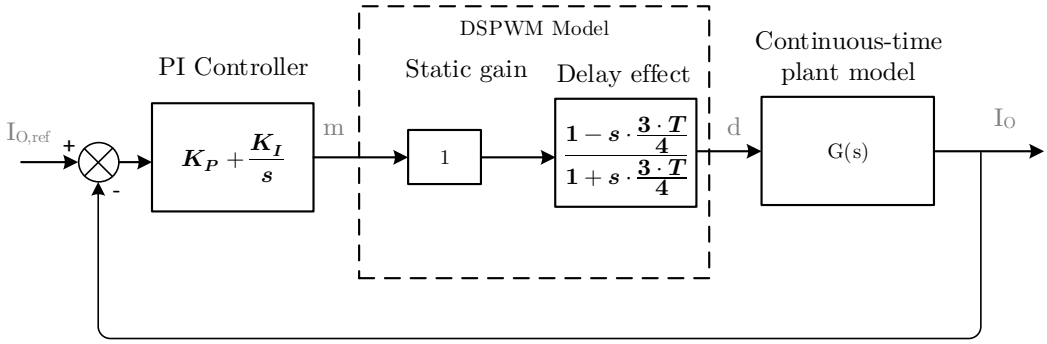

Figure 2.29. Block diagram of the continuous-time equivalent of the digital current control loop

Please note, that the computational delay T is valid for what was defined as s-PWM-start (single-update mode with symmetric-off-time) and a-PWM-double (double-update mode). The computational delay for the s-PWM-middle (single-update mode with symmetric-on-time) is $T/2$. Besides, the computational delay can be reduced with the approach that will be shown in Chapter 3.

2) Compensation method for ZOH deviation

The second approach is detailed in [55], and it is based on the analysis of the ZOH accuracy that also models the DSPWM in continuous-time domain. Please note that, in the DSPWM, there is a ZOH operation to obtain the modulating signal. The author enforces the continuous s-domain model for power converters, instead of the discrete z-domain model, because the electric power grids have a continuous dynamic behavior. This means that the digital controller, that can be exactly modeled in the z-domain, is most accurately design in continuous-time domain due to the s-domain model of the controlled plant. Besides, the author indicates that the analysis of the control system in the z-domain requires a uniform sampling/duty-cycle update frequency, but this is not true, a multirate approach is possible.

The ZOH model improves the accuracy of the DSPWM model better than the small-signal analysis presented with Padé approximation, but it is still an approximation of the DSPWM. Compensation of the ZOH model deviation is necessary.

The analysis is obtained with the overall open-loop transfer function, which means that a plant model and the controller must be known to obtain the deviation of the s-domain transfer function with the ZOH equivalent model. The modulating signal update (duty-cycle update) mode, regarding the sampling instant, changes the computational delay, which it is denoted as T_d. The time delay can be reduced by shifting the sampling instant towards the modulating signal update, as it will be shown

later. This improves the phase margin, which is useful in power converters with low switching frequency, f_{SW}. The followed strategy in this contribution is the comparison between the frequency response of the open-loop transfer functions in s-domain and z-domain, so the frequency-domain deviation transfer function is obtained.

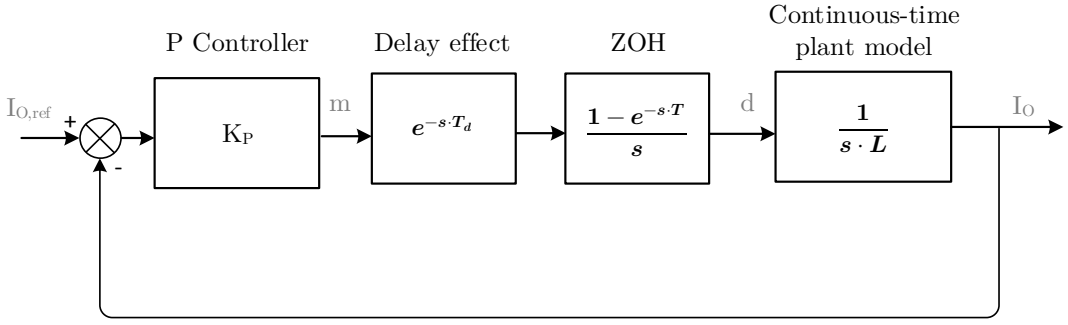

Figure 2.30. Block diagram of the continuous-time equivalent of digital current control loop for a L-filter.

The given example by the author is a single-phase inverter connected to a L-filter with a proportional controller, as presented in Figure 2.30, but the taken guide here is valid to other systems. On one hand, the s-domain open-loop transfer function including the computational delay is (2.23). On the other hand, the z-domain open loop transfer function including the fractional order delay (T_d might be fractional depending on the modulating signal update) is (2.24). The z-domain fractional order delay expression is a taken approximation from the author in [55], but also others like [56], and is only correct for a converter connected to the grid through a L-filter. The expression is obtained with the techniques in Appendix A with modified Z-transform. Therefore, the author from this contribution is supposing that the z-domain model is the most accurate.

$$G_{os}(s) = K_p \cdot e^{-s \cdot T_d} \cdot \frac{1 - e^{-s \cdot T}}{T \cdot s} \cdot \frac{1}{sL} \tag{2.23}$$

$$G_{oz}(z) = \left[1 - \frac{T_d}{T} + \frac{T_d}{T} \cdot z^{-1}\right] \cdot \frac{T \cdot K_p}{(z-1) \cdot L} \tag{2.24}$$

The respective frequency response of the open loop transfer functions in s-domain and z-domain are the following:

$$G_{os}(j\omega) = \frac{K_p}{\omega L} \cdot \left|\frac{\sin(\omega \cdot T/2)}{\omega \cdot T/2}\right| \cdot e^{-j\left(\frac{\pi}{2} + \omega \cdot \frac{T}{2} + \omega \cdot T_d\right)} \tag{2.25}$$

$$G_{oz}(j\omega) = \left[\left(1 - \frac{T_d}{T}\right) + \frac{T_d}{T} \cdot e^{-j\omega T}\right] \cdot \frac{T}{2L} \cdot \frac{K_p}{|\sin(\omega \cdot T/2)|} \cdot e^{-j\left(\frac{\pi}{2} + \omega \cdot \frac{T}{2}\right)} \tag{2.26}$$

Therefore, the deviation expression is (2.27). The magnitude and phase deviation are depicted in Figure 2.31 and Figure 2.32, respectively, as a function of the normalized computation delay and normalized frequency. Several conclusions can be found at these representations, mainly on computation delay singular points as 0, $T/2$ and T.

$$D(j\omega) = \frac{G_{oz}(j\omega)}{G_{os}(j\omega)} = \left[\frac{\omega \cdot T/2}{\sin(\omega \cdot T/2)}\right]^2 \cdot \left[\left(1 - \frac{T_d}{T}\right) \cdot e^{j\omega \cdot T_d} + \frac{T_d}{T} \cdot e^{j\omega(T_d - T)}\right] \tag{2.27}$$

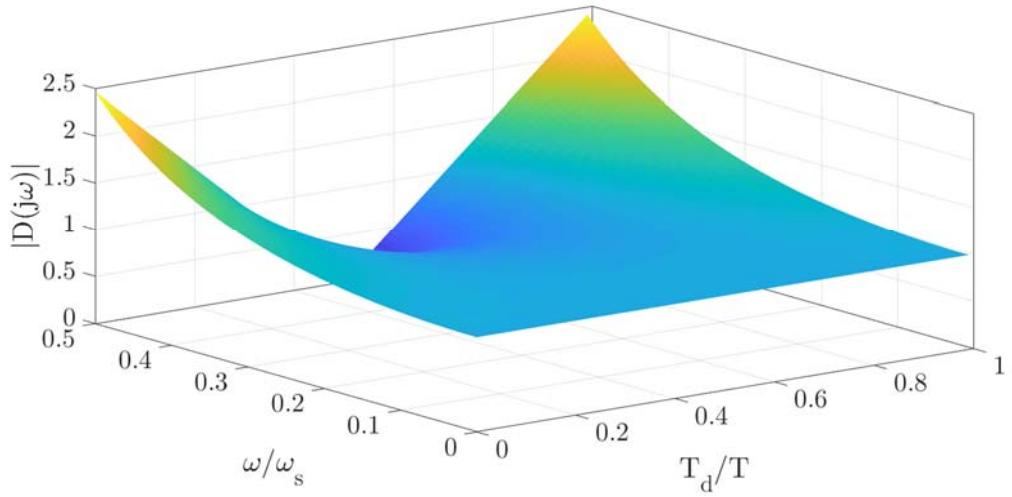

Figure 2.31. DSPWM deviation magnitude regarding normalized frequency ω and normalized computation delay T_d

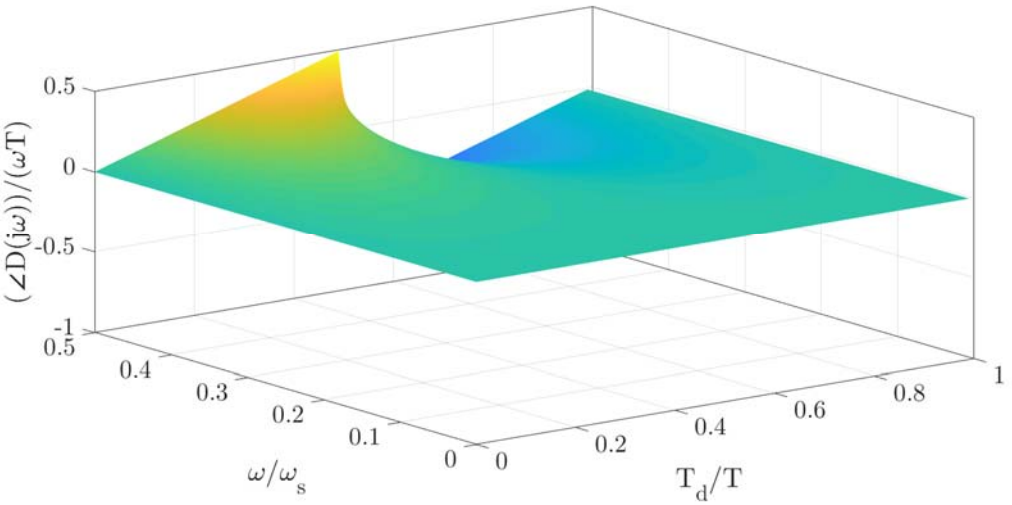

Figure 2.32. DSPWM deviation delay regarding normalized frequency ω and normalized computation delay T_d

The deviation magnitude increases as the modulating signal frequency increases and the computational delay is null or equal to the sampling period, T, but it falls when the computational delay is half the sampling period. The computational delay will never be null, because digital controllers have a finite calculation time, but it is interesting to visualize the deviation when the computational delay approaches the zero value. Also, a singular point is found at half the sampling period, because the exponential terms become zero when the modulating signal frequency is one-half the sampling period. Finally, the deviation magnitude is near to unity at low frequencies, but it is not exactly this value, so this deviation must be considered.

The deviation delay is almost null at all frequencies excepting singular point at $T_d = T/2$ around high frequency, where an advance is found below and a delay above this value. Therefore, gain compensation must be considered when the digital controller is designed in the continuous-time domain.

2.2.3.5. Discrete-time modelling of DSPWM

The usual option to obtain an accurate model of the digital controlled system is modelling the discrete-time system in *z*-domain, that considers the exact duration of the computation delay. Besides, tools, as the modified *Z*-transform, exactly model the duty-cycle update instant within the modulation period. Therefore, the sampled data system is transformed into a discrete-time equivalent, that can be used to directly design the controller in the discrete-time domain.

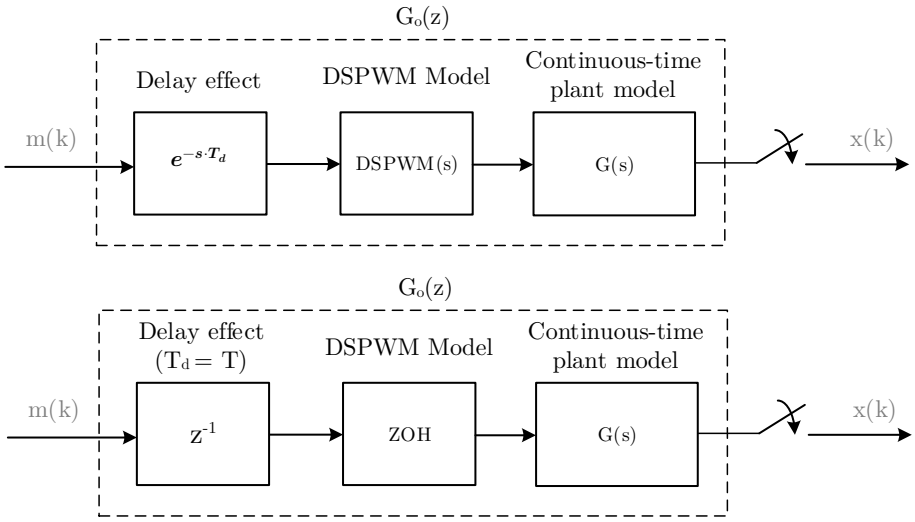

Figure 2.33. Equivalence between discrete-time plant transfer function of the converter including the computation delay and DSPWM

1) Modelling equivalences

The discrete-time transfer function $G_o(z)$, which models the computation delay, the PWM transfer function, the converter, and the sampler, is given by (2.28). As it is indicated in [50], a correct relationship between the DSPWM modelling and the standard digital control theory must be considered. As it was mentioned along this section, the ZOH function is internal to the PWM model, but usually appears cascaded to an ideal sampler, modelling the conversion from sampled time variables into continuous-time variables. Therefore, to correctly model the transfer function between the sampled time input variable and the continuous-time output variable of the modulator, a gain equal to T has to be added to the modulator transfer function $DSPWM(s)$.

$$G_o(z) = \mathcal{Z}[e^{-s \cdot T_d} \cdot T \cdot DSPWM(s) \cdot G(s)] \tag{2.28}$$

The PWM transfer function $T \cdot DSPWM(s)$ is like a ZOH, so the ZOH discretization method can be used to obtain the discrete-time plant transfer function. Figure 2.33 depicts the equivalence. This is the intuitive and usual discretization of the continuous-time plant model. For example, if the computational delay is T, the transfer function $G_o(z)$, is now described as (2.29)

$$G_o(z) = z^{-1} \cdot \mathcal{Z}[G_{h0}(s) \cdot G(s)] \tag{2.29}$$

If the plant model G(s) is (2.30), corresponding to a single-phase inverter with L-filter, and assuming $T_d = T$, then there is no difference between (2.28) and (2.29), derived in (2.31) and (2.32), respectively. The modified Z-transform bases are defined in Appendix A.

$$G(s) = \frac{1}{sL} \tag{2.30}$$

$$G_o(z) = z^{-1} \cdot \mathcal{Z}\left[T \cdot e^{-s\cdot\frac{T}{2}} \cdot \frac{1}{sL}\right] = z^{-1} \cdot \frac{T}{L} \cdot \mathcal{Z}_m\left[\frac{1}{s}\right]_{|m=1/2} = \frac{T}{L} \cdot \frac{1}{z(z-1)} \tag{2.31}$$

$$G_o(z) = z^{-1} \cdot \mathcal{Z}\left[\frac{1-e^{-sT}}{s} \cdot \frac{1}{sL}\right] = \frac{T}{L} \cdot \frac{1}{z(z-1)} \tag{2.32}$$

The authors in [50] suggest that the equivalence between the two approaches is justified, if it is considered that the current variation only depends on the average voltage value generated by the PWM. The multi-sampled system in z-domain is described as (2.33), where the Z-transform is done with a sampling period equal to T/N.

$$G_o(z) = \mathcal{Z}\left[e^{-s\cdot T_d} \cdot \frac{T}{N} \cdot DSPWM(s) \cdot G(s)\right] \tag{2.33}$$

2) Minimization of the computational delay

The computational delay can be minimized, as it was previously indicated, and detailed information about this topic is found in [57]. The increase of computational power of DSPs, microcontrollers, and FPGAs makes possible the control delay reduction. This is obtained shifting the current sampling instant towards the update instant of the modulating signal, leaving just enough time for the ADC to generate the new input sample and for the processor to control algorithm calculation. From the standpoint of controller, this implies a reduction of the feedback loop delay. The analyzed situation for the single-update (s-PWM-start) case is depicted in Figure 2.34, the double-update is easily interpolated from it.

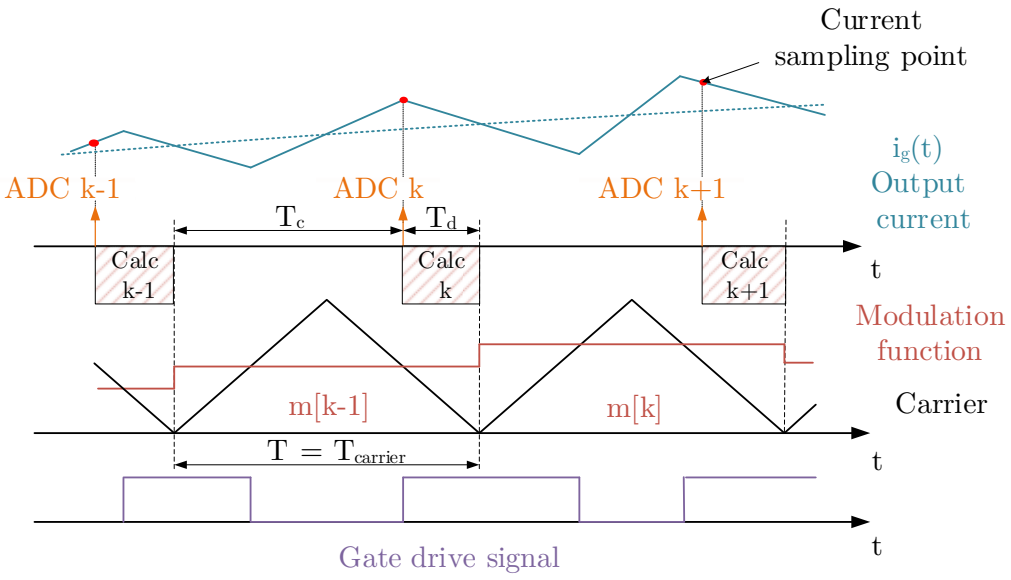

Figure 2.34. Sampling of current shifted towards the modulating signal update

In Figure 2.34, the sampled variable is the output current of the converter, but it could be another variable. The computation time is T_d, that is the time required by ADC and calculations, whereas the time T_c is the available time for other non-critical functions or external control loops.

An accurate discrete-time model of this approach is necessary, and it is obtained considering a ZOH for the PWM block and the modified *Z*-transform. The delay T_d is a fraction of the sampling period T, so the modified *Z*-transform must be used to correctly model the system. The modified *Z*-transform bases are completely defined in Appendix A, but, in the following, a brief recall is presented.

The fractional delay is defined as $(1-m)\cdot T$, where $0 \leq m \leq 1$, so the m factor is:

$$m = 1 - \frac{T_d}{T} \tag{2.34}$$

The discrete-time model of a continuous system composed of ZOH, $G_{h0}(s)$, and the plant model, $G(s)$, can be expressed as (2.35). The impulse response of $G_o(s)$ is $g_o(t)$, and $G_o(z,m)$ is the modified *Z*-transform of $G_o(s)$.

$$\mathcal{Z}\left[\underbrace{G_{h0}(s)\cdot G(s)}_{G_0(s)}\cdot e^{-s\cdot m\cdot T}\right] = \sum_{k=0}^{\infty} z^{-k}\cdot g_0(k\cdot T - T_d) = \mathcal{Z}_m[G_0(s)] = G_0(z,m) \tag{2.35}$$

Therefore, substituting the ZOH transfer function expression, the delayed model plant is (2.36).

$$G_o(z,m) = \mathcal{Z}\left[\frac{1-e^{-s\cdot T}}{s}\cdot G(s)\cdot e^{-s\cdot m\cdot T}\right] = \frac{z-1}{z}\cdot \mathcal{Z}_m\left[\frac{G(s)}{s}\right] \tag{2.36}$$

The modified *Z*-transform maintains the properties of the conventional *Z*-transform, since it is simply defined as the *Z*-transform of a delayed signal. Following the previous example plant model $G(s)$, corresponding to a single-phase inverter with L-filter, the discrete-time transfer function between the modulating signal and the delayed output current is (2.37). This expression was presented before in (2.24), but, this time, the proportional controller is not included.

$$G_o(z) = \frac{T}{L}\cdot\frac{z\cdot m - (m-1)}{z(z-1)} \tag{2.37}$$

In [57] is explored the achievable current loop bandwidth and voltage bandwidth on different m values. All of them increase as the m value increases, so simply by shifting the sampling instant towards the modulating signal update instant, a significant improvement in the achievable bandwidth can be obtained. Please note, with single-update mode, if m is null, the s-PWM-start situation is obtained, whereas m is 0.5, the s-PWM-middle is found. For other values of m, a filter is needed to reject the current ripple. This leads to the application of the concept to control other system variables, instead of the current control. The example of the output voltage control in an Uninterruptible Power Supply (UPS) is given in [57].

The previous analysis can be easily obtained for a three-phase converter as it is detailed in [48]. Considering the rotating dq reference frame model of current dynamics

in a L-filter with resistive effects as is shown in (2.38), a complex-valued transfer function is obtained. There is a complex-valued coefficient which correspond to the cross-coupling effects. The angular frequency of the rotating reference frame, ω_k, is time-variant for variable frequency applications, whereas for constant frequency applications is time-invariant.

$$\vec{G}_{dq}(s) = \frac{\vec{I}_{dq}(s)}{\vec{U}_{dq}(s)} = \frac{1}{R} \cdot \frac{1}{1 + s \cdot \frac{L}{R} + j\omega_k \cdot \frac{L}{R}} \tag{2.38}$$

If the computational time and DSPWM is also considered, the overall complex-valued open-loop transfer function is (2.39). Hence, the modified Z-transform is applied to this transfer function to obtain the expression for different computational delay, T_d, as it is expressed in (2.41).

$$G_{dq}^{OL}(s) = \frac{I_{dq}(s)}{U_{dq}^{ref}(s)} = \frac{1 - e^{-s \cdot T}}{s} \cdot e^{-s \cdot T_d} \cdot e^{-j\omega_k \cdot T_d} \cdot \frac{1}{R} \cdot \frac{1}{1 + s \cdot \frac{L}{R} + j\omega_k \cdot \frac{L}{R}} \tag{2.39}$$

$$G_{dq}^{OL}(z,m) = \frac{I_{dq}(z)}{U_{dq}^{ref}(z)} = \frac{z-1}{z} \cdot \mathcal{Z}_m \left[e^{-j\omega_k \cdot T_d} \cdot \frac{1}{R} \cdot \frac{1}{1 + s \cdot \frac{L}{R} + j\omega_k \cdot \frac{L}{R}} \right]_{|\ m\,=\,1-\frac{T_d}{T}} \tag{2.40}$$

$$\begin{gathered} G_{dq}^{OL}(z,m)_{|\ m\,=\,1-\frac{T_d}{T}} = \frac{1}{R + j\omega_k \cdot L} \cdot \left[\frac{1}{z} - \frac{\alpha_2 \cdot (z-1)}{z \cdot (z - \alpha_1)} \right] \cdot e^{-j\omega_k \cdot (1-m) \cdot T} \\ \alpha_0 = e^{-T \cdot R/L} \\ \alpha_1 = \alpha_0 \cdot e^{-j\omega_k \cdot T} \\ \alpha_2 = e^{-m \cdot T \cdot R/L} \cdot e^{-j\omega_k \cdot m \cdot T} \end{gathered} \tag{2.41}$$

The Table 2.3 is taken from the one presented in [48] for the resultant complex-valued transfer function of the three PWM strategies presented in Figure 2.11.

Table 2.3. Grid-tied converter with L-filter transfer functions for each strategy. Source: [48]

s-PWM-start (single-update mode) $\boldsymbol{T_d = T_{carrier} = T \ \mid \ m = 0}$	
$\boldsymbol{G_{dq}^{OL}(z) = \frac{1}{R + j\omega_k \cdot L} \cdot \frac{1 - \alpha_1}{z \cdot (z - \alpha_1)} \cdot e^{-j\omega_k \cdot T}}$ $\boldsymbol{\alpha_0 = e^{-T \cdot R/L} \qquad \alpha_1 = \alpha_0 \cdot e^{-j\omega_k \cdot T} \qquad \alpha_2 = 1}$	(2.42)
s-PWM-middle (single-update mode) $\boldsymbol{T_d = 1/2 \cdot T_{carrier} = 1/2 \cdot T \ \mid \ m = 1/2}$	
$\boldsymbol{G_{dq}^{OL}(z) = \frac{1}{R + j\omega_k \cdot L} \cdot \frac{(1 - \alpha_2) \cdot (z + \alpha_2)}{z \cdot (z - \alpha_1)} \cdot e^{-j\omega_k \cdot \frac{1}{2} T}}$ $\boldsymbol{\alpha_0 = e^{-T \cdot R/L} \qquad \alpha_1 = \alpha_0 \cdot e^{-j\omega_k \cdot T} \qquad \alpha_2 = e^{-\frac{1}{2} T \cdot R/L} \cdot e^{-j\omega_k \cdot \frac{1}{2} T}}$	(2.43)
a-PWM-double (double-update mode) $\boldsymbol{T_d = 1/2 \cdot T_{carrier} = T \mid m = 0}$	
$\boldsymbol{G_{dq}^{OL}(z) = \frac{1}{R + j\omega_k \cdot L} \cdot \frac{1 - \alpha_1}{z \cdot (z - \alpha_1)} \cdot e^{-j\omega_k \cdot T}}$ $\boldsymbol{\alpha_0 = e^{-T \cdot R/L} \qquad \alpha_1 = \alpha_0 \cdot e^{-j\omega_k \cdot T} \qquad \alpha_2 = 1}$	(2.44)

2.2.4. Examples of multirate applications in power electronics

The previous analysis is focused in some usual power electronics applications where multirate concepts can be found. They are related to the sampling and actuation instants with certain fractional delays, but there is not a rate change along the control loop or algorithm. In the following, some contributions are studied where multirate concepts are introduced. Each reference provides a different point of view of multirate analysis, that will be explained later.

2.2.4.1. Multirate PLL

In [7] a multirate PLL (Phase-Locked Loop) is presented, and a schematic of its structure is shown in Figure 2.35. The multirate PLL is a variable sampling rate system with some features similar to the single-rate zero-crossing sampling PLL, but it operates at two different sample rates. One sample rate is much higher than the input signal (carrier) frequency and the other sample rate is equal to the carrier frequency. Multirate PLL can provide accurate phase synchronization to severely disturbed signals, and it is an all-digital approach. The disturbance rejection is mainly determined by the frequency response of a high-order band-pass anti-aliasing filter. The anti-aliasing filter automatically adapts to the input-signal-frequency variations through the variable sample-rate operation of the system, which is achieved by modifying the processor timer and applying the over-sampling technique to the input signal.

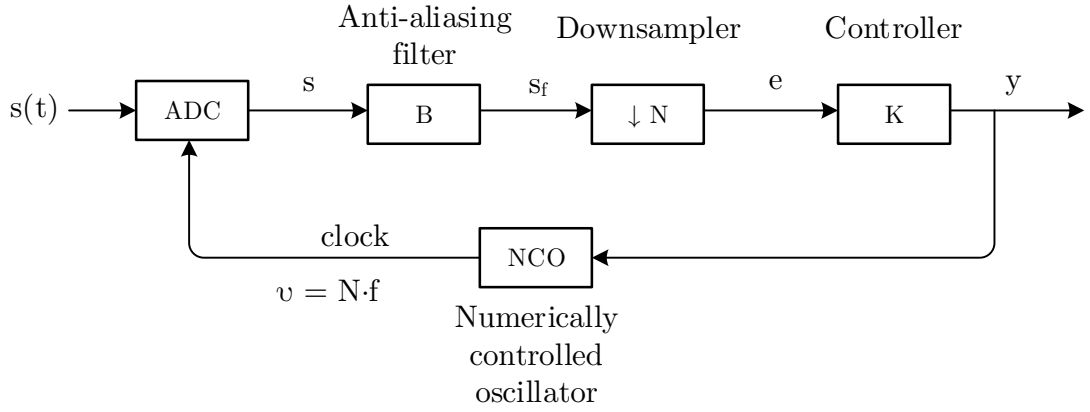

Figure 2.35. Multirate zero-crossing sampling digital PLL

The multirate PLL error signal, based on which the controller modifies the NCO frequency and, ultimately, sampling instants of the ADC, is derived from the input-signal samples. When the feedback action achieves zero error, the input signal is sampled exactly at zero crossings, and the PLL is locked. The relationship between the fast sample rate (frequency), υ, and the slow sample rate, f, is an integer N.

The main advantage of having the anti-aliasing filter in the digital part of the system comes from the fact that, in some applications, it would be very difficult to implement a practical analog anti-aliasing filter. In this case, the anti-aliasing filter is a bandpass filter, and its center frequency automatically tracks the carrier signal frequency.

The multirate PLL is a nonlinear system, so a linearization is needed to obtain a transfer-function model of the PLL and, then, to design the controller. In that document, the complex variable in the Z-transform of the fast sampling rate signals is denoted by p. The relationship between the two complex variable is $p^N = z$. As the system is linearized, the z-domain block is depicted in Figure 2.36, so a single-rate block diagram can be obtained. There is a time-varying block M since the input sinusoidal signal is sampled at the fast sampling frequency. The down sampler is represented by D. The PLL nominal frequency is denoted as $\Omega_q = 2\pi \cdot f_q$ and the phase shift as ϕ.

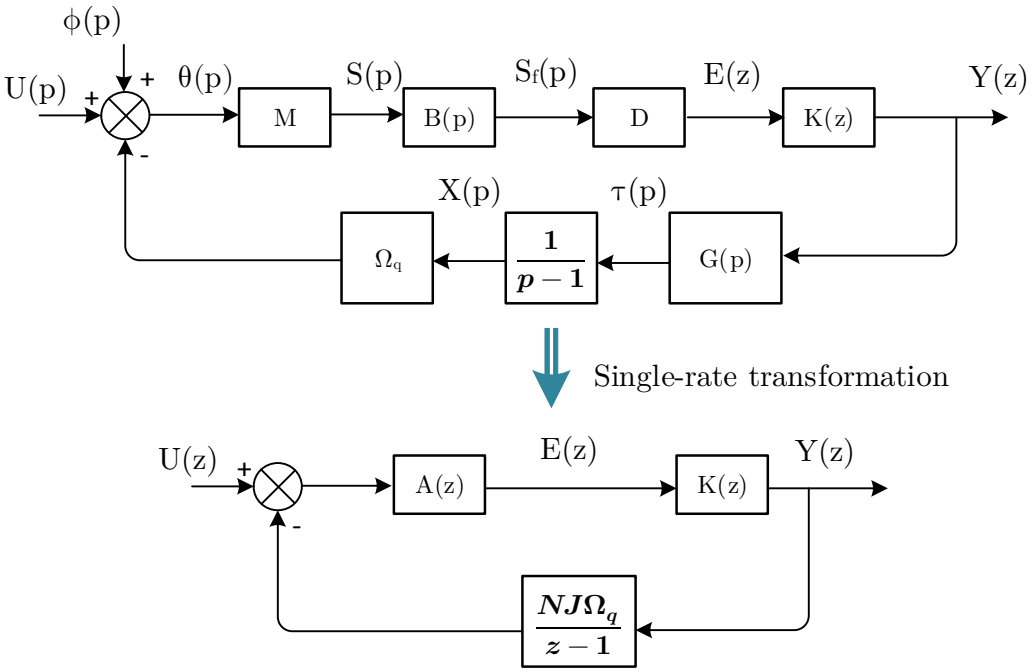

Figure 2.36. Block diagram of the multirate PLL

The time-varying block M and D are represented in the form of a complex mapping, because they cannot be represented in the form of a transfer function. Mapping M and D, it is obtained (2.45) and (2.46), respectively.

$$s(p) = \frac{S}{2} \cdot \left[\Theta\left(p \cdot e^{j\frac{2\pi}{N}}\right) + \Theta\left(p \cdot e^{-j\frac{2\pi}{N}}\right)\right] \tag{2.45}$$

$$E(z) = \frac{1}{N} \cdot \sum_{l=0}^{l=N-1} s_f\left(p \cdot e^{j\frac{2\pi \cdot l}{N}}\right) \tag{2.46}$$

The NCO generates N equal output samples, so the transfer function $G(p)$ is (2.47), where $J = Q/v_q^2$, being Q the slope of the NCO transfer characteristic.

$$G(p) = J \cdot \sum_{i=0}^{i=N-1} p^{-i} \tag{2.47}$$

Assuming $\phi(p) = 0$, the signal phase is given by the expression (2.48), having in mind $p^N = z$ and using $Y(z) = K(z) \cdot E(z)$.

$$\Theta(p) = U(p) - \frac{\Omega_q \cdot G(p)}{p-1} \cdot K(z) \cdot E(z) \tag{2.48}$$

By applying the previous expression, as well as the bandpass filter $B(p)$, (2.49) is obtained. Therefore, substituting $\Theta(p)$ and solving by $E(z)$, the single-rate expression (2.50) is obtained.

$$E(z) = \frac{S}{2N} \cdot \sum_{l=0}^{l=N-1} B\left(p \cdot e^{j \cdot \frac{2\pi \cdot l}{N}}\right) \cdot \left[\Theta\left(p \cdot e^{j \cdot \frac{2\pi}{N}(l+1)}\right) + \Theta\left(p \cdot e^{-j \cdot \frac{2\pi}{N} \cdot (l-1)}\right)\right] \tag{2.49}$$

$$E(z) = \frac{\mathcal{U}(z)}{1 + L(z)} \tag{2.50}$$

Where:

$$\mathcal{U}(z) = \frac{S}{2N} \cdot \sum_{l=0}^{l=N-1} B\left(p \cdot e^{j \cdot \frac{2\pi \cdot l}{N}}\right) \times \left[\mathrm{U}\left(p \cdot e^{j \cdot \frac{2\pi}{N}(l+1)}\right) + \mathrm{U}\left(p \cdot e^{-j \cdot \frac{2\pi}{N} \cdot (l-1)}\right)\right] \tag{2.51}$$

$$L(z) = K(z) \cdot \frac{S\Omega_q}{2N} \cdot \sum_{l=0}^{l=N-1} B\left(p \cdot e^{j \cdot \frac{2\pi \cdot l}{N}}\right) \times \left[\frac{\mathrm{G}\left(p \cdot e^{j \cdot \frac{2\pi}{N}(l+1)}\right)}{p \cdot e^{j \cdot \frac{2\pi}{N}(l+1)} - 1} + \frac{\mathrm{G}\left(p \cdot e^{-j \cdot \frac{2\pi}{N} \cdot (l-1)}\right)}{p \cdot e^{-j \cdot \frac{2\pi}{N} \cdot (l-1)} - 1}\right] \tag{2.52}$$

When the frequency perturbation has the form of a step function, it is possible to express $\mathcal{U}(z)$ as (2.53), where $A(z)$ is deduced from the previous and $U(z)$ has the form (2.54). The obtaining of $A(z)$ is an essential step that is not shown in this contribution, what makes difficult to get a better understanding of how the system is transformed to single-rate. Similarly, $L(z)$ can be expressed as is shown in (2.55).

$$\mathcal{U}(z) = A(z) \cdot U(z) \tag{2.53}$$

$$U(z) = \frac{z \cdot \omega_0 \cdot T_q}{(z-1)^2} \tag{2.54}$$

$$L(z) = K(z) \cdot A(z) \cdot \frac{N \cdot J \cdot \Omega_q}{z - 1} \tag{2.55}$$

The approach taken by the author is interesting, but a different path can be followed to obtain a better understanding of multirate analysis.

2.2.4.2. Multirate repetitive control

The multirate control is not a usual control implementation in DC/AC converters, but some contributions can be found in the literature, mainly in repetitive control area. It is well-known that repetitive control is a simple learning control method which was specially designed for this purpose. Distinguished by its high precision, simple implementation and little performance dependency on system parameters, repetitive control has been a major approach in cases where periodic exogeneous signal is dealt with. Repetitive control is based on the internal model principle, which states that a control system with a periodic signal generator of known period inside the closed loop can exactly track any reference signal with the same period.

In [58] a multirate repetitive controller is studied for DC/AC power converters because the periodic nature of the output voltage makes repetitive control (RC) an effective way to achieve low total harmonic distortion (THD). The multirate RC is depicted in Figure 2.37, where the plug-in repetitive controller $G_r(z^N)$ has an RC rate with a

sampling period of $T_s = N \cdot T$. The ratio between the feedback rate T and RC rate is N, and its relationship is:

$$z = e^{s \cdot T} \qquad z^N = e^{s \cdot T_s} \tag{2.56}$$

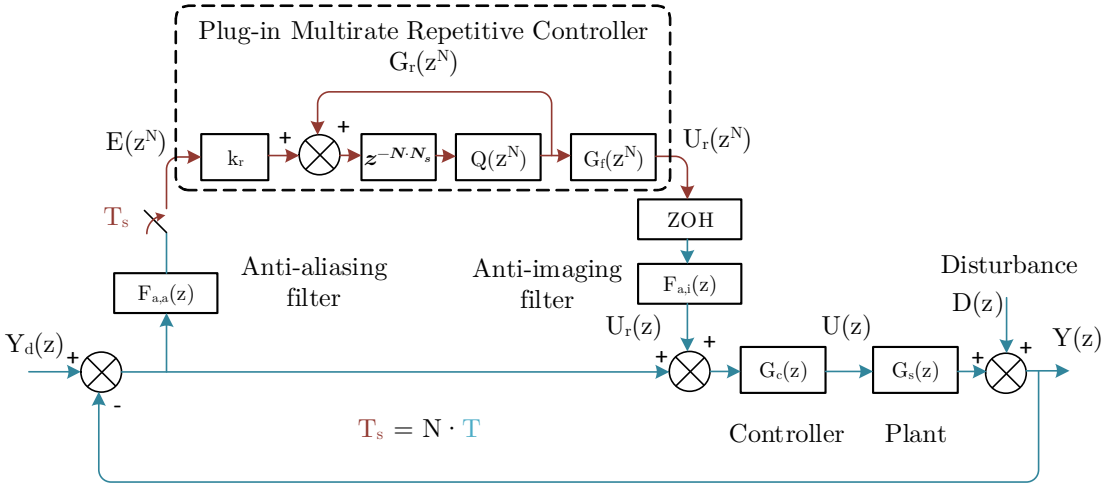

Figure 2.37. Multirate RC system

The RC block is formed by: anti-aliasing filter $F_{a,a}(z)$ and a downsampling process; RC gain k_r; $G_f(z^N)$ is designed to obtain a linear phase compensation or it is often designed as the inverse of the closed-loop feedback system; $Q(z^N)$ is a low-pass filter introduced to enhance robustness; ZOH for the interpolation and anti-imaging filter $F_{a,i}(z)$. The transfer function of the repetitive controller is (2.57).

$$G_r(z^N) = k_r \cdot \frac{z^{-N \cdot N_s} \cdot Q(z^N)}{1 - z^{-N \cdot N_s} \cdot Q(z^N)} \cdot G_f(z^N) \tag{2.57}$$

Where $N_s = (f_c/f)/N$ with f being the reference signal frequency and f_c being the sampling frequency. There is periodic signal generator of period N_s, so according to the internal model principle, this RC can achieve zero-error tracking of the periodic reference signal with that period.

To analyze and design the multirate RC, the closed-loop system is transformed to an equivalent system with a single sampling rate. In this contribution the internal representation (IR), that will be detailed later, is used to obtain such an equivalent. Hence, the open-loop system $G(z)$ without the plug-in RC (closed-loop with $G_c(z)$ and $G_s(z)$) in state-space form is (2.58), and its slow-rate state function is (2.59), where K is the slow-rate instant.

$$\begin{cases} x_f(k+1) = A_f \cdot x_f(k) + B_f \cdot u_f(k) \\ y_f(k) = C_f \cdot x_f(k) + \upsilon_f(k) \end{cases} \tag{2.58}$$

$$\begin{cases} x_s(K+1) = A_f^N \cdot x_s(K) + [A_f^{N-1} \cdot B_f + \cdots + A_f \cdot B_f + B_f] \cdot u_s(k) \\ y_s(K) = C_f \cdot x_s + \upsilon_s(K) \end{cases} \tag{2.59}$$

The equivalent RC transfer function is (2.60). The overall transfer function from $Y_d(z^N)$ to $Y(z^N)$ are derived as (2.61). Therefore, the stability of the system requires (2.62), so k_r and the lead step γ (it is introduced by $G_f(z^N)$) are designed.

$$\bar{G}(z^N) = C_s(z^N I - A_s)^{-1} \tag{2.60}$$

$$\frac{Y(z^N)}{Y_d(z^N)} = \frac{[1 - Q(z^N) \cdot z^{-N \cdot N_s} \cdot (1 - k_r \cdot G_f(z^N))] \cdot \bar{G}(z^N)}{1 - Q(z^N) \cdot z^{-N \cdot N_s} \cdot \left(1 - k_r \cdot G_f(z^N) \cdot \bar{G}(z^N)\right)} \tag{2.61}$$

$$\begin{gathered} \left| Q(z^N) \cdot z^{-N \cdot N_s} \cdot \left(1 - k_r \cdot G_f(z^N) \cdot \bar{G}(z^N)\right) \right| < 1 \\ z^N = e^{j\omega_N} \qquad \forall\ 0 < \omega_N < \frac{\pi}{T_s} \end{gathered} \tag{2.62}$$

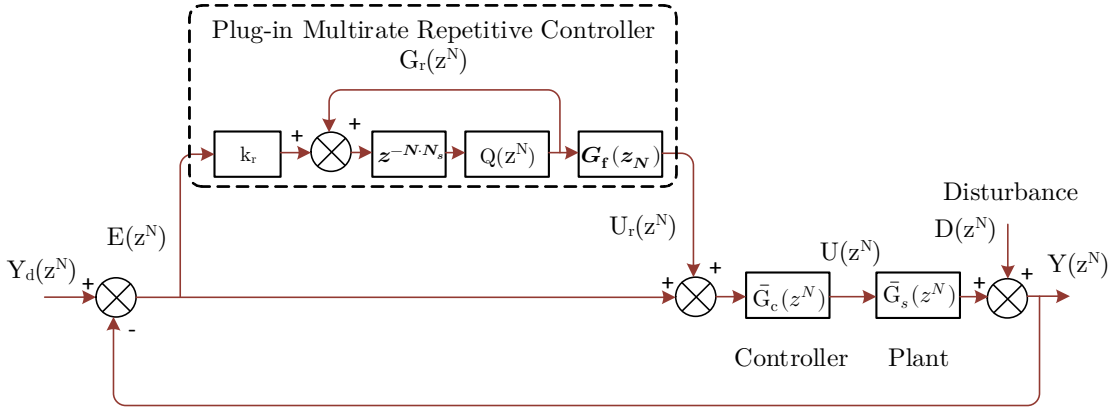

Figure 2.38. Equivalent single-rate RC

The anti-aliasing, anti-imaging, and low-pass filter Q are designed as a zero-phase window filter (2.63), but it has not practical implementation because it is a non-causal structure. This kind of filter is only used after all the data is known. However, in practice, q is usually small (such as $q = 1$ or $q = 2$).

$$\begin{gathered} F(z) = \sum_{i=1}^{q} a_i \cdot z^{-i} + a_0 + \sum_{i=1}^{q} a_i \cdot z^i \\ a_0 + 2 \cdot \sum_{i=1}^{q} a_i = 0 \end{gathered} \tag{2.63}$$

Now, the multirate system is defined, and a controller $G_c(z)$ is implemented after the system is modeled as $G_s(z)$. In [58], a state feedback controller is designed. In that case the author concludes that this scheme reduces the computation load and keeps the convergence speed and generates very low THD, but its limitation is that the peak tracking error might become large with nonlinear load. It shows that a higher N gets worst performances, so the RC rate multiplier, N, should be as close as possible to 1.

Recent contributions as [59] follow the lead about repetitive controllers, but, in this case, it is applied to a three-phase shunt active power filter (APF). The APF control scheme includes an inner PI control loop with a sampling rate identical to switching frequency and an external plug-in RC loop with a reduced sampling rate. They introduce the multirate fractional-order repetitive control (MRFORC), because it can provide high tracking accuracy for harmonic reference even in the presence of wide grid frequency variations.

2.3. Used multirate techniques

In this section, the most useful multirate tools are presented. Firstly, a general description of the Internal Representation (IR) modelling technique of multirate systems will be given, that is, the space-state approach, so a single-rate model is obtained to do the control design. Then, the External Representation (ER), that is, the transfer function approach, modelling technique of multirate systems is studied in detail, and a single-rate model is obtained to design the controller. These techniques will be applied in Chapter 4 for controller analysis and design in the power electronics field. Most information is taken from [14], which deeply details multirate systems.

2.3.1. Internal representation modelling

This section is meant to be a brief explanation about recurrence laws, based on Kranc methods to model non-conventional sampled systems, what is known as Internal Representation. The recurrence laws are successive substitutions in the space-state equations defined at base period T (greatest common divisor, GCD, of the input and output samplers of the system) with [G H; C D]. Therefore, a space-state system equivalent $\left[\bar{G}\ \overline{H};\ \bar{C}\ \bar{D}\right]$ is modeled in metaperiod T_0.

2.3.1.1. Definitions

The main approach is based on the Vectorial Switch Decomposition introduced by Kranc, that was previously depicted in Figure 2.5. This approach is based on the idea that inside a metaperiod T_0 there are N time intervals, and the non-conventional sampling sequence is expressed as the superposition of N sequences uniformly sampled inside a global metaperiod T_0.

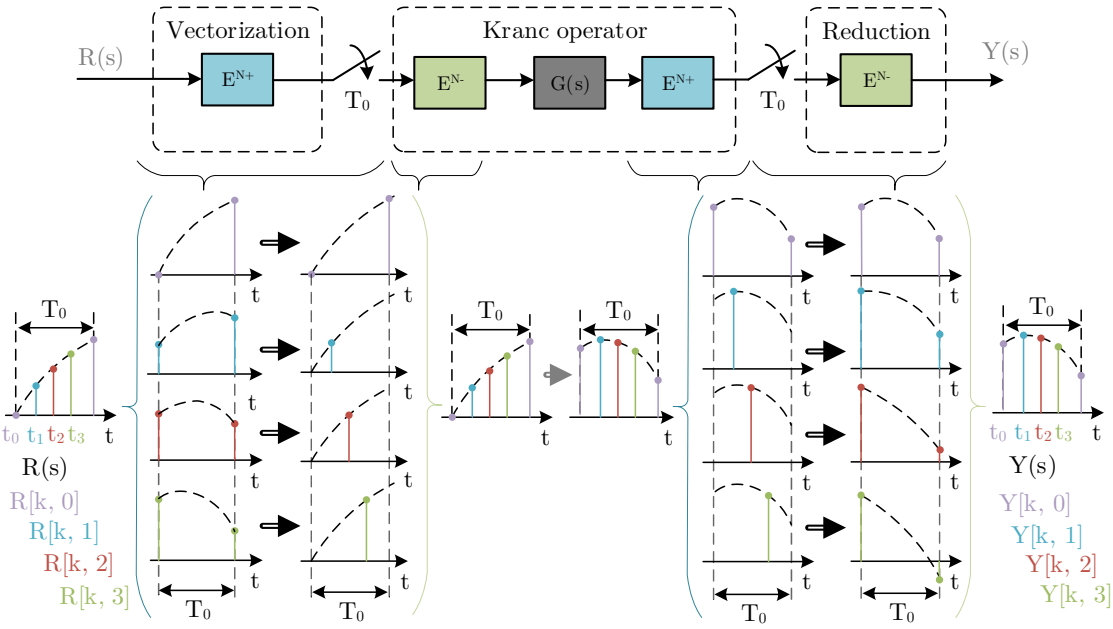

Figure 2.39. Compact representation of a multirate system

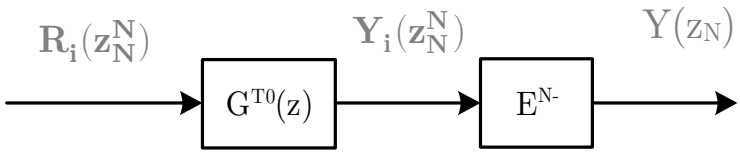

Figure 2.40. Single-rate equivalent system

The advancements and delays from the Vectorial Switch Decomposition can be arranged as vectors (2.64), and the multirate system is reorganized as it is depicted in Figure 2.39. The Kranc operator is defined as the embedded digital system defined in the metaperiod T_0, and it is composed of the delay block of the input sampler, the advancement block of the output sampler, and the state-space representation of the system (2.65). The Kranc operator obtains a single-rate equivalent system as it is depicted in Figure 2.40, where $z_N = e^{s \cdot T_0/N}$

$$E^{N+} = \begin{bmatrix} 1 \\ e^{s \cdot t_1} \\ e^{s \cdot t_2} \\ \vdots \\ e^{s \cdot t_{N-1}} \end{bmatrix} \qquad E^{N-} = [1 \quad e^{-st_1} \quad e^{-st_2} \quad ... \quad e^{-st_{N-1}}] \tag{2.64}$$

$$G^{T_0}(z) = (E^{N+} \cdot G(s) \cdot E^{N-})^{T_0} \tag{2.65}$$

The Kranc operator leads to different cases, that depends on the nature of the sampled system. There are two samplers, one at the input and other at the output, so different sampling instants can be found at each one. Therefore, considering T as the minimum time between sampling instants ($T = T_0/N$), the operators are classified as:

- **Regular Kranc**: Continuous-time nature of processes. The equivalent Z-transform of $G(s)$ at period T must be obtained in the space-state representation. Then, the recurrence laws get a space-state representation at period T_0.
- **ZOH Kranc**: Continuous-time nature of processes with ZOH at the input. The Z-transform of the overall system, $G_{h0}^T \cdot G(s)$, at period T must be obtained in the space-state representation, where G_{h0}^T is the transfer function of the ZOH at period T. Hence, there is a holding process at the input sampling. The successive substitution gets an equivalent space-state representation at period T_0.
- **Digital Kranc**: Discrete-time nature of processes. It is defined for a space-state representation of the discrete system at period T, $G^T(z)$, surrounded by samplers, and there are not ZOH discretization of a continuous-time system. Again, with successive substitutions, an equivalent space-state representation at period T_0 is found. Its main interest resides in controllers directly designed in discrete-time or those which, despite of being designed in continuous-time, are not discretized by a ZOH (these must use the ZOH-Kranc operator)

In the following, the recurrence laws allow the definition of any system depending on its nature and the sampling instants.

2.3.1.2. Recurrence Laws

The recurrence laws are deduced in [14] and the author analyzes the most general case: any number and any instant of input and output samplings. From them, an automatic Kranc-operator space-state representation, that internally represents the sampled system at metaperiod T_0, is obtained. Please note that the recurrence laws have one inherent restriction: the first sampling at the input and the output must be in the instant 0 of the metaperiod. Remember that the state-space representation of any system is:

$$\begin{aligned} x(k+1) &= G \cdot x(k) + H \cdot u(k) \\ y(k) &= C \cdot x(k) + D \cdot u(k) \end{aligned} \tag{2.66}$$

The final models are defined at metaperiod T_0, but they all internally work at period T, because they must rearrange correctly the sampling at the input and output. Kranc operators share the same parameters for their definition, graphically depicted in Figure 2.41, and those are:

- Space-state representation of the system at period T: $[G\ H;\ C\ D]$
- Number of samplings at the output of the system: n.
- Number of sampling at the input of the system: m.
- Number of T samplings in a metaperiod T_0: N.
- Vector with instant (T) differences between successive input samplings: *dif(·)*
- Vector with instants (T) with sampling at the output (instant j): *out(·)*
- Vector with instants (T) with sampling at the input (instant i): *in(·)*

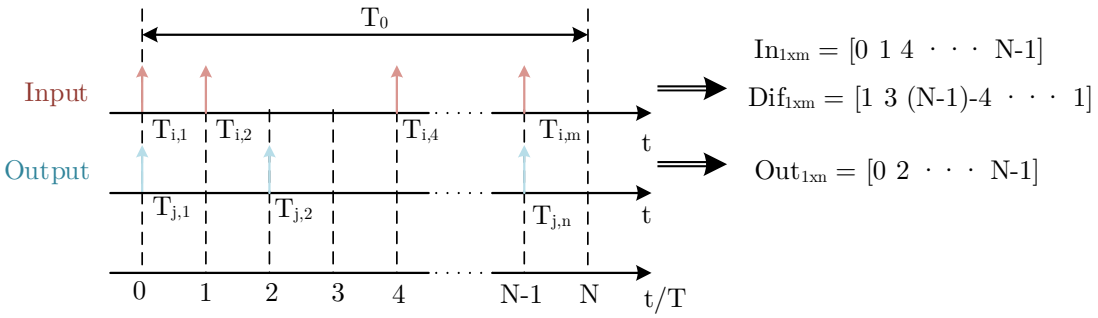

Figure 2.41. Graphical representation of the parameters for internal representation

1) Regular Kranc

The space-state system at metaperiod with non-conventional sampling is (2.67).

$$\begin{gathered} G^{T_0}(z) = \left|\begin{matrix} \bar{G} & \bar{H} \\ \bar{C} & \bar{D} \end{matrix}\right| \\ \bar{G} = G^N \\ \bar{H} = [G_{11}H \quad \cdots \quad G_{1m}H\ ] \qquad G_{1j} = G^{N-1-\sum_{x=1}^{j-1} dif(x)} \\ \bar{C} = \begin{bmatrix} C_1 \\ \vdots \\ C_n \end{bmatrix} \qquad C_i = CG^{out(i)} \\ \bar{D} = \begin{bmatrix} D_{11} & \cdots & D_{1m} \\ \vdots & \ddots & \vdots \\ D_{n1} & \cdots & D_{nm} \end{bmatrix} \qquad D_{ij} = C\Psi_{ij}H + \Omega_{ij} \end{gathered} \tag{2.67}$$

Considering the following coefficients of matrix D:

$$\Psi_{ij} = \begin{cases} G^{out(i)-1-\sum_{x=1}^{j-1} dif(x)} & ,out(i)-1-\sum_{x=1}^{j-1} dif(x) \geq 0 \\ 0 & ,out(i)-1-\sum_{x=1}^{j-1} dif(x) < 0 \end{cases}$$
$$\Omega_{ij} = \begin{cases} D\ , \left(out(i)-1-\sum_{x=1}^{j-1} dif(x) < 0\right) AND (i \geq j) AND\ NOT\big(out(i) < in(j)\big) \\ 0, \quad other\ cases \end{cases} \tag{2.68}$$

2) ZOH Kranc

The space-state system at metaperiod with non-conventional sampling is (2.69).

$$G^{T_0}(z) = \begin{vmatrix} \bar{G} & \overline{H} \\ \bar{C} & \overline{D} \end{vmatrix}$$
$$\bar{G} = G^N$$
$$\overline{H} = [G_{11}H \quad \cdots \quad G_{1m}H\ ] \qquad G_{1j} = \sum_{x=1}^{dif(j)} G^{N-x-\sum_{w=1}^{j-1} dif(w)}$$
$$\bar{C} = \begin{bmatrix} C_1 \\ \vdots \\ C_n \end{bmatrix} \qquad C_i = CG^{out(i)} \tag{2.69}$$
$$\overline{D} = \begin{bmatrix} D_{11} & \cdots & D_{1m} \\ \vdots & \ddots & \vdots \\ D_{n1} & \cdots & D_{nm} \end{bmatrix} \qquad D_{ij} = C\Psi_{ij}H + \Omega_{ij}$$

Considering the following coefficients of D matrix:

$$\Psi_{ij} = \begin{cases} \sum_{x=1}^{dif(j)} G^{out(i)-x-\sum_{w=1}^{j-1} dif(w)} & ,out(i)-x-\sum_{w=1}^{j-1} dif(w) \geq 0 \\ 0 & ,out(i)-x-\sum_{w=1}^{j-1} dif(w) < 0 \end{cases}$$
$$\Omega_{ij} = \begin{cases} D\ , \left(out(i)-dif(j)-\sum_{w=1}^{j-1} dif(w) < 0\right)\ AND \\ \Big(\big((i \geq j) AND\ NOT\big(out(i) < in(j)\big)\big)\ OR\ \big((i < j) AND (i+j=N)\big)\Big) \\ 0, \quad other\ cases \end{cases} \tag{2.70}$$

3) Digital Kranc

It is like the Regular Kranc operator, but its difference is on the nature of that system. In both techniques, the operator is applied to space-state representation at period T.

Therefore, the space-state system at metaperiod with non-conventional sampling is (2.71).

$$
\begin{gathered}
G^{T_0}(z) = \begin{vmatrix} \bar{G} & \bar{H} \\ \bar{C} & \overline{D} \end{vmatrix} \\
\bar{G} = G^N \\
\bar{H} = [G_{11}H \quad \cdots \quad G_{1m}H\ ] \qquad G_{1j} = G^{N-1-\sum_{x=1}^{j-1} dif(x)} \\
\bar{C} = \begin{bmatrix} C_1 \\ \vdots \\ C_n \end{bmatrix} \qquad C_i = CG^{out(i)} \\
\overline{D} = \begin{bmatrix} D_{11} & \cdots & D_{1m} \\ \vdots & \ddots & \vdots \\ D_{n1} & \cdots & D_{nm} \end{bmatrix} \qquad D_{ij} = C\Psi_{ij}H + \Omega_{ij}
\end{gathered}
\tag{2.71}
$$

Considering the following coefficients of D matrix:

$$
\Psi_{ij} = \begin{cases} G^{out(i)-1-\sum_{x=1}^{j-1} dif(x)} & , out(i) - 1 - \sum_{x=1}^{j-1} dif(x) \geq 0 \\ 0 & , out(i) - 1 - \sum_{x=1}^{j-1} dif(x) < 0 \end{cases}
\tag{2.72}
$$

$$
\Omega_{ij} = \begin{cases} D\ , \left(out(i) - 1 - \sum_{x=1}^{j-1} dif(x) < 0 \right) AND (i \geq j) AND\ NOT\big(out(i) < in(j)\big) \\ 0, \quad other\ cases \end{cases}
$$

2.3.2. External representation modelling

This section is meant to be a brief explanation about a different approach based on the same theorical concept, that is, the Vectorial Switch Decomposition. This approach is known as External Representation because a single-rate transfer function is obtained to model multirate systems. The obtained values are exactly those obtained in the IR when the input samplings are regularly distributed in the metaperiod T_0. If the samplings are irregularly distributed, the values do not correspond to those in the IR because it is expressed with a regular discrete variable. The irregularly distributed samplings are not in the scope of this document, but in [14] some adjustments are done in the discretization period and the gain to correctly model these systems.

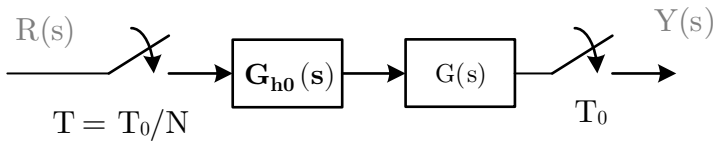

Figure 2.42. Analyzed regular case for external representation modelling

2.3.2.1. Definitions

The ER uses the previous notation where appears the discrete variable $z_N = e^{s \cdot T_0/N}$. This variable considers that there are N samplings inside the metaperiod T_0. Therefore, the expression z_N^{-i} is interpreted as a delay of i consecutive samplings. The distribution in time inside the metaperiod can be equidistant in time or not, that is, uniformly (regular) distributed or not (irregular).

Following Figure 2.39, $G(s)$ is preceded by ZOH operation at period T, and, from the point of view of ER, considering the contribution to the output of every input sequence, the p output sequence is (2.73).

$$Y_p(z_N^N) = \sum_{i=0}^{N-1} R_i(z_N^N) \cdot G_{p-1}(z_N^N) \tag{2.73}$$

Where:

- Z-transform of the input sequence at T_0 advanced $\boldsymbol{t_i}$ time instants: $R_i(z_N^N)$
- Z-transform of the impulse response at T_0 delayed $\boldsymbol{t_{i-p}}$ time instants: $G_{p-1}(z_N^N)$

The overall output sequence is (2.74), where each $Y_p(z_N^N)$ is multiplied by z_N^{-p} to correctly distribute it in the global sequence.

$$Y(z_N) = \sum_{p=0}^{N-1} z_N^{-p} \cdot Y_p(z_N^N) \tag{2.74}$$

However, the usual way to obtain the ER is through a polynomic expression that lead to close transfer function expression. Being $G(z_N) = B(z_N)/A(z_N)$, it must be found a polynomial $W(z_N)$ which is multiplied to $A(z_N)$ to obtain a denominator with only terms as $z_N^0, z_N^{-N}, z_N^{-2N}, etc.$ Therefore, if the numerator is divided by the denominator, the modified numerator coefficients are those in $z_N^0, z_N^{-N}, z_N^{-2N}, etc.$ So:

$$G(z_N) = \frac{B(z_N)}{A(z_N)} = \frac{B(z_N) \cdot W(z_N)}{A(z_N) \cdot W(z_N)} = \frac{B(z_N) \cdot W(z_N)}{A'(z_N)} \tag{2.75}$$

Where:

$$W(z_N) = \prod_{k=1}^{N-1} A\left(z_N \cdot e^{-j\frac{2\pi \cdot k}{N}}\right) = \frac{A'(z_N^N)}{A(z_N)} \tag{2.76}$$

The polynomial $W(z_N)$ relates the poles when the transfer function is defined at metaperiod T_0 (it is represented with the variable z_N^N) with the poles when it is defined at period T (it is represented with the variable z_N).

Please note that, after operating with (2.75), only the advanced functions, $G_i(z_N^N)$, are interesting because the delayed functions, $G_{-i}(z_N^N)$, can be easily obtained through the relation $G_{-i}(z_N^N) = z_N^{-N} \cdot G_{N-i}(z_N^N)$. Besides, the expression (2.75) is defined in two frequencies or rates (z_N^N, z_N). Therefore, some authors have defined it as dual-rate operator $\tilde{G}(z, N)$. Thus, the following is deduced from it:

- The denominator coefficients correspond to those of the transfer function expressed at metaperiod T_0 (slow rate).

- If the numerator coefficients (at fast rate) are summarized in groups of N coefficients (being N the multiplicity of the sampling), the n coefficients (being n the order of that polynomial) correspond to the same transfer function at T_0 (slow rate).

2.3.2.2. Polynomial $W(z_N)$ and operator z_N^{-i}

The most interesting tool to design the controllers for non-conventional sampling systems is the polynomial $W(z_N)$. For a given discretized system at period T (fast rate), a transfer function, $G(z_N)$, is obtained where the denominator is at slow rate and the numerator at fast rate. This is shown with a simple example where $N = 2$, so there is a sampling at half of each metaperiod:

$$G(z_2) = \frac{1 - z_2^{-1}}{1 - a \cdot z_2^{-1}} \tag{2.77}$$

Using (2.75):

$$\begin{gathered} G(z_2) = \frac{B(z_2) \cdot W(z_2)}{A(z_2) \cdot W(z_2)} = \frac{(1 - z_2^{-1}) \cdot (1 - a \cdot z_2^{-1} \cdot e^{j\pi})}{(1 - a \cdot z_2^{-1}) \cdot (1 - a \cdot z_2^{-1} \cdot e^{j\pi})} \\ G(z_2) = \frac{1 + (a-1) \cdot z_2^{-1} - a \cdot z_2^{-2}}{(1 - a^2 \cdot z_2^{-2})} \end{gathered} \tag{2.78}$$

It is verified the dual-rate nature of this transfer function, without forgetting that it is defined at fast rate. Besides, the variable z_2^{-1} from the numerator determines the middle sampling inside the metaperiod, and it helps to express the desired pattern (regular or irregular). In that example, the regular pattern is shown.

To relate the variable z_2^{-1} with a change in the desired pattern, some mathematical deducing is needed in the frequency domain. Considering a sinusoidal input $r(t) = e^{j\omega t}$ and considering (2.73):

$$\begin{gathered} Y_p(z_N^N) = \sum_{i=0}^{N-1} R_i(z_N^N) \cdot G_{p-i}(z_N^N) = \frac{1}{1 - e^{j\omega \cdot T_0} \cdot z_N^{-N}} \cdot \sum_{i=0}^{N-1} e^{j\omega \cdot t_i} \cdot G_{p-i}(z_N^N) \\ R_i(z_N^N) = \frac{e^{j\omega \cdot t_i}}{1 - e^{j\omega T_0} \cdot z_N^{-N}} \end{gathered} \tag{2.79}$$

Now, doing the Laplace transform and considering the delay e^{-st_p} to properly locate each periodic sequence of the output in time like in (2.74):

$$Y_p(s) = \frac{1}{T_0} \left[\sum_{i=0}^{N-1} e^{j\omega \cdot t_i} \cdot G_{p-i}(e^{j\omega \cdot T_0}) \cdot e^{-s \cdot t_p} \right] \cdot \sum_{k=-\infty}^{\infty} \frac{1}{s - j \cdot (\omega + k\omega_0)} \tag{2.80}$$

Where $\omega_0 = 2\pi / T_0$. Summarizing the other p-1 periodic sequences of the output to obtain the overall output sequence:

$$Y(s) = \frac{1}{T_0} \cdot \left[\sum_{p=0}^{N-1} \sum_{i=0}^{N-1} e^{j\omega \cdot t_i} \cdot G_{p-i}(e^{j\omega \cdot T_0}) \cdot e^{-s \cdot t_p} \right] \cdot \sum_{k=-\infty}^{\infty} \frac{1}{s - j \cdot (\omega + k\omega_0)} \tag{2.81}$$

Then, doing $k = 0$ to remove the repeated periodic copies that come from the sampling of the input signal, the expression of the system is:

$$G(j\omega) = \frac{1}{T_0} \cdot \sum_{p=0}^{N-1} \sum_{i=0}^{N-1} G_{p-i}(e^{j\omega \cdot T_0}) \cdot e^{-j\omega \cdot (t_p - t_i)} \tag{2.82}$$

If expressions $G_{p-i}(e^{j\omega \cdot T_0})$ of negative subscript are eliminated [60]:

$$G(j\omega) = \frac{1}{T_0} \cdot \sum_{i=0}^{N-1} G_i(e^{j\omega \cdot T_0}) \cdot \sum_{k=1}^{N} \exp\left(-j\omega \cdot \sum_{l=k}^{i-1+k} \tau_l\right) \tag{2.83}$$

Where τ_l is the time between samplings, and if $l > N$, $\tau_l = \tau_{l-N}$. The first terms of (2.83) are:

$$\begin{aligned} &\frac{N}{T_0} \cdot [G_0(e^{j\omega \cdot T_0}) + G_1(e^{j\omega \cdot T_0}) \cdot \left(\frac{e^{-j\omega \cdot \tau_1} + e^{-j\omega \cdot \tau_2} + \cdots + e^{-j\omega \cdot \tau_N}}{N}\right) + \\ &\quad + G_2(e^{j\omega \cdot T_0}) \cdot \left(\frac{e^{-j\omega \cdot (\tau_1 + \tau_2)} + e^{-j\omega \cdot (\tau_2 + \tau_3)} + \cdots + e^{-j\omega \cdot (\tau_N + \tau_1)}}{N}\right) \end{aligned} \tag{2.84}$$

Recalling the definition of each $G_{-i}(z_N^N)$, the overall expression of such system, $G(z_N)$, can also be written as (2.85). This is because of the Z-transform at metaperiod T_0 of the advanced expression $G_i(z_N^N) = \mathcal{Z}^{T_0}[e^{s \cdot t_i} \cdot G_{h0}^T \cdot G(s)]$, that must be correctly located in time with the delay z_N^{-i}.

$$G(z_N) = G_0(z_N^N) + G_1(z_N^N) \cdot z_N^{-1} + G_2(z_N^N) \cdot z_N^{-2} + \cdots + G_{N-1}(z_N^N) \cdot z_N^{-(N-1)} \tag{2.85}$$

Finally, comparing (2.84) and (2.85), it is shown that the transfer function can be obtained through $G(z_N)$ with the numerator and denominator modified by $W(z_N)$. The steps are the following:

1) Replace each z_N^{-N} by $e^{-j\omega \cdot T_0}$.
2) Replace each z_N^{-1} by $(e^{-j\omega \cdot \tau_1} + e^{-j\omega \cdot \tau_2} + \cdots + e^{-j\omega \cdot \tau_N})/N$. This is kind of a mean value of all possible values that the operator z_N^{-1} can take.
3) Replace each z_N^{-2} by $(e^{-j\omega \cdot (\tau_1 + \tau_2)} + e^{-j\omega \cdot (\tau_2 + \tau_3)} + \cdots + e^{-j\omega \cdot (\tau_N + \tau_1)})/N$.
4) Repeat the replacing procedure until $z_N^{-(N-1)}$.
5) Multiply by a global factor N/T_0

If the previous deduction is applied to the example in (2.78) the frequency-domain expression of the transfer function $G(z_2)$ is (2.86).

$$G(j\omega) = \frac{2}{T_0} \cdot \left[\frac{1 + \left(\frac{e^{-j\omega \cdot \tau_1} + e^{-j\omega \cdot \tau_2}}{2}\right) \cdot (a-1) - a \cdot e^{-j\omega \cdot T_0}}{(1 - a^2 \cdot e^{-j\omega \cdot T_0})}\right] \tag{2.86}$$

The considered sampling scheme depends on the values of τ_1 and τ_2. If $\tau_1 = \tau_2$, it is a regular scheme, whereas $\tau_1 \neq \tau_2$, it is an irregular one. Therefore, the gain of $G(j\omega)$ changes for a given ω and T_0, if the τ_1 and τ_2 values vary.

2.3.2.3. Pole and zero map at fast rate

On one hand, it is proven from the previous sections that the poles are set in the same locations, whatever the sampling scheme is. On the other hand, the zeros change its position depending on the sampling scheme.

The incorporation of $W(z_N)$ do that the poles are those from the transfer function at fast rate (defined as a_i) plus the ones from $W(z_N)$ that are in $a_i \cdot e^{j2\pi \cdot k/N}$, being $k = 1, 2, \ldots, N-1$.

The zeros are obtained with the previous analysis, but it is done in s-domain:

1) Replace each z_N^{-N} by $e^{-s \cdot T_0}$.
2) Replace each z_N^{-i} by $\sum_{k=1}^{N} \exp\left(-s \cdot \sum_{l=k}^{i-1+k} \tau_l\right) / N$

Then, the numerator is equalized to 0, but there are some implications that must be considered because it is in complex domain. To solve the equation, it is usually valid the Maximum Modulus Principle. If the numerator polynomial is called $g(s)$, and it is taken the function $f(s) = abs(g(s))$, where $abs(\cdot)$ is the absolute function, the function $f(s)$ allows the obtention of the values of s where $g(s)$ is null. Please note that $f(s)$ is defined as $f: C \rightarrow \Re^+ \cup \{0\}$, so the zeros of this function are relative minimum. Besides, it is demonstrated that all relative extrema of $f(s)$ are zeros of that function. Therefore, a minimum of $f(s)$ matches a zero of $g(s)$.

Following the example (2.86), the zeros are obtained equalizing the s-domain numerator to 0:

$$1 + \left(\frac{e^{-s\tau_1} + e^{-s \cdot \tau_2}}{2}\right) \cdot (a-1) - a \cdot e^{-s \cdot T_0} = 0 \tag{2.87}$$

For the regular case, $\tau_1 = \tau_2 = T_0/2$, and the following equation is obtained:

$$1 + \left(\frac{e^{-s \cdot T_0/2} + e^{-s \cdot T_0/2}}{2}\right) \cdot (a-1) - a \cdot e^{-s \cdot T_0} = 1 + e^{-s \cdot \frac{T_0}{2}} \cdot (a-1) - a \cdot e^{-s \cdot T_0} = 0 \tag{2.88}$$

The solutions are the zeros from the original transfer function $G(z_N)$ and the zero introduced by $W(z_N)$, which in regular sampling is canceled with the pole of $W(z_N)$. Therefore, the closest way to express a multirate regular sampling system in ER is through the expression at fast rate $G(z_N)$, but these deductions are useful for the irregular scheme in ER and better understanding of Chapter 4.

For example, if it is taken an irregular case where $\tau_1 = T_0/3$ and $\tau_1 = 2 \cdot T_0/3$, the zero from $W(z_N)$ changes its position, and it is not cancelled by the pole of $W(z_N)$. The equation that must be solved is:

$$1 + \left(\frac{e^{-s \cdot T_0/3} + e^{-s \cdot 2 \cdot T_0/3}}{2}\right) \cdot (a-1) - a \cdot e^{-s \cdot T_0} = 0 \tag{2.89}$$

This results in a zero that lead to an approximation of a transfer function at fast rate z_N of the irregular case. Hence, some corrections must be done due to this approximation in the discretization period and gain. In [14] the adjustments of the discretization period and static gain are shown.

2.4. Conclusions

This chapter has summarized many concepts that will be useful in the following ones. Basically, it has been divided into: state of the art, and multirate modelling techniques and notations.

The state of the art defines every notion that will be useful in the following chapters, where multirate examples in power electronics are analyzed. Then, because of the particularities of the actuation block, a brief explanation of the modulation techniques, that are in the scope of this document, is given. Principally, the DSPWM is one of the most interesting strategies in power electronics due to its simplicity of implementation, so the limitations and characteristics of this actuator are analyzed. Besides, a new approach was taken to reduce the actuation delay known as multisampling that has some particularities related to the filters, which has not been correctly studied in the literature. A correct modelling of this actuator is also important to maximize the response of the system.

This chapter briefly introduces the SHE modulation technique because it could be used with multirate methods, which involve extrapolation to get better responses. Besides, in the following chapter, a polynomial extrapolation technique is presented to compare its extrapolation of sinusoidal signals to the one obtained by multirate techniques and reference frame transformation technique.

The actuation block has been profoundly analyzed, so a few multirate possibilities will be introduced in this work making sure that the DSPWM modulation technique does not negatively affect. Therefore, focusing on DSPWM, there are two possibilities:

- Follow the modulation update strategy presented here. That could be done: by adapting switching frequency to a possible constrained sampling frequency; or by optimizing the maximum switching frequency with multirate approaches.
- Follow a multirate approach to update the modulation function more than two times per carrier period (similar to multisampling technique).

Finally, two examples of multirate application in power electronics are presented, each of them with a different approach in the approximation of their multirate system to a single-rate model. The first one is related to external representation, although it does not use exactly that notation. The second is related to internal representation, as it was mentioned. Therefore, a first contact of multirate techniques in power electronics was found.

Later, two modelling techniques are presented. The internal representation models a multirate system with any case of sampling at the input and output, whereas the external representation models multirate system where the fast rate only is at the input. On one hand, the IR has the problem that deals with inputs that are in the future to model a multirate system at the defined metaperiod, or slow rate. On the other hand, the ER deals with transfer functions defined at fast rate. However, the last one allows the design of controllers known as MRIC, using the notation presented before.

Chapter 3. Modelling and multirate applications

3.1. Introduction

In this chapter is analyzed the power converter model and how the multirate techniques can be applied to them based on the possibilities that can be found in practical applications.

First, the studied system, which is an AC/DC converter, is correctly model in the stationary and rotatory reference frames. Then a set of possible applications are presented where the multirate design can be applied, most of them related to the actuation, and it is essentially focused on extrapolation. The decimation of the actuation is an unusual situation, so it is not analyzed here, but there is a possibility when the switching frequency is very low due to the characteristics of the application.

This chapter gives context to Chapter 4, which have the aim of explaining multirate controllers for current control loop on extrapolation cases.

3.2. Voltage Source Converter modelling

3.2.1. Definitions of the current dynamics model

The studied power converter is the VSC, which is a three-phase AC/DC converter previously detailed in subsection 1.2.2as a 3L-DNPC-VSC. However, it can be described as a switching network where input and output (in bidirectional converters they are only defined by the energy flow direction) have a filter to correctly connect with a load or the electrical grid. The switching network must be controlled, so the mathematical model of the system is needed to obtain the model-based controller.

In the literature, different techniques can be found to correctly model AC/DC converters. Firstly, a switched model can be obtained, where the inputs are the control signals (defined by their duty-cycle), but it is a non-linear model. Then, the previously obtained switching functions are averaged along a switching period, T_{SW}, so a linear relationship is obtained between the duty-cycle and DC-bus voltage with the output sinusoidal signals. This model is defined in a stationary reference frame. Finally, if the

reference axes rotate with an angular speed equivalent to the fundamental frequency of the grid ($2\pi \cdot 50$ rad/s), the signals can be transformed to a synchronous reference frame, and they get a constant value. In three-phase systems, transformations are carried out to simplify the controller design and implementation. This is explained in Appendix B, but it will be briefly introduced in the following modelling. The previous averaged model is simplified, so converter and PWM modulator are approximated to the PWM gain (commonly unitary) and delay (one-half sampling period, $T/2$) as it was previously detailed in subsection 2.2.3 with the SPWM technique. Therefore, the converter topology does not impact on the system modelling and the subsequent analysis can be applied to 2L-VSC or multi-level topologies. The system is reduced to the modelling of grid filter as it will be shown in following subsections.

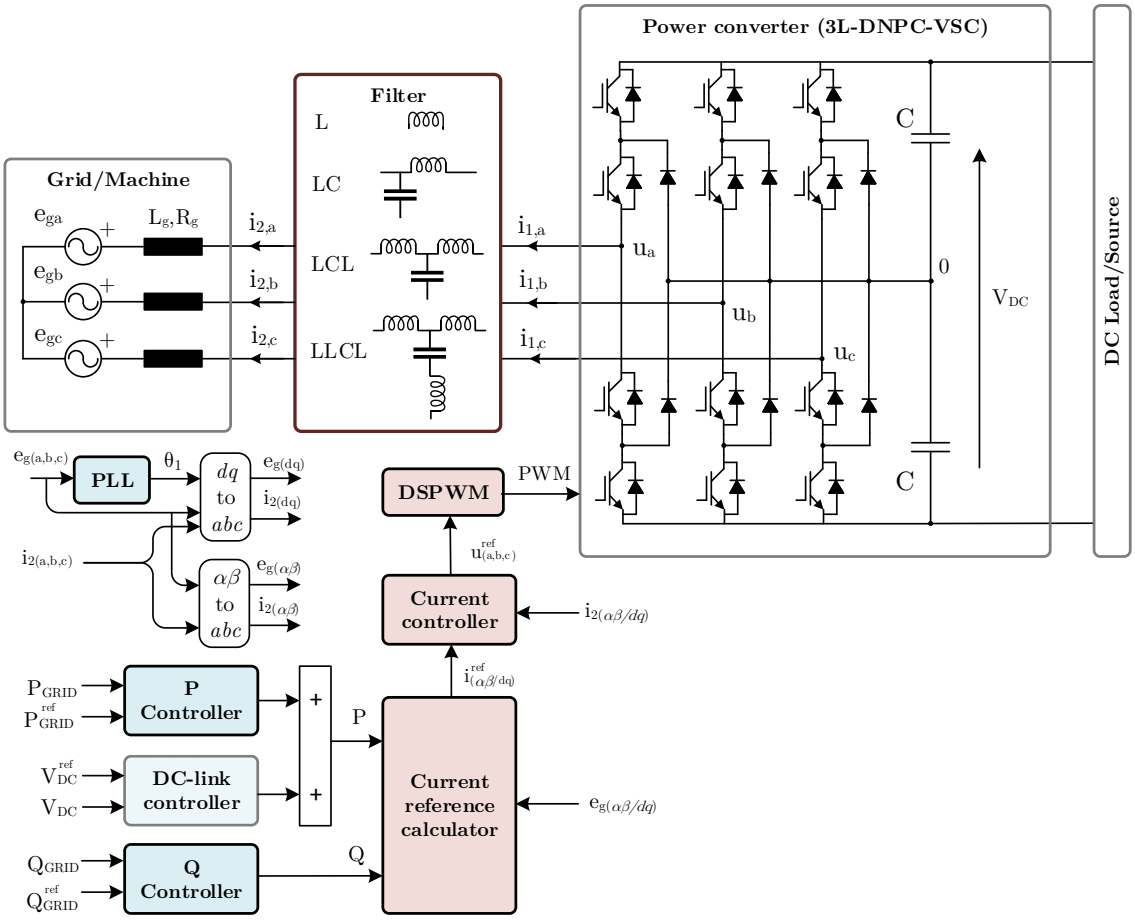

Figure 3.1. Schematic block diagram of the system under study

The system under study is depicted in Figure 3.1. The 3L-DNPC-VSC is connected to a three-phase three-wire symmetrical voltage system. The symmetrical voltage system is a three-phase inductive-resistive impedance with a voltage source. A constant and/or variable frequency converter operation can feed the inductive-resistive load. For motor-tied applications (commonly variable frequency operation), the power converter operates as a motor drive inverter and for grid-tied applications (usually constant frequency operation) the power converter operates as power (active and/or reactive) exchanger with the grid.

In motor-tied applications, the inductance represents motor stator leakage inductance and the resistance characterizes motor stator winding resistance. The three-phase voltage source is interpreted as the motor counter-electromotive force (back EMF), which depends on the motor type and operating point. In grid-tied applications, the inductive-resistive impedance model is related to the line-side harmonic-filter. For a L-filter, the inductance represents filter inductance and the resistance represents associated winding resistance. For a LCL-filter, the inductive-resistive model represents the low frequency model (equivalent L-filter) of the filter. The three-phase voltage-source specifies the power network supply grid voltage. Therefore, the following subsections are focused on the modelling of these popular filters. The transfer function, that will be found, relates the converter output voltage with the current towards the grid, because there is an inner current control loop in every VSC.

Special mention for LLCL-filter, that has recently emerged into grid-tied converters due to the improved filtering capability which ensuring a smaller physical size [61]. A small inductor is inserted in the branch loop of the capacitor for this filter, composing a LC series resonant circuit. The LLCL-filter has almost the same frequency-response characteristic as LCL-filter within half of the switching frequency range, so it can also be approximated to a L-filter, as it will be shown in the following.

3.2.2. L-filter model

Considering the schematic from Figure 3.2, the differential equations in time-domain that describe the circuit behavior are (3.1). The grid inductance determines whether the grid is weak (large value of L_g) or stiff (low value of L_g). Usually, the grid is stiff enough to neglect the grid impedance for modelling purposes. For machines, the inductance is always considered, so the inductive-resistive effects are modeled together in the differential equations.

$$\begin{aligned} u_a(t) &= R \cdot i_a(t) + L \cdot \frac{di_a(t)}{dt} + e_{g,a}(t) \\ u_b(t) &= R \cdot i_b(t) + L \cdot \frac{di_b(t)}{dt} + e_{g,b}(t) \\ u_c(t) &= R \cdot i_c(t) + L \cdot \frac{di_c(t)}{dt} + e_{g,c}(t) \end{aligned} \tag{3.1}$$

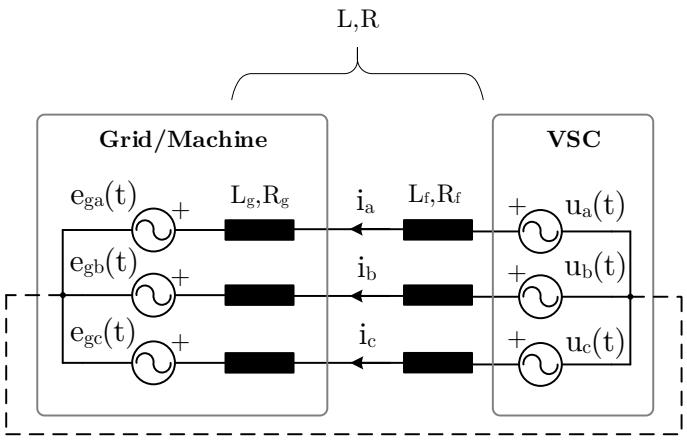

Figure 3.2. Schematic circuit of an L-filter

3.2.2.1. Stationary reference frame

If the variables are considered as vectors, and developing the transformation to the stationary $\alpha\beta$ reference frame, the expression (3.2) is obtained. The transformation matrix $[T_{abc\rightarrow\alpha\beta}]$ is detailed in Appendix B.

$$\vec{u}_{\alpha\beta}(t) = T_{abc\rightarrow\alpha\beta} \cdot \vec{u}_{abc}(t) = R \cdot \vec{i}_{\alpha\beta}(t) + L \cdot \frac{d\vec{i}_{\alpha\beta}(t)}{dt} + \vec{e}_{g,\alpha\beta}(t) \tag{3.2}$$

Where the $\alpha\beta$ representation is defined in the complex domain for each variable as $\vec{x}_{\alpha\beta}(t) = x_\alpha(t) + jx_\beta(t)$. The resultant complex-valued transfer function from the converter output voltage to the converter output current is (3.3). The transfer function describes a first-order time-delay element characteristics.

$$\vec{G}_{\alpha\beta}^{L-filter}(s)_{|\vec{e}_{g,\alpha\beta}(s)=0} = \frac{\vec{I}_{\alpha\beta}(s)}{\vec{U}_{\alpha\beta}(s)} = \frac{1}{L \cdot s + R} \tag{3.3}$$

3.2.2.2. Rotating reference frame

By applying the Park transformation (3.4) to (3.2), that is, to transform each complex-valued vector $\vec{x}_{\alpha\beta}$ from the stationary $\alpha\beta$ reference frame into the rotating dq reference frame, the linear differential equation (3.5) is obtained.

$$\vec{x}_{dq}(t) = \vec{x}_{\alpha\beta}(t) \cdot e^{-j\omega_k \cdot t} \tag{3.4}$$

$$\vec{u}_{dq}(t) = \vec{u}_{abc}(t) \cdot e^{-j\omega_k \cdot t} = R \cdot \vec{i}_{dq}(t) + L \cdot \frac{d\vec{i}_{dq}(t)}{dt} + \underbrace{j\omega_k \cdot L \cdot \vec{i}_{dq}(t)}_{cross-coupling} + \vec{e}_{g,dq}(t) \tag{3.5}$$

Where the dq representation is defined in the complex domain for each variable as $\vec{x}_{dq}(t) = x_d(t) + jx_q(t)$. The angular frequency of the rotating reference ω_k is time variant for variable frequency applications (machines) and time-invariant for constant frequency applications (grid at 50 Hz). A cross-coupling effect appears in the linear differential equation, which results in a complex-valued transfer function (3.6) with a new summand at the denominator.

$$\vec{G}_{dq}^{L-filter}(s)_{\vec{e}_{g,dq}(s)=0} = \frac{\vec{I}_{dq}(s)}{\vec{U}_{dq}(s)} = \frac{1}{L \cdot s + R + j\omega_k \cdot L} \tag{3.6}$$

The cross-coupling effects are usually canceled by the corresponding feedforward expression in each axis, so the transfer function is no longer complex-valued. Then, the transfer function for each axis is like the one presented in (3.3) for the stationary $\alpha\beta$ reference frame. However, for complex-valued controller designs, the cross-coupling effects must be considered, and one way to quantify it is by means of the quotient of the imaginary-part divided by the real-part of $\vec{G}_{dq}^{L-filter}$:

$$F_{dq}^{L-filter}(j\omega) = \frac{Im\{\vec{G}_{dq}^{L-filter}(j\omega)\}}{Re\{\vec{G}_{dq}^{L-filter}(j\omega)\}} = -\frac{\omega_k \cdot L}{R + j\omega \cdot L} \tag{3.7}$$

This cross-coupling function is a low-pass filter with the corner frequency $\omega_c = R/L$. Hence, the cross-coupling effects become significantly high for systems with large output angular frequencies ω_k and low resistance and/or high inductance.

Finally, the system in rotating dq reference frame can also be modeled in the continuous-domain space-state as (3.8). This will be useful because the IR multirate modelling needs this representation.

$$\begin{cases} \dot{\vec{x}}(t) = A \cdot \vec{x}(t) + B \cdot \vec{m}(t) \\ \vec{y}(t) = C \cdot \vec{x}(t) + D \cdot \vec{m}(t) \end{cases} \tag{3.8}$$

Where:

$$\begin{aligned} \vec{x}(t) = \vec{y}(t) = [i_d(t) \quad i_q(t)]^T \\ \vec{m}(t) = [u_d(t) \quad u_q(t) \quad e_{g,d}(t) \quad e_{g,q}(t)]^T \end{aligned} \tag{3.9}$$

$$\begin{aligned} A = \begin{bmatrix} -R/L & \omega_k \\ -\omega_k & -R/L \end{bmatrix} \quad B = \begin{bmatrix} 1/L & 0 & -1/L & 0 \\ 0 & 1/L & 0 & -1/L \end{bmatrix} \\ C = \begin{bmatrix} 1 & 0 \\ 0 & 1 \end{bmatrix} \qquad\qquad D = \mathcal{O}_{2x4} \end{aligned} \tag{3.10}$$

The terms in B related to the voltage $\vec{e}_{g,dq}$ are neglected because it is not a controllable variable, and it is considered as an external disturbance. In the case of this system, which operates with complex-valued signals, and for the sake of better understanding of the IR model technique presented before in subsection 2.3.1.2. , (3.11) shows the corresponding complex-valued state-space system.

$$\begin{cases} \dot{\vec{x}}(t) = A \cdot \vec{x}(t) + B \cdot \vec{m}(t) \\ \vec{y}(t) = C \cdot \vec{x}(t) + D \cdot \vec{m}(t) \end{cases} \tag{3.11}$$

Where:

$$\begin{aligned} \vec{x}(t) = \vec{y}(t) = [\vec{i}_{dq}(t)] \\ \vec{m}(t) = [\vec{u}_{dq}(t) \quad \vec{e}_{g,dq}(t)]^T \end{aligned} \tag{3.12}$$

$$\begin{aligned} A = \left[-\frac{R}{L} - j\omega_k \right] \quad B = [1/L \quad -1/L] \\ C = [1] \qquad\qquad D = \mathcal{O}_{1x2} \end{aligned} \tag{3.13}$$

3.2.3. LC-filter model

The LC filter is another usual interface between a voltage source and the power converter. It is usually used for grid-tied applications. The differential equations that define the schematic circuit in Figure 3.3 are (3.14).

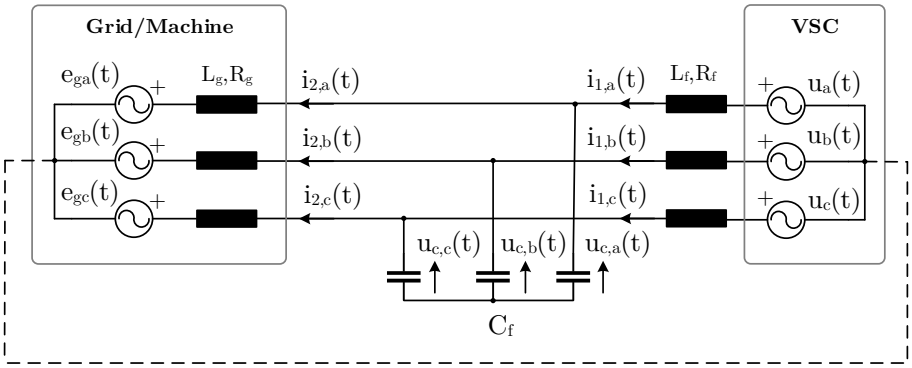

Figure 3.3. Schematic circuit of an LC-filter

$$\begin{aligned}\vec{u}(t) &= R_f \cdot \vec{i}_1(t) + L_f \cdot \frac{d\vec{i}_1(t)}{dt} + \vec{u}_c(t) \\ \vec{i}_1(t) &= C_f \cdot \frac{d\vec{u}_c(t)}{dt} + \vec{i}_2(t) \\ \vec{u}_c(t) &= R_g \cdot \vec{i}_2(t) + L_g \cdot \frac{d\vec{i}_2(t)}{dt} + \vec{e}_g(t)\end{aligned} \tag{3.14}$$

Where:

$$\vec{x}(t) = [x_a(t) \quad x_b(t) \quad x_c(t)]^T \tag{3.15}$$

3.2.3.1. Stationary reference frame

As it was deduced in the previous model, developing the transformation to the stationary $\alpha\beta$ reference frame, the expression (3.16) is obtained.

$$\begin{aligned}\vec{u}_{\alpha\beta}(t) &= R_f \cdot \vec{i}_{1,\alpha\beta}(t) + L_f \cdot \frac{d\vec{i}_{1,\alpha\beta}(t)}{dt} + \vec{u}_{c,\alpha\beta}(t) \\ \vec{i}_{1,\alpha\beta}(t) &= C_f \cdot \frac{d\vec{u}_{c,\alpha\beta}(t)}{dt} + \vec{i}_{2,\alpha\beta}(t) \\ \vec{u}_{c,\alpha\beta}(t) &= R_g \cdot \vec{i}_{2,\alpha\beta}(t) + L_g \cdot \frac{d\vec{i}_{2,\alpha\beta}(t)}{dt} + \vec{e}_{\alpha\beta}(t)\end{aligned} \tag{3.16}$$

Where the $\alpha\beta$ representation is defined in the complex domain for each variable as $\vec{x}_{\alpha\beta}(t) = x_\alpha(t) + jx_\beta(t)$.

The complex-valued transfer function in the stationary $\alpha\beta$ reference frame that relates the converter output voltage, $\vec{u}_{\alpha\beta}$, with the grid current, $\vec{i}_{2,\alpha\beta}$, is (3.17). The voltage $\vec{e}_{g,\alpha\beta}$ is considered as a disturbance.

$$\begin{aligned}\vec{G}_{\alpha\beta}^{LC-filter}(s) &= \frac{\vec{I}_{2,\alpha\beta}(s)}{\vec{U}_{\alpha\beta}(s)}_{|\vec{e}_{g,\alpha\beta}(s)=0} = \\ &= \frac{1}{C_f L_g L_f \cdot s^3 + C_f(L_g R_f + L_f R_g) \cdot s^2 + (C_f R_g R_f + L_f + L_g) \cdot s + R_g + R_f}\end{aligned} \tag{3.17}$$

The main objective of the LCL filter is to reduce the high-order current harmonics at the used switching frequency. For the n-harmonic, neglecting resistors effect, the transfer function between the grid current $\vec{i}^n{}_{2,\alpha\beta}$ and the converter output voltage $\vec{u}^n{}_{\alpha\beta}$ is (3.18). According to this transfer function, the LC filter resonance frequency (that corresponds to zero impedance) is given by (3.19).

$$H_{\alpha\beta}^n = \frac{\vec{I}^n{}_{2,\alpha\beta}(s)}{\vec{U}^n{}_{\alpha\beta}(s)} = \frac{1}{C_f L_g L_f \cdot s^3 + (L_f + L_g) \cdot s} \tag{3.18}$$

$$\omega_{res}^2 = (2\pi f_{res})^2 = \frac{L_g + L_f}{L_g \cdot L_f \cdot C_f} \tag{3.19}$$

To avoid resonance problems, the resonance frequency must be higher than 10 times the operating frequency (grid-tied applications, so grid frequency is $f_g = f_k$) and less than one-half of the switching frequency f_{SW}. Therefore, the equation (3.20) must be verified to avoid resonance problems due to large grid impedance variations, and possible capacitor values error.

$$10 \cdot f_g < f_{res} < f_{SW}/2 \tag{3.20}$$

Since the LC filter resonance frequency is in the middle of that boundary region, it is common to consider the capacitor impedance negligible for high and low frequencies. In this case, the converter will only see the impedance of the inductor. So, the transfer function (3.17) is approximated as (3.21).

$$\vec{G}_{\alpha\beta}^{LC-filter}(s) = \frac{\vec{I}_{2,\alpha\beta}(s)}{\vec{U}_{\alpha\beta}(s)}_{|\vec{e}_{g,\alpha\beta}(s)=0} \approx \frac{1}{(L_f + L_g) \cdot s + R_g + R_f} \tag{3.21}$$

3.2.3.2. Rotating reference frame

By applying the Park transformation, the linear differential equations (3.22) in the rotating dq reference frame are obtained.

$$\begin{aligned}
\vec{u}_{dq}(t) &= R_f \cdot \vec{i}_{1,dq}(t) + L_f \cdot \frac{d\vec{i}_{1,dq}(t)}{dt} + \underbrace{j\omega_k \cdot L_f \cdot \vec{i}_{1,dq}(t)}_{cross-coupling} + \vec{u}_{c,dq}(t) \\
\vec{i}_{1,dq}(t) &= C_f \cdot \frac{d\vec{u}_{c,dq}(t)}{dt} + j\omega_k \cdot C_f \cdot \vec{u}_{c,dq}(t) + \vec{i}_{2,dq}(t) \\
\vec{u}_{c,dq}(t) &= R_g \cdot \vec{i}_{2,dq}(t) + L_g \cdot \frac{d\vec{i}_{2,dq}(t)}{dt} + \underbrace{j\omega_k \cdot L_g \cdot \vec{i}_{2,dq}(t)}_{cross-coupling} + e_{g,dq}(t)
\end{aligned} \tag{3.22}$$

Where the dq representation is defined in the complex domain for each variable as $\vec{x}_{dq}(t) = x_d(t) + jx_q(t)$ and ω_k is the angular frequency of the rotating reference.

Again, a cross-coupling summand appears in the equations, so there is a new summand in the denominator of the complex-valued transfer function (3.23). It is a difficult transfer function to work with, but an approximation can be done if the capacitor is neglected, as in the stationary reference frame. Then, the approximated model is (3.25).

$$\vec{G}_{dq}^{LC-filter}(s) = \frac{\vec{I}_{2,dq}(s)}{\vec{U}_{dq}(s)}_{|\vec{e}_{dq}(s)=0} = \frac{1}{den(s)} \tag{3.23}$$

$$\begin{aligned}
den(s) = C_f L_g L_f \cdot s^3 + C_f \left((L_g R_f + L_f R_g) + j3\omega_k L_f L_g \right) \cdot s^2 + \\
+ \left(C_f (R_g R_f - 3L_f L_g \omega_k^2) + L_f + L_g + j2\omega_k C_f (L_f R_g + L_g R_f) \right) \cdot s + \\
+ R_g + R_f + j\omega_k \left(L_f + L_g + C_f (R_f R_g - L_f L_g \omega_k^2) \right) - C_f \omega_k^2 (L_f R_g + L_g R_f)
\end{aligned} \tag{3.24}$$

$$\vec{G}_{dq}^{LC-filter}(s) = \frac{\vec{I}_{2,dq}(s)}{\vec{U}_{dq}(s)}_{|\vec{e}_{g,dq}(s)=0} \approx \frac{1}{(L_f + L_g) \cdot s + R_g + R_f + j\omega_k \cdot (L_f + L_g)} \tag{3.25}$$

The system in rotating dq reference frame can also be modeled in the continuous-domain space-state with scalar variables as (3.26). A complex-valued space-state is shown in (3.29), which operates with complex-valued signals for a better understanding of IR modelling. For controller design purposes, the voltage $\vec{e}_{g,dq}$ is considered as a disturbance.

$$\begin{cases} \dot{\vec{x}}(t) = A \cdot \vec{x}(t) + B \cdot \vec{m}(t) \\ \vec{y}(t) = C \cdot \vec{x}(t) + D \cdot \vec{m}(t) \end{cases} \tag{3.26}$$

Where:

$$\begin{gathered}\vec{x}(t) = [i_{1,d}(t) \quad i_{1,q}(t) \quad i_{2,d}(t) \quad i_{2,q}(t) \quad u_{c,d}(t) \quad u_{c,q}(t)]^T \\ \overrightarrow{m}(t) = [u_d(t) \quad u_q(t) \quad e_{g,d}(t) \quad e_{g,q}(t)]^T \\ \vec{y}(t) = [i_{2,d}(t) \quad i_{2,q}(t)]^T\end{gathered} \tag{3.27}$$

$$A = \begin{bmatrix} -R_f/L_f & \omega_k & 0 & 0 & -1/L_f & 0 \\ -\omega_k & -R_f/L_f & 0 & 0 & 0 & -1/L_f \\ 0 & 0 & -R_g/L_g & \omega_k & 1/L_g & 0 \\ 0 & 0 & -\omega_k & -R_g/L_g & 0 & 1/L_g \\ 1/C_f & 0 & -1/C_f & 0 & 0 & \omega_k \\ 0 & 1/C_f & 0 & -1/C_f & -\omega_k & 0 \end{bmatrix} \tag{3.28}$$

$$B = \begin{bmatrix} 1/L_f & 0 & 0 & 0 \\ 0 & 1/L_f & 0 & 0 \\ 0 & 0 & -1/L_g & 0 \\ 0 & 0 & 0 & -1/L_g \\ 0 & 0 & 0 & 0 \\ 0 & 0 & 0 & 0 \end{bmatrix} \quad C = \begin{bmatrix} 0 & 0 & 0 & 1 & 0 & 0 \\ 0 & 0 & 1 & 0 & 0 & 0 \end{bmatrix} \quad D = \emptyset_{2x4}$$

$$\begin{cases} \dot{\vec{x}}(t) = A \cdot \vec{x}(t) + B \cdot \overrightarrow{m}(t) \\ \vec{y}(t) = C \cdot \vec{x}(t) + D \cdot \overrightarrow{m}(t) \end{cases} \tag{3.29}$$

Where:

$$\begin{gathered}\vec{x}(t) = [\vec{i}_{1,dq}(t) \quad \vec{i}_{2,dq}(t) \quad \vec{u}_{c,dq}(t)]^T \\ \overrightarrow{m}(t) = [\vec{u}_{dq}(t) \quad \vec{e}_{g,dq}(t)]^T \\ \vec{y}(t) = [\vec{i}_{2,dq}(t)]\end{gathered} \tag{3.30}$$

$$\begin{gathered} A = \begin{bmatrix} -R_f/L_f - j\omega_k & 0 & -1/L_f \\ 0 & -R_g/L_g - j\omega_k & 1/L_g \\ 1/C_f & -1/C_f & -j\omega_k \end{bmatrix} \\ B = \begin{bmatrix} 1/L_f & 0 \\ 0 & -1/L_g \\ 0 & 0 \end{bmatrix} \quad C = [0 \quad 1 \quad 0] \quad D = \emptyset_{1x2} \end{gathered} \tag{3.31}$$

3.2.4. LCL-filter model

The proceedings with LCL filter are like the ones shown in LC-filter modelling. The differential equations that define the schematic circuit in Figure 3.4 are (3.32).

$$\begin{gathered}\vec{u}(t) = R_1 \cdot \vec{i}_1(t) + L_1 \cdot \frac{d\vec{i}_1(t)}{dt} + \vec{u}_c(t) \\ \vec{i}_1(t) = C_f \cdot \frac{d\vec{u}_c(t)}{dt} + \vec{i}_2(t) \\ \vec{u}_c(t) = R_2^g \cdot \vec{i}_2(t) + L_2^g \cdot \frac{d\vec{i}_2(t)}{dt} + e(t)\end{gathered} \tag{3.32}$$

Now the grid-side impedance is $Z_2^g = Z_2 + Z_g$, so all previous models are also valid changing R_g and L_g by R_2^g and L_2^g, respectively. Besides, Z_f is called Z_1 now.

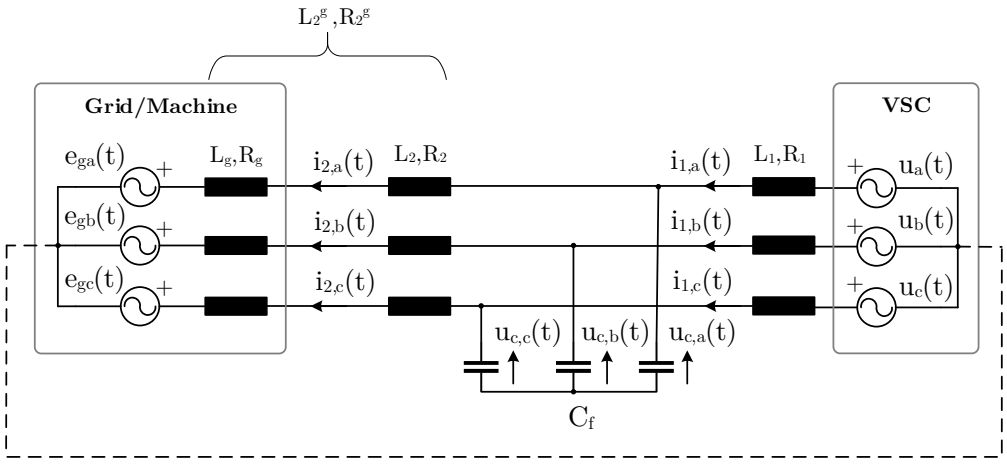

Figure 3.4. Schematic circuit of an LCL-filter

3.2.5. Discretization

The discretization method for the previous continuous-time system models is by means of ZOH operation. In the case of the complex-valued transfer function, the discrete-time model will be obtained as (3.33), where T is the discretization period, and $G(s)$ is the plant model in stationary $\alpha\beta$ or rotating dq reference frame, depending on the reference frame where the controller will be designed. If the system has a fractional delay, the modified Z-transform will be used as it is detailed in Appendix A.

$$G^T(z) = \mathcal{Z}^T\left[\frac{1-e^{-sT}}{s}\cdot G(s)\right] \tag{3.33}$$

The discrete-time space-state model with ZOH discretization at period T is defined by (3.34). This model will be useful for the multirate closed-loop system that will be detailed in the following chapter.

$$\begin{cases}\vec{x}(k+1) = G\cdot\vec{x}(k) + H\cdot\vec{m}(k)\\ \vec{y}(k) = C\cdot\vec{x}(k) + D\cdot\vec{m}(k)\end{cases} \tag{3.34}$$

Where:

$$\begin{gathered}G = e^{A\cdot T}\\ H = [e^{A\cdot T} - I]\cdot A^{-1}\cdot B\end{gathered} \tag{3.35}$$

Every digital implementation of control algorithm has an inherent unit delay T, usually known as computational delay, which lead to a new state. The computational delay has also to be considered for a correct choice of the transformation angle to get the rotating dq reference frame. Since the transformation angle is delayed by the computational time, the transformation law (3.36) between the stationary and rotating frame is applied. The formulation distinguishes between applied voltage by the VSC, $\vec{u}^{VSC}(t)$, and the calculated variable that is based on the samples taken T seconds before, $\vec{u}^{ref}(t)$. Thus, the new state is $\vec{u}^{VSC}(k)$(3.37).

$$\vec{u}^{ref}_{dq}(t-T) = \vec{u}^{ref}_{\alpha\beta}(t-T)\cdot e^{-j\omega_k\cdot(t-T)} \tag{3.36}$$

Applying transformation law (3.37), the complex-valued transfer function of the computational delay in dq-frame is obtained (3.38).

$$\vec{u}_{dq}^{VSC}(t) = \vec{u}_{dq}^{ref}(t-T)\cdot e^{-j\omega_k\cdot T} \tag{3.37}$$

$$\vec{G}_{dq}^{sample\rightarrow update}(s) = \frac{\vec{U}_{dq}^{VSC}(s)}{\vec{U}_{dq}^{ref}(s)} = e^{-s\cdot T}\cdot \underbrace{e^{-j\omega_k\cdot T}}_{cross-coupling} \tag{3.38}$$

This cross-coupling term must be added to each model in dq-frame, whereas in the $\alpha\beta$-frame is only considered the unit delay. Therefore, the corresponding discrete space-state L-filter model in $\alpha\beta$-frame and dq-frame are (3.39) and (3.40), respectively.

$$\begin{gathered}
\vec{x}(k) = \left[\vec{u}_{\alpha\beta}^{VSC}(k) \quad \vec{\imath}_{\alpha\beta}(k)\right]^T \quad \vec{y}(k) = \left[\vec{\imath}_{\alpha\beta}(k)\right] \\
\overrightarrow{m}(k) = \left[\vec{u}_{\alpha\beta}^{ref}(k) \quad \vec{e}_{g,\alpha\beta}(k)\right]^T \\
G = \begin{bmatrix} 0 & 0 \\ \dfrac{1-e^{-\frac{R}{L}\cdot T}}{R} & e^{-\frac{R}{L}\cdot T} \end{bmatrix} \quad H = \begin{bmatrix} 1 & 0 \\ 0 & -\dfrac{1-e^{-\frac{R}{L}\cdot T}}{R} \end{bmatrix} \\
C = [0 \quad 1] \qquad D = \mathcal{O}_{1x2}
\end{gathered} \tag{3.39}$$

$$\begin{gathered}
\vec{x}(k) = \left[\vec{u}_{dq}^{VSC}(k) \quad \vec{\imath}_{dq}(k)\right]^T \quad \vec{y}(k) = \left[\vec{\imath}_{dq}(k)\right] \\
\overrightarrow{m}(k) = \left[\vec{u}_{dq}^{ref}(k) \quad \vec{e}_{g,dq}(k)\right]^T \\
G = \begin{bmatrix} 0 & 0 \\ \dfrac{1-e^{-(\frac{R}{L}+j\omega_k)\cdot T}}{R+j\omega_k\cdot L} & e^{-(\frac{R}{L}+j\omega_k)\cdot T} \end{bmatrix} \quad H = \begin{bmatrix} e^{-j\omega_k\cdot T} & 0 \\ 0 & -\dfrac{1-e^{-(\frac{R}{L}+j\omega_k)\cdot T}}{R+j\omega_k\cdot L} \end{bmatrix} \\
C = [0 \quad 1] \qquad D = \mathcal{O}_{1x2}
\end{gathered} \tag{3.40}$$

$$\begin{gathered}
\vec{x}(k) = \left[\vec{u}_{\alpha\beta}^{VSC}(k) \quad \vec{\imath}_{1,\alpha\beta}(k) \quad \vec{\imath}_{2,\alpha\beta}(k) \quad \vec{u}_{c,\alpha\beta}(k)\right]^T \quad \vec{y}(k) = \left[\vec{\imath}_{2,\alpha\beta}(k)\right] \\
\overrightarrow{m}(k) = \left[\vec{u}_{\alpha\beta}^{ref}(k) \quad \vec{e}_{g,\alpha\beta}(k)\right]^T \\
G = \begin{bmatrix} 0 & 0 & 0 & 0 \\ -\dfrac{e^{-\frac{(R_f+1)\cdot T}{L_f}}\cdot\left(e^{T/L_f}+R_g\cdot e^{\frac{R_f}{L_f}\cdot T}\right)}{R_f+R_g} & e^{-\frac{R_f}{L_f}\cdot T} & 1 & e^{-T/L_f} \\ -\dfrac{e^{-\frac{R_g}{L_g}\cdot T}\cdot\left(R_g\cdot e^{\frac{(R_g+1)\cdot T}{L_g}}+1\right)}{R_f+R_g} & 1 & e^{-\frac{R_g}{L_g}\cdot T} & e^{T/L_g} \\ -\dfrac{\cosh\left(\frac{T}{C_f}\right)\cdot 2}{R_f+R_g} & e^{T/C_f} & e^{-T/C_f} & 1 \end{bmatrix}
\end{gathered} \tag{3.41}$$

$$B = \begin{bmatrix} 1 & \dfrac{e^{-\frac{(R_f+1)\cdot T}{L_f}}\cdot\left(e^{T/L_f}-R_f\cdot e^{\frac{R_f}{L_f}\cdot T}\right)}{R_f+R_g} \\ 0 & -\dfrac{e^{-\frac{R_g}{L_g}\cdot T}\cdot\left(R_f\cdot e^{\frac{(R_g+1)\cdot T}{L_g}}-1\right)}{R_f+R_g} \\ 0 & \dfrac{\cosh\left(\frac{T}{C_f}\right)\cdot 2}{R_f+R_g} \end{bmatrix} \quad C = [0 \quad 0 \quad 1 \quad 0] \quad D = \mathcal{O}_{1x2}$$

The discrete space-state LC-filter model in $\alpha\beta$-frame is (3.41). The dq-frame discrete-time equivalent is not represented here due to its unworkable large symbolic expression, but it is easily obtained following the correct steps of discretization and application of the unit delay with cross-coupling effect.

The LCL-filter case is effortlessly extrapolated from the LC-filter, as it was previously indicated. From the previous deduction is clear that LC and LCL-filters have a large expression model, but they could be approximated to an L-filter at low frequencies. Therefore, the L-filter model will be used to design controllers and to analyze multirate control techniques in Chapter 4.

3.3. Multirate applications

3.3.1. Purpose

This subsection exposes a few possible applications where the multirate cases can be found in VSC controllers. The scope of this document will be in MRIC or extrapolation cases, where there is a sampling at low rate, but the actuation can be updated with a fast rate. There are MROC or decimation cases where the signal is sampled at fast rate, but there is a limitation in the actuation with slow rate, so an optimum controller must be found to get the best possible response. However, this last proposal is not analyzed in this work, and future research will be carried out.

3.3.2. Reduction of the DSPWM delay

In subsection 2.2.3.2. there is a proposal of a different actuation for the DSPWM modulator. As it was previously said, there is a problem with multisampling and it is that the current is sampled at instants that are not carrier signal minima and maxima, which leads to the sampling of switching noise. The target of multisampling is to reduce the $T/2$ delay in the DSPWM process, which is inherent to ZOH operations, by updating the modulating signal more than two times each carrier period. This can be achieved with two techniques: compensation by advancing the modulating signal phase; extrapolation of the sinusoidal signal.

3.3.2.1. Phase advancing compensation

As authors in [41] suggest, the $T/2$ delay can be compensated by phase advancing the modulating signal waveform. The usual phase compensation also includes T delay, characteristic to the digital processing of the signal. If it is not included in the controller design loop, the overall temporal phase compensation is $3T/2$. That is, the overall delay can be contained within the plant model, or it can be compensated.

The phase advancing, which is in radians, must be the corresponding to the controlled frequency of the sinusoidal modulating signal. The VSC is usually connected to three-wire grid, so the controlled frequencies are the fundamental 50 Hz and its harmonics

(typically -5, 7, -11 and 13 with positive or negative sequence), which must have their corresponding phase advancing.

The phase advancing of $T/2$ can be applied in either stationary $\alpha\beta$ reference frame or rotating dq reference frame. In the stationary reference frame, the phase advancing is obtained by multiplying output signal of the controller $u_{h_n,\alpha\beta}$ by the corresponding complex number as it is denoted by (3.42), where n is the harmonic order, that might be negative. Hence, at each current controller output, there is a phase advancing algorithm as it is depicted in Figure 3.5.

$$\vec{u}^*_{h_n,\alpha\beta} = \vec{u}_{h_n,\alpha\beta} \cdot e^{j\omega_n \cdot T/2} \tag{3.42}$$

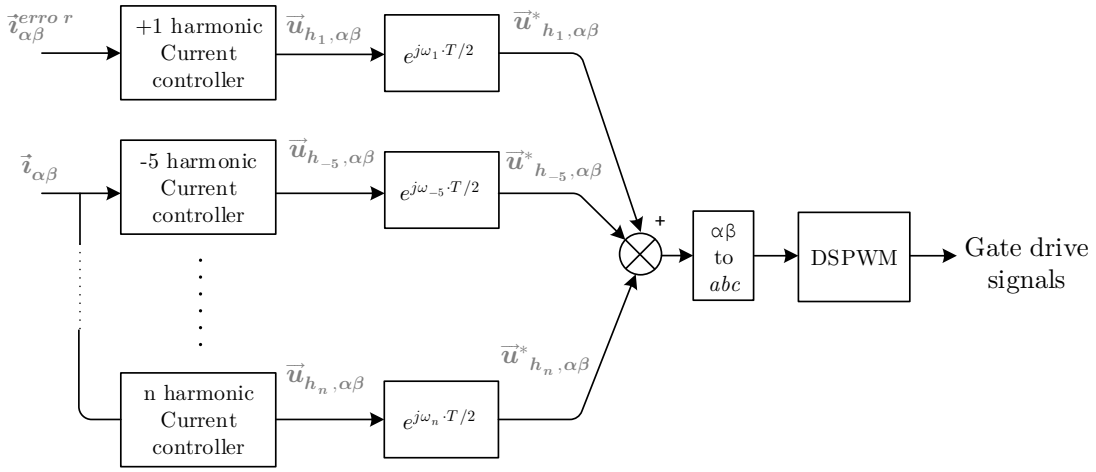

Figure 3.5. Block diagram of phase delay compensation in stationary reference frame

In the rotating reference frame, the phase advancing is applied through the reference frame transformation to $\alpha\beta$-frame, that is sum of phase from PLL θ_1 and phase advancing of $\omega_n \cdot T/2$ radians, as it is shown in (3.43). Hence, at each current controller output there is a phase advancing block as it is depicted in Figure 3.6. Please note that in the dq-frame the frequency of each harmonic changes to the referenced one to the fundamental frequency.

$$\vec{u}^*_{h_n,\alpha\beta} = \vec{u}_{h_{(n-1)},dq} \cdot e^{j(\theta_1+\omega_n \cdot T/2)} \tag{3.43}$$

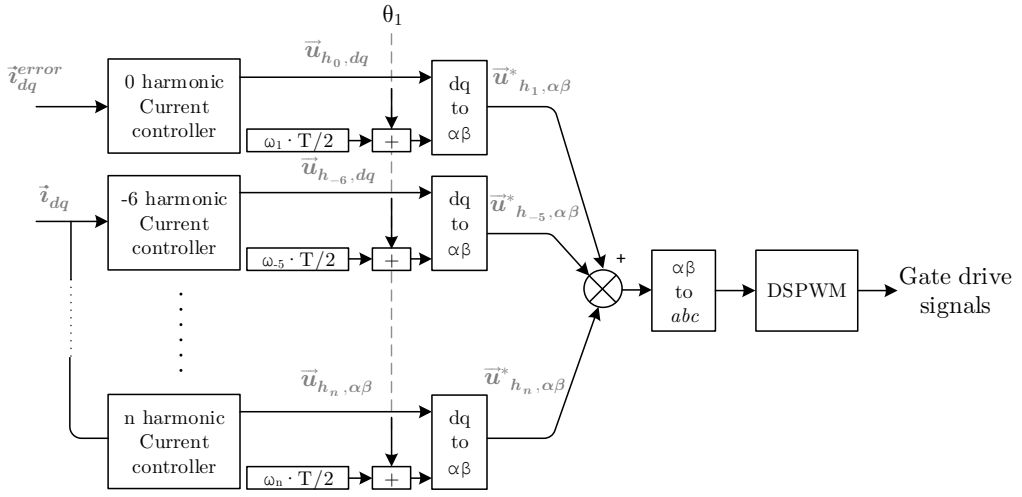

Figure 3.6. Block diagram of phase delay compensation in rotating reference frame

Figure 3.7 illustrates the effect of phase advancing, so the delayed signal in double-update mode approximately matches the same point in carrier signal as naturally-sampled signal. The approximation is better with higher modulation index m_a, in the given example, modulation index is exactly the unity, but the crossing fails with low duty-cycle. However, it obtains a good approximation.

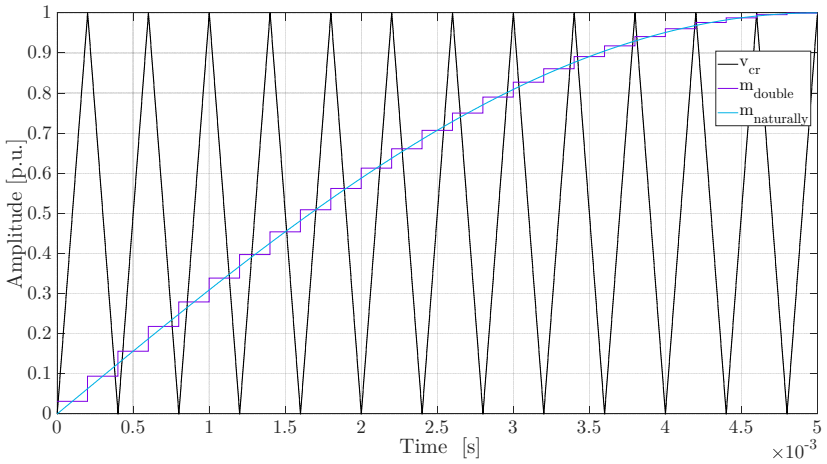

Figure 3.7. Regular sampling with phase advanced modulating signal (double-update mode). Parameters: $f_{SW} = 2.5\ kHz$, $f_1 = 50\ Hz$, $T = 200\ \mu s$, $m_a = 1$

Therefore, the model must consider this compensation to correctly design the controller because Z-transform by means of ZOH operation already considers this $T/2$ delay. Besides, this alternative does not fit well the amplitude at higher frequencies. The next subsection proposes a new approach on the modulating signal update where the last deduction is correctly treated.

3.3.2.2. Extrapolation of the modulating signal

The multisampling approach lead to the possibility of a new alternative where the modulating signal is updated a N number of times greater than one within a half carrier period (considering double-update mode). The basic principle is exactly the same that was explained in subsection 2.2.3.2. , but, now, the sampling instants take place in the carrier maxima and minima. Hence, switching noise is not sampled, and the modulating signal is extrapolated with multirate techniques that will be presented in Chapter 4 or using the sinusoidal extrapolation presented here with single-rate controllers. The proposed method is depicted in Figure 3.8.

There are some polynomial extrapolation methods that will be shown later in this chapter that extrapolate the sinusoidal signal, but it is not the most accurate way. The best extrapolation method is deduced by taking advantage of the rotating dq reference frame transformation. Basically, the extrapolated signal in discrete-time follows the expression (3.44), where N is a number that relates the fast rate T and the slow rate T_0.

$$\begin{gathered} \vec{u}^{E}_{h_n,\alpha\beta}[k \cdot T_0 + p \cdot T] = \vec{u}_{h_{(n-1)},dq}[k \cdot T_0] \cdot e^{j \cdot \theta_1 [k \cdot T_0 + p \cdot T]} \\ k \in \mathbb{N} \\ p = 0, 1, 2, \ldots, N-1 \end{gathered} \tag{3.44}$$

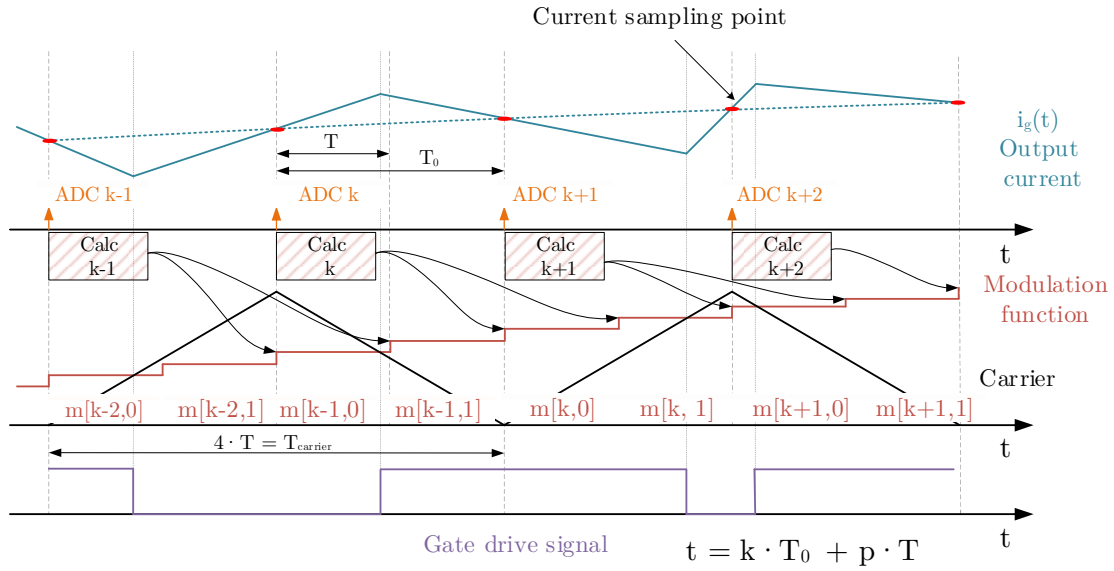

Figure 3.8. Proposed extrapolation method for DSPWM for $N = 2$ (double-update mode)

This approach requires future values of phase θ_1, which are easily extrapolated because the grid frequency does not change a lot (usually 50 Hz), and due to its integration, the phase θ_1 is a ramp signal. The extrapolation in (3.44) fits right the sinusoidal signal of 50 Hz, because the given phase is the corresponding to the fundamental frequency, but it is incorrect for other harmonics. The correct treatment of every harmonic is (3.45). However, the PLL only gives the fundamental voltage phase, so other proposal must be carried out. If the harmonics match their zero-crossings (equivalent initial phase), each harmonic phase can be found as (3.46). Also, each harmonic must have its own *dq*-frame which lead to additional computational burden due to the transformation to each reference frame.

$$\vec{u}^{E}_{h_n,\alpha\beta}[k \cdot T_0 + p \cdot T] = \vec{u}_{h_{(n-1)},dq}[k \cdot T_0] \cdot e^{j \cdot \theta_n [k \cdot T_0 + p \cdot T]} \qquad k \in \mathbb{N} \qquad p = 0, 1, 2, \ldots, N-1 \tag{3.45}$$

$$\theta_n(k) = n \cdot \theta_1(k) \tag{3.46}$$

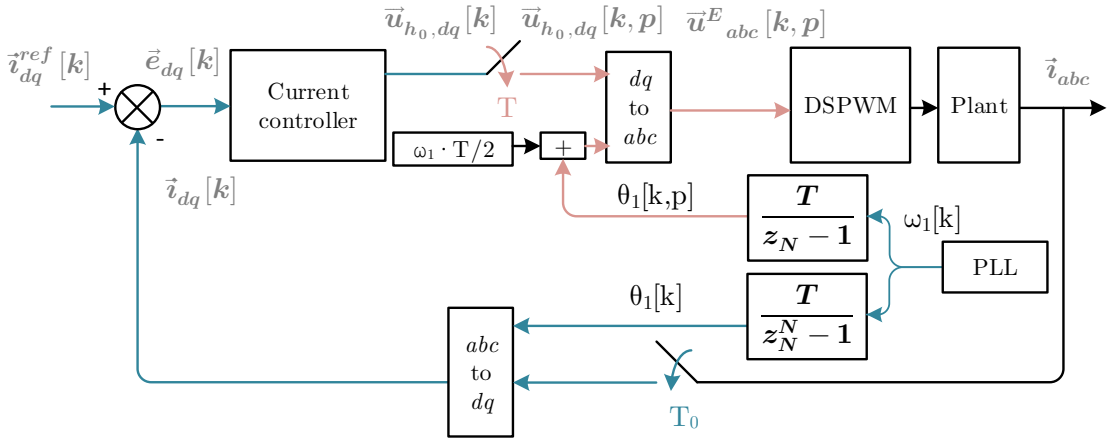

Figure 3.9. Block diagram of the current control loop with extrapolation of modulating signal

This document will be only focused on the grid fundamental frequency (50 Hz) for simplicity. As an example, a simple approach is given, the modulating signal is extrapolated with this technique, without considering the effects of extrapolation in the controller design, and its scope is the minimization of the $T/2$ delay. The block diagram of this structure is presented in Figure 3.9. For greater precision, the phase advancing can also be applied to this technique, being T the fast rate.

The extrapolated modulating signal is compared at different situations in Figure 3.11. On one hand, the modulating signal at fast rate without phase advancing is compared with the one at slow rate without (a) and with (b) phase advancing. On the other hand, the modulating signal at fast rate with phase advancing is compared with the one at slow rate without (c) and with (d) phase advancing. It is shown that the extrapolation obtains better approximations of carrier crossings of the naturally-sampled modulating signal. Mainly, it gets correct crossings at low duty-cycle values.

There is an issue with this approach that was previously presented in Figure 2.27. The modulating signal must not cross the carrier more than one time per one-half carrier period T_{SW}, and this could occur due to discrete values of the modulating signal. Therefore, to ensure only one carrier crossing per $T_{SW}/2$, the first crossing is considered as the correct, and the switching device is forced to only switch that time. This approach allows real-time operation of the DSPWM actuator. Figure 3.10 and Figure 3.12 depict the parametric simulation of the case where there is no phase advancing in the extrapolated signal. Please note that the anomalous values are consequence of the time step resolution of the parametric simulation.

From the parametric simulation, it is seen that the amplitude error is reduced at high frequencies, but the delay almost matches $T/2$ at low frequencies. At high frequencies the delay takes values around $T_0/2$, and it is inevitable to ensure one crossing per $T_{SW}/2$.

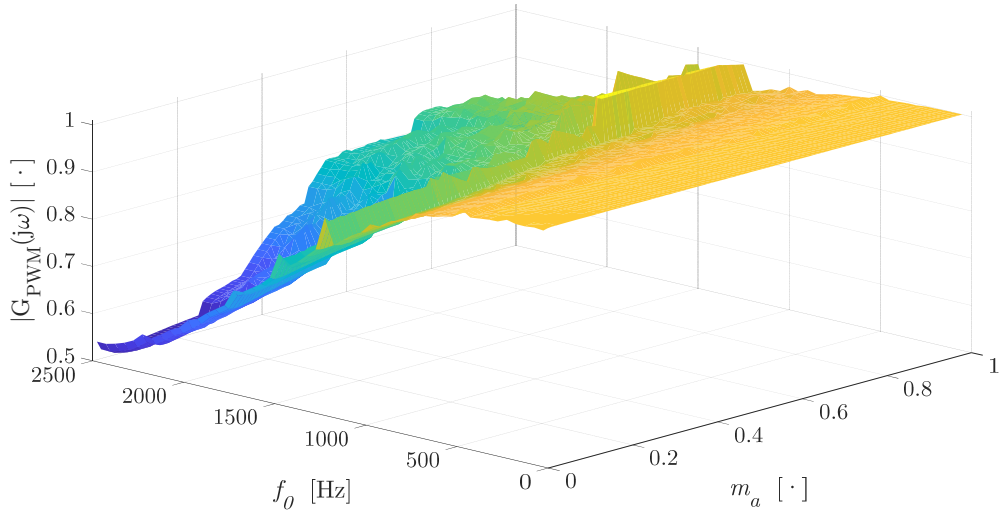

Figure 3.10. Parametric DSPWM simulation of extrapolated modulating signal regarding modulating frequency f_0 and amplitude modulation index m_a. Parameters: $f_{SW} = 2.5$ kHz, $f_1 = 50$ Hz, $T_0 = 200$ μs, $N = 4$

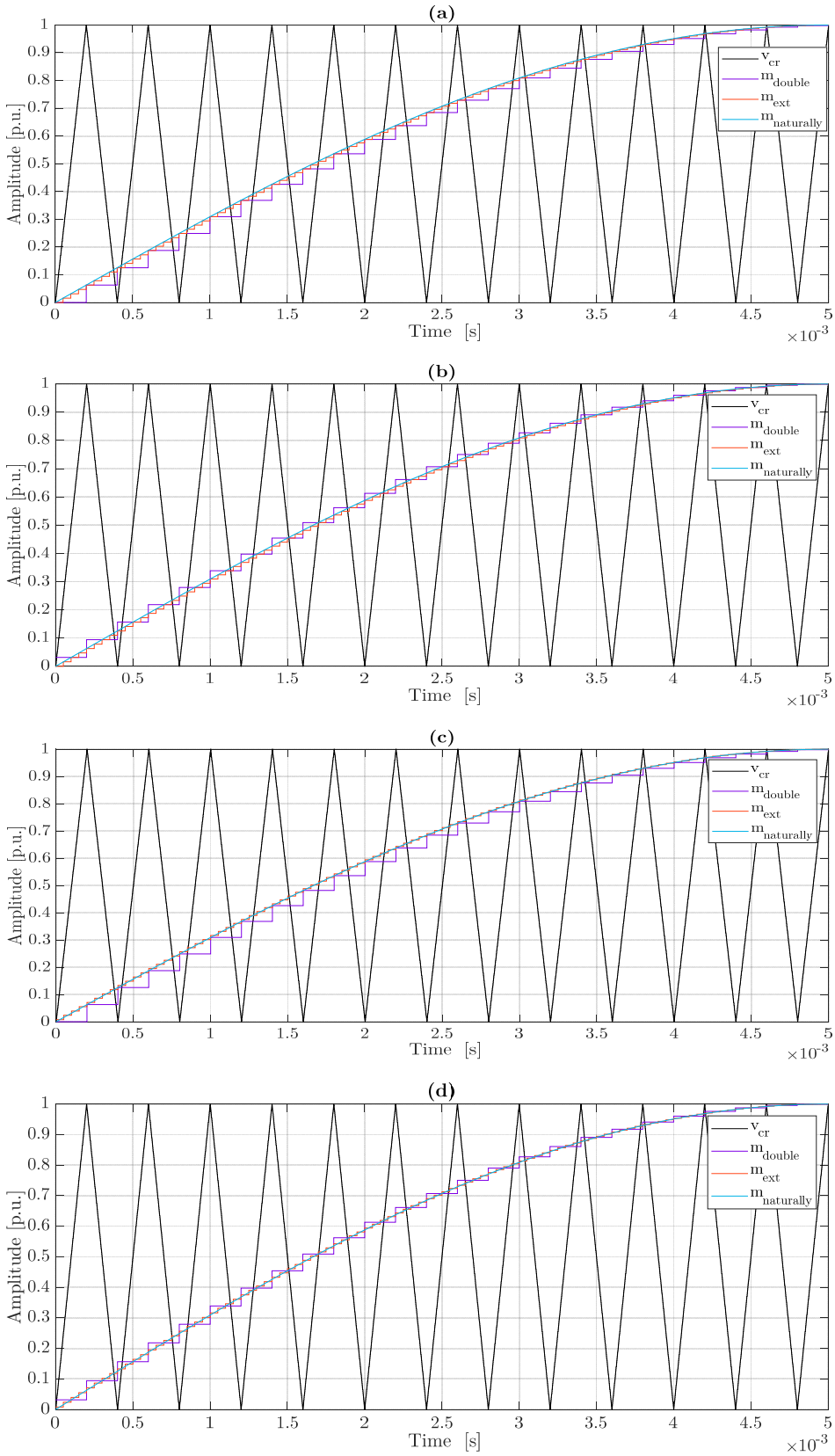

Figure 3.11. Carrier crossing comparison of modulating signals: (a) non-advanced m_{ext} and non-advanced m_{double}; (b) non-advanced m_{ext} and advanced m_{double}; (c) advanced m_{ext} and non-advanced m_{double}; (d) advanced m_{ext} and advanced m_{double}. Parameters: $f_{SW} = 2.5\ kHz$, $f_1 = 50\ Hz$, $T_0 = 200\ \mu s$, $m_a = 1$, $N = 4$

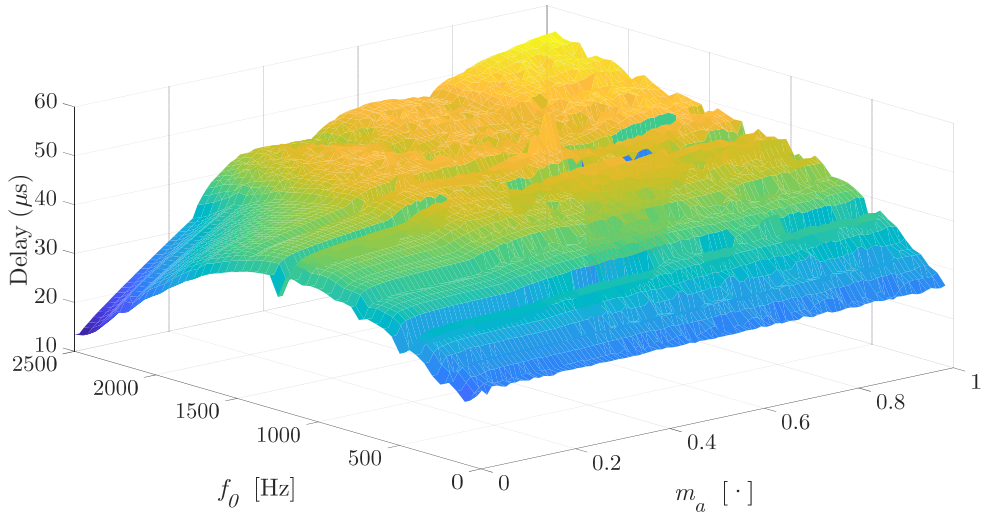

Figure 3.12. Parametric DSPWM simulation of extrapolated modulating signal regarding modulating frequency f_0 and amplitude modulation index m_a. Parameters: $f_{SW} = 2.5$ kHz, $f_1 = 50$ Hz, $T_0 = 200$ μs, $N = 4$

Besides, the simulation presented here takes a relationship between rates of N = 4, which is a low value. Higher N will get right carrier crossing. Other variables are involved in this case as DWPM clock or computational burden to obtain the extrapolated values, which are not in the scope of this work, but they will be analyzed in the future. To obtain right gate drive signals for the semiconductor devices some considerations are also involved as dead-times. This is an interesting proposal to use multirate controllers, although it could be only used for control action of single-rate controllers.

3.3.3. Extrapolation for SHE modulation

3.3.3.1. Definitions

Modulation techniques as SHE (subsection 2.2.2.4.) requires high sampling rates of the modulating signal, which will be the highest in the control loop and will be known as T. A reasonably magnitude of T is theoretically located at the range of little of tens or units of μs. The simplicity of a voltage regulator for linear load does not suppose a barrier for working with equivalent control and modulating rate, $T = T_0$. However, there are applications with additional functionalities (regulation of DC-bus voltage, DC midpoint NPC balance, apparent power and line current, among others), so executing the associated routine with that rate T is not feasible. Instead, the high temporal resolution of the modulating signal $\vec{u}^E$ can be obtained by extrapolating the control action $\vec{u}$. Hence, the situation is $T < T_0$. Figure 3.13 depicts a schematic of the open loop controller with extrapolation of the modulating signal, where is easily differentiated between the low rate instants $k \cdot T_0$ and the high rate instants $k \cdot T_0 + p \cdot T$. In the schematic is also presented a filter after the extrapolation or up-sampling process, which is an anti-imaging filter needed in such processes. However, this block it

is not in the scope of this document, but it will be analyzed in the future for practical applications.

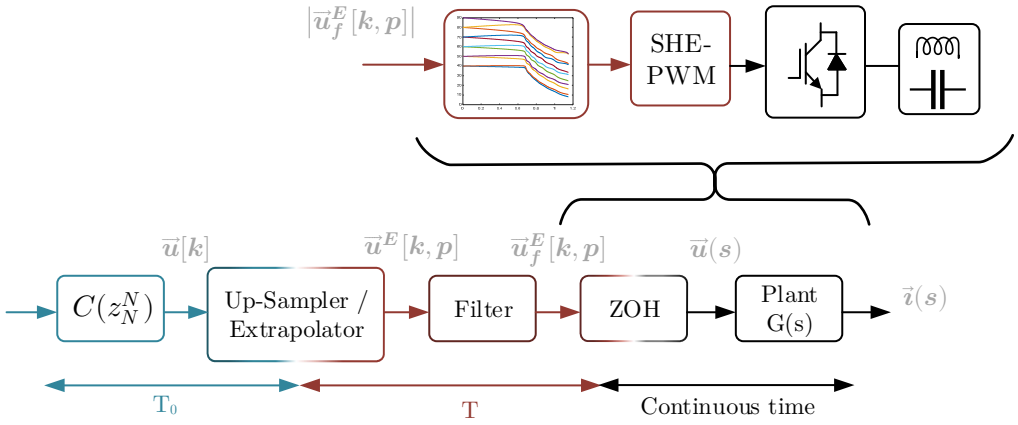

Figure 3.13. Block diagram of the proposed open loop controller for SHE

Please note, as in the previous subsection, that the extrapolation is the process of estimating, beyond the original observation range, the value of a variable based on its relationship with the previous observed values until that instant. It is like the interpolation, which produces estimates between known observations, but extrapolation is subject to greater uncertainty and higher risk of producing meaningless results. Usually, the tendency of the variable is estimated with the most recent consecutive samples of the modulating signal $\vec{u}$, they are known as polynomial extrapolators. This polynomial extrapolation will be briefly introduced in this section, but there is a more accurate technique to extrapolate a sinusoidal variable, as it was detailed in 3.3.2.2. Therefore, this approach supposes a sampling rate adaptation with an evident computational burden reduction for the microprocessor.

3.3.3.2. Polynomial extrapolation

This subsection is focused on the polynomial extrapolation proposal for the previous approach, that has been studied in the literature by few authors.

The up-sampling process is linear but time variant, so no function can be defined to express it. The closest mathematically formulation of the polynomial up-sampler in the time domain is given by (3.47), which means that the N samples of the extrapolated vector $\vec{x}^E$ are expressed in function of the M last samples of input vector $\vec{x}$. This formulation is based on the Taylor power series with M terms. The parameter M matches up with the number of power series to calculate the new samples and M-1 with the order of the polynomial employed, except when $M = 0$. The number of extrapolated samples is $N - 1$.

$$\vec{x}^E[N \cdot k + p] = \vec{x}^E[k,p] \underset{E_{M\times N}}{\Longleftrightarrow} \begin{cases} if\ M = 0\ \& \begin{cases} p = 0 & \vec{x}[k] \\ p \neq 0 & 0 \end{cases} \\ if\ M > 0 \qquad \sum_{r=0}^{M-1} \frac{1}{r!} \left(\sum_{i=0}^{r} \binom{r}{i} (-1)^i \vec{x}[k-i] \right) \left(\frac{p}{N} \right)^r \\ p = 0, \ldots N-1; \end{cases} \tag{3.47}$$

Where:

- Number of used input samples to estimate the signal tendency: $M \geq 0$
- Sampling rate multiplier: $N \geq 1$
- The samples of $\vec{x}^E$ can be linearly indexed $\vec{x}^E[N \cdot k + p]$ or in matrix way $\vec{x}^E[k, p]$. This is useful for a better understanding of the following explanation.

The corresponding transfer function of the extrapolation process between a vector that has been up-sampled $\vec{X}_p(z_N)$ (expand process of $M = 0$ and $N > 1$, that is $E_{0\times N}$) with the original signal $\vec{X}(z_N^N)$ is (3.48).

$$\vec{H}^p_{M\times N}(z_N^N) = \frac{\vec{X}_p(z_N^N)}{\vec{X}(z_N^N)} = \sum_{r=0}^{M-1} \frac{(1 - z_N^{-N})^r}{r!} \left(\frac{p}{N}\right)^r \quad M > 0 \tag{3.48}$$

This is the partial transfer function $\vec{H}^p_{M\times N}(z_N^N)$ that relates every p sample at each $N \cdot k$ sample. The signal $\vec{X}^E_p(z_N)$ is obtained by correctly positioning each p sample calculated every N $\cdot\, k$ instant.

$$\vec{X}^E_p(z_N) = z_N^{-p} \cdot \vec{X}_p(z_N^N) \tag{3.49}$$

The extrapolated signal at high rate $\vec{X}^E(z_N)$ can be expressed as (3.50), to finally obtain the transfer function that relates the output with the extrapolated input, by means of $E_{0\times N}$, as (3.51).

$$\vec{X}^E(z_N) = \sum_{p=0}^{N-1} \vec{X}^E_p(z_N) = \sum_{p=0}^{N-1} z_N^{-p} \cdot \vec{X}_p(z_N^N) = \vec{X}(z_N^N) \cdot \sum_{p=0}^{N-1} z_N^{-p} \cdot H^p_{M\times N}(z_N^N) \tag{3.50}$$

$$\vec{H}^C_{M\times N}(z_N) = \frac{\vec{X}^E(z_N)}{\vec{X}(z_N^N)} = \sum_{p=0}^{N-1} \left(z_N^{-p} \cdot \sum_{r=0}^{M-1} \frac{(1 - z_N^{-N})^r}{r!} \left(\frac{p}{N}\right)^r \right) \tag{3.51}$$

In Figure 3.14 are depicted up-sampling examples where a 50 Hz normalized vector is extrapolated with four different combination of M and N. Only real parts of the vectors $\vec{x}^E$ and $\vec{x}$ have been exhibited. Besides, the ideally extrapolated version of $\vec{x}$ has been plotted with a dashed black line. It is shown how the extrapolation fails during the first M-1 sampling instants of $\vec{x}$ because the initial conditions (there are M-1 delay terms, z_N^{-N}) of the filter are null. For example, in (d) the extrapolator does not work right until eighth sample of the input.

It can be recognized that there is an extrapolation error associated to all techniques. The obtained error in the M-1 order Taylor polynomial is defined as the extrapolation error $\vec{e}^E[k]$.

$$\vec{e}^E[k] = \vec{x}[k] - \vec{x}^E[k] \tag{3.52}$$

As it is well-known in digital signal processing, the up-sampling process has an inherent effect where high frequency components are added. The effect is known as imaging and the new components are images. Hence, the extrapolation error is composed by the fundamental component error $\vec{e}^E_0[k]$ and its images $\vec{e}^E_i[k]$.

$$\vec{e}^E[k] = \vec{e}^E_0[k] + \sum_{\substack{i=-\lfloor N/2 \rfloor \\ i\neq 0}}^{\lceil N/2 \rceil - 1} \vec{e}^E_i[k] \tag{3.53}$$

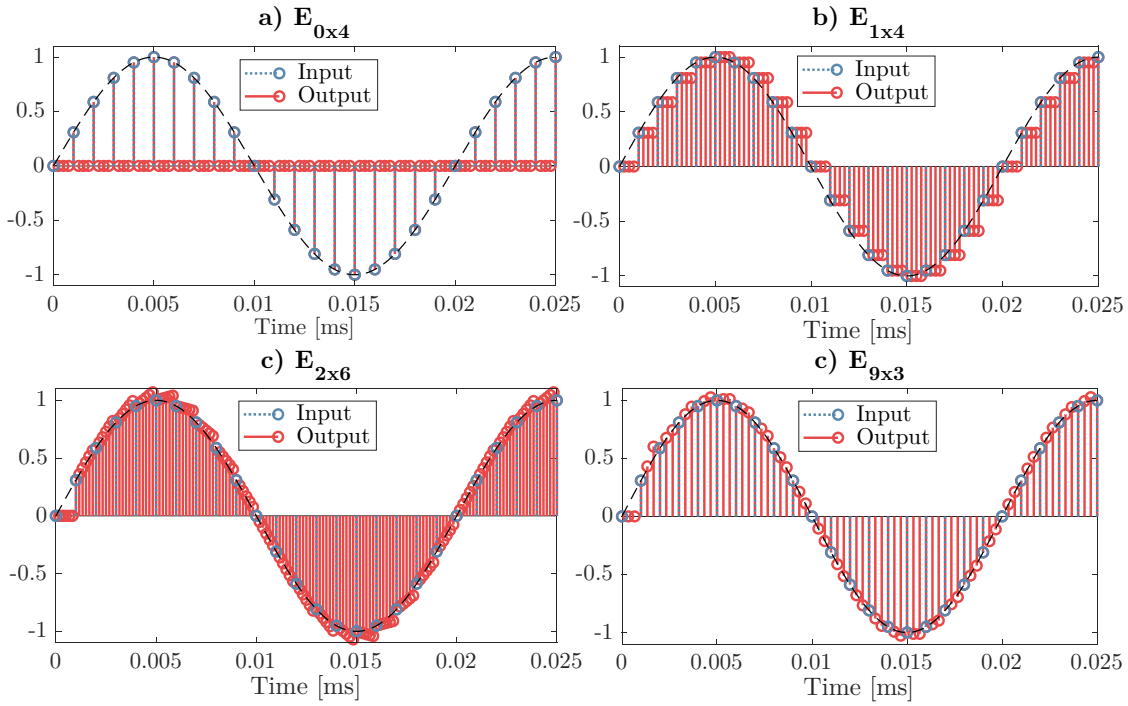

Figure 3.14. Time domain characterization of up-sampling. Parameters: $f_1 = 50$ Hz, $T_0 = 1$ ms

Although the input only contains the fundamental component, the output will be composed of fundamental and N-1 images. They come from the repeated components out of the Nyquist band (limited by $\Omega_{\text{Nyq}} = \pm\pi$, being $\Omega = \omega \cdot T_0$), that is repeated every 2π. At the new high rate, they are inside the new Nyquist band. Figure 3.15 depicts the previous explanation. The images must be eliminated by means of low pass filter.

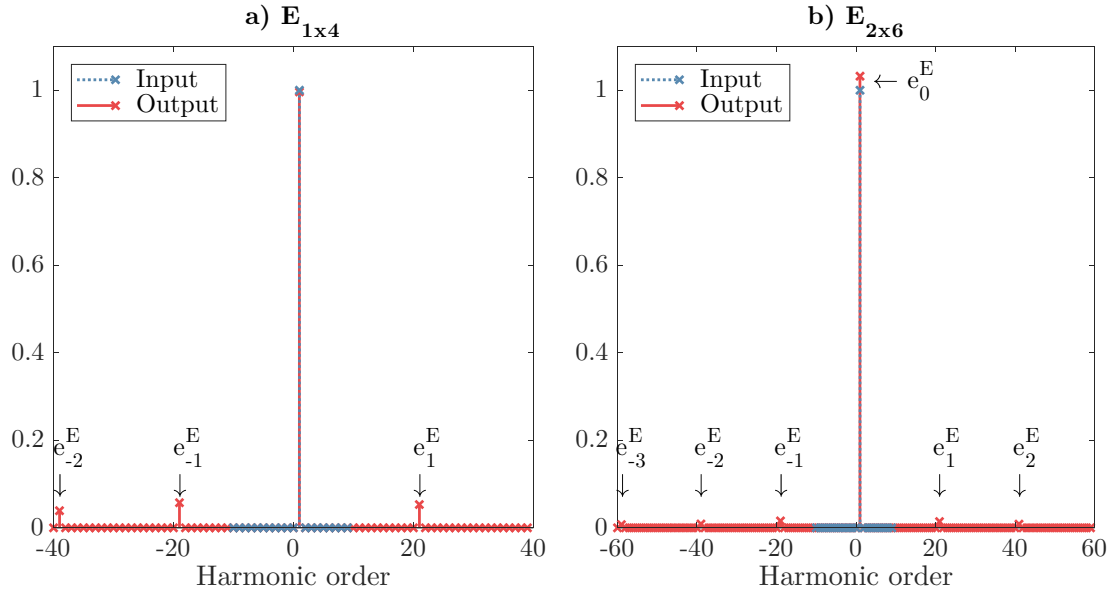

Figure 3.15. Frequency spectrum of vectors. Parameters: $f_1 = 50$ Hz, $T_0 = 1$ ms

3.3.3.3. Sinusoidal extrapolation

As it was presented in the latter discussion, the better method of approximating a sinusoidal variable is by means of rotating reference frame transformation and multirate control techniques that will be presented in the following chapter. The polynomial extrapolation has error in its estimations. The basis of sinusoidal extrapolation has already been explained in the subsection 3.3.2.2. In this case, there is not such a transfer function as the polynomial extrapolation because this process is non-linear and time variant, but there is an interesting line of research to obtain such an expression.

3.3.4. Hierarchical control structures

3.3.4.1. Possibilities

The hierarchical control structures are a good example of control applications in power electronics where there are different control rates in each level, but in every level the actuation variables could be extrapolated to obtain suitable reference variables to the control loop below.

Microgrids with power converter units are great examples of hierarchical control in power electronics, although there are hierarchical structures with control loops at different rates in every power electronics application.

3.3.4.2. Microgrids

The rising interest about Microgrids (MG) comes from the diffusion need of renewable energy resources because it is an attractive way to integrate Distributed Generators (DG), Energy Storage Systems (EES) and loads (L) in small power systems. It is related with the distribution electric grid where medium voltage converters have great presence. Hence, MG could be connected or isolated from the utility grid. When they are connected to the grid they are singular and flexible entities, which can provide supporting for power electric systems.

Great advances have been done in real-time operation and control of MG, as well as the elimination of parallel connection of power converters without the use of dedicated communication structure. The solution was the local control droop but has some limitations due to voltage/frequency deviations.

The usual solution to avoid deviation problems and to ensure correct operation is to use a centralized communication system with low bandwidth. This is the solution that could be improved by using multirate techniques. However, the actual tendency is focused is DGs directly connected to the MG, which are classified as: grid-forming, grid-feeding, and grid-supporting. The communications, in this case, are achieved by means of PLC (Power Line Communication) and DBS (Distributed Bus Signaling), and instead of a centralized bulk data, a MAS (Multi-Agent System) is used. More detailed information can be found in [62].

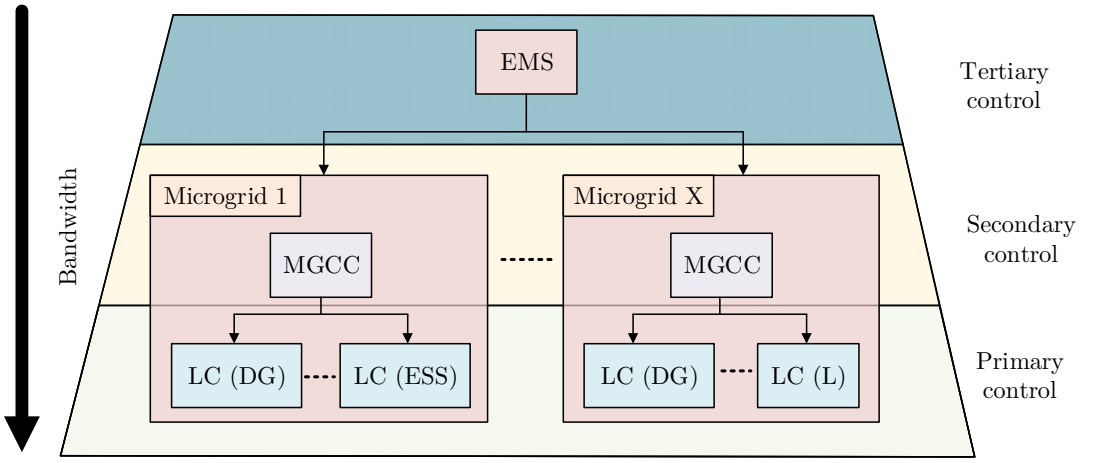

Figure 3.16. Regulation pyramid of MG

The conventional control structure in MG follows a hierarchical path, as Figure 3.16 depicts, which has been inherited from large power systems:

- **Primary control**: It is responsible of the power, voltage and frequency control of each individual power converter. The droop control and virtual impedance are used upon the voltage and current control loops. There are centralized [63], [64] and decentralized [62] architectures. The main goal of this level is to administrate the renewable resource and an uncertainty load. Parallelized converters are usually configurated as grid-supporting with droop techniques. The controller of each element is known as Local Controller (LC).
- **Secondary control**: It regulates the power quality to control voltage/frequency deviations, unbalance and harmonics. Optionally, it performs the synchronization between MG and utility grid. The voltage and frequency deviations from their nominal values are inevitable in steady state. Besides, the accurate active/reactive power delivery cannot be achievable by most usual droop mechanisms. Using digital communications, this control level can enhance the performance and controllability of the global MG. There are centralized and decentralized implementations, being the centralized case the most usual. There is only one controller known as MicroGrid Central Controller (MGCC). The MGCC takes voltage and frequency variables that have been remotely measured and transferred through a low bandwidth communication bus. Those variables are compared with their references to calculate the needed compensation, so these are sent through the communication channel to every primary control unit. In the distributed case, the primary and secondary control merge into a new local controller that uses less communication tasks.
- **Tertiary control**: It oversees power exchange regulation with the utility grid or/and other MG. This level also includes efficiency and economic improvements that is referred as Energy Management System (EMS). The temporal scale is the slowest.

3.3.4.3. Multirate application

From the previous discussion, there are two possibilities where the multirate approach is possible to enhance the dynamic performance:

- **Centralized primary voltage control**: The remote controller of grid-forming power converter needs a communication bus which restricts the updating rate of that controller. It is an unusual possibility because the tendency is on droop techniques for grid-supporting DG.
- **Centralized secondary control**: In Figure 3.17 is shown how the secondary control works at different rate due to communication buses. This is inherent to every hierarchical control. Therefore, the system dynamics could be improved with the incorporation of multirate techniques. The measurement and references are taken at slow rate and the actuation could take place at fast rate to get suitable references for primary control. MRIC structures as the ones shown in the following chapter could improve the system performance. The controlled plant is not obtained in this document, but the analysis in this document could be extrapolated to this case, if the controlled plant is correctly modeled.

These proposals can be used with other hierarchical control structures like the usual inner current control loop which works at fast rate and an outer voltage and/or power control loop at slow rate. The outer control loop receives samples at slow rate and could provide references at fast rate to the inner control loop. These cases are not in the scope of this document, but it is proven that the analysis for the current controller in Chapter 4 can be easily carried out for the outer control loops, if the controlled plant is known. Please note that in the scope of this document is analysis of multirate control techniques for the inner current control loop.

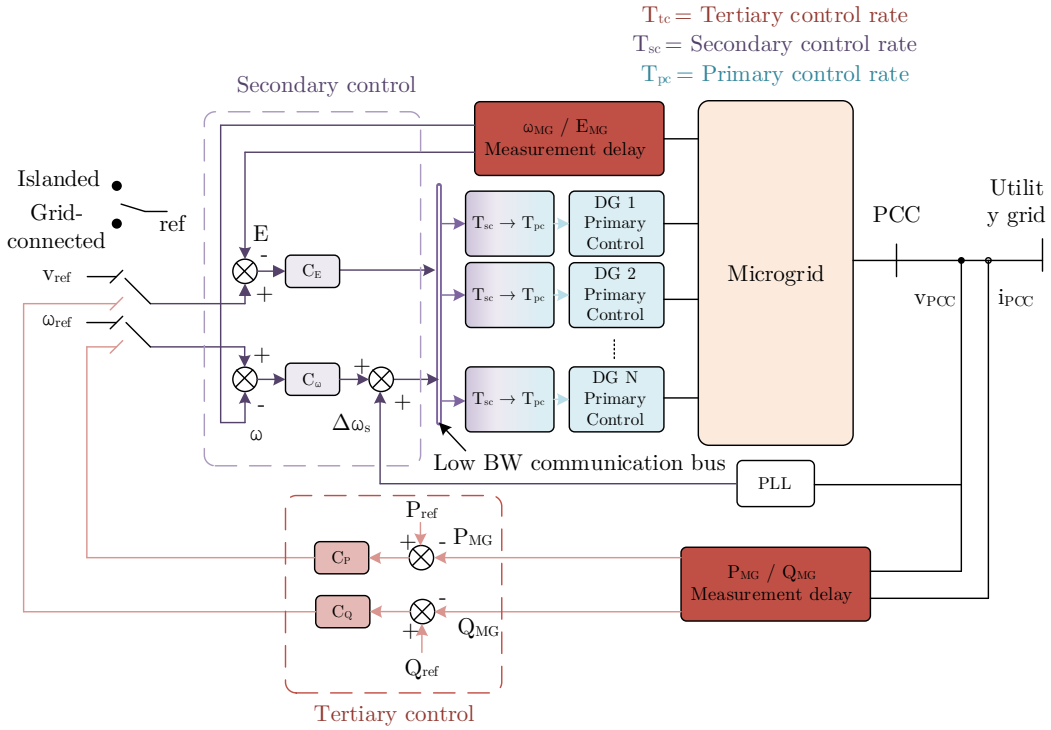

Figure 3.17. Control structure of secondary and tertiary control levels

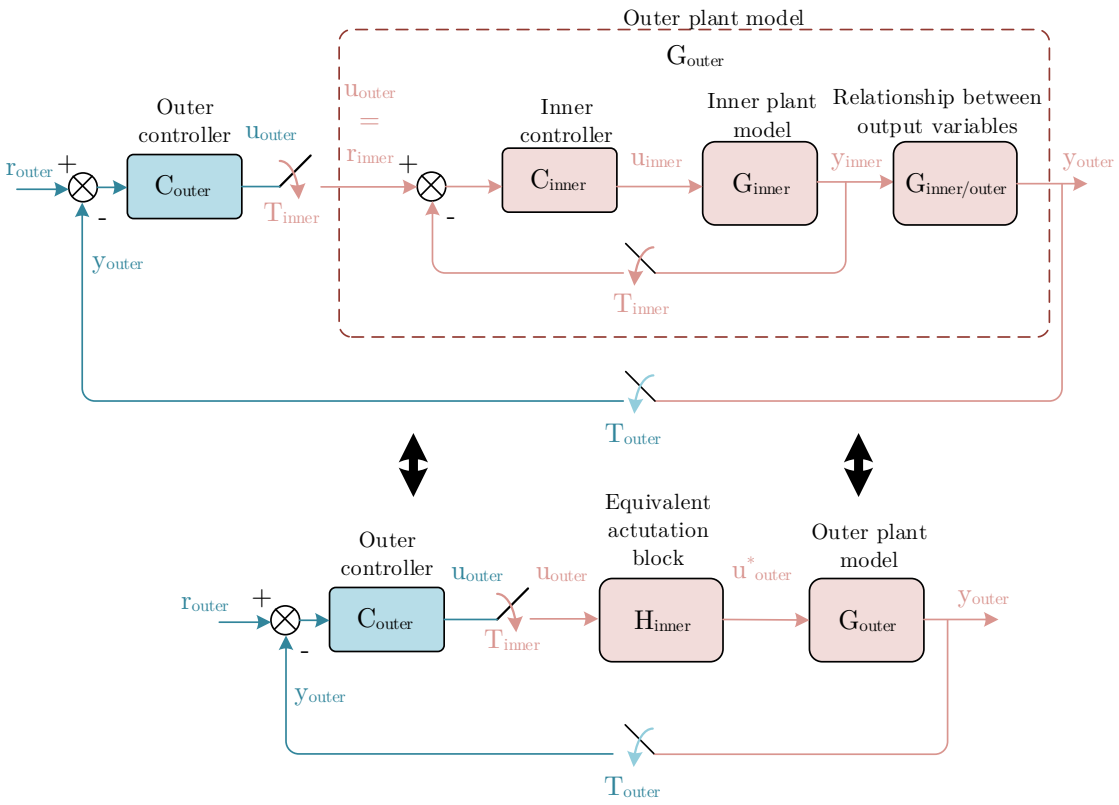

Figure 3.18. Hierarchical control with different rates per control level

Basically, the simplified outer and inner control loop could be arranged as it is depicted in Figure 3.18. Notice that it has been generalized for every control level. For example, the inner control loop takes care of current, whereas the outer controls P/Q and the DC-bus voltage (Appendix C). The figure also depicts an alternative representation, where the actuation block for the outer loop represents the equivalent inner control phase delay and rate change. This application has possible multirate techniques to be applied, that have been neglected nowadays.

3.3.5. Other multirate possibilities

3.3.5.1. Fast power semiconductor devices

As it was presented in Chapter 1, there is new power semiconductor devices that provide fastest switching frequencies f_{SW}. Some applications may require an additional computational burden for their algorithms, so the sampling period is maintained equal to the needed control period T_0, but the actuation can be followed by means of double-update mode. Hence, the modulating signal is at fast rate T as in subsection 3.3.2, but now the switching rate, that is the carrier period T_{SW}, satisfy the equivalence $T_{SW} = 2 \cdot T$ to get the double-update mode. The relationship between rates involved in the system is (3.54), being N the sampling rate multiplier.

$$T_{SW} = 2 \cdot T = 2 \cdot T/N \tag{3.54}$$

This is an interesting application for future applications where the economic or technical constraints require different control rates. However, in recent years, the processing times have been reduced, so this application is only suitable for application where the economical constraints lead to slower digital signal processors.

This application was explained in Figure 1.7, where it is compared with the constrained sampling possibility (slow single-rate controller) and the optimum situation (fast single-rate controller).

3.3.5.2. Computational burden of extra algorithms

There are some applications that requires extra algorithms which are not essential for the converter control such as repetitive controller. This kind of algorithms follow other rate due to their computational burden, and calculated values are applied one time each N control periods. They need a correct modelling of their control branch, and multirate techniques could be useful in that cases.

For example, in subsection 2.2.4.2. a multirate repetitive controller that works at slower rate is introduced. It must be correctly designed because they have effect on actuation signal.

3.4. Conclusions

This chapter has detailed the modelling of the inner plant model of the VSC, which is needed for the current controller. The most usual three filters have been studied in stationary and rotating reference frames to get the transfer function expression as well the space-state version. The most detailed one for multirate applications will be the L-filter due to its importance in MV applications. Also, the LC and LCL filters can be approximated to an L-filter, because the low frequencies response is very similar to the L-filter one. Models have been shown in continuous-time, but in the next chapter correct rates will be applied. The unique characteristics of multirate techniques requires this expression in continuous-time to later obtain correct single-rate equivalents or MRIC design.

Later, new multirate applications for power electronics have been presented to obtain the right context for the next chapter. Firstly, the reduction of the DSPWM delay has been analyzed through two paths: phase advancing and extrapolation. Comparison reflected that extrapolation is a useful approach. The DPSWM was detailed without changing T_{SW}, what led to some issues with the carrier crossings, but they are useful for low modulating signal frequencies. The sinusoidal extrapolation approach must stand out, because it is a useful tool for multirate applications in AC systems. Next, the multirate ideas (extrapolations) were related to SHE modulation technique. Two extrapolation techniques were proposed for this case: polynomial extrapolation and non-linear sinusoidal extrapolation. The second one might have got better responses, but it is interesting to know the polynomial extrapolation technique for further applications.

Then, the hierarchical control structures were studied, specifically the Microgrid case what is a representative new division in power electronics, but every power converter control has more than one control loop. The outer control loop on simpler cases are the DC-bus voltage and P/Q regulators, but they are not in the scope of this document, although Appendix C gives some insight on DC-bus regulator.

This document is focused in the inner current control loop that uses the detailed models presented at the beginning of this chapter. However, the conclusions and methodology in Chapter 4 are easily extrapolated to hierarchical cases. There is detailed information of the outer control loop in Appendix C, although they are not strictly necessary for the case under study because the DC-bus voltage regulation can be carried out by other system, and the current reference could be directly given to get the correct power exchange. Still, it is not the most realistic application, but this research is focused in multirate applications for current control loop.

Finally, two last applications are given, and fast switching is the taken approach for Chapter 4. It will be focused in explanations about DSPWM situation with or without changing T_{SW}, but the actuation will be always faster than sampling. SHE modulation technique is not analyzed with simulations because this work does not want to get the reader in confusion. However, the conclusions can be easily extrapolated for SHE modulation or even other modulation techniques. On the other hand, the additional algorithm at different rate are possibilities that are being a matter of research, so a few points and example were only given.

Chapter 4. Multirate controllers

4.1. Introduction

This chapter details how concepts from previous chapters merge in multirate control design techniques for VSCs. The chapter is split in three sections: proposed single-rate controllers, time-domain multirate analysis and model-based multirate controllers. Each one of them will study complex-valued controllers in stationary and rotating reference frame for an VSC with L-filter. Therefore, there is a first section to define the complex-valued controllers that will be used for the multirate case. Note that those controllers are some of many possibilities, so other single-rate controllers for each reference frame are possible.

The analyzed system and multirate approach have been already described, so a simplified block diagram is depicted in Figure 4.1. This figure shows that the double-update mode is chosen because its delay is known (overall delay of $3T/2$) and each modulating signal update has its own crossing.

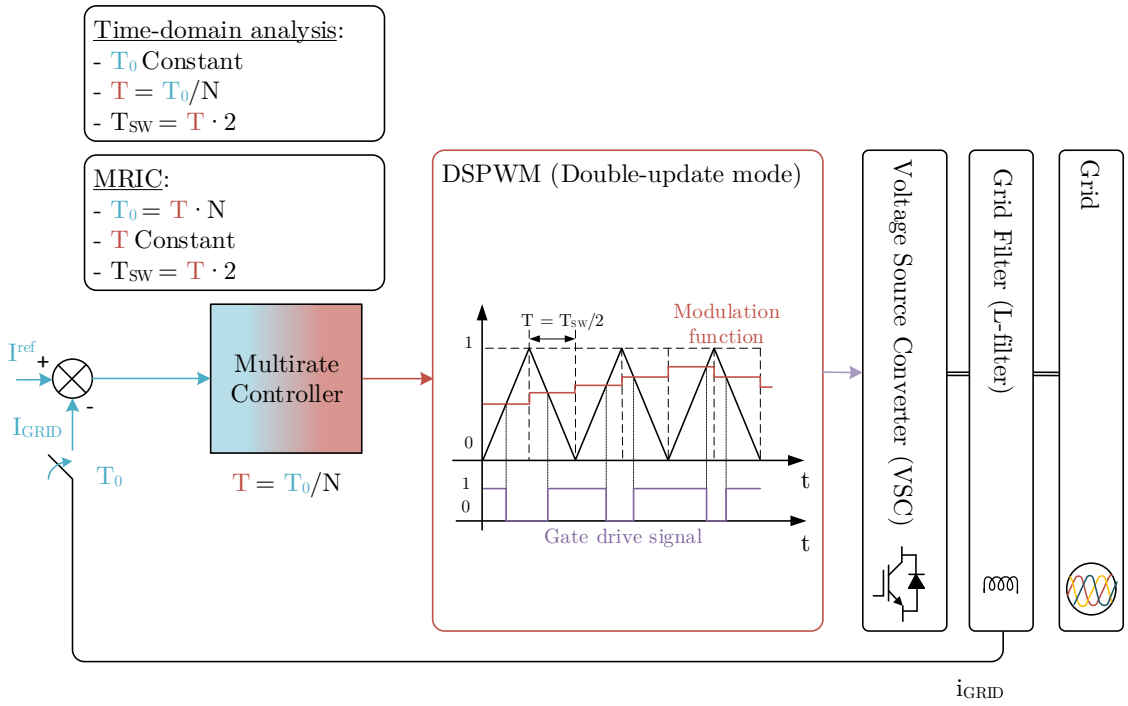

Figure 4.1. Simplified block diagram of the controlled system

Initially, the time-domain multirate analysis will be carried out. This analysis takes the proposed single-rate controllers and transforms them into multirate cases. The methodology is based on correctly model the system and open loop transfer function at metaperiod T_0, that is the slowest rate in the closed-loop system. The used technique is the internal representation by means of recurrence laws based on Kranc methodology. Finally, a closed-loop transfer function at single-rate metaperiod is obtained. Hence, this technique examines when the actuation and control rate get faster than the sampling rate, without changing the designed controller.

Later, an alternative multirate technique will be presented to design what is known as MRIC. It is a model-based multirate controller, of which design depends on the input to be tracked. In this document, there are sinusoidal and continuous variables, depending on the reference frame. The controller is split in two parts acting at different sampling rates and its design is approached regarding characteristics of each available sampling rate. The control target is to reach similar performances to those the faster single rate controller would achieve.

There are other design alternatives that will be studied in future research, but these two techniques are a good beginning in power electronics.

Notice that the parameters and voltage level of the system under study are corresponding to Low Voltage. The reason is that these are the parameters of the experimental setup 3L-DNP-VSC in laboratory. Hence, future experimental test could be compared with the following results. Still, the controller problematics are MV applications, so this document treats that point of view. However, the test is easily extrapolated to MV setup.

4.2. Proposed single-rate controllers

4.2.1. Stationary reference frame

The present subsection will define the bases of the current controller in $\alpha\beta$-frame for multirate analysis. This current controller is based on a stationary reference frame implementation of an integrator in the synchronous reference frame, which was firstly proposed by [56]. The proposed controller is known as Reduced Order Generalized Integrator (ROGI) and is suitable for three-phase VSC. It is a resonant controller for each harmonic sequence that is controlled. In this document, the fundamental harmonic is controlled following the depicted structure in Figure 4.2. Please note, as it was previously followed with the complex-valued models, in the following, the complex space vector notation will be used. In complex space vector notation, transfer functions have complex coefficients, poles do not necessarily appear in conjugate pairs, and frequency responses are not necessarily symmetrical around zero.

Following the strategy in [56], the controller design is deduced in the discrete-time domain, that is based on the state variable technique because it allows easy tuning of

controller and takes into account the digital signal processor (DSP) delay as a part of the system to stabilize. The delay is considered equal to sample time.

The digital ROGI implementation is shown in (4.1), which is the discrete-time version of a continuous time system with a pole at $jh\omega_1$, being h the harmonic order. This document is focused in the positive fundamental sequence, but this controller usually includes -1, -5 and +7 sequences. The goal in this document is to prove that this controller could be implemented and correctly analyzed in multirate cases.

$$\vec{G}^{h}_{\alpha\beta}(z) = \frac{\vec{X}^{h}_{\alpha\beta}(z)}{\vec{E}_{\alpha\beta}(z)} = \frac{1}{z - e^{jh\omega_1 \cdot T}} \tag{4.1}$$

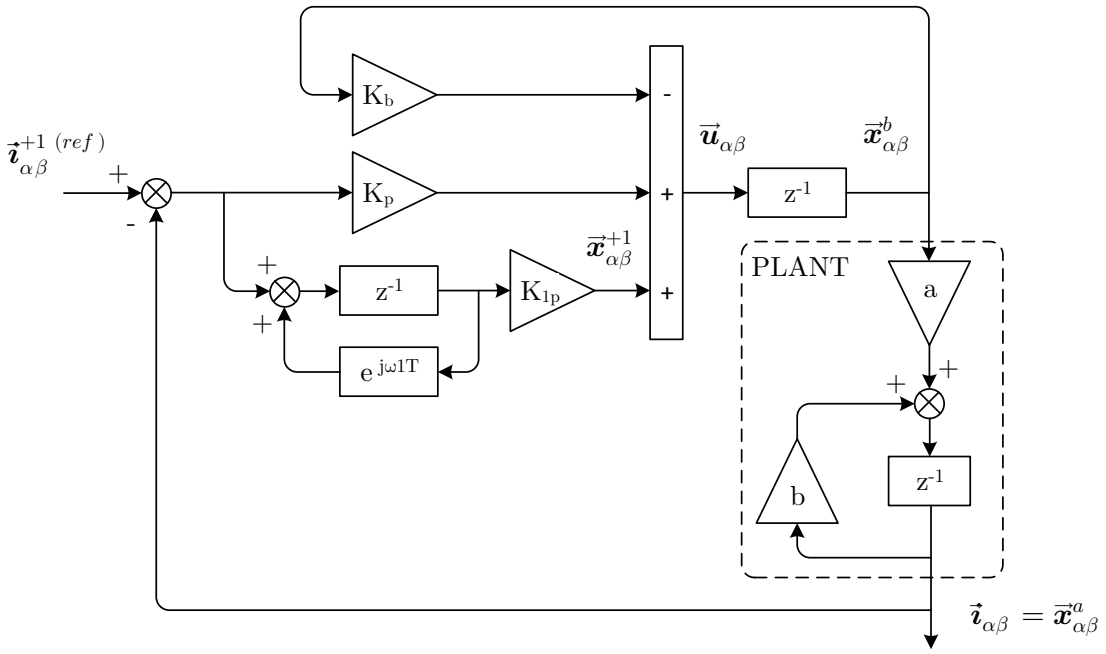

Figure 4.2. Block diagram of ROGI-based current control system

To perform full state feedback, the signal $\vec{x}^{b}$, which is the calculated voltage vector to apply at the previous instant, is included in the controller because it is an additional state of the system to stabilize. The plant model, which will be analyzed in the following, is the complex-valued version of the L-filter as it is shown in (4.2).

$$\begin{gathered} \vec{G}^{L-filter}_{\alpha\beta}(z)_{|\vec{e}_{\alpha\beta}(z)=0} = \frac{\vec{I}_{\alpha\beta}(s)}{\vec{X}^{b}_{\alpha\beta}(s)} = \frac{a}{z-b} \\ a = \frac{1 - e^{-\frac{R}{L}T}}{R} \quad b = e^{-\frac{R}{L}T} \end{gathered} \tag{4.2}$$

Considering $\vec{i}^{ref}_{\alpha\beta}$ and $\vec{e}_{\alpha\beta}$ as two external perturbations that do not affect the closed-loop stability, then the open-loop system can be described as (4.3).

$$\begin{bmatrix} \vec{x}^{b}_{\alpha\beta} \\ \vec{x}^{a}_{\alpha\beta} \\ \vec{x}^{+1}_{\alpha\beta} \end{bmatrix}_{k+1} = \underbrace{\begin{bmatrix} 0 & 0 & 0 \\ a & b & 0 \\ 0 & 1 & e^{j\omega_1 \cdot T} \end{bmatrix}}_{G} \cdot \begin{bmatrix} \vec{x}^{b}_{\alpha\beta} \\ \vec{x}^{a}_{\alpha\beta} \\ \vec{x}^{+1}_{\alpha\beta} \end{bmatrix}_{k} + \underbrace{\begin{bmatrix} 1 \\ 0 \\ 0 \end{bmatrix}}_{H} \cdot \vec{u}_{\alpha\beta} \tag{4.3}$$

The signal $\vec{u}_{\alpha\beta}$ is calculated as a linear combination of the different states $\vec{x}^{b}_{\alpha\beta}$, $\vec{x}^{a}_{\alpha\beta}$, $\vec{x}^{+1}_{\alpha\beta}$ and employing appropriate feedback gain vector $L = [K_b \quad K_p \quad K_{1p}]^T$. The closed-loop system results in (4.5) by imposing the feed-back law (4.4).

$$\vec{u}_{\alpha\beta}(k) = -L \cdot x(k) \tag{4.4}$$

$$x(k+1) = (G - H \cdot L) \cdot x(k) = G_{CL} \cdot x(k) \tag{4.5}$$

Any tool from control theory of linear systems could be used to obtain the gain vector to achieve the desired closed-loop behavior of the system. Here, the linear quadratic regulator (LQR) theory is used. This strategy frees the designer from choosing the location of the closed-loop poles and generally produces a robust closed-loop system. As the LQR theory says, L must be chosen to minimize the cost function (4.6).

$$J = \sum_{k=0}^{\infty} x^H(k) \cdot Q \cdot x(k) + R \cdot \left|\vec{u}_{\alpha\beta}(k)\right|^2 \tag{4.6}$$

Where $(\cdot)^H$ denotes transpose conjugate, $Q \in \mathbb{C}^{(2+r)\times(2+r)}$ is a Hermitian matrix (with $r = 1$), and $R \in \mathbb{R}$ denotes weighting factors. The solution is obtained by solving Riccati's algebraic equation.

The parameters from the analyzed VSC are presented in Table 4.1. Please note that the VSC output voltage amplitude must accomplish the following limit $\left|\vec{u}_{\alpha\beta}\right| < U_{DC}/\sqrt{2}$, if the power invariance transformation is carried out (Appendix B) and THSPWM is the modulation technique.

Table 4.1. 3l-DNPC-VSC parameters

Name	Symbol	Value
Filter resistor	R	9.1 $m\Omega$
Filter inductor	L	750 μH
Fundamental frequency	f_1	50 Hz
Switching frequency	f_{SW}	2.5 kHz
Sampling period	T	200 µs
Grid line-to-line voltage	e_g^{rms}	400 V_{rms}
DC-bus voltage	U_{DC}	700 V

The correct DC-bus voltage is chosen as a function of the grid voltage e_g^{rms}, because there must be enough voltage gap between them, that is, $U_{DC} > 1.2 \cdot \sqrt{2} \cdot e_g^{rms}$. This is important to get a correct power flow and transitory actuation VSC voltage.

By applying the LQR method, with $R = 10$ and $Q = diag([10 \quad 10 \quad 1])$, the following gain vector is obtained. The R and Q values are deduced by trial and error method.

$$L = [0.3700 \; + \; j \cdot 0.0094 \quad 1.5637 \; + \; j \cdot 0.0816 \quad 0.1748 \; + \; j \cdot 0.0576]^T \tag{4.7}$$

The resultant closed-loop pole/zero map is depicted in Figure 4.3. The poles are not conjugate complex because the model is complex-valued. The time response to step change in magnitude is shown in Figure 4.4. It has an over-shoot of 27 % due to the position of complex poles and the settling time is 5 ms, which could be deduced from pole modulus, around 0.814, as (4.8).

$$t_s = T \cdot \frac{\ln 0.01}{\ln |z_p|} \tag{4.8}$$

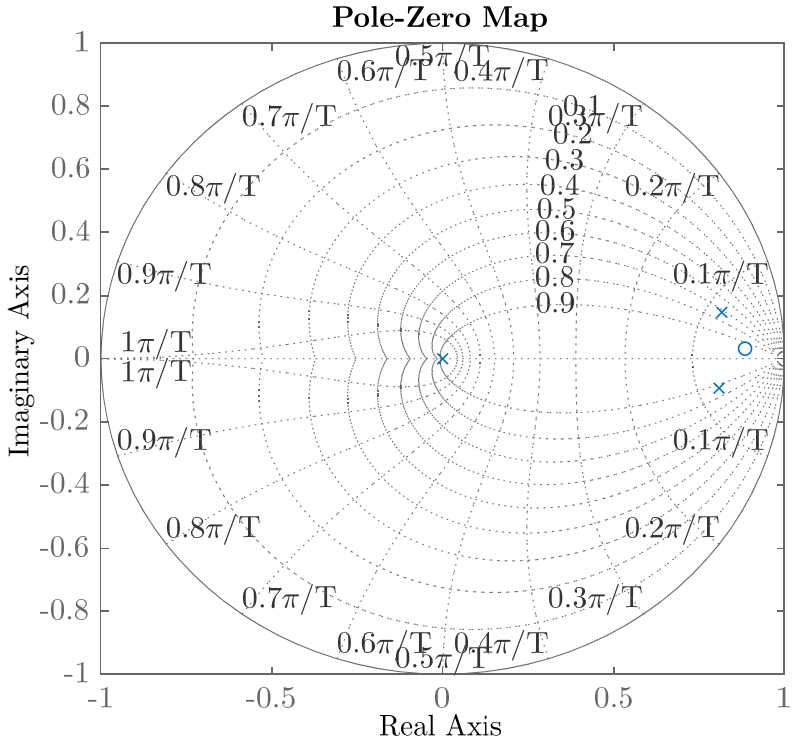

Figure 4.3. Pole-zero map of ROGI-controlled closed-loop transfer function

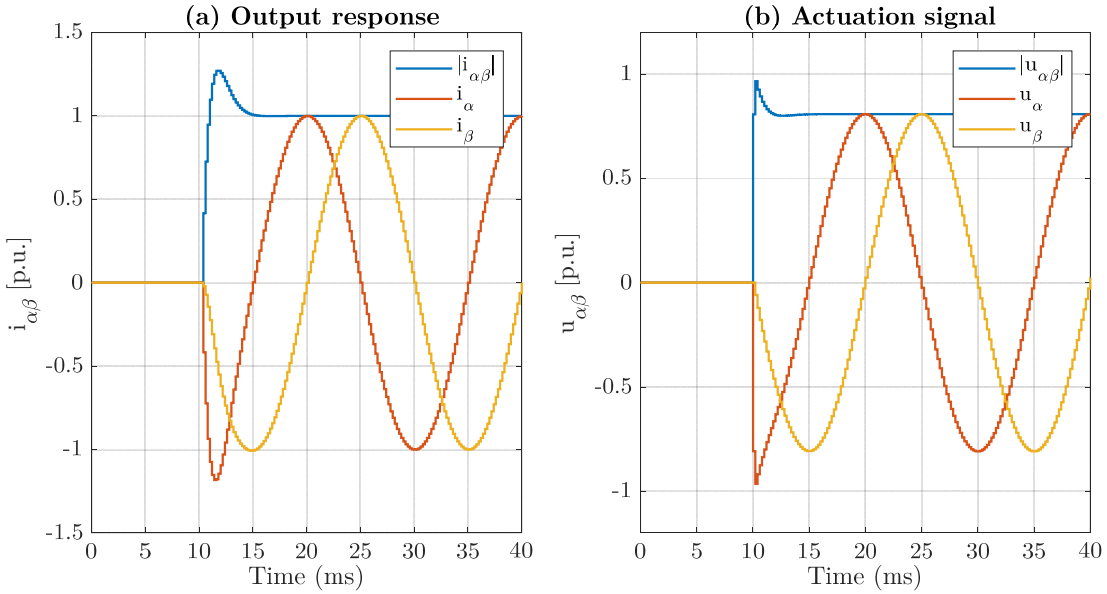

Figure 4.4. Time response of ROGI-based current control system. (a) Output current; (b) VSC voltage

Note that the actuation voltage $|\vec{u}_{\alpha\beta}|$ is normalized to its maximum value $U_{DC}/\sqrt{2}$, as it was imposed before. The voltage is close to its maximum value, so smother voltage signals could be obtained by choosing new weight for R and Q.

The reference current is set to 50 A_{rms} (active power) to test controller characteristics, but a detailed example should be carried out with active and reactive power reference to obtain the corresponding current (current reference calculation from Appendix B).

In the following, this controller will be extrapolated to multirate cases to analyze its response with different rates multipliers N.

4.2.2. Rotating reference frame

The rotating reference frame discrete time-domain model for the L-filter was deduced in subsection 3.2.5, but it is remembered here as a transfer function (4.9).

$$\begin{gathered} \vec{G}_{dq}^{Plant}(z) = \frac{1}{R + j\omega_1 \cdot L} \cdot \frac{1 - \alpha_1}{z \cdot (z - \alpha_1)} \cdot e^{-j\omega_1 \cdot T} \\ \alpha_0 = e^{-\frac{R}{L} \cdot T} \quad \alpha_1 = \alpha_0 \cdot e^{-j\omega_1 \cdot T} \\ K_S = G_{dq}^{Plant}(z = 1) = \frac{1}{R + j\omega_1 \cdot L} \cdot e^{-j\omega_1 \cdot T} \end{gathered} \tag{4.9}$$

The gain of the system under steady-state plant conditions ($G_{dq}^{Plant}(z = 1)$) is time invariant (the angular frequency of the rotating reference frame can change, but it is considered constant, ω_1, for this case) and complex-valued. Also, the location of one pole depends on the rotating reference frame frequency.

The chosen *dq*-frame controller is the one shown in [48]. Like conventional PI-based control approaches, the discrete-time domain current controller should provide a proportional and an integral control path. Besides, the controller must compensate the cross-coupling effects due to computational (unitary) delay. The proposed controller is (4.10), where can be seen that the zero z_0 is used to compensate the frequency depended system pole at α_1. This zero-pole cancellation allows a theoretically ideal decoupling of the inductive-resistive cross-coupling dynamics.

$$\begin{gathered} \vec{G}_{dq}^{c}(z) = \frac{\vec{U}_{dq}^{ref}(z)}{\vec{E}_{dq}^{error}(z)} = K_{rz} \cdot \left[\underbrace{\frac{z}{z-1}}_{integrative} - \underbrace{\frac{z_0}{z-1}}_{proportional} \right] \cdot \underbrace{e^{j\omega_1 \cdot T}}_{\substack{Delay \\ decoupling}} = \\ = K_{rz} \cdot \frac{z - z_0}{z - 1} \cdot e^{j\omega_1 \cdot T} \\ z_0 = \alpha_1 \end{gathered} \tag{4.10}$$

The complex-valued controller proportional gain K_{rz} is used to compensate the system gain for steady-state plant conditions. Considering the open-loop transfer function, the gain is calculated as (4.11). The additional real-valued factor $\gamma > 0$ is introduced to shape the command response.

$$\begin{gathered} K_{rz} = K_0 \cdot (R + j\omega_1 \cdot L) \cdot (K_1 + j \cdot K_2) \\ K_0 = \gamma \cdot \frac{1}{\alpha_0^2 - 2 \cdot \alpha_0 \cdot \cos(\omega_1 \cdot T) + 1} \\ K_1 = 1 - \alpha_0 \cdot \cos(\omega_1 \cdot T) \\ K_2 = -\alpha_0 \cdot \sin(\omega_1 \cdot T) \end{gathered} \tag{4.11}$$

The block diagram of the current controller is shown in Figure 4.5. The open-loop transfer function is obtained as (4.12), so the closed-loop control transfer function is deduced as (4.13). The example given is based on the VSC parameters from Table 4.1. Figure 4.6 depicts the pole-zero map for open and closed-loop transfer functions for $\gamma = 0.26$. From the analysis, it is deduced that the closed-loop poles are complex-conjugate.

$$G_{dq}^{OL}(z) = \frac{\gamma}{z^2 - z} \tag{4.12}$$

$$G_{dq}^{CL}(z) = \frac{\gamma}{z^2 - z + \gamma} \tag{4.13}$$

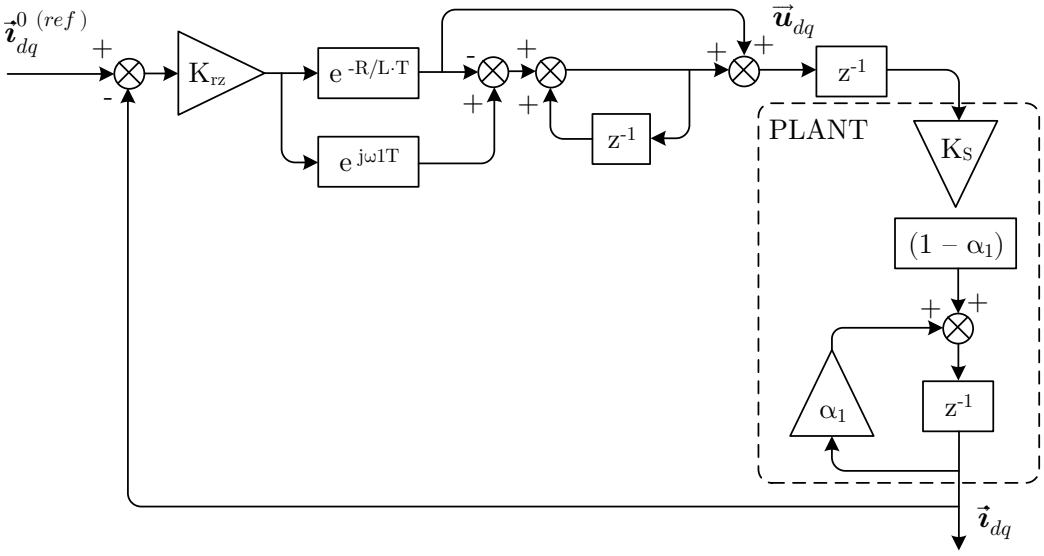

Figure 4.5. Block diagram of dq-frame complex-valued current control system

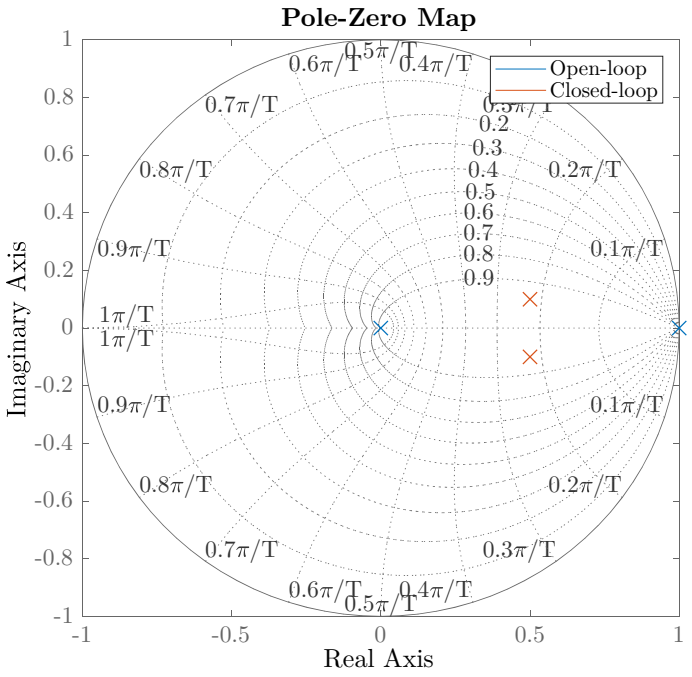

Figure 4.6. Pole-zero map of open and closed-loop transfer functions in dq-frame

Figure 4.7 represents the time response to step of *50* A_{rms} (exchange of active power, being $e_q = 0$) with $\gamma = 0.26$, so with lower values more damped response is obtained, and with greater values, more over-shoot. The over-shoot is almost zero, and the settling time is *2 ms*, which could be deduced from pole modulus, around 0.51, from (4.8). The cross-coupling effect can be seen in this figure due to the value of q component on the actuation signal. Please note, that only active power is involved in this example and the actuation signal is normalized to $U_{DC}/\sqrt{2}$.

A pole-zero cancellation controller will not be so accurate in experimental setups due to the drift in value of filter parameters. This design and models assume symmetrical distribution of inductive-resistive system parameters for d- and q-current control paths, which is usual in grid-tied applications, but they are not in salient pole synchronous machines.

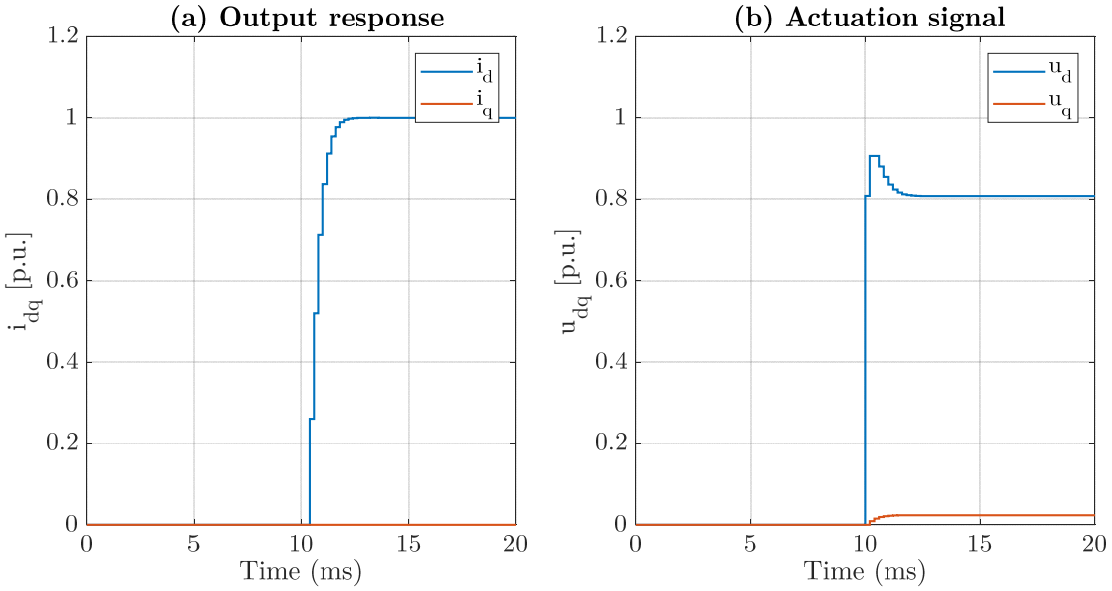

Figure 4.7. Time response of complex-valued dq-frame current control system. (a) Output current; (b) VSC voltage

4.3. Time-domain multirate analysis

4.3.1. Definitions

To analyze a multirate control system with time-domain technique there are a few steps that must be considered:

1) Modelling regulator and plant with Kranc operators. The usual Kranc operator is the ZOH-Kranc.
2) Obtaining the open-loop transfer function of regulator and plant at metaperiod T_0.
3) Obtaining the discrete pole-zero map from closed-loop transfer function.

The controller and plant internal model are obtained by means of ZOH-Kranc with the recurrence laws from 2.3.1.2. Hence, the internal representation of the plant is shown in

(4.14) and controller one in (4.15). In Figure 4.8 is shown how the controller and plant are arranged. A ZOH operation at period T is before controller and plant, and the measurement is taken every T_0 time units, so the controller input is sampled at period T but the signal changes every T_0. From the internal representations, and Kranc methodology, is deduced that the controller has one input but N outputs, whereas the plant has N inputs and one output. Please note, that the introduced situation here is the regular one, but similar deducing path might be taken for irregular cases.

Note that the vector notation is not used here to better understanding of the reader, but all variables are vectors.

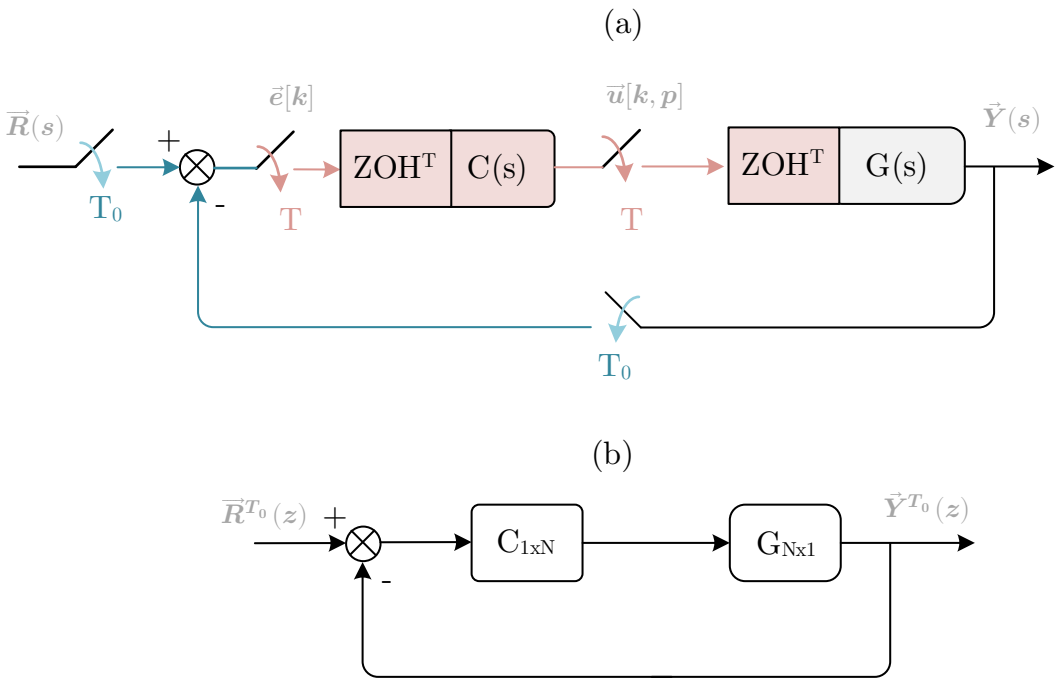

Figure 4.8. Block diagram of proposed multirate system. (a)Distribution of signals on the closed-loop; (b) Equivalent discrete closed loop at metaperiod T_0

$$\begin{aligned} x_G[(k+1)\cdot T_0] &= \bar{G}_G \cdot x_G[k\cdot T_0] + \bar{H}_G \cdot \begin{bmatrix} u[k\cdot T_0] \\ u[k\cdot T_0 + T] \\ \vdots \\ u[k\cdot T_0 + (N-1)\cdot T] \end{bmatrix} \\ y_G[k\cdot T_0] &= \bar{C}_G \cdot x_G[k\cdot T_0] + \overline{D}_G \cdot \begin{bmatrix} u[k\cdot T_0] \\ u[k\cdot T_0 + T] \\ \vdots \\ u[k\cdot T_0 + (N-1)\cdot T] \end{bmatrix} \end{aligned} \tag{4.14}$$

$$\begin{aligned} x_C[(k+1)\cdot T_0] &= \bar{G}_C \cdot x_C[k\cdot T_0] + \bar{H}_C \cdot e[k\cdot T_0] \\ \begin{bmatrix} u[k\cdot T_0] \\ u[k\cdot T_0 + T] \\ \vdots \\ u[k\cdot T_0 + (N-1)\cdot T] \end{bmatrix} &= \bar{C}_C \cdot x_C[k\cdot T_0] + \overline{D}_C \cdot e[k\cdot T_0] \end{aligned} \tag{4.15}$$

From these equations is deduced that the model is defined at metaperiod T_0, but it internally works at period T, their relationship is the multiplier N. Finally, a single-rate

system is obtained as (4.16). The pole-zero map is easily obtained from the quadruple $\left[\bar{G}_{OL}, \overline{H}_{OL}, \bar{C}_{OL}, \overline{D}_{OL}\right]$, as well as the transfer function at metapeiod T_0.

$$\begin{aligned}
\begin{bmatrix} x_C[(k+1)\cdot T_0] \\ x_G[(k+1)\cdot T_0] \end{bmatrix} &= \underbrace{\begin{bmatrix} \bar{G}_C & 0 \\ \overline{H}_G \cdot \bar{C}_C & \bar{G}_G \end{bmatrix}}_{\bar{G}_{OL}} \cdot \begin{bmatrix} x_C[k\cdot T_0] \\ x_G[k\cdot T_0] \end{bmatrix} + \underbrace{\begin{bmatrix} \overline{H}_C \\ \overline{H}_G \cdot \overline{D}_C \end{bmatrix}}_{\overline{H}_{OL}} \cdot e[k\cdot T_0] \\
y_G[k\cdot T_0] &= \underbrace{[\overline{D}_G \cdot \bar{C}_C \quad \bar{C}_G]}_{\bar{C}_{OL}} \cdot \begin{bmatrix} x_C[k\cdot T_0] \\ x_G[k\cdot T_0] \end{bmatrix} + \underbrace{[\overline{D}_G \cdot \overline{D}_C]}_{\overline{D}_{OL}} \cdot e[k\cdot T_0]
\end{aligned} \tag{4.16}$$

The transfer function is the Z-transform of the impulse response of the system. It can be expressed in terms of the state-space matrices as (4.17).

$$G_{OL}^{T_0}(z) = \frac{Y^{T_0}(z)}{R^{T_0}(z)} = \bar{C}_{OL} \cdot \left(z \cdot I - \bar{G}_{OL}\right)^{-1} \cdot \overline{H}_{OL} + \overline{D}_{OL} \tag{4.17}$$

The following sections will analyze the proposed controllers applying this multirate technique to predict the closed-loop response with constant metaperiod T_0 and different rate multipliers N.

This strategy could be followed with other control structures to obtain the single-rate equivalent at given metaperiod. It must be highlighted that the input and output of the analyzed signal path must be sampled at metaperiod to get such an equivalent.

4.3.2. Stationary reference frame

The proportional resonator ROGI-based controller presented in subsection 4.2.1 is analyzed here with this time-domain technique. The parameters for the given example VSC are in Table 4.1, but, in here, the sampling period becomes the metaperiod $T_0 = 200\ \mu s$, and the controller rate is T_0/N. Hence, the equivalent single-rate system is always at metaperiod. This gives a look on how the closed-loop poles change, if the control/actuation rate is changed to get faster, whereas the sampling rate is kept constant.

In this example, the chosen gain vector is the same as it was presented in (4.7), but other R and Q values can be taken to improve the response of the system.

Figure 4.9 depicts the pole-zero map of the closed-loop transfer function at metaperiod T_0 with every value of rate multiplier N. It is clearly seen how an extra zero appears with negative real part with $N = 2$ and it changes its location with higher N values. Besides, the pole in the origin changes its value with higher N, but it is always around it. These two changes are related to the extrapolation operation in this control structure, because with high N, the delay between closed-loop output ($\vec{\imath}_{\alpha\beta}$) and input ($\vec{\imath}_{\alpha\beta}^{*+1(ref)}$) is no longer T_0, is T_0/N, and these zero-pole changes are modelling that fractional delay.

On the other hand, the original two poles and zero near to $z = 1$ change its location towards unstable regions, so the settling time and over-shoot are worst

In Figure 4.10 is represented the bode diagram of each open-loop transfer function. The frequency responses are similar, and all of them keep the resonance in 50 Hz.

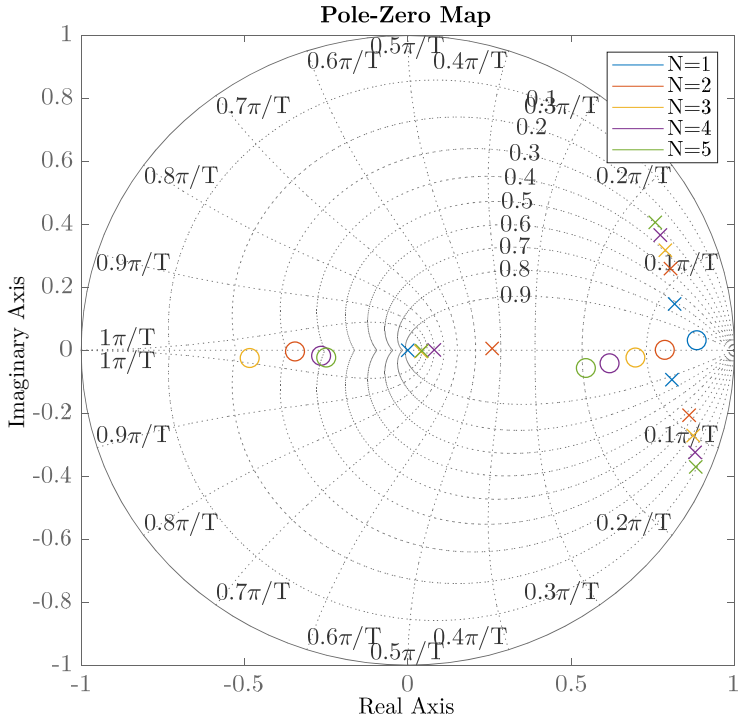

Figure 4.9. Pole-zero map of αβ-frame closed-loop transfer function at $T_0 = 200\ \mu s$

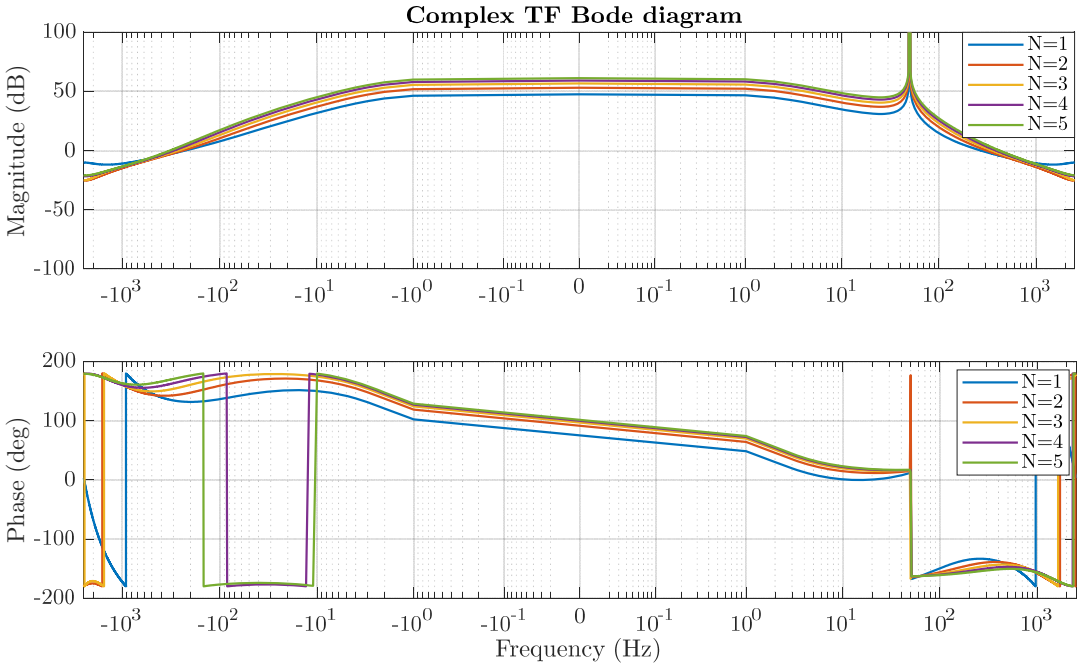

Figure 4.10. Bode diagram of αβ-frame complex-valued open-loop transfer function at $T_0 = 200\ \mu s$

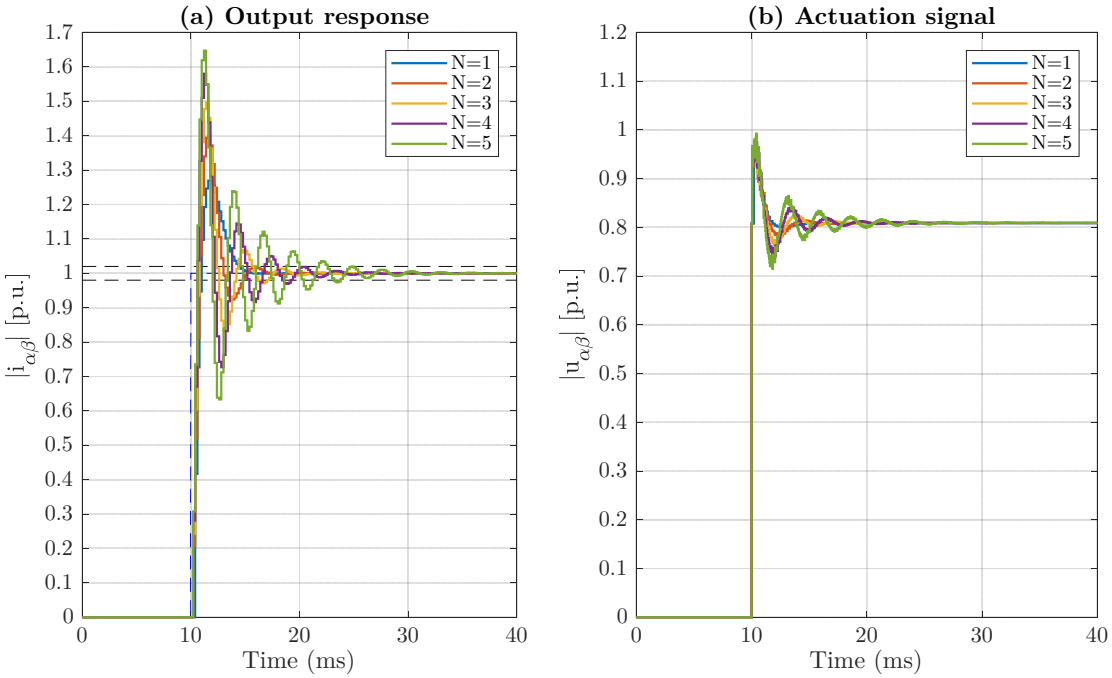

Figure 4.11. Time response of complex-valued αβ-frame current control system: (a) Output current; (b) VSC voltage

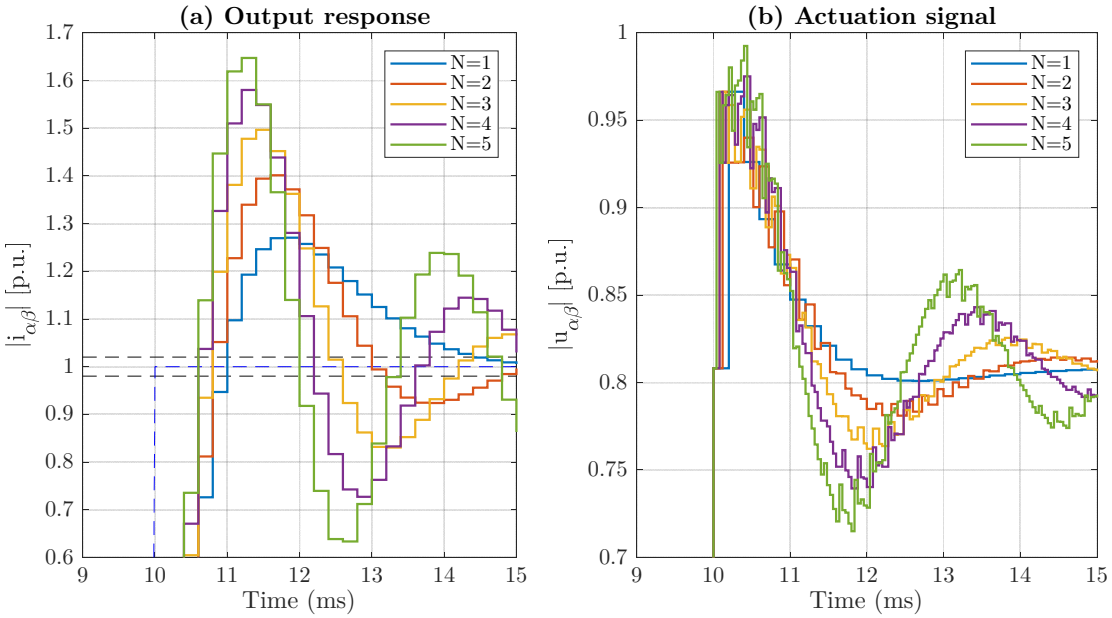

Figure 4.12. Zoom on time response of complex-valued αβ-frame current control system: (a) Output current; (b) VSC voltage

Finally, the time-response is depicted in Figure 4.11 and Figure 4.12. It is clear how the time-response gets worse with higher N. It could be consequence of the extrapolation operation that the controller carries out. In Figure 4.12(b), the actuation signal takes some incoherent values, because the error is kept constant during a T_0 period.

4.3.3. Rotating reference frame

Following the same steps as previous subsection, the *dq*-frame complex-valued controller from subsection 4.2.2 is analyzed here with this time-domain technique to get an equivalent single-rate open-loop transfer function. The VSC parameters for these results are presented in Table 4.1. The real-valued parameter γ is set to 0.26, but it could be changed to get better results.

Figure 4.13 shows how the closed-loop poles and zero change with different rate multipliers N. Again, a negative real zero appears due to multirate operation. The conjugate complex poles follow a clear pattern with higher N values.

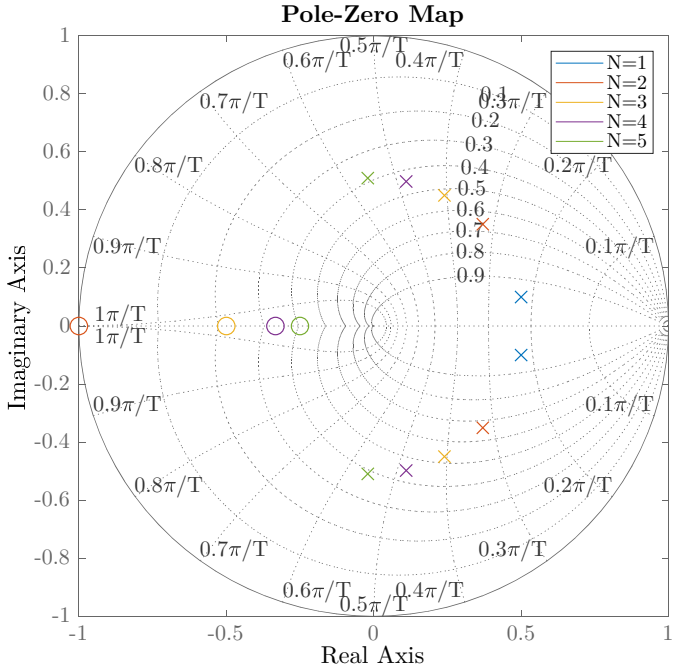

Figure 4.13. P Pole-zero map of dq-frame closed-loop transfer function at $T_0 = 200\ \mu s$

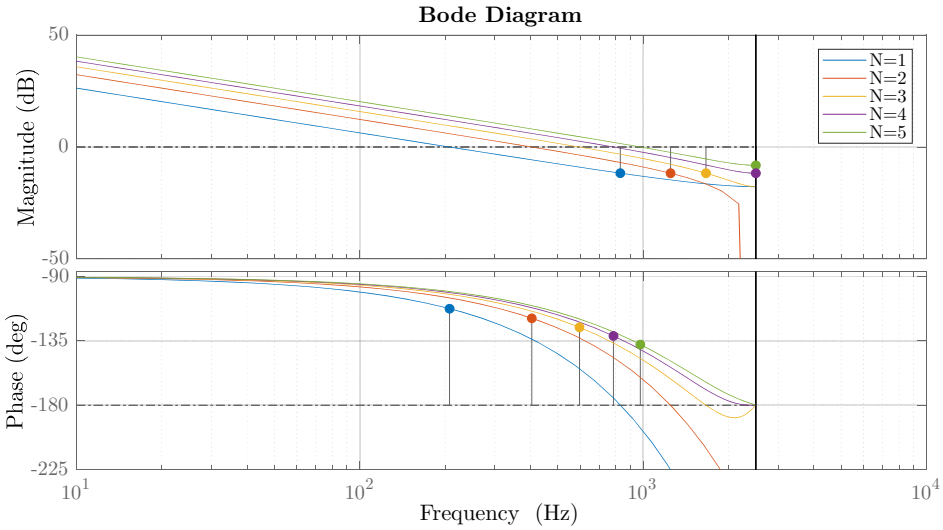

Figure 4.14. Bode diagram of dq-frame open-loop transfer function at $T_0 = 200\ \mu s$

Because of pole-zero cancelation, the obtained open-loop transfer function always has real-valued coefficients, so the Bode diagram is symmetrical, so is depicted in Figure 4.14 with positive frequencies. It can be seen how the gain margin is practically constant, but the phase margin is reduced with higher N values.

Finally, the step response is shown in Figure 4.15. As can be foreseen from the pole-zero map, with that γ, the conjugate poles change their position towards locations where the over-shoot is greater, but the settling time is nearly 2 ms in all cases. Smoother responses could be found with lower values for γ in each case, which will lead to slower systems. Besides, the actuation signal does not practically change during a metaperiod for different rate multipliers. The block that will extrapolate the sinusoidal values will be the *dq*-frame to $\alpha\beta$-frame (or directly to abc-frame) transformation that is always after the controller. Note that the actuation signal goes into overmodulation region for $N > 2$.

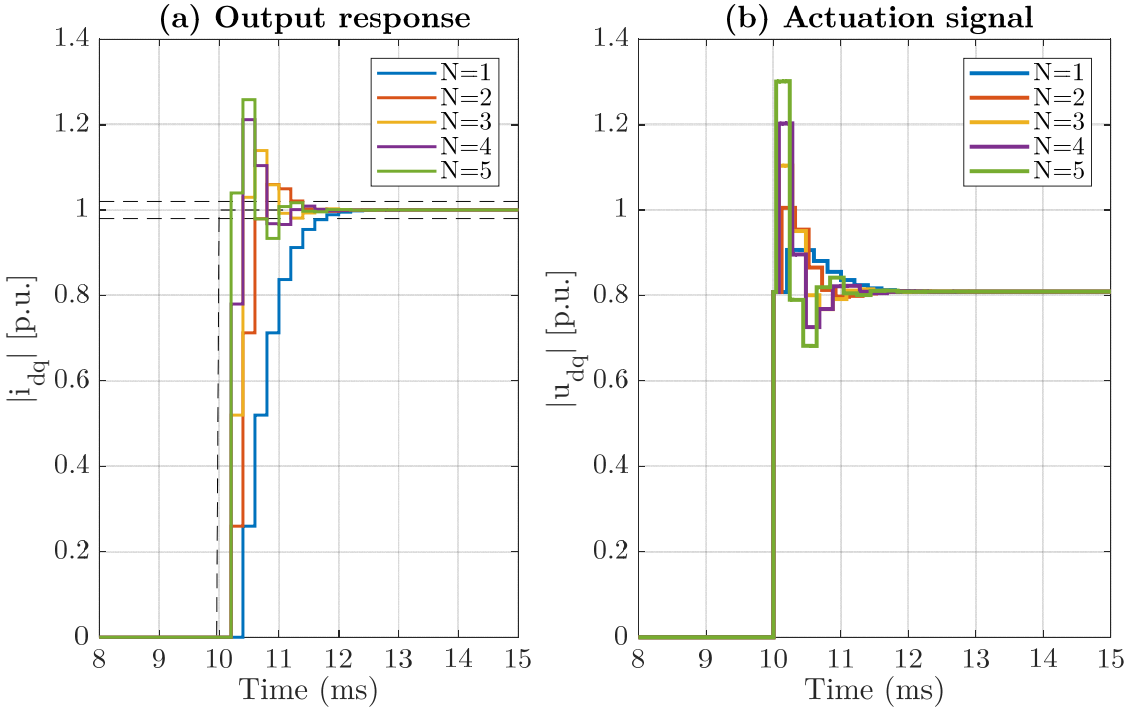

Figure 4.15. Time response of dq-frame current control system: (a) Output current; (b) VSC voltage

4.3.4. Detailed model

This section compares the previous mathematical model-based responses with the one obtained by a detailed model simulation of the VSC. That is, the simulation is carried out by Matlab Simulink using the detailed model of 3L-DNPC-VSC along with its L-filter, which is connected to the grid. To focus the analysis on the current controller response, the DC-bus is already controlled by a DC voltage source. Besides, the VSC is synchronized with the grid by means of SRF-PLL presented in Appendix C.2.3. The SRF-PLL input voltage is measured every T_0, but the phase is extrapolated for every fast rate T_0/N. The system parameters are reminded in Table 4.2, the used controllers

in Table 4.3, and the SRF-PLL controller in Table 4.4. Note that the *dq*-frame controller only needs the parameter γ, because the complex-valued static gain and the zero depend on the rate T_0/N. The power invariance transformation is the one used here for change from *abc* reference frame to $\alpha\beta$ and *dq*.

The studied responses are analyzed for a step change in active power of 20 kW, so the corresponding current is 50 A_{RMS}. The change is taken place when the VSC is already synchronized (forcing $e_d = 0$).

The responses, in the stationary $\alpha\beta$ reference frame, are presented in Figure 4.16(a), whereas the correspondent actuation signals are in Figure 4.16(b). Note that the responses are almost identical, as it is shown in Figure 4.12.

Table 4.2. VSC parameters for multirate time-domain analysis in detailed model

Name	Symbol	Value
Filter resistor	R	9.1 $m\Omega$
Filter inductor	L	750 μH
Fundamental frequency	f_1	50 Hz
Switching frequency	f_{SW}	$1/(\mathrm{T}_0/N \cdot 2)$
Sampling period	T_0	200 µs
Grid line-to-line voltage	e_g^{rms}	400 $\mathrm{V}_{\mathrm{rms}}$
DC-bus voltage	U_{DC}	700 V

Table 4.3. Controllers parameters for multirate time-domain analysis in detailed model

Name	Symbol	Value
Full-state feedback controller in $\alpha\beta$-frame		
Delay state constant	K_b	$0.3705 + j0.0094$
Proportional constant	K_p	$1.5661 + j0.819$
Integral constant 1st harmonic	K_{1p}	$0.1748 + j0.0575$
Complex-valued PI in *dq*-frame		
Real-valued factor	γ	0.26

Table 4.4. SRF-PLL parameters

Name	Symbol	Value
Proportional constant	K_p	918.5474
Integral constant	K_I	$3.8683 \cdot 10^5$

Figure 4.17 shows the responses for the rotating *dq* reference frame. The over-shoot is lower than expected in Figure 4.15, but the actuation signal is very similar. This results from the overmodulation region where the actuation signal transitorily enters. The settling time is 2 *ms,* as expected.

These results correlate the mathematical expression with the detailed model in simulation. Hence, the performance of that system is not affected by parasitic perturbances.

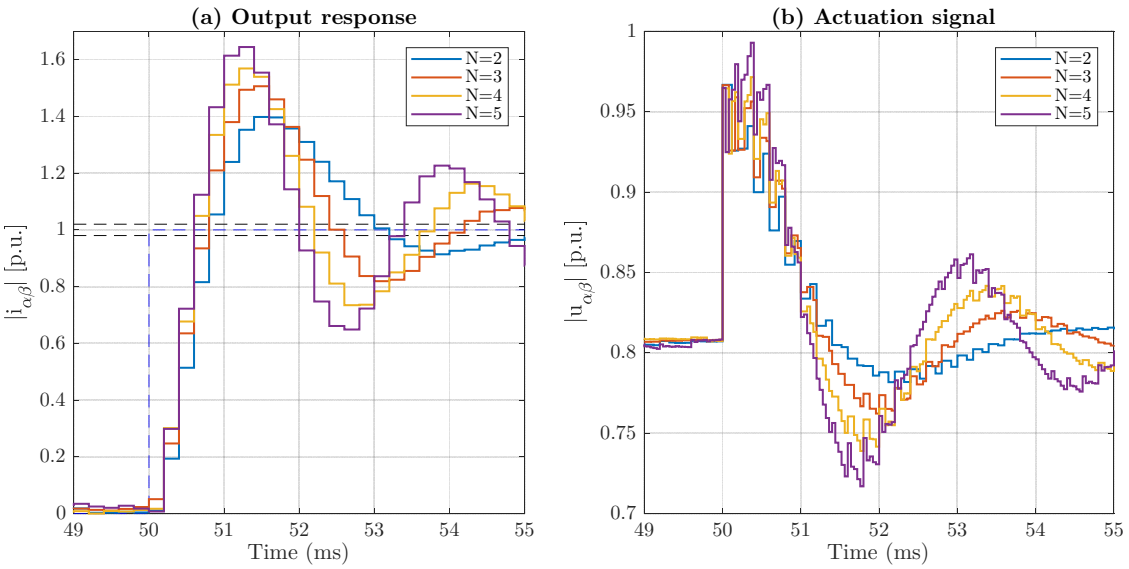

Figure 4.16. Time response of detailed system in αβ-frame: (a) Output current; (b) VSC voltage

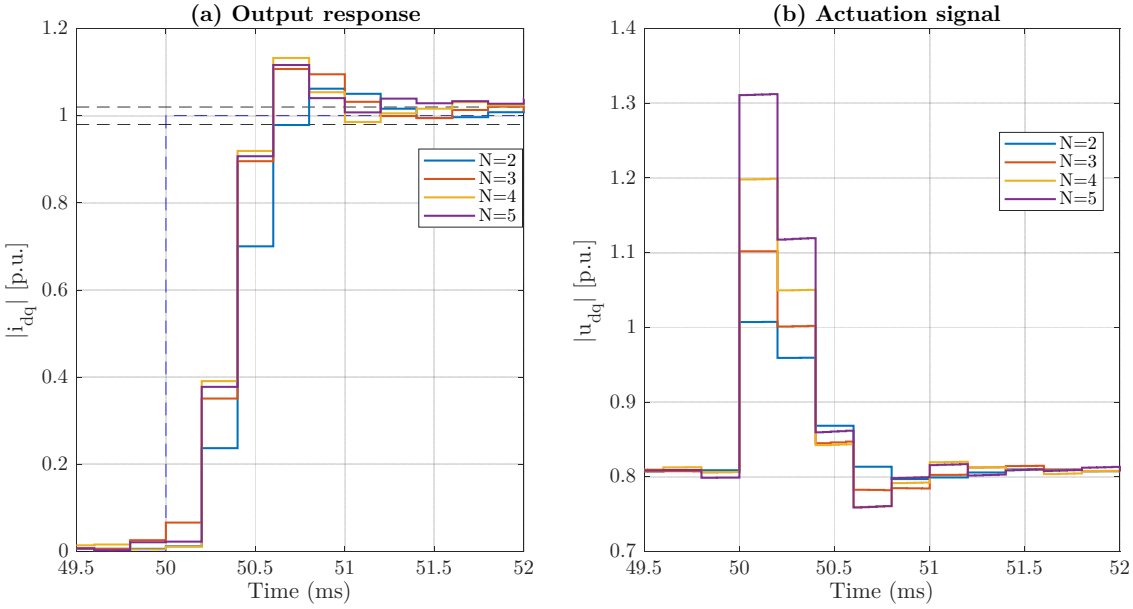

Figure 4.17. Time response of detailed system in dq-frame: (a) Output current; (b) VSC voltage

4.3.5. Discussion

From the previous analysis, it can be realized that this is not the correct way to operate with multirate applications, but it gives the right analysis tool when this path is taken due to hardware or software constraints. The feedback signal is sampled at slow rate, but the controller operates at fast rate, so the extrapolation is carried out by the controller, which structure is related to its design at single-rate situation. On one hand, the LQR design does not fit well to redesign this multirate case in $\alpha\beta$-frame. On the other hand, the real-valued parameter γ allows the redesign of the multirate case, if

it is reduced to get more damped responses. Therefore, advanced techniques must be considered to correctly calculate the extrapolated values of the actuation signal.

However, the use of the IR representation gives a powerful tool to analyze several control structures, and this control loops can extrapolate de actuation signal, although it does not get better transitory responses.

4.4. Model-based multirate controller

4.4.1. Definitions

From the previous analysis is deduced that other approach must be taken to analyze VSCs where the data acquisition is more constrained in time than the PWM actuator. Hence, the multirate controller must be correctly designed and, to do so, the steps given in [14] and [31] are followed here. Basically, the controller design is model-based and depends on the input that is tracked, so two alternatives are given for the L-filter model: $\alpha\beta$-frame (sinusoidal inputs); and dq-frame (continuous inputs). The controller is composed of two parts, each one at different rate, and the control target is to reach similar performances to those the faster single-rate controller would achieve. This design strategy is based on the ER presented in 2.3.2.

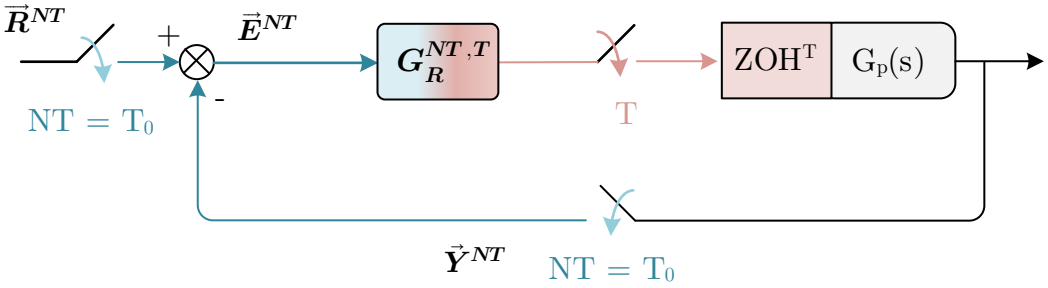

Figure 4.18. Block diagram of model-based multirate control approach

In the following, NT will be the slow rate (metaperiod T_0) and T will be the fast rate, where N is the rate multiplier, which is assumed to be an integer. The considered control loop is presented in Figure 4.18. The plant is the corresponding to each reference frame transformation of an L-filter, so it is a complex-valued SISO (Single-Input Single-Output) and LTI system. Its input is regularly sampled at fast rate T, and its output is sampled at slow rate NT to be fed back. The multirate controller, $G_R^{NT,T}$, is designed to get error signal at slow rate NT and to obtain N control actions upon the plant in each metaperiod NT.

In the following, to better understanding in notation, the signals are not represented with vector form, but all of them are vectors and the transfer functions might be complex-valued. It is consequence from the reference frame that it is used for representing three-phase VSC controlled system. All conclusions are valid for vector signals. Also, for clear representation of z variable at each rate, the fastest rate (T) Z-transform will take directly $z = z_N$, whereas the slow rate (NT) will take $z^N = z_N^N$.

4.4.1.1. Basic multirate operations

The 'skip' (down-sampling) and 'expand' (up-sampling) operations must be considered for transformations between periods. If the *Z*-transform referred to period NT is defined as:

$$Y^{NT} \triangleq \mathcal{Z}_{NT}\{y[k]\} = \sum_{k=0}^{\infty} y[k \cdot NT] \cdot z^{-k \cdot N} \tag{4.18}$$

it can be expressed that:

- Expand operator creates a T-sequence from a NT-sequence, introducing (N-1) zero-valued samples, as follows:

$$\begin{gathered} [Y^{NT}(z^N)]^T \triangleq \bar{Y}^T(z) \triangleq \sum_{k=0}^{\infty} \bar{y}[k \cdot T] \cdot z^{-k} \\ \begin{cases} \bar{y}[k \cdot T] = y[k \cdot T] & \forall k = \lambda N \\ \bar{y}[k \cdot T] = 0 & \forall k \neq \lambda N \end{cases} \quad \lambda \in Z^+ \end{gathered} \tag{4.19}$$

- Skip operator creates a NT-sequence from a T-sequence, as follows:

$$[Y^T(z)]^{NT} \triangleq \bar{Y}^{NT}(z^N) \triangleq \sum_{k=0}^{\infty} \bar{y}[k \cdot NT] \cdot z^{-k \cdot N} = Y^{NT}(z^N) \tag{4.20}$$

Some known skip-expand properties used here are the following:

1) The skip operation does not commutate.

$$[X^T(z)Y^T(z)]^{NT} \neq [X^T]^{NT}[Y^T]^{NT}(z^N) \tag{4.21}$$

2) The expand commutes.

$$[X^{NT}(z^N)Y^{NT}(z^N)]^T = [X^{NT}]^T[Y^{NT}]^T(z^N) \tag{4.22}$$

3) Skip operation to different original rate signals.

$$[X^T(z)[Y^{NT}]^T(z)]^{NT} = [X^T]^{NT} \cdot Y^{NT}(z^N) \tag{4.23}$$

The operator $[\cdot]^T$ (applied to a system) is defined as the *Z*-transform of the T-period discretized impulse response of that system.

4.4.1.2. Plant

The continuous-time domain plant $G_p(s)$, discretized at slow rate, is defined as G_p^{NT} (discretized with ZOH at period NT, so the numerator and denominator are $z^{-i \cdot N}$), whereas at fast rate is G_p^T (discretized with ZOH at period T, so the numerator and denominator are polynomials in z^{-i}).

$$G_p^{NT}(z^N) = \frac{B_p^{NT}(z^N)}{A_p^{NT}(z^N)} = \frac{Y^{NT}(z^N)}{U^{NT}(z^N)} \quad G_p^T(z) = \frac{B_p^T(z)}{A_p^T(z)} = \frac{Y^T(z)}{U^T(z)} \tag{4.24}$$

When a system is regularly sampled with a fast rate at the input, but slow rate at the output, the polynomial $W(z_N)$ is used to obtain a dual-rate expression of the plant. The polynomial is remembered here as (4.25), being n the plant order.

$$W_A^T(z) = \frac{\prod_{i=1}^{n}(z^N - \alpha_{i,NT})}{\prod_{i=1}^{n}(z - \alpha_{i,T})} = \frac{[A^{NT}(z^N)]^T}{A^T(z)} = \frac{\bar{A}(z^N)}{A^T(z)} = \\ = \prod_{i=1}^{n}(z^{N-1} + \alpha_{i,T} \cdot z^{N-2} + \cdots \alpha_{i,T}^{N-1}) \tag{4.25}$$

The transfer function pole at slow rate and fast rate are $\alpha_{i,NT}$ and $\alpha_{i,T}$, respectively. Besides, it is seen that:

$$[A^{NT}(z^N)]^T = W_A^T(z) \cdot A^T(z) \tag{4.26}$$

From the previous, the fast sampling discrete time model can be expressed as (4.27).

$$G_p^T(z) = \frac{B_p^T(z)}{A_p^T(z)} = \frac{B_p^T(z) \cdot W_A^T(z)}{A_p^T(z) \cdot W_A^T(z)} = \frac{\widetilde{B}_p^T(z)}{[A_p^{NT}(z^N)]^T} = \frac{Y^T(z)}{U^T(z)} \tag{4.27}$$

Therefore, from (4.27), it can be deduced the relationship (4.28), and making a skip operation to the T-sequences, that is resampling at NT, the result is (4.29).

$$\widetilde{B}_p^T \cdot U^T = [A_p^{NT}]^T \cdot Y^T \tag{4.28}$$

$$\left[\widetilde{B}_p^T \cdot U^T\right]^{NT} = [[A_p^{NT}]^T \cdot Y^T]^{NT} \rightarrow \left[\widetilde{B}_p^T \cdot U^T\right]^{NT} = A_p^{NT} \cdot [Y^T]^{NT} \tag{4.29}$$

The $\left[\widetilde{B}_p^T \cdot U^T\right]^{NT}$ is indivisible because the skip operation does not commutate. The opposite situation is feasible, that is, the transformation of a slow rate discrete time sequence into a fast rate sequence. The dual rate operator that carries out this situation depends on the input signal. For example, for step signals is used the dual-rate ZOH (DRZOH) that is shown in (4.30).

$$[H_{NT}(s)]^T = \frac{U_H^T}{[U^{NT}]^T} = \left[\frac{1 - e^{-NT \cdot s}}{s}\right]^T = \frac{1 - z_N^{-N}}{1 - z_N^{-1}} = \left(1 + z_N^{-1} + \cdots + z_N^{-(N-1)}\right) \\ [H_{NT}(s)]^T = W_R^T \tag{4.30}$$

Therefore, it is likely to get the following transfer function of the plant with DRZOH (4.31).

$$Y^T = [U^{NT} H_{NT} G_p(s)]^T = [U^{NT}]^T [H_{NT} G_p(s)]^T \tag{4.31}$$

If (4.30) is known, it is found the relationship (4.32). Then, the dual-rate discrete time operator is defined as (4.33), where $G_p^{NT,T}$ is a transfer function from an expanded slow input (NT) to a fast output (T).

$$[H_{NT} G_p(s)]^T = W_R^T [H_T G_p(s)]^T \tag{4.32}$$

$$\tilde{G}(z, N) = G_p^{NT,T} = \frac{Y^T}{[U^{NT}]^T} = W_R^T G_p^T = W_R^T \cdot \frac{B_p^T}{A_p^T} = W_R^T \cdot \frac{B_p^T W_A^T}{A_p^T W_A^T} = W_R^T \cdot \frac{\widetilde{B}_p^T}{[A_p^{NT}]^T} \tag{4.33}$$

Thus, the sampled output with period NT is obtained from the previous as (4.34), which is the slow sampled discrete time model.

$$\left[\frac{Y^T}{[U^{NT}]^T}\right]^{NT} = \frac{[Y^T]^{NT}}{[[U^{NT}]^T]^{NT}} = \frac{[Y^T]^{NT}}{U^{NT}} = \frac{\left[W_R^T \widetilde{B}_p^T\right]^{NT}}{\left[[A_p^{NT}]^T\right]^{NT}} = \frac{B_p^{NT}}{A_p^{NT}} \tag{4.34}$$

This relationship helps to understand expand and skip operations on model-based multirate controller design.

4.4.1.3. Closed-loop multirate control

The block diagram depicted in Figure 4.18 lead to the detailed version in Figure 4.19. This multirate control scheme, or dual-rate controller, is composed by slow and fast parts, that are connected by an expand or up-sampling operation and a rate converter.

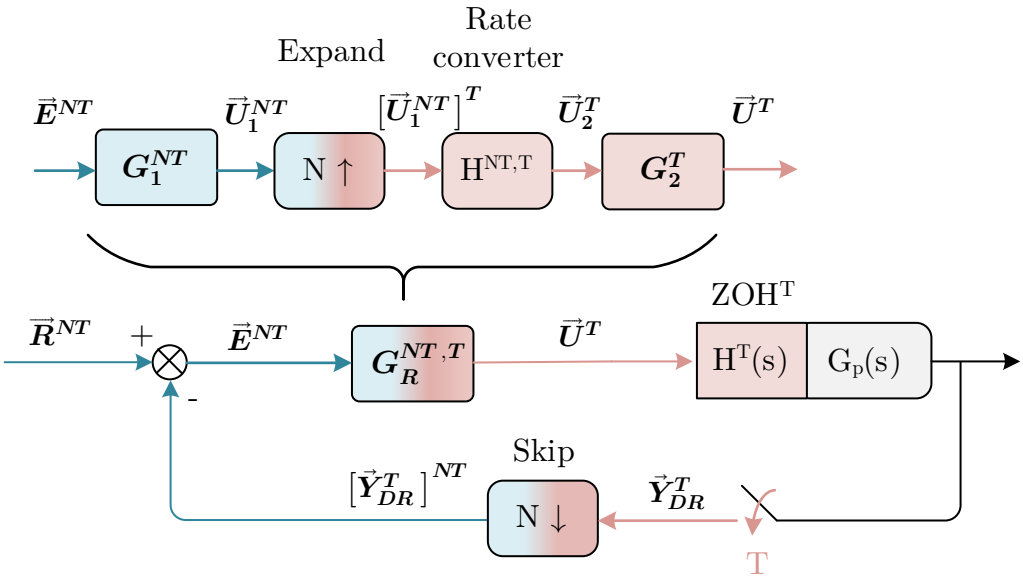

Figure 4.19. Block diagram of the MRIC

The output of multirate controlled system is (4.35), which is proven by combining (4.36) and (4.37).

$$Y_{DR}^T = G_p^T G_R^{NT,T}[R^{NT} - [Y_{DR}^T]^{NT}]^T = G_p^T \underbrace{G_2^T H^{NT,T}[G_1^{NT}]^T}_{G_R^{NT,T}}[R^{NT} - [Y_{DR}^T]^{NT}]^T \quad (4.35)$$

$$Y_{DR}^T = G_p^T U^T \quad U^T = G_R^{T,NT}[E^{NT}]^T \quad (4.36)$$

$$\begin{gathered}[U_1^{NT}]^T = [G_1^{NT} E^{NT}]^T = [G_1^{NT}]^T [E^{NT}]^T \\ U^T = G_2^T H^{NT,T}[U_1^{NT}]^T = G_2^T H^{NT,T}[G_1^{NT}]^T [E^{NT}]^T \\ E^{NT} = R^{NT} - [Y_{DR}^T]^{NT}\end{gathered} \quad (4.37)$$

4.4.1.4. Controller design

For a given continuous time plant, $G_p(s)$, a continuous-time controller is designed (it is directly designed in discrete time, then transformed to continuous domain), $G_R(s)$, to obtain the closed-loop transfer function $M(s)$. If the discrete time closed-loop transfer function at each rate are M^T and M^{NT} with their respective controller, the design goal is to obtain a multirate controller with similar response to that at fast rate, T, from a slow sampling, NT, of system output.

Considering (4.35) and the equivalence $Y_{DR}^T \equiv M^T R^T$, the dual-rate controller $G_R^{NT,T}$ is obtained as (4.39), where a fast and slow part can be identified.

$$Y_{DR}^T = G_p^T G_R^{NT,T}[R^{NT} - [M^T R^T]^{NT}]^T \equiv M^T R^T \quad (4.38)$$

$$G_R^{NT,T} = \underbrace{\frac{M^T R^T}{G^T}}_{Fast\ part} \cdot \underbrace{\frac{1}{[R^{NT} - [M^T R^T]^{NT}]^T}}_{Expanded\ slow\ part} \tag{4.39}$$

If the fast-skipped output response and the slow single-rate loop output should match (4.40), then (4.42) is found.

$$[Y_{DR}^T]^{NT} = [Y^T]^{NT} = Y^{NT} = M^{NT} R^{NT} \tag{4.40}$$

$$\begin{aligned} Y_{DR}^T = G_p^T G_R^{NT,T} [R^{NT} - Y^{NT}]^T = G_p^T G_R^{NT,T} ([R^{NT}]^T - [Y^{NT}]^T) = \\ = G_p^T G_R^{NT,T} ([R^{NT}]^T - [M^{NT} R^{NT}]^T) = \ G_p^T G_R^{NT,T} [R^{NT}]^T (1 - [M^{NT}]^T) = M^T R^T \end{aligned} \tag{4.41}$$

$$G_R^{NT,T} = \underbrace{\frac{M^T}{G_p^T}}_{G_2^T} \cdot \underbrace{\frac{R^T}{[R^{NT}]^T}}_{H^{NT,T}} \cdot \underbrace{\frac{1}{1 - [M^{NT}]^T}}_{[G_1^{NT}]^T} \tag{4.42}$$

Then the controller is composed of:

- Fast part:

$$G_2^T(z) = \frac{M^T(z)}{G_p^T(z)} \tag{4.43}$$

- Slow part:

$$G_1^{NT}(z^N) = \frac{1}{1 - M^{NT}(z^N)} \tag{4.44}$$

- Rate converter:

$$H^{NT,T}(z) = \frac{R^T(z)}{[R^{NT}]^T(z)} \tag{4.45}$$

The following statements about these results must stand out:

1) For steps changes in reference, it achieves the same discrete-time response as fast single-rate controller, $G_R^T(z)$, does, but some ripple could eventually appear. This ripple is avoided, if the fast part $G_2^T(z)$ is changed by taking $M_R^T(z)$ as given by (4.46) instead of $M^T(z)$, but the response does not match the fast single-rate controlled plant response. The intersampling ripple could appear depending on $G_p^T(z)$ numerator roots. If the fast controller is taken as (4.47) the dual-rate controller $G_R^{NT,T}(z)$ does not cancel the numerator of the process transfer function, avoiding the ripple, but the matching $Y_{DR}^T = Y^T$ does not hold.

$$M_R^T(z) = \frac{Y_R^T(z)}{R^T(z)} = \frac{G_p^T(z) G_R^T(z)}{1 + G_p^T(z) G_R^T(z)} \tag{4.46}$$

$$G_2^T(z) = \frac{M_R^T(z)}{G_p^T(z)} = \frac{G_R^T(z)}{1 + G_p^T(z) G_R^T(z)} \tag{4.47}$$

2) The reference input defines the rate converter $H^{NT,T}(z)$, which is basically defined as an extrapolator block. For step reference inputs, the DRZOH (4.48) is enough, because it replies the sample N-1 times at fast rate. Although for sinusoidal signals, there is not such a transfer function, but the reference frame

transformation in (4.49) can be used. This sinusoidal extrapolation takes the vector amplitude and signal phase θ_1 is extrapolated. First the signal in stationary reference frame is transformed into rotating reference frame at slow rate, NT, then it is transformed back to the stationary reference frame at fast rate, T. Due to its unique implementation, the expand operation is only involved to correctly implement the DRZOH in the rate change on the rotating reference frame (4.50). Please note that the vector notation is expressed here to connect with the mission of this document, without losing generality of all previous analysis.

$$H^{NT,T}(z) = \frac{R^T(z)}{[R^{NT}]^T(z)} = \frac{1-z^{-N}}{1-z^{-1}} \tag{4.48}$$

$$\vec{R}^T_{\alpha\beta}[k\cdot NT + p\cdot T] = \underbrace{\vec{R}^{NT}_{\alpha\beta}[k\cdot NT]\cdot e^{-j\cdot\theta_1[k\cdot NT]}}_{Rotating-frame\ (\left[\vec{R}^{NT}_{dq}\right]^T\cdot\vec{H}^{NT,T})} \cdot \underbrace{e^{j\cdot\theta_1[k\cdot NT+p\cdot T]}}_{Stationary-frame} \tag{4.49}$$
$$k\in\mathbb{N}$$
$$p = 0,1,2,\ldots,N-1$$

$$\vec{H}^{NT,T}(z) = \frac{\vec{R}^T_{dq}(z)}{\left[\vec{R}^{NT}_{dq}\right]^T(z)} = \frac{1-z^{-N}}{1-z^{-1}} \tag{4.50}$$

3) In general, the stability margins of the dual-rate (DR) controlled system are between those of the slow and fast single-rate discrete-time schemes [31].
4) If the plant is non-minimum phase, the cancelation of unstable pole-zero pairs must be avoided. If that is done, $G_2^T(z)$ is computed as (4.47). If $G_1^{NT}(z^N)$ is maintained, the output does not match the output predicted by the closed loop transfer function. However, if M_R^{NT} is computed by using (4.51), the response will follow the fixed one by M_R^T.

$$[M^T R^T]^{NT} = M^{NT} R^{NT} \tag{4.51}$$

5) This approach works for unstable plants, as far there is not pole cancellation in (4.43), which is avoided by using (4.47) instead.
6) The controller is usually designed in discrete-time and its equivalent in continuous-time is found to apply this technique. For sinusoidal signals there is an inherent $T/2$ (or $NT/2$) delay on the transfer function Z-transform due to ZOH operator, as it was analyzed in Chapter 2. Instead applying ZOH method, the bilinear transform (Tustin's method) can be used to convert a s-domain transfer function to z-domain. The transform preserves stability and maps every point of the frequency response of the continuous-time transfer function to a corresponding point in the frequency response of the discrete-time transfer function, although to a somewhat different frequency, and this is called frequency warping. When designing a digital filter as an approximation of a continuous-time filter, the frequency response (both amplitude and phase) of the digital filter can be designed to match the frequency response of the continuous filter at a specified frequency ω_0 (resonant frequency, or in this case, the fundamental frequency that is controlled, ω_1). The Tustin's transform with pre-warping is (4.52).

$$s \leftarrow \frac{\omega_0}{\tan\left(\frac{\omega_0 T}{2}\right)} \cdot \frac{z-1}{z+1} \tag{4.52}$$

7) The input-output stability is ensured because controller is designed to match some given responses and possible ripple is avoided. However, the robustness of the result should be analyzed, as any other control design approach based on (partial) model cancellation. The system internal stability requires that none of the four functions (4.53) should have unstable poles. In the multirate setting, this is achieved by implementing (4.47).

$$\underbrace{\left(1+G_p(s)G_R(s)\right)^{-1}}_{Sensitivity\ (S)} \quad S(s)G_R(s) \quad S(s)G_p(s) \quad G_R(s)S(s)G_p(s) \tag{4.53}$$

4.4.2. Stationary reference frame

This subsection takes the parameters in Table 4.1, and obtains the corresponding $\alpha\beta$-frame MRIC with a specified rate multiplier N. In this occasion, the chosen gain vector (4.54) is obtained with $R = 1$ and $Q = diag([2.8 \quad 2.8 \quad 0.3] \cdot 10^{-3})$ for the fast single-rate system with parameters in Table 4.1.

$$K = [0.0832 \ + \ j \cdot 0.0026 \quad 0.3235 \ + \ j \cdot 0.0204 \quad 0.0112 \ + \ j \cdot 0.0113] \tag{4.54}$$

Following the steps on previous section, the MRIC controller could be obtained for whatever N multiplier. This technique is based on comparing the single-rate fast controlled system response with the one obtained with MRIC controller, which slowest rate part has a period NT. Firstly, a numerical example is given to describe each step. This example keeps constant $T = 200\ \mu s$ and the output current is sampled with NT period, where $N = 2$. The controller has the gains K described by (4.54). The controller with rate T is (4.55) and the plant at the same rate is (4.56). Please note that the delay, that is its feedback state, is included in the plant model.

$$G_R^T(z) = \frac{(0.3235 + j \cdot 0.02041) \cdot z - (0.3104 + j \cdot 0.02936)}{z - (0.998 + j \cdot 0.06279)} \tag{4.55}$$

$$G_p^T(z) = \frac{0.2663}{z^2 - (0.9144 - j \cdot 0.002619) \cdot z - (0.08299 + j \cdot 0.002613)} \tag{4.56}$$

Therefore, to obtain the slow part of the controller, (4.55) and (4.56) are converted to the s-domain, separately. Applying the feedback law, the closed-loop transfer function is found as (4.57).

$$M(s) = \frac{-(449.4 + j1174)s^2 + (4.3 + j6.34) \cdot 10^6 s + (18.82 + j5.12) \cdot 10^8}{s^3 + (1.19 + j1.40) \cdot 10^4 \ s^2 + (9.34 + j2.62) \cdot 10^6 \ s + (19.41 + j4.65) \cdot 10^8} \tag{4.57}$$

The poles (p) and zero (z) of $M(s)$ are (4.58), where it is clearly seen that the system is stable, and it has a non-minimum phase zero. Notice that due to the complex-valued definition of transfer function in this system, the complex poles are not conjugate.

$$\begin{array}{ll} p_1 = -(1.15 + j1.43) \cdot 10^4 & z_1 = (6.12 - j1.55) \cdot 10^3 \\ p_2 = -210.21 + j399.25 & z_2 = -189.14 + j156.47 \\ p_3 = -218.16 - j99.68 & \end{array} \tag{4.58}$$

Then, the closed-loop transfer function with NT period is (4.59).

$$\begin{aligned} M^{NT}(z^N) &= \frac{num}{z^6 - (1.17 - j0.18)z^4 - (0.32 + j0.51)z^2 + (0.52 + j0.32)} \\ num &= (19.16 - j8.61) \cdot 10^{-3} z^6 + (11.49 + j4.37) \cdot 10^{-2}\ z^4 - \\ &\quad -(7.06 - j3.63) \cdot 10^{-3} z^2 - (10.28 + j4.86) \cdot 10^{-2} \end{aligned} \tag{4.59}$$

Thus, taking (4.44), the slow part of the controller is (4.60), whereas the fast part is obtained as (4.61) taking (4.47) to ensure stable response, although it will not match the designed one at fast rate.

$$\begin{aligned} G_1^{NT}(z^N) &= \frac{num}{z^6 - (1.31 - j0.16)z^4 - (0.33 + j0.52)z^2 + (0.64 + j0.37)} \\ num &= (1.02 - j0.009)z^6 - (1.19 - j0.203)z^4 - \\ &\quad -(0.337 + j0.522)z^2 + (0.53 + j0.317) \end{aligned} \tag{4.60}$$

$$\begin{aligned} G_2^{T}(z) &= \frac{num}{z^3 - (1.912 + j0.0602)z^2 + (0.9159 + j0.0576)z} \\ num &= (0.324 + j0.0204)z^3 - (0.606 + j0.047)z^2 + \\ &\quad +(0.257 - j0.0235)\ z + (0.0257 + j0.0032) \end{aligned} \tag{4.61}$$

The rate converter is implemented as explained in (4.49). Responses are depicted in Figure 4.20, and detailed one in Figure 4.21, with a reference step of 50 A_{rms} (active power, forcing $e_q = 0$). The actuation signal and the output response practically follow the response imposed by the fast single-rate controller, which is the design goal.

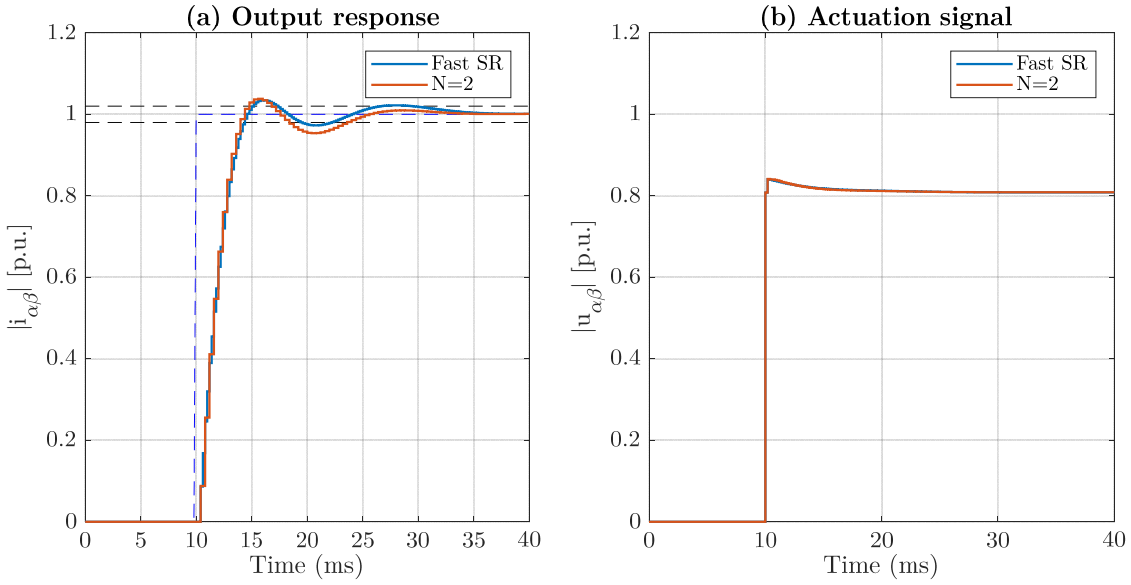

Figure 4.20. MRIC response (N=2) compared to the single-rate (SR) fast controlled system for αβ-frame

The responses differ due to the application of (4.47) to ensure stability. However, the differences are minimum, because the over-shoot is approximately equivalent, and the settling time is a few *ms* lower.

Figure 4.22 depicts the responses with high N values. From this figure is deduced that the response gets worse, but it has a clear explanation: the output is sampled in a very low rate NT, and extrapolation is carried out by the controller. Nevertheless, the

actuation signal is not excessively high, the over-shoot is approximately increased by 4%, and the settling time is almost equal.

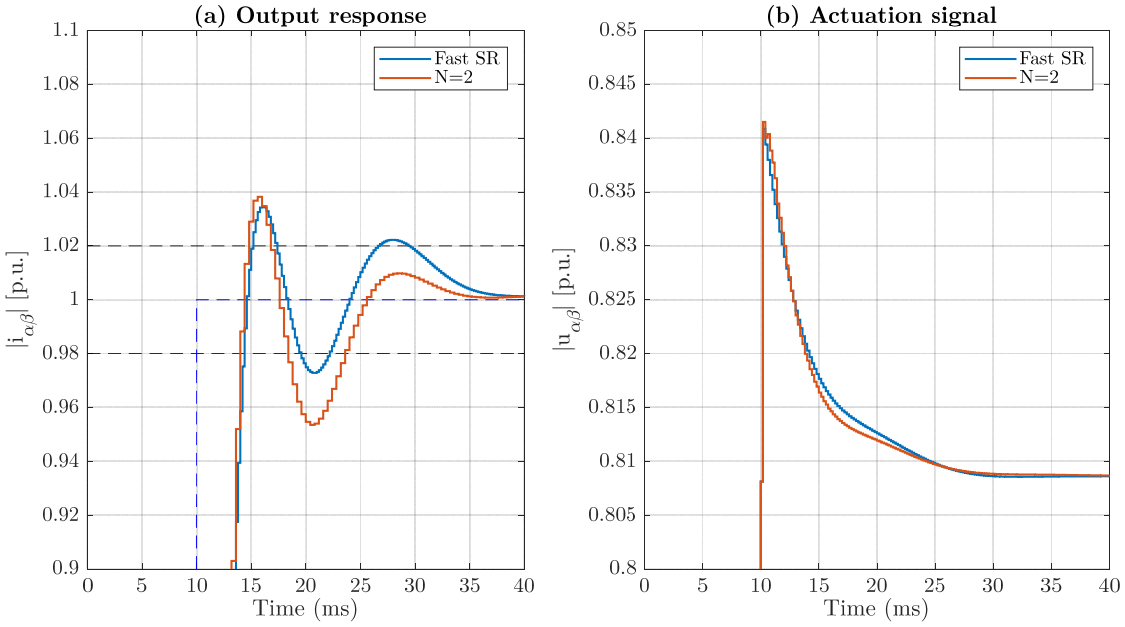

Figure 4.21. Detailed MRIC response (N=2) compared to the single-rate (SR) fast controlled system for αβ-frame

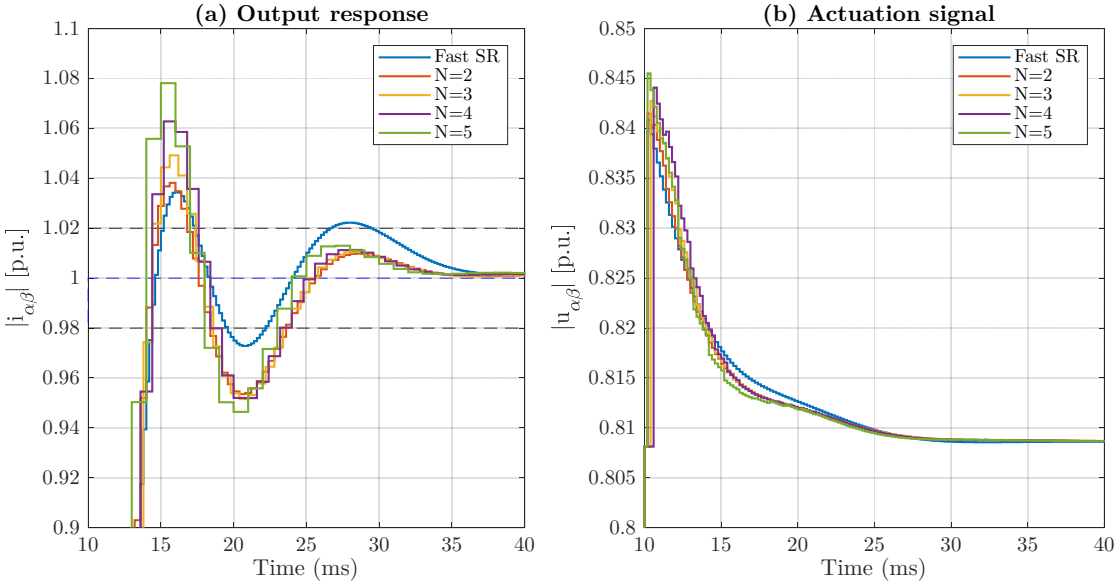

Figure 4.22. MRIC response with different values of N compared to the single-rate fast controlled system for αβ-frame

The stability margins of the MRIC controlled system are between those of the slow and fast single-rate discrete-time schemes. The fast single-rate discrete-time stability is ensured, but the one corresponding to the slow single-rate discrete-time system depends on N. If the NT period for that controller is excessively slow, the system could be unstable. To analyze this situation, pole-zero map of $M_R^{NT}(z^N)$ is examined for different values of N in Figure 4.23. In this case $M_R^{NT}(z^N)$ is taken as (4.62), where

$G_R^{NT}(z^N)$ has the same gain vector (4.54) that was obtained for $G_R^T(z)$. Besides, the pole-zero map is only shown for comparison purposes, but note that the z variable is z^N for every N. From this representation, the system is unstable for $N > 12$.

$$M_R^{NT}(z^N) = \frac{Y_R^{NT}(z^N)}{R_R^{NT}(z^N)} = \frac{G_p^{NT}(z^N)G_R^{NT}(z^N)}{1 + G_p^{NT}(z^N)G_R^{NT}(z^N)} \tag{4.62}$$

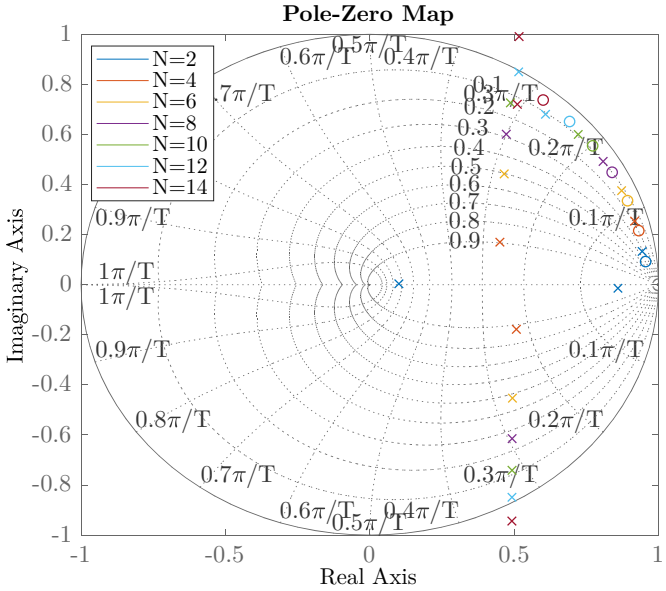

Figure 4.23. Pole-zero map of $M_R^{NT}(z^N)$ for αβ-frame

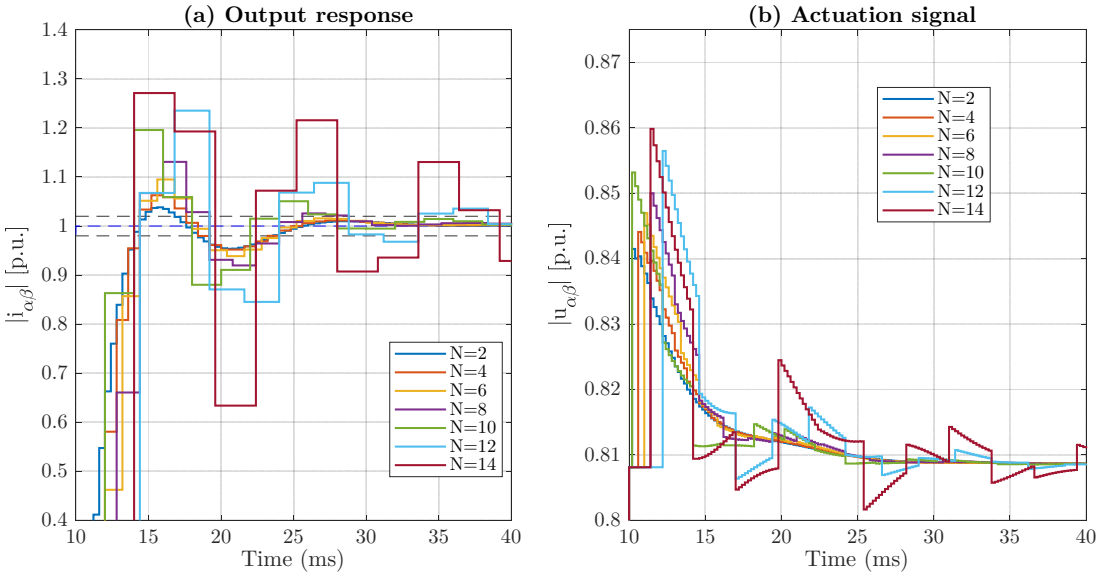

Figure 4.24. MRIC response with high N values for αβ-frame

However, the MRIC has stable response for $N = 14$ as depicted in Figure 4.24, but it has large oscillations. Although the MRIC becomes unstable for $N = 16$, the stability is only ensured for $N < 12$. Also, that rate multiplier means that the 50 Hz signal is sampled every $N \cdot T = 2.4\ ms$, so there are only 8 samples per signal period, which is highly dangerous, because every sinusoidal signal is usually sampled at least 10 times

every signal period (the theoretical limit is set by Nyquist criterion on 2 samples per signal period). Hence, the rate multiplier, N, limit is on $N \leq 10$.

4.4.3. Rotating reference frame

This subsection presents the MRIC in dq-frame, using the single-rate controller presented in 4.2.2. The parameters are in Table 4.1, where the actuation signal $T = 200\ \mu s$ is the fastest rate in the system, and the sampling rate of the output current is changed by rate multiplier N, so the sampling period is NT. The tuning parameter to shape the system response is chosen as $\gamma = 0.2868$.

First, a numerical example is given to analyze its transfer functions and response. This example set $N = 2$, and the controller with period T is (4.63) and plant with same period is (4.64). Please note that the delay is included in the plant model.

$$G_R^T(z) = \frac{(1.072 + j0.1013)z - (1.074 + j0.3373)}{z - 1} \tag{4.63}$$

$$G_p^T(z) = \frac{(0.2651 - j0.02506)}{z^2 - (0.9956 - j0.06264)z} \tag{4.64}$$

Therefore, to obtain the slow part of the controller, $M_R^T(z)$ (obtained though (4.63) and (4.64)) is converted to the s-domain, so the closed-loop transfer function is found as (4.65). The transfer function only has real value coefficients, so the pole-zero cancellation is already applied (non-conjugate complex pole cancellation). Two different paths have been taken here and previous subsection to prove that $M(s)$ can be obtained by either of them.

$$M(s) = \frac{-1652s + 1.31 \cdot 10^7}{s^2 + 6245s + 1.31 \cdot 10^7} \tag{4.65}$$

The poles (p) and zero (z) of $M(s)$ are (4.66), where it is clearly seen that the system is stable, and it has a non-minimum phase zero.

$$\begin{aligned} p_1 &= (-3.1224 + j1.8317) \cdot 10^3 \\ p_2 &= (-3.1224 - j1.8317) \cdot 10^3 \end{aligned} \quad z_1 = 7.933 \cdot 10^3 \tag{4.66}$$

Then, the closed-loop transfer function with NT period is (4.67).

$$M^{NT}(z^N) = \frac{0.2868z^2 + 0.3691}{z^4 - 0.4264z^2 + 0.08225} \tag{4.67}$$

The slow part of the controller is (4.68) from (4.44), whereas the fast part is obtained as (4.68) taking (4.47) to ensure stable response, although it will not match the designed one at fast rate.

$$G_1^{NT}(z^N) = \frac{z^4 - 0.4264z^2 + 0.08225}{z^4 - 0.7132z^2 - 0.2868} \tag{4.68}$$

$$G_2^T(z) = \frac{(1.072 + j0.1013)z^2 - (1.074 + j0.03373)z}{z^2 - z + 0.2868} \tag{4.69}$$

The rate converter is implemented as (4.70), or also by an equivalent obtained from (3.51) with $H_{1\times N}^C(z)$.

$$H^{NT,T}(z) = \frac{z^2 - 1}{z^2 - z} \tag{4.70}$$

Responses are depicted in Figure 4.25 with a reference step of 50 A_{rms} (active power, forcing $e_q = 0$). The actuation signal and the output response exactly follow the imposed response by the fast single-rate controller, which is the design goal despite of applying expression (4.47). Regardless of the feedback signal is sampled every NT, the actuation signal is like the one obtained with fast SR controlled system. Hence, this MRIC system gets extraordinary results.

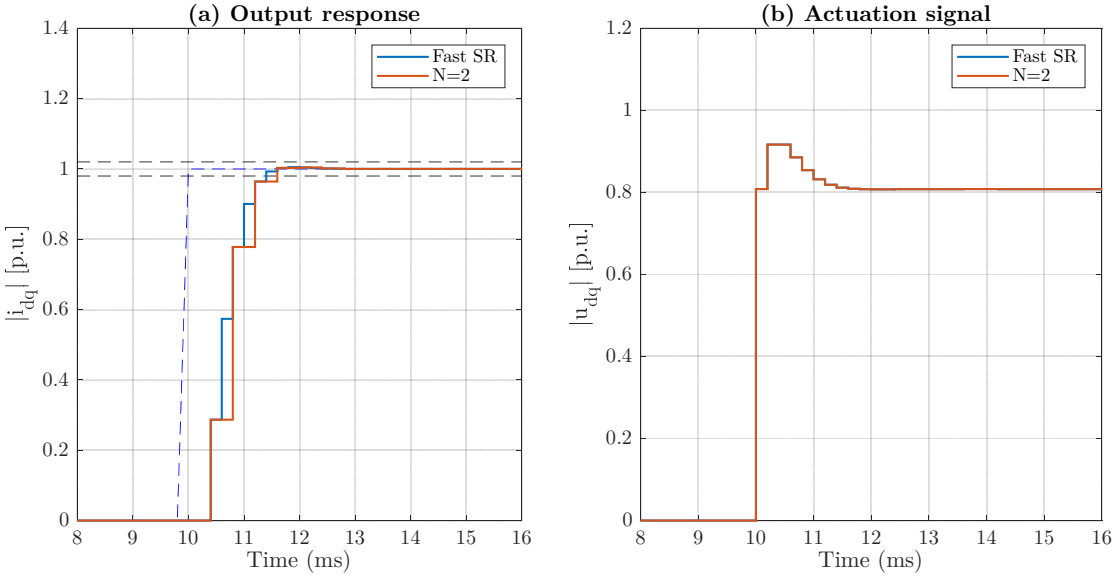

Figure 4.25. MRIC response (N=2) compared to the single-rate (SR) fast controlled system for dq-frame

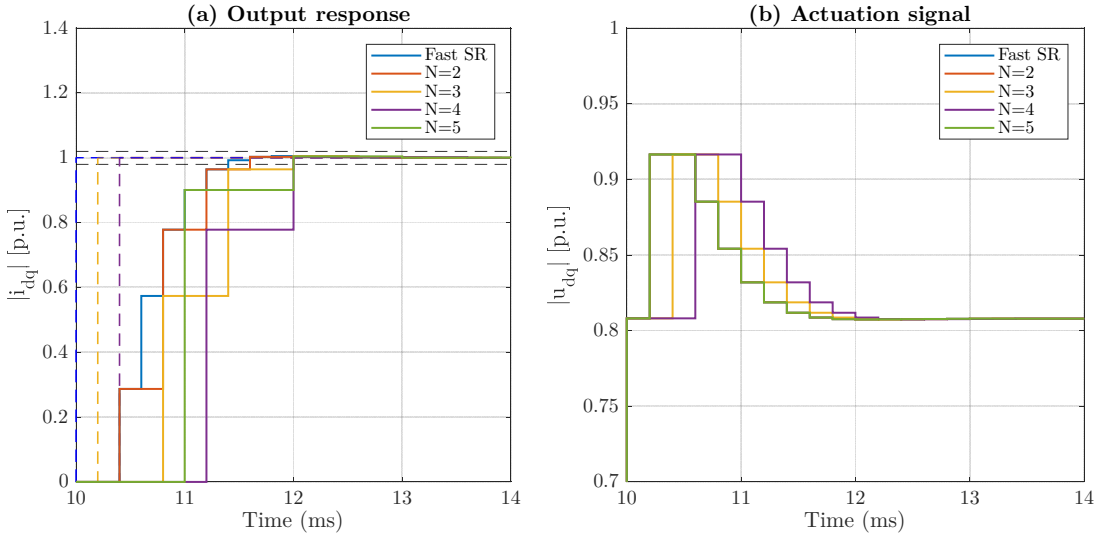

Figure 4.26. MRIC response with different values of N for dq-frame

Figure 4.26 shows the responses with higher N values. For $N = 3$ and $N = 4$ the output response seems to be delayed. If the step is given in an instant between NT sampling periods, the reference will be delayed. Hence, if the step instant is at the

beginning of the simulation, that is, instant 0, the response is exactly equivalent, as is shown in Figure 4.27.

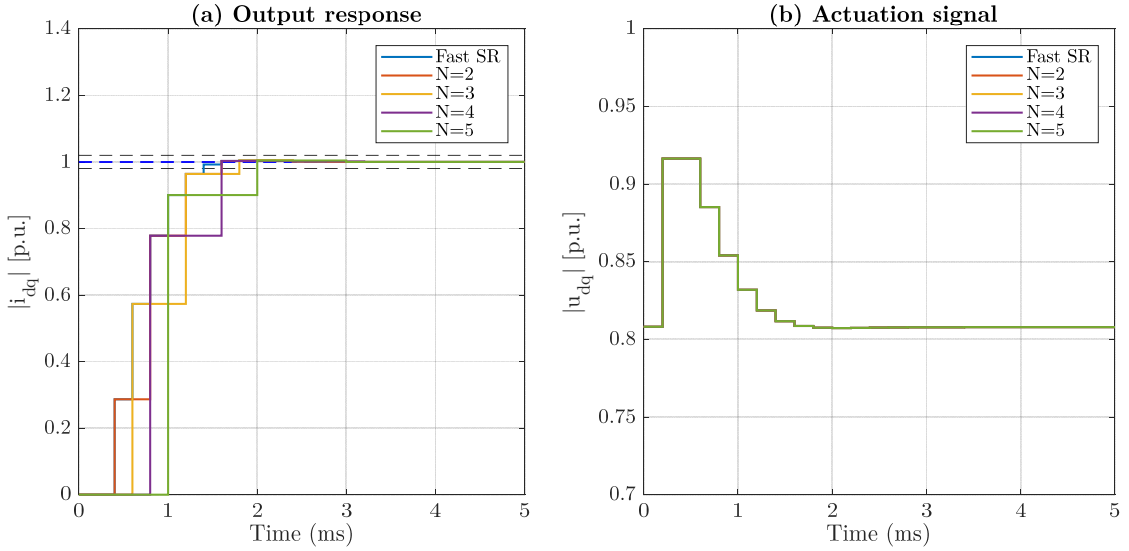

Figure 4.27. MRIC controlled dq-frame system response with different values of N and step instant placed in 0 ms

The stability could be analyzed again by taking $M_R^{NT}(z^N)$. If the pole-zero cancellation controller is correctly implemented, the closed-loop transfer function always has the expression (4.71). Therefore, the system will be stable as long the parameter γ is correctly selected.

$$M_R^{NT}(z^N) = \frac{\gamma}{z^{2N} - z^N + \gamma} \tag{4.71}$$

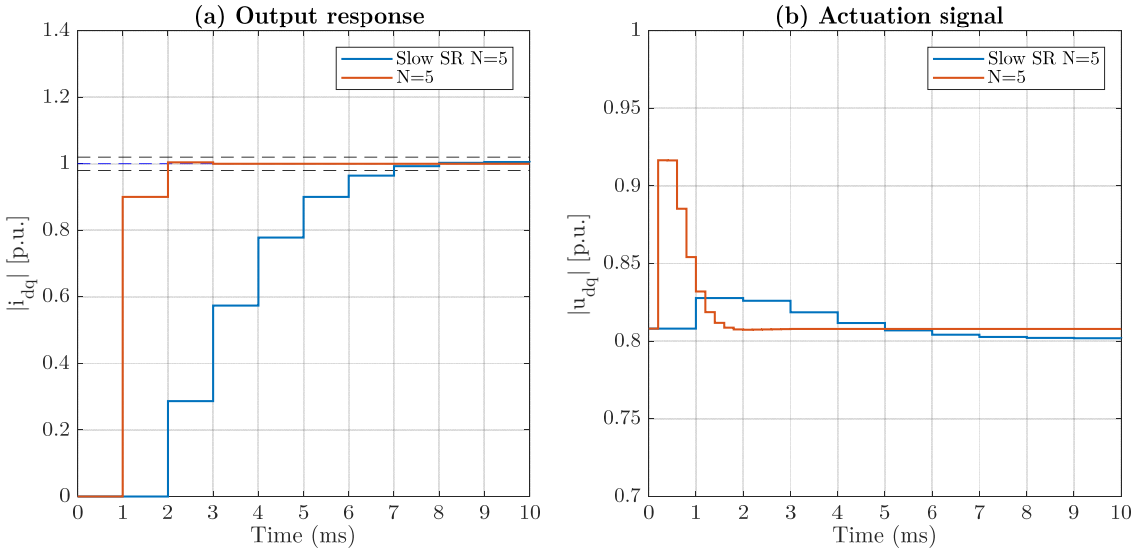

Figure 4.28. Comparison of slow single-rate (SR) response to the one with MRIC controlled dq-frame system

However, the signal converted to *dq*-frame has a frequency of 50 Hz, so, as it was previously indicated, the signal must have at least 10 samples at each signal period. Then the limit rate multiplier is $N \leq 10$.

From Figure 4.27 is deduced that MRIC controllers has a great potential in quick responses. For example, with $N = 5$ the current matches the reference in 3 samples. In Figure 4.28, the MRIC controlled system response is compared to the one obtained with M_R^{NT}, being $N = 5$ and $\gamma = 0.2868$. To get such quick responses, the system needs great actuation signals, so MRIC controller provides better actuation values.

Finally, to transform the actuation signal from dq-frame to $\alpha\beta$-frame, the algorithm requires that the phase would be also extrapolated, or obtained through a PLL working at fast rate T. The second approach is taken on this analysis, although this MRIC approach can also be followed in the PLL system, but it will be analyzed in the future.

4.4.4. Detailed model

This section compares the previous mathematical model-based responses with the one obtained by a detailed model simulation of the VSC. That is, the simulation is carried out by Matlab Simulink using the detailed model of 3L-DNPC-VSC along with its L-filter, which is connected to the grid. To focus the analysis on the current controller response, the DC-bus is already controlled by a DC voltage source. Besides, the VSC is synchronized with the grid by means of SRF-PLL presented in Appendix C.2.3. The SRF-PLL input voltage is measured every T seconds. The system parameters are reminded in Table 4.5, the used controllers in Table 4.7, and the SRF-PLL controller in Table 4.6. Note that the dq-frame controller only needs the parameter γ, because the complex-valued static gain and zero depend on the rate T, that is, the designed fast-rate controller. The power invariance transformation is the used one here for change from abc reference frame to $\alpha\beta$ and dq.

The studied responses are analyzed for a step change in active power of 20 kW, so the corresponding current is 50 A_{RMS}. The change is taken place when the VSC is already synchronized (forcing $e_d = 0$).

Table 4.5. VSC parameters for multirate time-domain analysis in detailed model

Name	Symbol	Value
Filter resistor	R	9.1 $m\Omega$
Filter inductor	L	750 μH
Fundamental frequency	f_1	50 Hz
Fast rate	T	200 μs
Switching frequency	f_{SW}	2.5 kHz
Sampling period	NT	$N \cdot T$
Grid line-to-line voltage	e_g^{rms}	400 V_{rms}
DC-bus voltage	U_{DC}	700 V

Table 4.6. SRF-PLL parameters

Name	Symbol	Value
Proportional constant	K_p	918.5474
Integral constant	K_I	$3.8683 \cdot 10^5$

Table 4.7. Controllers parameters for multirate time-domain analysis in detailed model

Name	Symbol	Value
Full-state feedback controller in $\alpha\beta$-frame		
Delay state constant	K_b	$0.0837 + j0.0026$
Proportional constant	K_p	$0.3235 + j \cdot 0.0204$
Integral constant 1st harmonic	K_{1p}	$0.0112 + j \cdot 0.0113$
Complex-valued PI in *dq*-frame		
Real-valued factor	γ	0.2868

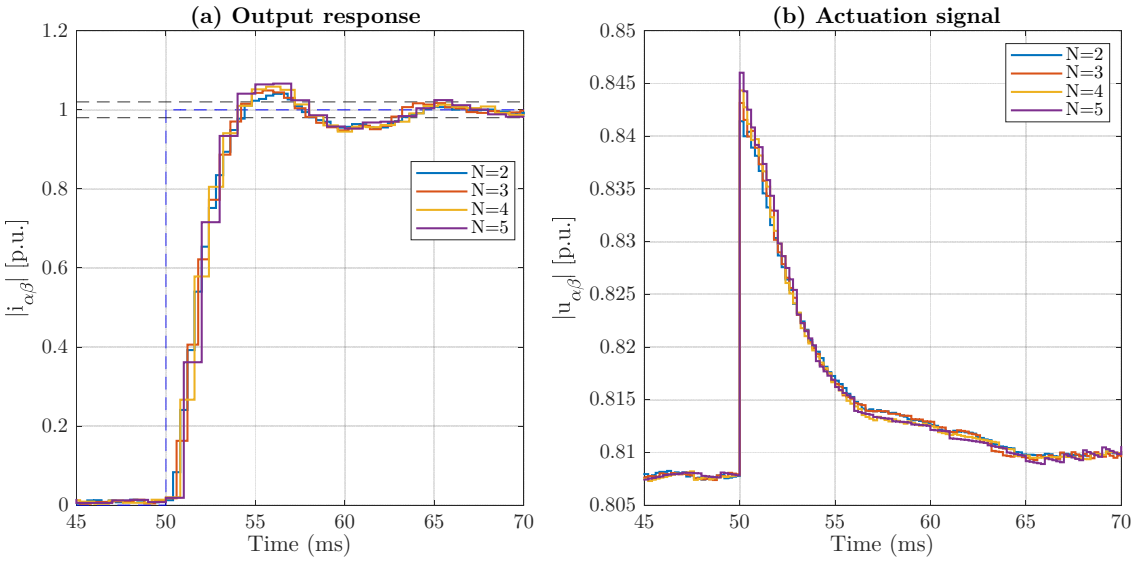

Figure 4.29. Time response of detailed MRIC system in $\alpha\beta$-frame: (a) Output current; (b) VSC voltage

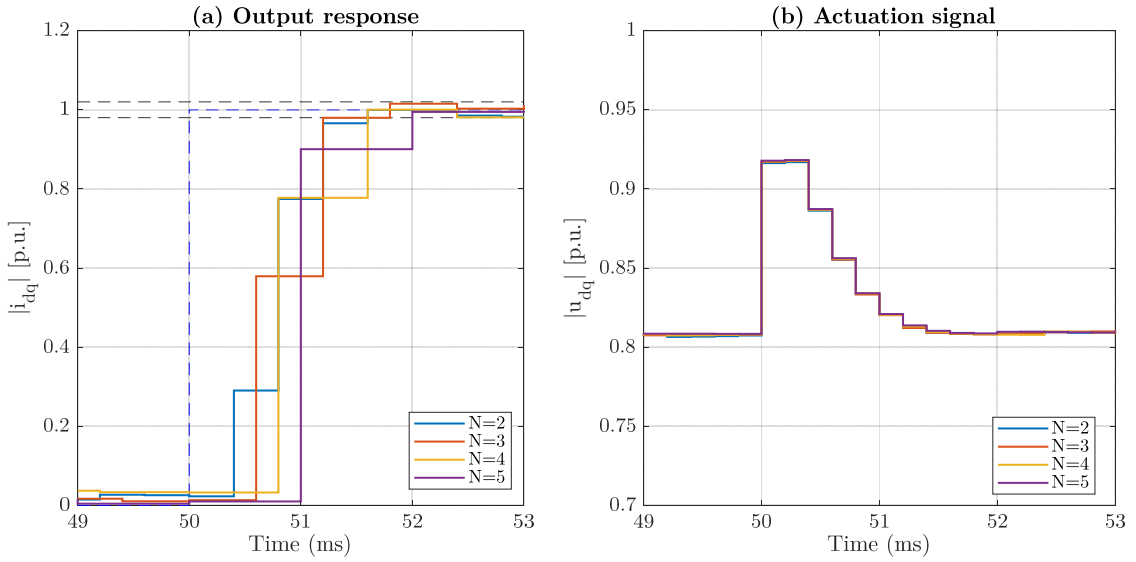

*Figure 4.30. Time response of detailed MRIC system in **dq**-frame: (a) Output current; (b) VSC voltage*

The responses, in the stationary $\alpha\beta$ reference frame, are presented in Figure 4.29(a), whereas the corresponding actuation signal is in Figure 4.29(b). Note that the responses are almost identical to those calculated in Figure 4.22.

Figure 4.30 shows the responses for the rotating dq reference frame. The responses and actuation signal are as expected in Figure 4.27.

Hence the detailed simulation exactly follows the mathematical model and this multirate technique could be easily applied to experimental tests.

4.4.5. Discussion

The model-based MRIC controller provides great responses, if it is considered that the current is being sampled every NT seconds. On one hand, for the $\alpha\beta$-frame, the MRIC-controlled system can get similar responses to the obtained one with single-rate fast controlled system, although it does not exactly match them. On the other hand, for the dq-frame, the MRIC-controlled system obtains exactly the same time responses, which is great considering that error is being tracked every NT seconds instead of T.

This model-based approach obtains excellent results, but the stability and robustness analysis are subordinated to those for the single-rate slow and fast systems. Better tools must be found to ensure the performance of the system. Besides, the designer should be able to get the best possible response for a given plant, and sampling periods or rates (T and NT). For example, in [31] and [14] is detailed another model-based controller design to achieve model reference tracking with minimum time response, whereas the control magnitude is being bounded, and a cancellation controller is used.

Notice that the rate multiplier is bounded to 10, if T is 200 μs, because the sinusoidal signal that it is being followed has a frequency of 50 Hz and the systems need at least 10 samples at each signal period of 20 ms.

The controller implementation is straightforward, and it allows for a reduction in the measurement processing. It is also convenient in the case of slower sampling due to technical limitations and for distributed control systems, by splitting the control into a slow rate part to be sent through the communication channel and a fast part to be locally computed. The presented simulations here studied the case where the sampling frequency has been reduced and the switching frequency was preserved to typical values for medium voltage application around 2.5-10 kHz. Other situations could be found as the ones presented in section 3.3, but other controllers are implemented to each case. The scope of this document is on demonstrate the model-based multirate approach to current control loop, which is usual in VSC applications.

4.5. Conclusions

This chapter has analyzed multirate controllers in the VSC current control loop in each reference frame. First, single-rate controllers for dq and $\alpha\beta$-frame were presented, and it should be emphasized that complex-valued model and controllers were used. The vector approach gives a simpler analysis of those multirate examples, and it also

provides the most suitable approach for three-phase systems. Usually, each axis is independently analyzed, and cross-coupling effects are compensated by feed-forward paths. There are some applications where the passive resistive-inductive effects are different in each axis (three-phase machines), and there is no choice but to apply the decoupled approach. Nevertheless, this is not that situation, because it is a grid-tied converter.

Each controller is correctly defined because they are needed to obtain the multirate method. Firstly, the time-domain analysis of the multirate situation is carried out. In this occasion the sampling is kept constant, whereas the actuation frequency is increased. The structure of the controllers is equivalent, and it is only adapted to each new actuation frequency. This approach only analyzed each new equivalent system, but it did not get better with each new rate multiplier. From results for each reference frame, it can be deduced that if the actuation and control rate are fastest, the system could get into unstable regions and should be corrected. Besides, the controller is not designed for such situation and does not correctly adapt sampling rates. Therefore, the model-based MRIC controller was introduced to get better responses and to take advantage of the multirate situation. On one hand, this controller design in $\alpha\beta$-frame did not get exactly the same response, but very close ones. These results could be related to the extrapolation technique in the rate converter or maybe this control design approach is not mean to be applied to systems where sinusoidal (vector) signals are controlled. On the other hand, the controller design in dq-frame achieved the same responses, which is great considering that the current is being sampled at N times lower rate than the actuation is being applied.

However, this document is only focused in the current control loop, but other control loop in VSC could be involved. For example, the DC-bus voltage control loop is usually at slower rate than the inner current control, which is the one that applies the actuation signal obtained by this controller, so the model-based MRIC tactic could be followed.

Finally, it must be considered that anti-aliasing and anti-imaging filters are not involved in these examples, because only one frequency is being analyzed. Besides, the anti-aliasing filters for current sampling could be avoided, if sampling instants are correctly synchronized with minima and maxima of the carrier signal, as it was presented in subsection 2.2.2.3. Anti-imaging filters are not needed because the rate converter performance is always subordinated to the fundamental frequency in this application. However, these filters must be considered to provide robustness and stability to the system. Using this method, the controller will not be pending on other high frequencies harmonics that could get through the samplers.

Chapter 5. Conclusions and future works

5.1. Conclusions

The multirate approach for power converters is a very promising alternative for sampling frequency limited MV applications due to actuation signal optimization. This is a relatively new multirate method in power electronics field, so it can lead to better alternatives and applications.

This work firstly presented the multirate bases and definitions that have been useful for understanding what is the actual situation of this control theory branch. The multirate analysis has been studied for a long time, because, in all cases, it must work with equivalents single-rate discrete-time analysis, that has already matured. The most useful contribution, what supports all following studies, was given by Kranc. The problem with this method is that the samplers cannot be placed wherever wants the designer, because it requires future values that are obviously unknown.

Then, the state of the art analyzed what are the possible modulation techniques. Although this work has been focused in DSPWM, the SHE is a great alternative where the multirate approach could be useful. A profound and detailed analysis have been shown for DSPWM and its modelling alternatives. That section gave solid reasons for modelling this actuation system as a unitary gain system with a one-half T delay. Then, it provided a relationship with a possible alternative, that is the multisampling. However, this technique has some troubles with switching noise that could be solved with a multirate approach, what lead to solutions where the actuation signal is extrapolated, but the one-half delay is reduced, and so it does the overall phase delay of the closed-loop current control. That is the reason why the DSPWM system has been profoundly inspected. Besides, this fractional delay is related to multirate situation, as it was seen by modelling equivalence between ZOH operation and modified Z-transform application to that one-half delay.

To prove that there are multirate possibilities in power electronics, two alternatives were presented. Each one of them took a different path to design the control system. On one hand, the author with RC used IR to get a single-rate equivalent for the system and to analyze its stability. On the other hand, the PLL design was obtained by means of ER, although it had not used exactly the same notation of this document. Therefore, there are two conceivable tactics to analyze multirate system: Internal Representation and External Representation. These terms are multirate analogous to

single-rate usual ones, known as space-state and traditional SISO representations. From those multirate techniques could be concluded that the most intuitive approach is the IR, but what gives powerful tools for multirate controller modelling is the ER, as it has been shown afterwards with the model-based MRIC controller.

Obviously, the following chapter must have provided the system model for what has been designed the controllers. Given that two possible control reference frames are possible in power electronics, the two options have been evaluated. Besides, for analysis convenient, better understanding of multirate techniques from Chapter 4 and accurate modelling, the complex-valued transfer function and space-state models were presented. Hence, all signals were vector with their real and imaginary parts, and they were no longer scalar variables. This is not the usual method, but in recent years it is getting higher importance.

This system must have been placed at correct multirate context, so few possible applications were presented. First, the reduction of DSPWM delay was studied by means of actuation signal extrapolation, and it was compared to usual phase advancing technique. It was confirmed that they get similar carrier crossings, but the signal extrapolation got more accurate results. The problem with extrapolation has been already mentioned, it supposed future values and get into uncertainties. Besides, it does not reduce the delay for some modulating signal frequencies because only one switch per half carrier period is allowed. This technique is used to replace the multisampling, because it does not sample switching noise, and delay reduction is also achieved. Note that it is possible to use a usual single-rate controller and extrapolate its modulating sinusoidal signal or design a MRIC. Second multirate alternative has been also related to the actuation system, that is the SHE modulation. In this occasion, it was also presented the polynomial extrapolation, which must be known, but it is less useful for sinusoidal extrapolation than the one presented using reference frame transformation from rotating to stationary. The sinusoidal extrapolation presented here extrapolates module and phase values separately. However, it is not possible to get a transfer function from this technique, so the possible inferences are unknown. What it is safe to say is that, it will not affect, if only one frequency is extrapolated. Then, although it has not been tested in this document, it must be noticed that there is one possible niche for multirate applications in every hierarchical control structure. These control loops use different sampling rates for each level, so correct analysis must be followed. Finally, the possibility of fastest power semiconductor devices will be opened in near future, and the possibility of high computational burden might require extrapolation or MRIC techniques.

The last chapter represents the major contribution of this work. Using complex-valued controllers for each reference frame, a grid-tied VSC was analyzed. Firstly, using IR technique, a technique for analyze systems with different rates along the loop was examined. The designer can see how the equivalent single-rate transfer function changes its pole-zero map with each different rate multiplier. However, this is not the best way to design a multirate controller. Hence, based on the literature, the model-based MRIC controller was presented. It is a dual-rate controller, being its sampling

frequency slower than the actuation. With this technique, the designer can get similar temporal responses to those obtained by the fast single-rate designed controller. The dual-rate controller is composed by a slow part, rate converter and fast part, and it must stand out that the rate converter is what makes the difference in this controller, because it is the part that extrapolates the variable. Each reference frame has its own rate converter. In this occasion, stability and robustness tools are missed to analyze its frequency response. For the moment, the time-domain responses are enough, considering complexity of multirate systems.

Along this work, it has been mentioned that rate changes in digital signal processing requires anti-aliasing and anti-imaging filters to avoid alias frequencies when down-sampling or image frequencies when up-sampling, respectively. For given examples in this document, these filters have not been needed for two reasons that are explained subsequently. First, the anti-aliasing filter would have been needed for sampling feedback signal, but sampling at carrier maxima and minima, high frequency harmonics are avoided. Second, the anti-imaging would have been needed for every rate converter that has generated an extrapolation, but these extrapolations are straightforward for one frequency and there is no reason to introduce such a low pass filter that could have generated phase delay.

Note that MRIC controller design has considered the continuous-time model of plant and controller. The reason is that to obtain the slow and fast parts of the controller the designer must have a basis to apply the discrete-time transformation to each discrete-time period.

This work has been hard because, at the beginning, it was difficult to find multirate contributions in power electronics or control theory in general. When Kranc methodology was found, the following contributions were easily noticeable because all authors had begun its research with that methodology. Other alternatives, as MROC, can be also applied in power electronics, but the fresh topic of multirate in power electronics requires calm and clear presentation of adapted notation in this field. The gates are open for future implementation of other multirate control techniques in power electronics.

5.2. Future works

This document leaves several new topics for experimental tests and other applications of multirate techniques. In the subsequent, some future works are enumerated:

1) Experimental results

If something important has been left in this document is experimental result from MRIC controller. The DNPC converter software platform is not ready for applications with several sampling rates in its routine. Hence, the alternatives are: intelligent strategy to achieve slower rates by neglecting some samples or changing the digital platform for another new alternative. Due to timing issues on writing this work, these alternatives have not been applied, but its implementation will be made in near future.

Besides, the document introduces the MV power converter issue, but the simulation results were given for the LV 3L-DNPC-VSC that the research group has in its laboratory. Therefore, the results obtained in this work can be compared soon with experimental results. Nevertheless, the methodology of this work makes easy the implementation of MV simulations or experimental results, if such voltage levels are available.

Also, more sophisticated grid-tied filters have been used in MV converters as LLCL-filters, so delay implications and stability of such systems must be analyzed in the future for multirate applications.

In conclusion, several experimental setups must be planned soon to validate simulation results.

2) Digital filters

In the future would be needed to implement anti-aliasing and anti-imaging filters into the control loop due to rate changes. Therefore, the best low-pass filter solution must be taken to have the lowest possible phase delay. Although it could be multirate algorithms that do not need such filters. A deeply insight on multirate digital signal processing must be shown.

3) Multirate controllers

This work has introduced only one MRIC option, but there are new design strategies to increase the performance of the controller. Besides, this controller could be implemented in networked controllers, that is, controllers that work online and they could lose some information packages and/or have delay troubles.

Future research on multirate controllers will be also focused on finding frequency analysis tools or possible approximations.

Besides, this work has only analyzed MRIC situations, that is slow sampling, fast actuation. However, there is also the opposite solution, i.e., fast sampling, slow actuation. The controller for this situation is known as MROC. This solution is interesting for situations where the controller needs fast sampling rate to provide the best possible sample for its control action, which will be applied at slowest rate. It is possible to find this case in applications where the power converter is constrained by switching frequency. Lower switching frequency means lower power losses. However, an important concern in this approach is the noise sensibility increasing due to high sampling frequency of the controlled variable. Hence, additional techniques as optimization or state estimation are needed. Besides, MROC design is inferred in internal representation, instead of external representation as MRIC.

Table 5.1 summarizes several applications where multirate techniques could be useful in power electronics. This table gives an overall look of the future possibilities of this control theory on optimizing power converter operation. The most exotic application is variable sampling rate applications where the fast sampling is only needed in transient-state, but, in steady-state, it only needs a few samples. Hence, the computational

burden can be reduced for other algorithms (e.g. impedance estimation). On the other hand, the additional control algorithms could be implementing a calculation faster or slower than the inner control where they apply their control action. Hence, MRIC or MROC (extrapolation or decimation) multirate analysis techniques (single-rate equivalents) are needed to ensure stability.

Table 5.1. Multirate application identification in power electronics

Application		**Multirate controller**
High switching frequency	Delay reduction of inner control loop	MRIC - Extrapolation
	SHE modulation optimization	
	Fast power semiconductor devices	
Low switching frequency		MROC - Decimation
Cascaded control structures	Networked control systems (divided sole controller)	MRIC - Extrapolation
	Hierarchical control structures	
Variable sampling on control loops		MRIC -Extrapolation
Fast synchronization		MRIC -Extrapolation
Additional control algorithms (e.g. Repetitive controller)		MRIC /MROC - Extrapolation/Decimation

4) Sinusoidal extrapolation

An interesting research for future applications in power electronics is the sinusoidal extrapolation. The future goal will be to find a closed expression for sinusoidal extrapolation, that is, a SISO transfer function. In this way, the designer will be able to study frequency interference of this algorithm.

Chapter 6. Budget

This chapter will describe the theoretical cost of the whole project.

6.1. Material cost

In this section, the cost of the different materials (hardware and software) are detailed and the VAT (21%) is included.

Table 6.1. Material Costs (VAT included)

Item		Unit Price (€)	Units	Total cost (€)
Hardware	Windows PC i7 3.6 GHz	1000	1	1000
Hardware total cost				1000
Software	MATLAB	0	1	0
	Microsoft Office 365	0	1	0
Software total cost				0
Material total cost				1000

6.2. Professional fees

In this section the different Professional fees are calculated. These fees are calculated as gross incomes. It includes all the professional activities related with the project.

Table 6.2. Professional fees (gross salary)

Activity	Salary (€/month)	Time (months)	Total cost (€)
Engineering	1200	5	6000
Typing	1000	1	1000
Material total cost			7000

6.3. Total cost

Table 6.3. Additional costs and total

Material cost (€)	1000
Professional fees (€)	7000
Printing (€)	90
Transport (€)	250
Material total cost (€)	8340

Appendix A. Multirate modelling techniques bases

A.1. Signals between sampling instants

When the inherent sampling rate of a given system is too low relative to the frequency contained in the signals, additional effort may be needed in gaining knowledge of the signals between the sampling instants. These methods are useful as analytical tools for study of digital control systems with nonuniform or multirate sampling. This analysis has been adapted from [65].

A.1.1. The delayed *Z*-transform

One way of representing the details of a signal between the sampling instants with sampling period T is to delay the analog signal by ΔT, where $0 < \Delta < 1$; then the delayed signal is sampled by a conventional sampler at $t = kT, k = 0, 1, 2, ...$ By changing the amount of the time delay ΔT, the signal information between sampling instants might be recovered. Figure A.1 shows a system with a fictitious time delay ΔT at the output, and the delayed signal is sampled by a sampler with period T.

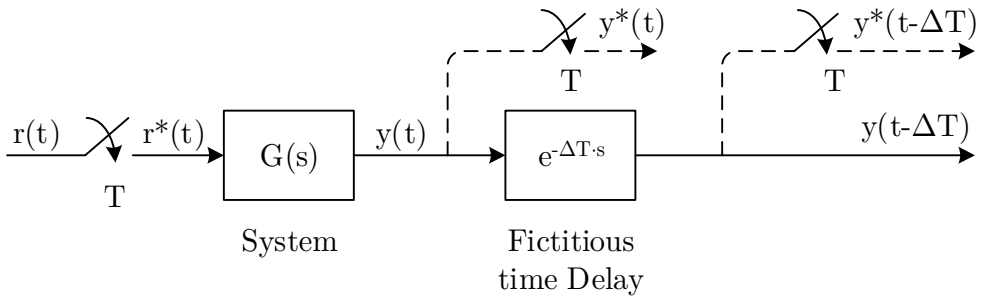

Figure A.1. A sampled-data system with fictitious time delay and sampler

The sampled output of the fictitious time delay is expressed as $(A.1)$.

$$y^*(t - \Delta T) = \sum_{k=0}^{\infty} y(kt - \Delta T) \cdot \delta(t - kT) \qquad (A.1)$$

The *Z*-transform of the last equation is defined as the delayed *Z*-transform and is written $(A.2)$.

$$Y(z, \Delta) = \sum_{k=0}^{\infty} y(kT - \Delta T) z^{-k} \qquad (A.2)$$

In Figure A.2 is illustrated the step of first shifting the signal $y(t)$ by ΔT and then sampling the shifted signal $y(t-\Delta T)$ by the ideal sampler starting from $t=0$. Please note that, since $\Delta < 1$, the shifting theorem $(A.3)$ cannot be used.

$$\mathcal{L}[f(t-nT)u_s(t-nT)] = z^{-n} \cdot F(z) \tag{A.3}$$

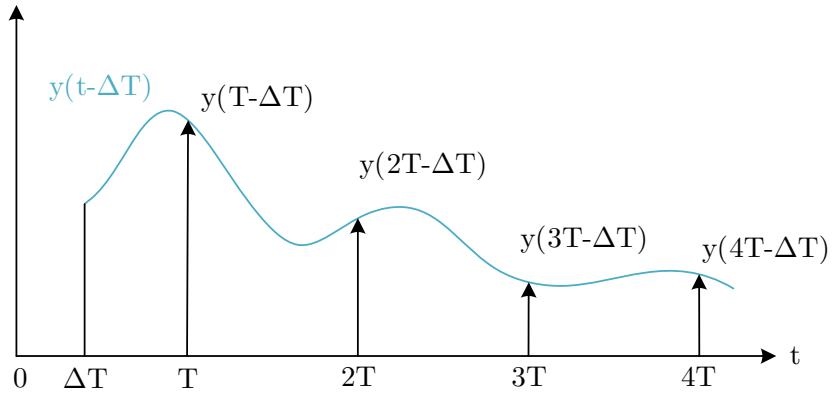

Figure A.2. Waveforms depicting the operations of the delayed Z-transform

Although the application of the delayed Z-transform seems straightforward, the fact that, when $\Delta \neq 0$, the first sample is always zero may cause some analytical problems.

A.1.2. The modified *Z*-transform

To overcome the difficulty with the delayed Z-transform, a new factor m is introduced, such that $(A.4)$. Since Δ lies between zero and one, m also lies in the same range.

$$m = 1 - \Delta \tag{A.4}$$

Substituting $(A.4)$ in $(A.2)$ yields $(A.5)$.

$$Y(z, \mathrm{m}) = Y(z, \Delta)|_{\Delta=1-m} = \sum_{k=0}^{\infty} y(kT - T + mT)z^{-k} \tag{A.5}$$

Then, by means of the shifting theorem in $(A.3)$, the last equation is written as $(A.6)$, where $0 < m < 1$.

$$Y(z, \mathrm{m}) = z^{-1} \sum_{k=0}^{\infty} y(kT + mT)z^{-k} \tag{A.6}$$

The equation $(A.6)$ is defined as the modified Z-transform of $y(t)$ and it is denoted as $(A.7)$ or $(A.8)$.

$$\mathcal{Z}_m[y(t)] = Y(z, m) \tag{A.7}$$

$$\mathcal{Z}_m[y(t)] = Y(z, \Delta)|_{\Delta=1-m} \tag{A.8}$$

Note that, when $\Delta = 0$, the delayed Z-transform reverts to the Z-transform. Nevertheless, when $\Delta = 0$, $\mathrm{m} = 1$, and $(A.6)$ gives $(A.9)$.

$$Y(z, m)|_{m=1} = z^{-1} \sum_{k=0}^{\infty} y[(k+1)T]z^{-k} = Y(z) - y(0) \tag{A.9}$$

Then, when $m = 1$, the modified Z-transform is not equal to $Y(z)$ unless $y(t = 0) = 0$. On the other hand, when $m = 0$ ($\Delta = 1$), the function $y(t)$ is first delayed by one sampling period before taking the Z-transform ($A.10$).

$$Y(z, m)|_{m=0} = Y(z, 0) = z^{-1} \cdot Y(z) \tag{A.10}$$

Figure A.3 depicts the following steps of taking the modified Z-transform.

1) The time function $y(t)$ is first shifted to the left (time advance) by mT, where $0 < m < 1$. This gives $y(t + mT)$.
2) The shifted time function $y(t + mT)$ is sampled by an ideal sampler starting from $t = 0$.
3) The sampled sequence is shifted to the right by one sampling instant T.

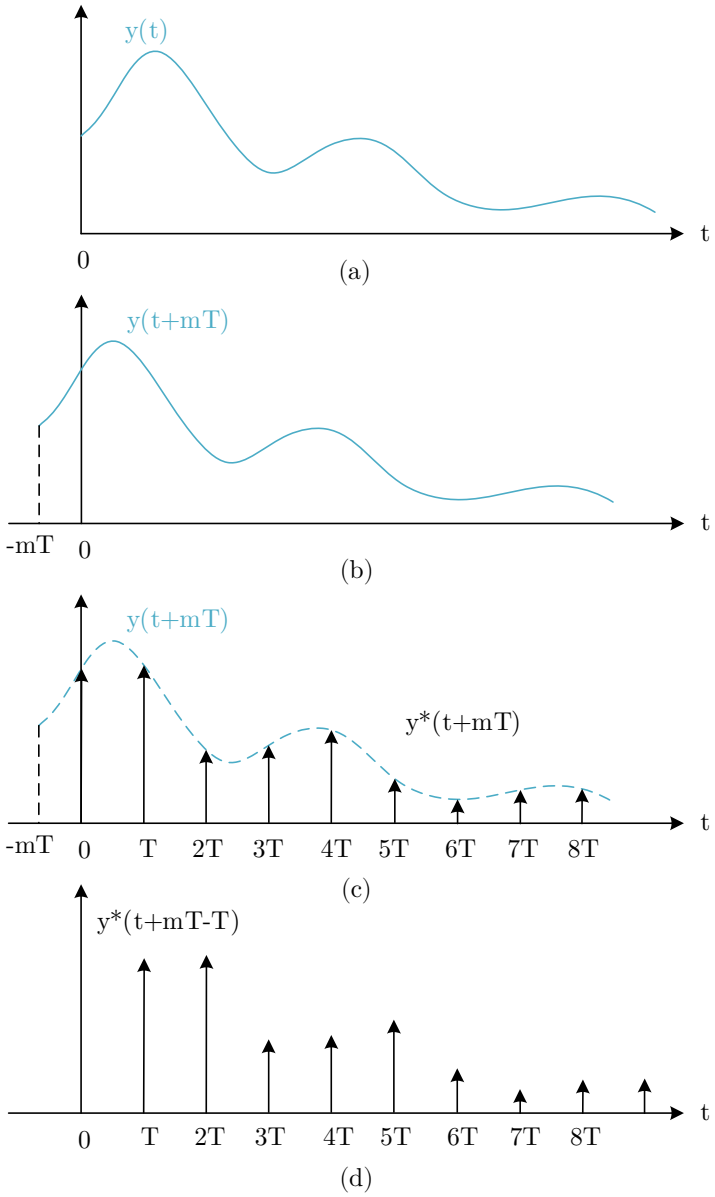

Figure A.3. Steps illustrating the modified Z-transform: (a) Time function $y(t)$; (b) $y(t)$ is shifted left by mT, $0 < m < 1$; (c) $y(t + mT)$ is sampled starting at $t = 0$; (d) The sampled sequence is shifted to the right by T

Two alternative expressions for the modified *Z*-transforms of $(A.6)$ are shown here. These expressions are derived using the complex convolution of the Laplace transform. The first approach is $(A.11)$.

$$Y(z,m) = z^{-1} \sum \left[residues\ of\ Y(s) \frac{e^{m \cdot T \cdot s} \cdot z}{z - e^{T \cdot s}}\ at\ the\ poles\ of\ Y(s) \right] \tag{A.11}$$

Where the residues of $Y(s)$ are deduced as $(A.12)$, being:

- Number of multiple poles: h
- Multiple pole order in $s = s_i$: n_i
- Number of simple poles: l

$$\begin{aligned} Y(z,m) = \sum_{i=1}^{h} \frac{1}{(n_i - 1)!} \cdot \lim_{s \to s_i} \frac{d^{n_i - 1}}{ds^{n_i - 1}} \left[(s - s_i)^{n_i} \cdot \frac{Y(s) \cdot e^{m \cdot T \cdot s} \cdot z}{z - e^{T \cdot s}} \right] \\ + \sum_{j=h+1}^{l} \lim_{s \to s_j} \left[(s - s_j) \cdot \frac{Y(s) \cdot e^{m \cdot T \cdot s} \cdot z}{z - e^{T \cdot s}} \right] \end{aligned} \tag{A.12}$$

The second approach is $(A.13)$, being ω_s the sampling frequency.

$$Y(z,m) = \frac{1}{T} \sum_{n=-\infty}^{\infty} Y(s + jn\omega_s) e^{-(1-m)(s+jn\omega_s)T} \,|_{z=e^{T \cdot s}} \tag{A.13}$$

Setting $m = 1$ in $(A.14)$, it is obtained that

$$Y(z,m)|_{m=1} = \frac{1}{T} \sum_{n=-\infty}^{\infty} Y(s + jn\omega_s) \,|_{z=e^{T \cdot s}} = Y(z) \tag{A.14}$$

In this case, since $y(0) = 0$ is implied in that expression, $Y(z,m) = Y(z)$ when $m = 1$.

These equations are subject to different conditions of validity and are useful for various purposes. Equation $(A.6)$ is the most general and it is valid for any function $y(t)$. Equation $(A.11)$ is valid for any $y(t)$ that has a Laplace transform $Y(s)$. Equation $(A.13)$ is valid only if $y(0) = 0$, and thus, it is not valid for functions that have a jump discontinuity at $t = 0$.

A.1.3. The inverse Modified *Z*-transform

The inverse *Z*-transform of $F(z,m)$ gives the values of $f(t)$ in between the sampling instants for a given value of m. The inverse modified *Z*-transform operation is denoted by $\mathcal{Z}_m^{-1}$ and may be carried out by either the power-series method or the inversion formula.

In the power-series method, just as in the ordinary *Z*-transform, the function $F(z,m)$ is expanded into a power series in z^{-1} by long division $(A.15)$. The coefficient $f(kT - T + mT)$ corresponds to a value of $f(t)$ between $t = (k-1)T$ and $t = kT$ for any value of m between 0 and 1, and $k = 1,2,...$

$$F(z,m) = f(mT)z^{-1} + f(T + mT)z^{-2} + \cdots + f(kT - T + mT)z^{-k} + \cdots \tag{A.15}$$

Just as in the *Z*-transform method, the inverse modified Z-transform can be carried out by means of the inversion integral $(A.16)$.

$$\mathcal{Z}_m^{-1}[F(z,m)] = f(kT,m) = \frac{1}{2\pi j}\oint_{\Gamma} F(z,m)z^{k-1}dz \qquad (A.16)$$

Where Γ is a closed path in the z-plane that encloses all the singularities of $F(z,m)z^{k-1}$.

A.1.4. The modified *Z*-transfer function

The modified Z-transform method can also be applied to discrete-data systems and it defines the modified Z-transfer function.

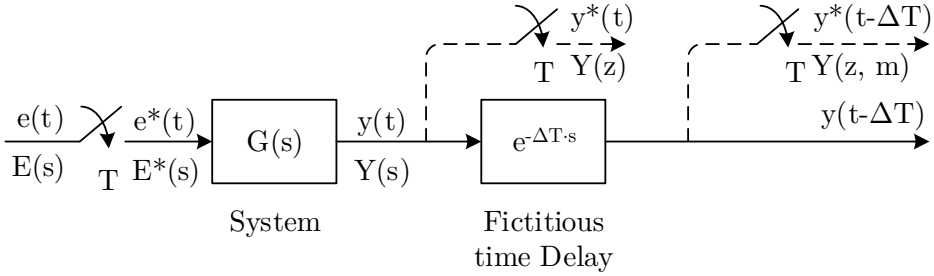

Figure A.4. Discrete-data system with a fictitious time delay

Considering Figure A.4, the modified Z-transform of the output $y(t)$ is defined as $(A.17)$.

$$\mathcal{Z}_m[y(t)] = Y(z,m) = z^{-1}\sum_{k=0}^{\infty} y(kT+mT)z^{-k} \qquad (A.17)$$

The modified Z-transform in the last expression can be used for the determination of the input-output transfer relation of the system. Substituting $Y(s) = G(s)E^*(s)$ in $(A.13)$, it is obtained $(A.18)$.

$$Y(z,m) = \frac{1}{T}\sum_{n=-\infty}^{\infty} G(s+jn\omega_s)E^*(s+jn\omega_s)e^{-(1-m)(s+jn\omega_s)T}\,|_{z=e^{T\cdot s}} \qquad (A.18)$$

Since $E^*(s+jn\omega_s) = E^*$, the last equation becomes $(A.19)$.

$$Y(z,m) = E(z)\frac{1}{T}\sum_{n=-\infty}^{\infty} G(s+jn\omega_s)e^{-(1-m)(s+jn\omega_s)T}\,|_{z=e^{T\cdot s}} = E(z)G(z,m) \qquad (A.19)$$

In the last equation $G(z,m)$ denotes the modified Z-transform of $G(s)$ and is expressed as $(A.20)$. Hence, the modified Z-transform of a system with the transfer function $G(s)$ is defined in exactly the same way as that of a signal, so $(A.11)$ is also applicable.

$$G(z,m) = \frac{1}{T}\sum_{n=-\infty}^{\infty} G(s+jn\omega_s)e^{-(1-m)(s+jn\omega_s)T}\,|_{z=e^{T\cdot s}} \qquad (A.20)$$

Note that the modified Z-transform of a sampled signal $e^*(t)$ is just the Z-transform of the signal.

$$\mathcal{Z}_m[E^*(s)] = E(z) \qquad (A.21)$$

In Table A.1 are presented a few examples of usual transfer functions, but more examples can be found in [65].

Table A.1. Modified z-transforms examples

Laplace Transform $F(s)$	Time Function $f(t), t>0$	z-transform $F(z)$	Modified z-transform $F(z,m)$
1	$\delta(t)$	1	0
$\frac{1}{s}$	$u_s(t)$	$\frac{z}{z-1}$	$\frac{1}{z-1}$
$\frac{1}{s^2}$	t	$\frac{Tz}{(z-1)^2}$	$\frac{mT}{z-1}+\frac{T}{(z-1)^2}$
$\frac{1}{s+a}$	e^{-at}	$\frac{z}{z-e^{-aT}}$	$\frac{e^{-amT}}{z-e^{-aT}}$
$\frac{a}{s(s+a)}$	$1-e^{-at}$	$\frac{z(1-e^{-aT})}{(z-1)(z-e^{-aT})}$	$\frac{z(1-e^{-amT})+(e^{-amT}-e^{-aT})}{(z-1)(z-e^{-aT})}$
$\frac{\omega}{s^2+\omega^2}$	$\sin\omega t$	$\frac{z\sin\omega T}{z^2-2z\cos\omega T+1}$	$\frac{\sin m\omega T+\sin(1-m)\omega T}{z^2-2z\cos\omega T+1}$
$\frac{s}{s^2+\omega^2}$	$\cos\omega t$	$\frac{z(z-\cos\omega T)}{z^2-2z\cos\omega T+1}$	$\frac{\cos m\omega T-\cos(1-m)\omega T}{z^2-2z\cos\omega T+1}$

A.1.5. Example

Here, an example using $(A.12)$ is given for the L-filter model with its corresponding ZOH operation as $(A.22)$.

$$G_{h0}(s)\cdot G_{\alpha\beta}^{L-filter}(s)=\frac{1-e^{-sT}}{s}\cdot\frac{1}{L\cdot s+R} \tag{A.22}$$

Applying the modified Z-transform, it is obtained $(A.24)$.

$$\begin{aligned} G_{\alpha\beta}^{L}(z,m)=z^{-1}\cdot\frac{(1-z^{-1})}{L}\cdot\Bigg[&\left\{Residue\ of\left(\frac{1}{s\left(s+\frac{R}{L}\right)}\cdot\frac{e^{mT\cdot s}\cdot z}{z-e^{T\cdot s}}\right)in\ s=0\right\}+\\ &+\left\{Residue\ of\left(\frac{1}{s\left(s+\frac{R}{L}\right)}\cdot\frac{e^{mT\cdot s}\cdot z}{z-e^{T\cdot s}}\right)in\ s=-\frac{R}{L}\right\}\Bigg] \end{aligned} \tag{A.23}$$

$$\begin{aligned} G_{\alpha\beta}^{L}(z,m)=z^{-1}\cdot\frac{(1-z^{-1})}{L}\cdot\Bigg[&\lim_{s\to 0}\left[\ \cancel{s}\cdot\frac{1}{\cancel{s}\left(s+\frac{R}{L}\right)}\cdot\frac{e^{mT\cdot s}\cdot z}{z-e^{T\cdot s}}\ \right]+\\ &+\lim_{s\to-\frac{R}{L}}\left[\ \cancel{\left(s+\frac{R}{L}\right)}\cdot\frac{1}{s\cancel{\left(s+\frac{R}{L}\right)}}\cdot\frac{e^{mT\cdot s}\cdot z}{z-e^{T\cdot s}}\ \right]\Bigg] \end{aligned} \tag{A.24}$$

Operating, the expression becomes $(A.25)$, and finally $(A.26)$.

$$G^L_{\alpha\beta}(z,m) = z^{-1} \cdot \frac{(1-z^{-1})}{L} \left[\frac{L}{R} \cdot \frac{z}{z-1} - \frac{L}{R} \cdot \frac{e^{-\frac{R}{L} mT} \cdot z}{z - e^{-\frac{R}{L} T}} \right] \tag{A.25}$$

$$G^L_{\alpha\beta}(z,m) = \frac{z \cdot \left(1 - e^{-\frac{R}{L} mT}\right) - e^{-\frac{R}{L} T} + e^{-\frac{R}{L} mT}}{z \cdot R \cdot \left(z - e^{-\frac{R}{L} T}\right)} \tag{A.26}$$

If $(A.10)$ is also considered for modified Z-transfer function, the final expression is $(A.27)$. It is clear that the pole location does not change, whereas the numerator performance the delay effect on the transfer function with the location of a new zero.

$$z \cdot G^L_{\alpha\beta}(z,m) = \frac{z \cdot \left(1 - e^{-\frac{R}{L} mT}\right) - e^{-\frac{R}{L} T} + e^{-\frac{R}{L} mT}}{R \cdot \left(z - e^{-\frac{R}{L} T}\right)} \tag{A.27}$$

In Figure A.5 is shown a pole-zero map of this example for different m values, being the parameter values those form Table A.2 and using expression $(A.26)$.

Table A.2. Example parameters for modified z-transfer function

Name	Symbol	Value
Filter resistor	R	9.1 $m\Omega$
Filter inductor	L	750 μH
Sampling period	T	200 µs

From Figure A.5 can be seen that the zero is moving towards the origin with higher values of m $(\Delta = 1 - m)$, that is, less delay. Although the zeros with $m < 0.5$ fall outside the unit circle, the system stability is ensured.

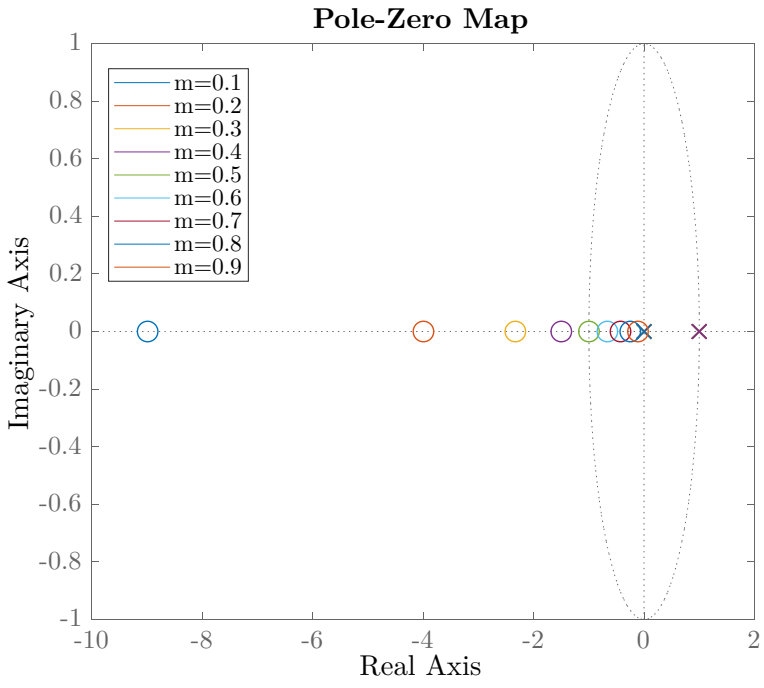

Figure A.5. Pole-zero map of modified Z-transfer function $G^L_{\alpha\beta}(z,m)$

In Figure A.6 is represented the phase difference between two modified Z-transfer function. It is checked that the phase difference is exactly $m \cdot T = 0.1 \cdot 200\ \mu s$ at low frequencies, but it varies when the signal frequency is $\omega > 0.1 \cdot \omega_s$. Hence, it must be considered at the controlled frequencies.

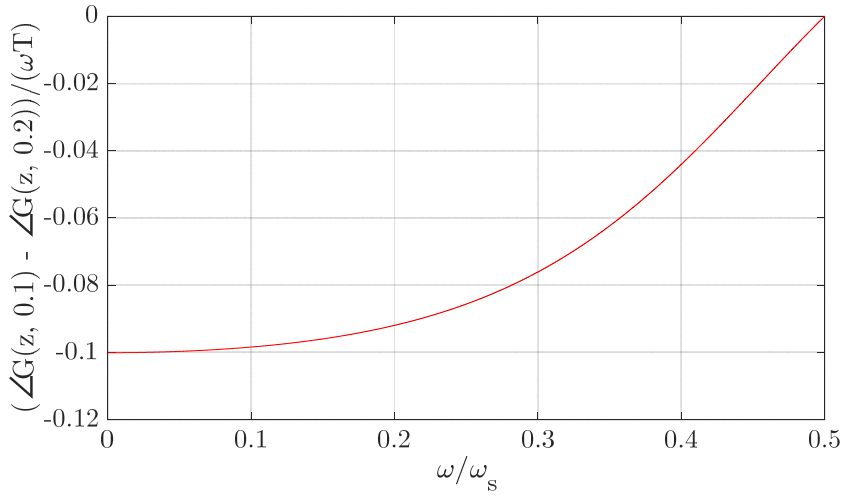

Figure A.6. Phase difference between two modified Z-transfer function $G^{L}_{\alpha\beta}(z, m)$

Finally, this fractional delay is shown in Figure A.7 with the time-domain response of the transfer function. The output signal at period T is compared to the output signal with period $T/N = 200\ \mu s/10$ (the input of this system is updated every T seconds). Note that the time delay is $(1 - m) \cdot T$.

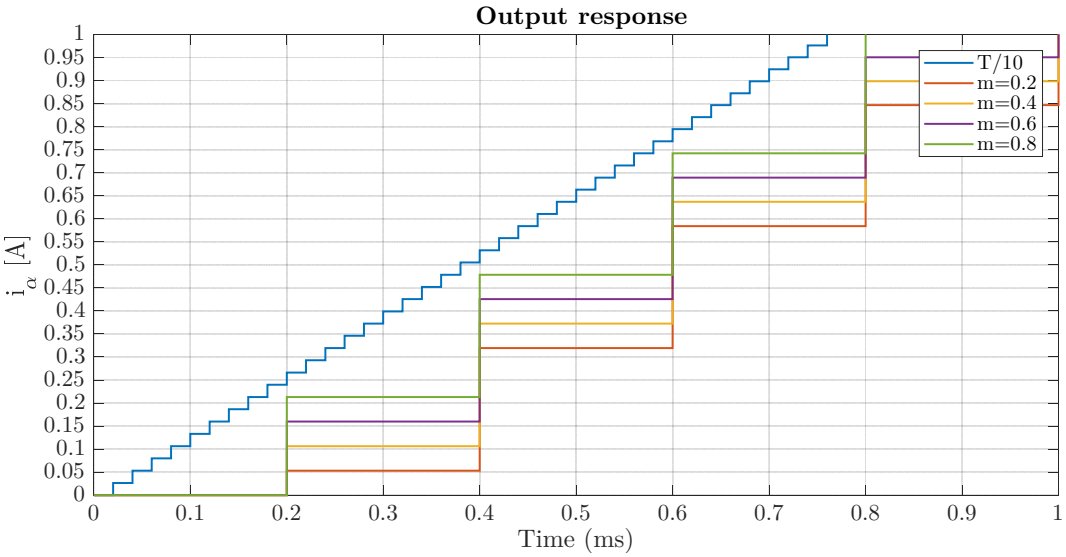

Figure A.7. Time-domain response of the modified Z-transfer function $G^{L}_{\alpha\beta}(z, m)$

Therefore, this approach allows to the designer to accurately model fractional delays in discrete-time domain. Besides, this approach can be applied to multirate systems as it will be shown in the following section.

A.2. Multirate Sampler-Decomposition method

A versatile method of analyzing multirate system is to decompose the fast-rate sampler into N parallel-connected slow-rate samplers with time-delay and time-advances units, as shown in Figure A.8. Since now the samplers are all at the same sampling rate, the ordinary *Z*-transform method analysis may be applied.

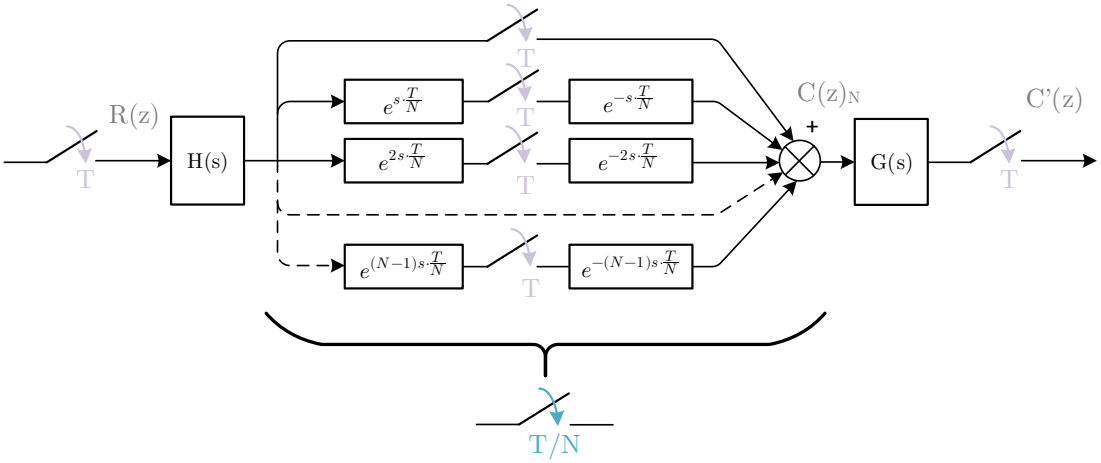

Figure A.8. Sampler-Decomposition or Vectorial Switch Decomposition method

The *Z*-transform of $e^{\frac{kT}{N}\cdot s}\cdot G(s)$ or $e^{-\frac{kT}{N}\cdot s}\cdot G(s)$ can be determined from the modified *Z*-transform of $G(s)$ as $(A.28)$ or $(A.29)$.

$$\mathcal{Z}\left[e^{\frac{kT}{N}\cdot s}\cdot G(s)\right] = [z\cdot G(z,m)]|_{m=k/N} \tag{A.28}$$

$$\mathcal{Z}\left[e^{-\frac{kT}{N}\cdot s}\cdot G(s)\right] = G(z,m)|_{m=1-k/N} \tag{A.29}$$

A simple example, with an arbitrary closed-loop system, is analyzed here to better understanding of this procedure. The system is based on a PI controller in the *dq*-frame plant L-filter (cross-coupling effects already compensated) is shown in Figure A.9. The rate multiplier in this case is $N = 2$. The PI controller use the constants $(A.30)$ and system parameters are those from Table A.2.

$$K_p = 1.654 \quad K_I = 1.28\cdot 10^3 \tag{A.30}$$

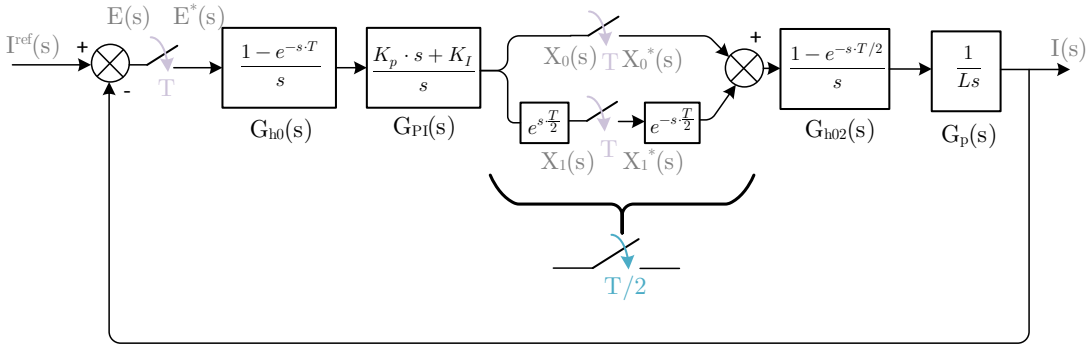

Figure A.9. Closed-loop multirate digital system

Therefore, the closed-loop transfer function equivalent is $(A.31)$. Note that expression $(A.32)$ represents the slow single-rate equivalent open-loop transfer function.

$$G_{dq}^{CL}(z) = \frac{\mathcal{Z}[G_{h02}G_p(s)]\mathcal{Z}[G_{h0}G_{PI}(s)] + \mathcal{Z}\left[G_{h02}G_p(s)e^{-s\cdot\frac{T}{2}}\right]\mathcal{Z}\left[G_{h0}G_{PI}(s)e^{s\cdot\frac{T}{2}}\right]}{1 + \mathcal{Z}[G_{h02}G_p(s)]\mathcal{Z}[G_{h0}G_{PI}(s)] + \mathcal{Z}\left[G_{h02}G_p(s)e^{-s\cdot\frac{T}{2}}\right]\mathcal{Z}\left[G_{h0}G_{PI}(s)e^{s\cdot\frac{T}{2}}\right]} \quad (A.31)$$

$$G_{dq}^{OL}(z) = \mathcal{Z}[G_{h02}G_p(s)]\mathcal{Z}[G_{h0}G_{PI}(s)] + \mathcal{Z}\left[G_{h02}G_p(s)e^{-s\cdot\frac{T}{2}}\right]\mathcal{Z}\left[G_{h0}G_{PI}(s)e^{s\cdot\frac{T}{2}}\right] \quad (A.32)$$

Where each term is defined as follows:

$$\begin{aligned}\mathcal{Z}[G_{h02}G_p(s)] &= \mathcal{Z}\left[\frac{1-e^{-s\cdot\frac{T}{2}}}{s}\cdot\frac{1}{Ls}\right] = \mathcal{Z}\left[\frac{1}{Ls^2}\right] - \mathcal{Z}_m\left[\frac{1}{Ls^2}\right]_{m=1-\frac{1}{2}} = \\ &= \frac{T}{L}\cdot\frac{z}{(z-1)^2} - \frac{T}{L}\cdot\left(\frac{\frac{1}{2}}{z-1} + \frac{1}{(z-1)^2}\right) = \frac{T/2}{L}\frac{1}{z-1}\end{aligned} \quad (A.33)$$

$$\begin{aligned}\mathcal{Z}\left[G_{h02}G_p(s)e^{-s\cdot\frac{T}{2}}\right] &= \mathcal{Z}_m\left[\frac{1}{Ls^2}\right]_{m=1-\frac{1}{2}} - \frac{1}{z}\cdot\mathcal{Z}\left[\frac{1}{Ls^2}\right] = \\ &= \frac{T}{L}\cdot\left(\frac{\frac{1}{2}}{z-1} + \frac{1}{(z-1)^2}\right) - \frac{T}{L}\cdot\frac{1}{(z-1)^2} = \frac{T/2}{L}\cdot\frac{1}{z-1}\end{aligned} \quad (A.34)$$

$$\mathcal{Z}[G_{h0}G_{PI}(s)] = (1-z^{-1})\cdot\mathcal{Z}\left[\frac{K_P s + K_I}{s^2}\right] = K_p + \frac{K_I T}{z-1} \quad (A.35)$$

$$\begin{aligned}\mathcal{Z}\left[G_{h0}G_{PI}(s)e^{s\cdot\frac{T}{2}}\right] &= (1-z^{-1})\cdot z\cdot\mathcal{Z}_m\left[\frac{K_P s + K_I}{s^2}\right]_{m=\frac{1}{2}} = \\ &= K_P + K_I\cdot\frac{T}{2} + \frac{K_I T}{z-1}\end{aligned} \quad (A.36)$$

The numerical equivalent closed-loop expression is $(A.37)$.

$$G_{dq}^{CL}(z) = \frac{0.4582z - 0.3897}{z^2 - 1.542z + 0.6103} \quad (A.37)$$

The time-domain responses of the multirate and single-rate equivalent closed-loop are compared in Figure A.10.

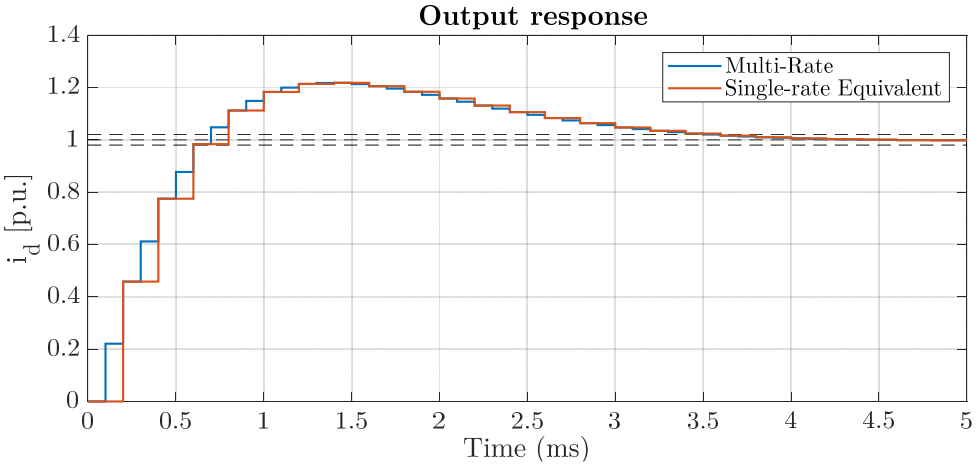

Figure A.10. Time-domain response of multirate and single-rate equivalent closed-loop system.

Although there is a ZOH operation with period T before the controller, it is only referred to the input signal, while the controller operates at high rate $T/2$.

The results are the same that could be obtained by using the time-domain multirate method of section 4.3. The approach is different, but this two methodologies are based in the Vectorial Switch Decomposition that was introduced by Kranc in 1957 [19]. If these two approaches are compared, the most simple and intuitive is the presented one in section 4.3.

Appendix B. Vector representation of three-phase variables

B.1. Spatial vector

Every three-phase variable (voltage, current, flux, etc.) might be represented in a tridimensional space with three orthogonal axes, known as *a*, *b*, and *c*, like follows.

$$\vec{s}(t) = \left[s_a(t) + s_b(t) \cdot e^{j\frac{2\pi}{3}} + s_c(t) \cdot e^{j\frac{4\pi}{3}} \right] \tag{B.1}$$

Where $s_a(t)$, $s_b(t)$, and $s_c(t)$ represent the instantaneous values of $\vec{s}_a$, $\vec{s}_b$, and $\vec{s}_c$, respectively.

For balanced three-phase systems, the instantaneous sum of currents results zero, so the current vector moves in a plane defined by (*B.* 2).

$$i_a(t) + i_b(t) + i_c(t) = 0 \tag{B.2}$$

This equation defines a plane $\mathcal{X}$ that is perpendicular to the vector $[1 \quad 1 \quad 1]^T$ in the space *abc,* as it is depicted in Figure B.1(a). The space $\alpha\beta\gamma$ is defined by:

- The α axis is the *a* axis projection on the plane $\mathcal{X}$.
- The β axis, that is perpendicular to the α axis, is defined by the right-hand rule.
- The γ axis, that is co-lineal with the vector $[1 \quad 1 \quad 1]^T$, and it is the result of vector product $\alpha \times \beta$. The component upon the γ axis is known as zero component, and it is the instantaneous sum of *a*, *b*, and *c*.

Figure B.1 (b) represents the location of the *abc* axes when they are projected upon the $\alpha\beta$ plane. Hence, the components α and β from the vector $\vec{s}$ are expressed as (*B.* 3).

$$\vec{s}_{\alpha\beta}(t) = s_\alpha(t) + j s_\beta(t) = k \cdot \left[s_a(t) + s_b(t) \cdot e^{j\frac{2\pi}{3}} + s_c(t) \cdot e^{j\frac{4\pi}{3}} \right] \tag{B.3}$$

Where k is constant that defines the transformation type (invariance power or amplitude). The third component, known as γ, is zero and normal to the *abc* axes and it is deduced as (*B.* 4).

$$s_\gamma(t) = k \cdot \left[s_a(t) \cdot \cos\left(\frac{\pi}{4}\right) + s_b(t) \cdot \cos\left(\frac{\pi}{4}\right) + s_c(t) \cdot \cos\left(\frac{\pi}{4}\right) \right] \tag{B.4}$$

This component is null for balanced systems, and in real systems characterizes the current through the neutral line in a star connection. Usually, the $\alpha\beta\gamma$ is referred as $\alpha\beta$ due to omitting of γ.

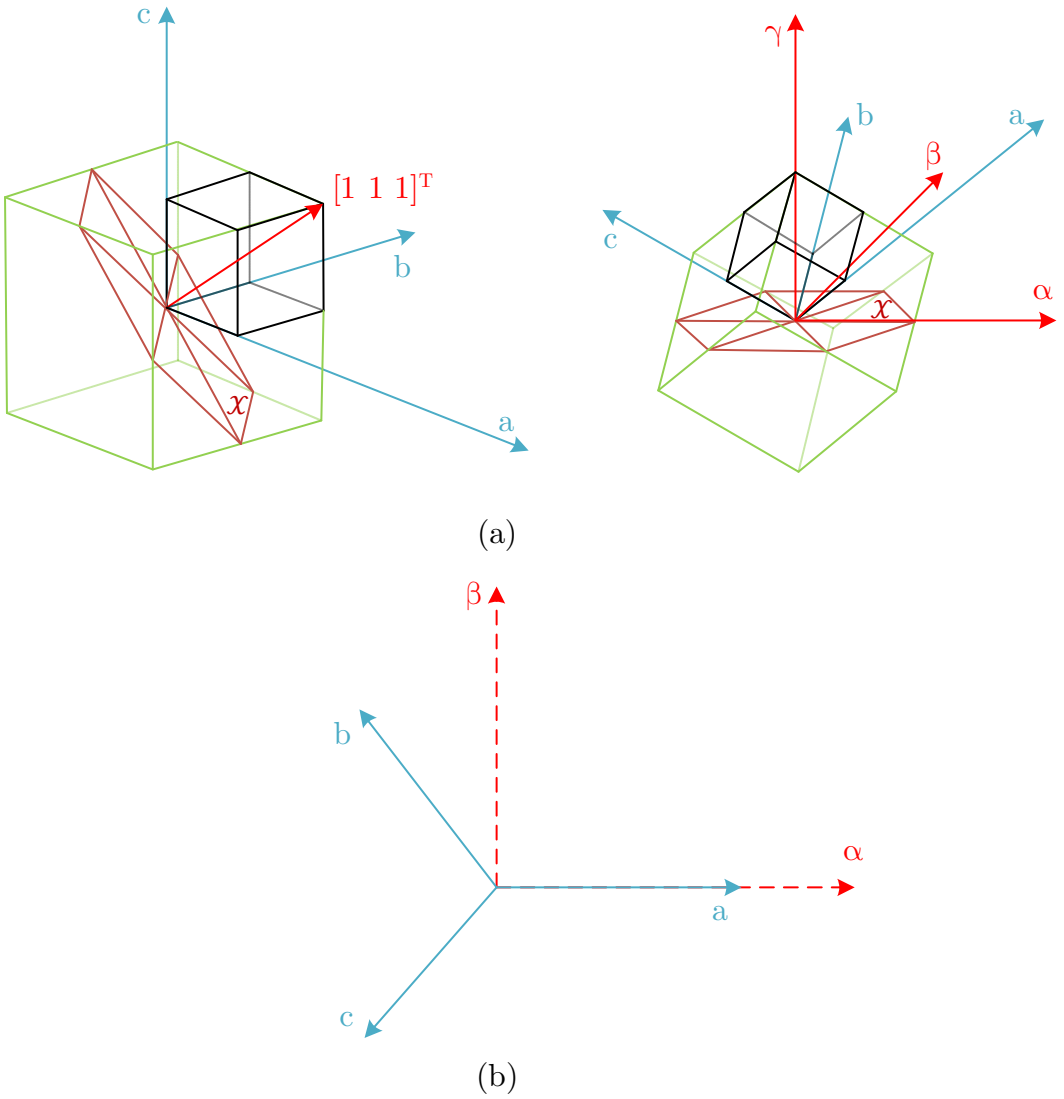

Figure B.1. (a) Cartesian coordinate system for variables abc, and αβ plane representation; (b) Location of abc axes when they are projected in the αβ plane

The transformation of three-phase variables to spatial vectors is divided in two alternatives:

- Stationary abc reference frame to stationary $\alpha\beta\gamma$ reference frame: It transforms three-phase variables into a vector with real and imaginary parts. The vector is moving with a rotating speed ω.
- Stationary $\alpha\beta\gamma$ reference frame to rotating *dq0* reference frame. The vector is transformed to time-invariant values. This is achieved by using a rotating reference frame that is moving at the same speed than the signals. The vector become a constant value signal.

B.2. Stationary $\alpha\beta$ reference frame

There are two possible transformations that define the value of k, the constant that is multiplying the transformation matrix.

- **Power invariance transformation**: The goal is to equalize the power in $\alpha\beta$-frame and abc-frame, that is $(B.5)$. Operating, the constant must have the value $k = \sqrt{2/3}$ to achieve the equivalence. Therefore, the equation $(B.3)$ is rewritten as $(B.6)$.

$$p(t) = u_\alpha(t) \cdot i_\alpha(t) + u_\beta(t) \cdot i_\beta(t) = u_a(t) \cdot i_a(t) + u_b(t) \cdot i_b(t) + u_c(t) \cdot i_c(t) \tag{B.5}$$

$$\begin{aligned} \vec{s}_{\alpha\beta}(t) &= s_\alpha(t) + j s_\beta(t) = \sqrt{\frac{2}{3}} \cdot \left[s_a(t) + s_b(t) \cdot e^{j\frac{2\pi}{3}} + s_c(t) \cdot e^{j\frac{4\pi}{3}} \right] \\ &= \sqrt{\frac{2}{3}} \cdot \left[s_a(t) - \frac{1}{2} \cdot s_b(t) - \frac{1}{2} \cdot s_c(t) + j\frac{\sqrt{3}}{2} \cdot \big(s_b(t) - s_c(t) \big) \right] \end{aligned} \tag{B.6}$$

Using the direct transformation $(abc \rightarrow \alpha\beta\gamma)$ in matrix form is $(B.7)$, and its inverse $(\alpha\beta\gamma \rightarrow abc)$ is $(B.8)$.

$$\vec{s}_{\alpha\beta}(t) = k \cdot T_{abc\rightarrow\alpha\beta\gamma} \cdot \vec{s}_{abc}(t) = \begin{bmatrix} s_\alpha(t) \\ s_\beta(t) \\ s_\gamma(t) \end{bmatrix} = \sqrt{\frac{2}{3}} \cdot \underbrace{\begin{bmatrix} 1 & -\frac{1}{2} & -\frac{1}{2} \\ 0 & \frac{\sqrt{3}}{2} & -\frac{\sqrt{3}}{2} \\ \frac{1}{\sqrt{2}} & \frac{1}{\sqrt{2}} & \frac{1}{\sqrt{2}} \end{bmatrix}}_{T_{abc\rightarrow\alpha\beta\gamma}} \cdot \begin{bmatrix} s_a(t) \\ s_b(t) \\ s_c(t) \end{bmatrix} \tag{B.7}$$

$$\vec{s}_{abc}(t) = k \cdot T_{\alpha\beta\gamma\rightarrow abc} \cdot \vec{s}_{\alpha\beta}(t) = \begin{bmatrix} s_a(t) \\ s_b(t) \\ s_c(t) \end{bmatrix} = \sqrt{\frac{2}{3}} \cdot \underbrace{\begin{bmatrix} 1 & 0 & \frac{1}{\sqrt{2}} \\ -\frac{1}{2} & \frac{\sqrt{3}}{2} & \frac{1}{\sqrt{2}} \\ -\frac{1}{2} & -\frac{\sqrt{3}}{2} & \frac{1}{\sqrt{2}} \end{bmatrix}}_{T_{\alpha\beta\gamma\rightarrow abc}} \cdot \begin{bmatrix} s_\alpha(t) \\ s_\beta(t) \\ s_\gamma(t) \end{bmatrix} \tag{B.8}$$

- **Amplitude invariance transformation**: In this transformation the abc vector amplitude is equalized with the $\alpha\beta$ vector amplitude. Operating, the constant must have the value $k = 2/3$ to achieve the equivalence. Hence, the equation $(B.3)$ is rewritten as $(B.9)$.

$$\begin{aligned} \vec{s}_{\alpha\beta}(t) &= s_\alpha(t) + j s_\beta(t) = \frac{2}{3} \cdot \left[s_a(t) + s_b(t) \cdot e^{j\frac{2\pi}{3}} + s_c(t) \cdot e^{j\frac{4\pi}{3}} \right] \\ &= \frac{2}{3} \cdot \left[s_a(t) - \frac{1}{2} \cdot s_b(t) - \frac{1}{2} \cdot s_c(t) + j\frac{\sqrt{3}}{2} \cdot \big(s_b(t) - s_c(t) \big) \right] \end{aligned} \tag{B.9}$$

Using the direct transformation $(abc \rightarrow \alpha\beta\gamma)$ in matrix form is $(B.10)$, and its inverse $(\alpha\beta\gamma \rightarrow abc)$ is $(B.11)$.

$$\vec{s}_{\alpha\beta}(t) = k \cdot T_{abc\rightarrow\alpha\beta\gamma} \cdot \vec{s}_{abc}(t) = \begin{bmatrix} s_\alpha(t) \\ s_\beta(t) \\ s_\gamma(t) \end{bmatrix} = \frac{2}{3} \cdot T_{abc\rightarrow\alpha\beta\gamma} \cdot \begin{bmatrix} s_a(t) \\ s_b(t) \\ s_c(t) \end{bmatrix} \tag{B.10}$$

$$\vec{s}_{abc}(t) = T_{\alpha\beta\gamma\rightarrow abc} \cdot \vec{s}_{\alpha\beta}(t) = \begin{bmatrix} s_a(t) \\ s_b(t) \\ s_c(t) \end{bmatrix} = T_{\alpha\beta\gamma\rightarrow abc} \cdot \begin{bmatrix} s_\alpha(t) \\ s_\beta(t) \\ s_\gamma(t) \end{bmatrix} \tag{B.11}$$

On one hand, for the power invariance transformation, the amplitude of each vector is equal to the line-to-line root-mean-square (RMS) vale of the original three-phase signal. On the other hand, for the amplitude invariance transformation, the instantaneous power is (*B*. 12).

$$p(t) = \frac{3}{2} \cdot \left[u_\alpha(t) \cdot i_\alpha(t) + u_\beta(t) \cdot i_\beta(t)\right] = u_a(t) \cdot i_a(t) + u_b(t) \cdot i_b(t) + u_c(t) \cdot i_c(t) \quad (B.12)$$

B.3. Rotating *dq* reference frame

To perform this transformation, the vector $\vec{s}_{\alpha\beta}$, that is moving with a rotating speed of ω, is multiplied by the operator $e^{-j\theta} = e^{-j\omega t}$, so the new components dq are constant (balanced system and a sole harmonic). The mathematical expression is (*B*. 13) and a graphical representation is depicted in Figure B.2.

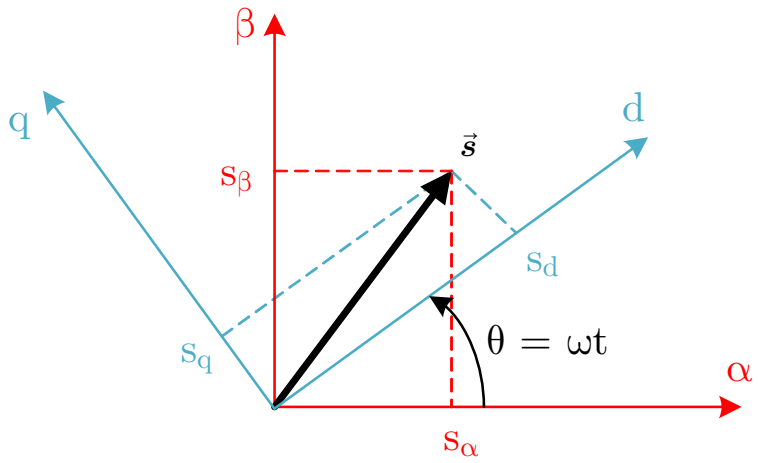

Figure B.2. Graphical representation of $\alpha\beta\gamma \rightarrow dq0$ transformation

$$\begin{aligned} \vec{s}_{dq}(t) = s_d(t) + j s_q(t) = \vec{s}_{\alpha\beta}(t) \cdot e^{-j\theta} = \left(s_\alpha(t) + j s_\beta(t)\right) \cdot (\cos\theta - j\sin\theta) = \\ = s_\alpha(t) \cdot \cos\theta + s_\beta(t) \cdot \sin\theta + j(-s_\alpha(t) \cdot \sin\theta + s_\beta(t) \cdot \cos\theta) \end{aligned} \quad (B.13)$$

Where θ is:

$$\theta(t) = \int_0^t \omega(\tau) d\tau + \theta(0) \quad (B.14)$$

Note that $e^{-j\theta}$ is valid for three-phase signal with positive sequence, so, for negative sequence, the operator must be $e^{j\theta}$.

The matrix expression of the transformation and its inverse are (*B*. 15) and (*B*. 16), respectively.

$$\vec{s}_{dq0}(t) = T_{\alpha\beta\gamma \rightarrow dq0} \cdot \vec{s}_{\alpha\beta\gamma}(t) = \begin{bmatrix} s_d(t) \\ s_q(t) \\ s_0(t) \end{bmatrix} = \begin{bmatrix} \cos\theta & \sin\theta & 0 \\ -\sin\theta & \cos\theta & 0 \\ 0 & 0 & 1 \end{bmatrix} \cdot \begin{bmatrix} s_\alpha(t) \\ s_\beta(t) \\ s_\gamma(t) \end{bmatrix} \quad (B.15)$$

$$\vec{s}_{\alpha\beta\gamma}(t) = T_{dq0 \rightarrow \alpha\beta\gamma} \cdot \vec{s}_{dq0}(t) = \begin{bmatrix} s_\alpha(t) \\ s_\beta(t) \\ s_\gamma(t) \end{bmatrix} = \begin{bmatrix} \cos\theta & -\sin\theta & 0 \\ \sin\theta & \cos\theta & 0 \\ 0 & 0 & 1 \end{bmatrix} \cdot \begin{bmatrix} s_d(t) \\ s_q(t) \\ s_0(t) \end{bmatrix} \quad (B.16)$$

For balanced systems, the component γ could be avoided, and third column and row are not necessary.

In the following, an example of grid voltage vector location is deduced in dq-frame. The three-phase grid voltage is expressed in $\alpha\beta$-frame as $(B.17)$ by means of power invariance transformation, the RMS value of line-to-line voltage is E and its frequency ω_1.

$$\vec{e}_{\alpha\beta}(t) = \sqrt{\frac{2}{3}} \cdot e_m \cdot (\cos(\omega_1 t) + j\sin(\omega_1 t)) = E \cdot e^{j\omega_1 t} \tag{B.17}$$

Usually, the grid flux vector $\vec{\Psi}_{\alpha\beta}$, that is obtained through $(B.18)$, is oriented to coincide with the d axis (grid control like synchronous machine control), so the grid voltage vector $\vec{e}_{\alpha\beta}$ is placed in the q axis. This is depicted in Figure B.3.

$$\vec{\Psi}_{\alpha\beta}(t) = \int_0^t E \cdot e^{j\omega_1 t}\, dt = \frac{\vec{e}_{\alpha\beta}(t)}{j\omega_1} = \frac{E}{\omega_1} \cdot e^{j(\omega_1 t - \frac{\pi}{2})} \tag{B.18}$$

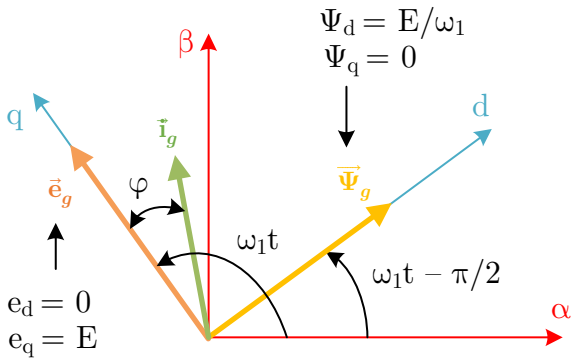

Figure B.3. Grid voltage and flux vectors location in dq reference frame

However, the grid voltage could be also oriented to the d axis, and in some simulations of this work, where only active power is carried out, the taken approach is this for the rotating reference frame. Therefore, the real part of current vector takes the reference value.

The apparent power is defined in dq-frame with power invariance transformation as $(B.19)$.

$$\vec{S}_g = P_g + jQ_g = \vec{e}_g \cdot \vec{i}_g^{\,*} = (e_d + je_q) \cdot (i_d + ji_q) = (e_d i_d + e_q i_q) - j(e_d i_q - e_q i_d) \tag{B.19}$$

Hence, there are two alternatives to provide a current reference based on the desired power exchange:

- If $e_d = 0$, P_g is controlled by i_q and Q_g by i_d

$$P_g = e_q i_q \quad Q_g = e_q i_d \tag{B.20}$$

- If $e_q = 0$, P_g is controlled by i_d and Q_g by i_q

$$P_g = e_d i_d \quad Q_g = e_d i_q \tag{B.21}$$

Appendix C. VSC basic control loops

The current control loop is the most inner controller in a VSC, and it is the one studied for the multirate cases in this document. However, to get the full controllability of the VSC, there are two other basic control structures for grid-tied purposes: DC-bus voltage control; and grid synchronization. The DC-bus voltage control provides the active power exchange to keep constant voltage in the capacitor banks. Hence, the exchanged active power is subordinated to the connected DC source (Back-to-Back disposition, batteries, etc.) or simply the VSC works as STATCOM (static synchronous compensator) and it only provides reactive power to the grid. On the other hand, the grid synchronization is necessary for every grid-tied application.

This appendix provides a general view for the possible application of the DC-bus voltage control loop, but it is possible to make first multirate approaches with a DC-bus already controlled by other VSC or DC voltage source.

These control loops could be designed with multirate purposes. The DC-bus voltage control is usually performed at slower sampling rate because it is supposed to be slower than the inner current control loop. And multirate PLL allows fast synchronization, despite of voltage sampling rate However, they are not in the scope of this work and they will be analyzed in future works.

C.1. DC-bus voltage control

C.1.1. DC-bus Modelling

There are two options to model the DC-bus voltage plant. The first option is based on the power flow between AC and DC sides. The second one is based on the stored energy in the DC-bus capacitors bank, i.e. the energy balance. The choice for this explanation is the second approach.

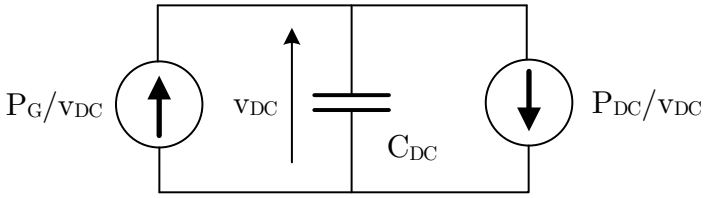

Figure C.1. Power flow in the DC-bus

The power flow in the DC-bus is described by equation ($C.1$), and the equivalent circuit is depicted in Figure C.1.

$$v_{DC}(t) \cdot C_{DC} \cdot \frac{dv_{DC}(t)}{dt} = P_G - P_{DC} \tag{C.1}$$

Being C_{DC} is the DC-bus total capacitor, P_g is the grid active power, and P_{DC} the DC-bus active power.

The equation $(C.1)$ can be rewritten as a function of the stored energy in the capacitor $(C.2)$. Besides, to linearize the expression, it is defined $u_{DC} = v_{DC}^2$, so the reference and feedback signal values must be squared.

$$\frac{1}{2} \cdot C_{DC} \cdot \frac{dv_{DC}^2(t)}{dt} = P_G - P_{DC} \rightarrow \frac{1}{2} \cdot C_{DC} \cdot \frac{du_{DC}(t)}{dt} = P_G - P_{DC} \tag{C.2}$$

Therefore, the DC-bus voltage model is $(C.3)$. The DC-bus active power can be supposed as a disturbance or can be used as a feedforward for the controller. Note that the VSC losses have been neglected.

$$G_{DC}(s) = \frac{U_{DC}(s)}{P_G(s)} = \frac{2}{s \cdot C_{DC}} \tag{C.3}$$

Finally, the model is discretized by means of ZOH $(C.4)$ and the final closed-loop scheme is shown in Figure C.2. Note that DC-bus controller provides an active power exchange with the grid to keep constant the DC-bus voltage. The actuation signal is given to the current reference calculator, so this controller must provide the reference with the sampling rate that was defined for the current reference and current feedback signals. Besides, to obtain better performances the current controller phase delay should be considered before the plant model, but this document has worked with multirate current controllers that are not easily analyzed.

$$G_{DC}(z) = \mathcal{Z}[G_{h0}G_{DC}(s)] = \frac{2}{C_{DC}} \cdot \frac{T}{z-1} \tag{C.4}$$

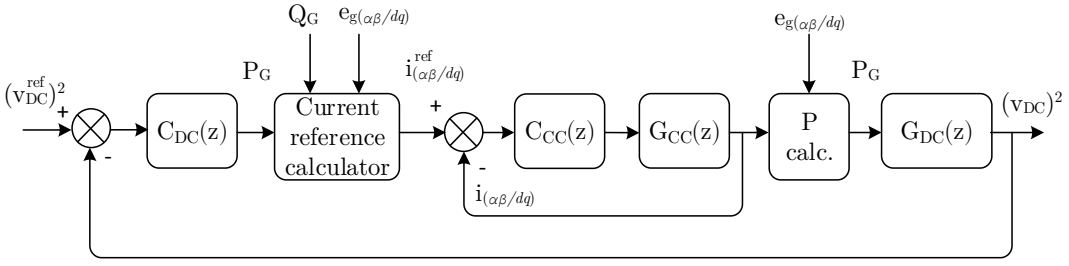

Figure C.2. DC-bus voltage closed-loop control

C.1.2. DC-bus Controller

The proposed controller is a PI as it is shown in equation $(C.5)$, so the closed-loop transfer function is $(C.6)$.

$$C_{DC}(z) = k_P \cdot \frac{z-\alpha}{z-1} \tag{C.5}$$

$$M_{DC}(z) = \frac{2k_PT}{C_{DC}} \cdot \frac{z-\alpha}{z^2 - \left(2 - \frac{2k_PT}{C_{DC}}\right) \cdot z + 1 - \frac{2k_PT}{C_{DC}} \cdot \alpha} \tag{C.6}$$

For pole-placement design, the denominator of $M_{DC}(z)$ is compared with $(C.7)$.

$$\begin{gathered} D(z) = (z - \rho \cdot e^{j\vartheta}) \cdot (z - \rho \cdot e^{-j\vartheta}) = z^2 - (2\rho\cos\vartheta) \cdot z + \rho^2 \\ \rho = e^{-(\xi\omega_n T)} \quad \vartheta = \omega_n T\sqrt{1-\xi^2} \end{gathered} \tag{C.7}$$

Finally, the PI controller constants are.

$$\begin{gathered} k_P = \frac{C_{DC}}{T} \cdot (1 - \rho\cos\vartheta) \\ \alpha = \frac{1-\rho^2}{2 \cdot (1 - \rho\cos\vartheta)} \\ k_I = \frac{k_P}{T} \cdot (1 - \alpha) \end{gathered} \tag{C.8}$$

The controller dynamics are obtained by means of damping factor $\xi = 1/\sqrt{2}$ (it usually obtains the most damped and fastest response) and defining a settling time as $(C.9)$, to obtain ω_n, and, finally, the PI constants.

$$t_s = T \cdot \frac{\ln 0.01}{\ln \rho} \tag{C.9}$$

This outer control loop must provide a response slower than the inner current controller. Regularly, the settling time of this DC-bus voltage controller is set 10 times higher than the current controller settling time.

For possible saturations due to the maximum power that can provide the VSC, an anti-windup control is included. The anti-windup constant is $(C.10)$.

$$k_{aw} = \frac{1}{k_P} \tag{C.10}$$

As a conclusion, the sampling period T must be adapted to that is defined for the inner current controller.

C.2. Grid synchronization

C.2.1. Objectives

To correctly control a VSC is essential to be synchronized with the grid phase. Good synchronizing systems can maximize the power factor, so its aims are:

- For a given grid voltage measurements, that are contaminated with noise, the module and phase of the fundamental harmonic must be recovered.
- Fast synchronization. If there is not synchronization, the controllers cannot operate.
- The phase signal must be noise-free.

Some usual options are:

- Zero-crossing detection. It is very sensitive to noise.
- Phase-Locked Loop (PLL). It is the chosen option due to its reliability.

C.2.2. Phase-Locked Loop (PLL)

The PLL is a feedback system which generates a signal with constant amplitude and equivalent phase to the input signal. The basic structure is presented in Figure C.3 and is composed of:

- **Phase Detector**: It is a non-linear system that provides a signal proportional to the phase difference of the input signals.
- **Loop filter**: It is a low-pass filter that rejects noise and harmonics other than fundamental. Besides, it defines the PLL dynamics (stable and locked speed), so a PI is usually used.
- **Voltage Controller Oscillator (VCO)**: It is a non-linear dispositive that generates an oscillation of which frequency is proportional to the input voltage.

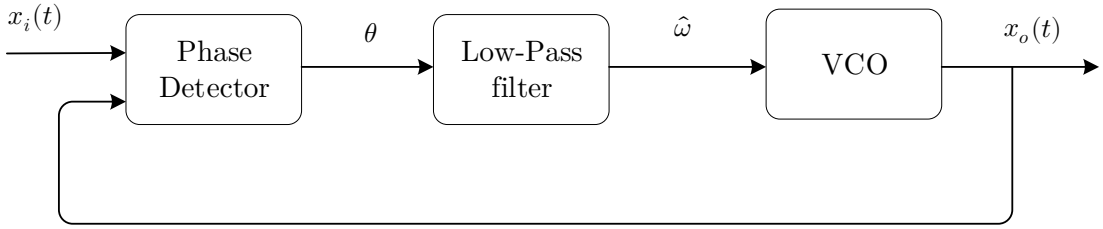

Figure C.3. Usual structure of monophasic PLL

The previous explanation is useful to describe the three-phase PLL. There are some options, but the Synchronous Reference Frame PLL (SFR-PLL) is the most used in three-phase systems. Figure C.4 shows the SRF-PLL scheme, where the phase θ is detected by means of the rotating dq reference frame transformation to grid voltage. Considering normal operation of SRF-PLL, the voltage components e_α and e_β are in quadrature, so the following equations express how the phase is detected.

$$\begin{bmatrix} e_\alpha \\ e_\beta \end{bmatrix} = k \cdot \begin{bmatrix} e_m \cdot \sin(\theta + \theta_{initial}) \\ -e_m \cdot \cos(\theta + \theta_{initial}) \end{bmatrix} \tag{C.11}$$

Applying the rotating dq transformation with an estimated phase $\hat{\theta}$ the following deduction is obtained:

$$\begin{bmatrix} e_d \\ e_q \end{bmatrix} = k \cdot \begin{bmatrix} \cos\left(\hat{\theta}\right) & \sin\left(\hat{\theta}\right) \\ -\sin\left(\hat{\theta}\right) & \cos\left(\hat{\theta}\right) \end{bmatrix} \cdot \begin{bmatrix} e_m \cdot \sin(\theta + \theta_{initial}) \\ -e_m \cdot \cos(\theta + \theta_{initial}) \end{bmatrix}$$
$$\begin{bmatrix} e_d \\ e_q \end{bmatrix} = k \cdot \begin{bmatrix} e_m \cdot \sin\left(\theta + \theta_{initial} - \hat{\theta}\right) \\ -e_m \cdot \cos\left(\theta + \theta_{initial} - \hat{\theta}\right) \end{bmatrix} \tag{C.12}$$

$$e_d = k \cdot e_m \cdot \sin\delta \approx \; k \cdot e_m \cdot (\theta + \theta_{initial} - \hat{\theta}) \tag{C.13}$$

Where e_m is the signal amplitude and k the transformation constant (power or amplitude invariance).

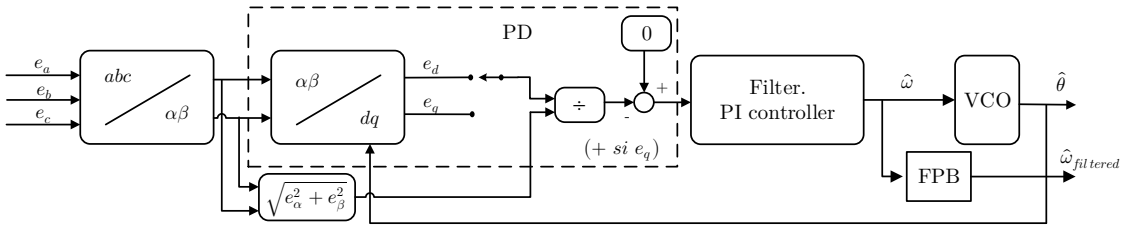

Figure C.4. Block diagram of the SRF-PLL

The PI controller makes zero the direct (e_d) or quadrature (e_q) component of the grid voltage (as it is explained in Appendix B.3, the direct component is usually set to zero). With ideal conditions (free-distortion or disbalance) an SRF-PLL with great bandwidth can accurately and quickly detect the phase and amplitude. For the sake of the PI dynamics, the input signal is always normalized ($C.14$), so it is not sensitive to amplitude changes.

$$e_d(p.u.) = \sin\delta \approx \left(\theta + \theta_{initial} - \hat{\theta}\right) \tag{C.14}$$

To get fastest responses, an initial frequency is given $\omega_{initial}$ to the integrator of the PI controller.

To get only the positive sequence of the grid and avoid all other harmonics from the SRF-PLL input signal, there are some adaptative pass-band filters. The most usual is the DSOGI (Dual Second Order General Integrator), that algorithm estimates positive and negative sequence of the grid voltage.

C.2.3. SRF-PLL controller

The plant to be controlled is an integrator, so the discrete-domain plant is ($C.15$) by means of ZOH.

$$G_{PLL}(z) = \frac{T}{z-1} \tag{C.15}$$

The PI controller is ($C.16$), thus the closed-loop transfer function is ($C.17$). Figure C.5 represents the closed-loop block diagram.

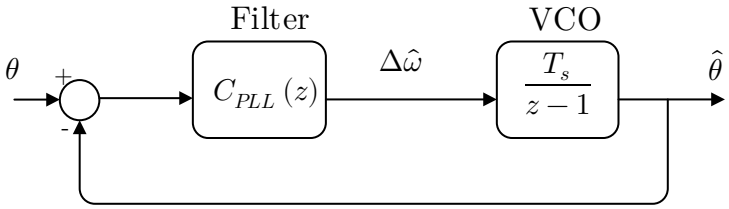

Figure C.5. Block diagram of closed-loop SRF-PLL control system

$$C_{PLL}(z) = k_P \cdot \frac{z-\alpha}{z-1} \tag{C.16}$$

$$M_{PLL}(z) = k_P \cdot T \cdot \frac{z-\alpha}{z^2 - (2 - k_P\alpha)\cdot z + 1 - k_P T\alpha} \tag{C.17}$$

Using the pole-placement technique the denominator of $M_{PLL}(z)$ is compared with ($C.18$).

$$D(z) = (z - \rho \cdot e^{j\vartheta}) \cdot (z - \rho \cdot e^{-j\vartheta}) = z^2 - (2\rho\cos\vartheta) \cdot z + \rho^2$$
$$\rho = e^{-(\xi\omega_n T)} \quad \vartheta = \omega_n T\sqrt{1-\xi^2} \tag{C.18}$$

Finally, the constants are:

$$k_P = \frac{2}{T} \cdot (1 - \rho\cos\vartheta)$$
$$\alpha = \frac{1-\rho^2}{2 \cdot (1 - \rho\cos\vartheta)} \tag{C.19}$$
$$k_I = \frac{k_P}{T} \cdot (1 - \alpha)$$

The system dynamics are defined by damping factor of $\xi = 1/\sqrt{2}$ and a natural frequency ω_n that is obtained through the expression (C. 20) for the desired settling time.

$$t_s = T \cdot \frac{\ln 0.01}{\ln \rho} \tag{C.20}$$

The settling time is set to 10 *ms* in this work, and the sampling rate T for the PLL is defined as the fastest one in every multirate test, so it is related to the actuation sampling rate. Note that the controllers will not be initiated until the VSC is totally synchronized.

References

[1] N. G. Hingoranl, L. Gyugyi, and M. E. El-Hawary, *Understanding FACTS: Concepts and technology of flexible ac transmission systems*. 1999.

[2] H. Abu-Rub, J. Holtz, and J. Rodriguez, "Medium-Voltage Multilevel Converters—State of the Art, Challenges, and Requirements in Industrial Applications," *IEEE Trans. Ind. Electron.*, vol. 57, no. 8, pp. 2581–2596, 2010.

[3] D. Krug, S. Bernet, S. S. Fazel, K. Jalili, and M. Malinowski, "Comparison of 2.3-kV medium-voltage multilevel converters for industrial medium-voltage drives," *IEEE Trans. Ind. Electron.*, vol. 54, no. 6, pp. 2979–2992, 2007.

[4] N. Mohan, T. M. Undeland, and W. P. Robbins, *Power Electronics Converters, Applications, and Design*, vol. 4. 2007.

[5] J. C. Balda and A. Mantooth, "Power-Semiconductor Devices and Components for New Power Converter Developments: A key enabler for ultrahigh efficiency power electronics," *IEEE Power Electron. Mag.*, vol. 3, no. 2, pp. 53–56, 2016.

[6] S. Madhusoodhanan *et al.*, "Comparison study of 12kV n-type SiC IGBT with 10kV SiC MOSFET and 6.5kV Si IGBT based on 3L-NPC VSC applications," in *2012 IEEE Energy Conversion Congress and Exposition, ECCE 2012*, 2012, pp. 310–317.

[7] S. Pavljašević and F. Dawson, "Synchronization to disturbed utility-network signals using a multirate phase-locked loop," *IEEE Trans. Ind. Electron.*, vol. 53, no. 5, pp. 1410–1417, 2006.

[8] J. R. de Carvalho, C. A. Duque, M. V. Ribeiro, A. S. Cerqueira, T. L. Baldwin, and P. F. Ribeiro, "A PLL-based multirate structure for time-varying power systems harmonic/ interharmonic estimation," *IEEE Trans. Power Deliv.*, vol. 24, no. 4, pp. 1789–1800, 2009.

[9] A. J. V Miller and M. B. Dewe, "The application of multi-rate digital signal processing techniques to the measurement of power system harmonic levels," *IEEE Trans. Power Deliv.*, vol. 8, no. 2, pp. 531–539, 1993.

[10] Bin Wu, J. Pontt, J. Rodriguez, S. Bernet, and S. Kouro, "Current-Source Converter and Cycloconverter Topologies for Industrial Medium-Voltage Drives," *IEEE Trans. Ind. Electron.*, vol. 55, no. 7, pp. 2786–2797, Jul. 2008.

[11] S. Alonso, "Comparative Analysis of Multilevel Converters for Medium-Voltage Applications," University of Alcalá de Henares, 2017.

[12] R. H. Baker, "High-Voltage Converter Circuit," 1980.

[13] A. Nabae, I. Takahashi, and H. Akagi, "A New Neutral-Point-Clamped PWM Inverter," *IEEE Trans. Ind. Appl.*, vol. IA-17, no. 5, pp. 518–523, Sep. 1981.

[14] Á. M. Cuenca Lacruz, "Modelado, análisis y diseño de sistemas de control con muestreo no convencional," Universidad Politécnica de Valencia, 2004.

[15] J. Sklansky and J. R. Ragazzini, "Analysis of errors in sampled-data feedback systems," *Trans. Am. Inst. Electr. Eng. Part II Appl. Ind.*, vol. 74, no. 2, pp. 65–71, May 1955.

[16] W. Boykin and B. Frazier, "Multirate sampled-data systems analysis via vector operators," *IEEE Trans. Automat. Contr.*, vol. 20, no. 4, pp. 548–551, Aug. 1975.

[17] R. Aracil, A. J. Avello, and V. Feliu, "Multirate sampling technique in digital control systems simulation," *IEEE Trans. Syst. Man. Cybern.*, vol. SMC-14, no. 5, pp. 776–780, Sep. 1984.

[18] J. Salt and P. Albertos, "Multirate controllers design by rate decomposition," in *Proceedings of the 39th IEEE Conference on Decision and Control (Cat. No.00CH37187)*, vol. 5, pp. 4895–4900.

[19] G. Kranc, "Input-output analysis of multirate feedback systems," *IRE Trans. Autom. Control*, vol. 3, no. 1, pp. 21–28, Nov. 1957.

[20] J. R. Ragazzini and G. F. Franklin, *Sampled-data control systems*. McGraw-Hill, 1958.

[21] E. I. Jury, "A Note on Multirate Sampled-Data Systems," *IEEE Trans. Automat. Contr.*, vol. AC-12, no. 3, pp. 319–320, 1967.

[22] D. G. J. Didaleusky and R. F. Whitbeck, "Multi-Rate Digital Control Systems with Simulation Applications," Ohio, 1980.

[23] M. Araki and K. Yamamoto, "Multivariable multirate sampled-data systems: State-space description, transfer characteristics, and Nyquist criterion," *IEEE Trans. Automat. Contr.*, vol. 31, no. 2, pp. 145–154, Feb. 1986.

[24] R. E. Kalman and J. E. Bertram, "A unified approach to the theory of sampling systems."

[25] M. Araki and T. Hagiwara, "Pole assignment by multirate sampled-data output feedback," in *1985 24th IEEE Conference on Decision and Control*, 1985, pp. 189–193.

[26] T. Hagiwara and M. Araki, "Design of a stable state feedback controller based on the multirate sampling of the plant output," *IEEE Trans. Automat. Contr.*, vol. 33, no. 9, pp. 812–819, 1988.

[27] L. F. Godbout, D. Jordan, and I. S. Apostolakis, "Closed-loop model for general multirate digital control systems," *IEE Proc. D Control Theory Appl.*, vol. 137, no. 5, p. 329, 1990.

[28] I. S. Apostolakis and D. Jordan, "Robust design of reduced order multirate compensators using constrained optimization techniques," in *[1992] Proceedings of the 31st IEEE Conference on Decision and Control*, pp. 1774–1779.

[29] P. M. Thompson, "Gain and phase margins of multi-rate sampled-data feedback systems," *Int. J. Control*, vol. 44, no. 3, pp. 833–846, 1986.

[30] P. Albertos, "Block multirate input-output model for sampled-data control systems," *IEEE Trans. Automat. Contr.*, vol. 35, no. 9, pp. 1085–1088, 1990.

[31] J. Salt and P. Albertos, "Model-based multirate controllers design," *IEEE Trans. Control Syst. Technol.*, vol. 13, no. 6, pp. 988–997, Nov. 2005.

[32] Á. Cuenca, J. Salt, A. Sala, and R. Piza, "A Delay-Dependent Dual-Rate PID

Controller Over an Ethernet Network," *IEEE Trans. Ind. Informatics*, vol. 7, no. 1, pp. 18–29, Feb. 2011.

[33] P. E. Barry, "Optimal control of multirate systems."

[34] N. Amit and J. D. Powell, "Optimal digital control of multirate systems," Jan. 1981.

[35] J. Glasson, D.P.; Dowd, "Research in Multirate Estimation and Control-Optimal Sample Rate Selection," MA, 1981.

[36] R. Meyer and C. Burrus, "A unified analysis of multirate and periodically time-varying digital filters," *IEEE Trans. Circuits Syst.*, vol. 22, no. 3, pp. 162–168, Mar. 1975.

[37] P. Khargonekar, K. Poolla, and A. Tannenbaum, "Robust control of linear time-invariant plants using periodic compensation," *IEEE Trans. Automat. Contr.*, vol. 30, no. 11, pp. 1088–1096, Nov. 1985.

[38] P. Misra, "Time-invariant representation of discrete periodic systems," *Automatica*, vol. 32, no. 2, pp. 267–272, Feb. 1996.

[39] J. Tornero and P. Albertos, "A New Methodology for Modelling, Analysis and Control Design of Non-Conventional Sampled Data Systems," *IFAC Proc. Vol.*, vol. 19, no. 6, pp. 227–232, May 1986.

[40] Y. Yamamoto and M. Araki, "Frequency responses for sampled-data systems—their equivalence and relationships," *Linear Algebra Appl.*, vol. 205–206, pp. 1319–1339, Jul. 1994.

[41] D. G. Holmes and T. A. Lipo, "Pulse Width Modulation for Power Converters: Principles and Practice," *Pulse Width Modul. Power Convert. Pract.*, vol. 00, no. June 1949, pp. 531–554, 2003.

[42] Chumei Feng and V. G. Agelidis, "On the comparison of fundamental and high frequency carrier-based PWM techniques for multilevel NPC inverters," in *2002 IEEE 33rd Annual IEEE Power Electronics Specialists Conference. Proceedings (Cat. No.02CH37289)*, vol. 2, pp. 520–525.

[43] B. Li, R. Yang, D. Xu, G. Wang, W. Wang, and D. Xu, "Analysis of the Phase-Shifted Carrier Modulation for Modular Multilevel Converters," *IEEE Trans. Power Electron.*, vol. 30, no. 1, pp. 297–310, Jan. 2015.

[44] R. Rojas, T. Ohnishi, and T. Suzuki, "An improved voltage vector control method for neutral-point-clamped inverters," *IEEE Trans. Power Electron.*, vol. 10, no. 6, pp. 666–672, 1995.

[45] H. S. Patel and R. G. Hoft, "Generalized Techniques of Harmonic Elimination and Voltage Control in Thyristor Inverters: Part I--Harmonic Elimination," *IEEE Trans. Ind. Appl.*, vol. IA-9, no. 3, pp. 310–317, May 1973.

[46] P. N. Enjeti and R. Jakkli, "Optimal power control strategies for neutral point clamped (NPC) inverter topology," *IEEE Trans. Ind. Appl.*, vol. 28, no. 3, pp. 558–566, 1992.

[47] S. Kouro, R. Bernal, H. Miranda, Cé. A. Silva, and J. Rodriguez, "High-Performance Torque and Flux Control for Multilevel Inverter Fed Induction Motors," *IEEE Trans. Power Electron.*, vol. 22, no. 6, pp. 2116–2123, Nov. 2007.

[48] N. Hoffmann, F. W. Fuchs, M. P. Kazmierkowski, and D. Schroder, "Digital Current Control in a Rotating Reference Frame - Part I: System Modeling and the Discrete Time-Domain Current Controller with Improved Decoupling Capabilities," *IEEE Trans. Power Electron.*, vol. 31, no. 7, pp. 5290–5305, 2016.

[49] D. G. Holmes, T. A. Lipo, B. P. McGrath, and W. Y. Kong, "Optimized Design of Stationary Frame Three Phase AC Current Regulators," *IEEE Trans. Power Electron.*, vol. 24, no. 11, pp. 2417–2426, Nov. 2009.

[50] S. Buso and P. Mattavelli, *Digital Control in Power Electronics*. 2015.

[51] H. S. Patel and R. G. Hoft, "Generalized Techniques of Harmonic Elimination and Voltage Control in Thyristor Inverters: Part I--Harmonic Elimination," *IEEE Trans. Ind. Appl.*, vol. IA-9, no. 3, pp. 310–317, May 1973.

[52] D. M. Van De Sype, K. De Gussemé, A. P. Van Den Bossche, and J. A. Melkebeek, "Small-signal laplace-domain analysis of uniformly-sampled pulse-width modulators," *PESC Rec. - IEEE Annu. Power Electron. Spec. Conf.*, vol. 6, pp. 4292–4298, 2004.

[53] L. Corradini, W. Stefanutti, and P. Mattavelli, "Analysis of Multisampled Current Control for Active Filters," *Ind. Appl. IEEE Trans.*, vol. 44, no. 6, pp. 1785–1794, 2008.

[54] E. Tedeschi, P. Mattavelli, D. Trevisan, and L. Corradini, "Repetitive Ripple Estimation in Multi-sampling Digitally Controlled dc-dc Converters," in *IECON 2006 - 32nd Annual Conference on IEEE Industrial Electronics*, 2006, pp. 1685–1690.

[55] J. Ma, X. Wang, F. Blaabjerg, L. Harnefors, and W. Song, "Accuracy analysis of the zero-order hold model for digital pulsewidth modulation," in *2017 IEEE Energy Conversion Congress and Exposition (ECCE)*, 2017, pp. 5767–5774.

[56] C. A. Busada, S. Gomez Jorge, A. E. Leon, and J. A. Solsona, "Current Controller Based on Reduced Order Generalized Integrators for Distributed Generation Systems," *IEEE Trans. Ind. Electron.*, vol. 59, no. 7, pp. 2898–2909, 2012.

[57] P. Mattavelli, F. Polo, F. Dal Lago, and S. Saggini, "Analysis of control-delay reduction for the improvement of UPS voltage-loop bandwidth," *IEEE Trans. Ind. Electron.*, vol. 55, no. 8, pp. 2903–2911, 2008.

[58] B. Zhang, K. Zhou, and D. Wang, "Multirate repetitive control for PWM DC/AC converters," *IEEE Trans. Ind. Electron.*, vol. 61, no. 6, pp. 2883–2890, 2014.

[59] C. Xie, X. Zhao, M. Savaghebi, L. Meng, J. Guerrero, and J. Vasquez, "Multi-Rate Fractional-Order Repetitive Control of Shunt Active Power Filter," *IEEE J. Emerg. Sel. Top. Power Electron.*, vol. 6777, no. c, pp. 1–1, 2016.

[60] H. W. Thomas and N. P. Lutte, "z-transform analysis of nonuniformly sampled digital filters," *Proc. Inst. Electr. Eng.*, vol. 119, no. 11, p. 1559, 1972.

[61] M. Huang, X. Wang, P. C. Loh, and F. Blaabjerg, "LLCL-Filtered Grid Converter with Improved Stability and Robustness," in *IEEE Transactions on Power Electronics*, 2016.

[62] T. Dragicevic, D. Wu, Q. Shafiee, and L. Meng, "Distributed and Decentralized

Control Architectures for Converter-Interfaced Microgrids," *Chinese J. Electr. Eng.*, vol. 3, no. 2, pp. 41–52, 2017.

[63] A. Mohd, E. Ortjohann, D. Morton, and O. Omari, "Review of control techniques for inverters parallel operation," *Electr. Power Syst. Res.*, vol. 80, no. 12, pp. 1477–1487, Dec. 2010.

[64] T. C. Green and M. Prodanović, "Control of inverter-based micro-grids," *Electr. Power Syst. Res.*, vol. 77, no. 9, pp. 1204–1213, Jul. 2007.

[65] B. C. Kuo, *Digital Control Systems*, 2nd ed. Oxford University Press, 1992.

Universidad de Alcalá

Escuela Politécnica Superior

ESCUELA POLITECNICA SUPERIOR

Universidad de Alcalá